THE PREDICTION OF DEFIBRILLATION OUTCOME USING TIME-FREQUENCY POWER SPECTRUM METHODS

A thesis submitted in partial fulfilment of the requirements of Napier University for the degree of Doctor of Philosophy

By
Nopadol Uchaipichat

June, 2005

School of the Built Environment,
Napier University,
Edinburgh, Scotland, U.K.

The following has been excluded at the request of the university

Pages 307 - 336

ABSTRACT

A study was conducted to investigate the use of time-frequency methods to predict the outcome of defibrillation for patients presenting with ventricular fibrillation. Both wavelet transform and short time Fourier transform methods were applied to extract characteristic features from a data base of pre-shock signals. A Bayes classifier was developed for classifying between those outcomes where a return of spontaneous circulation (ROSC) was achieved and those where it was not (NOROSC). Probability distribution functions were estimated using multidimensional histogram and Gaussian kernel smoothing techniques. Cross validation was employed to improve the confidence of results. Three formats of feature sets including the original feature sets, normalised feature sets, and principal component analysis (PCA) feature sets were used in the classification. The optimal pre-shock length and temporal location were investigated. In related studies the *a posterior* probability function was employed to indicate the probability of successful shock (PROSC) and the effect of wavelet central frequency was also studied.

The best classification performance for the original, normalised, and PCA feature sets were 58±2% specificity at 90±4% sensitivity, 59±3% specificity at 90±4% sensitivity, and 56±3% specificity at 92±4% sensitivity respectively. Overall it was found that the analysis employing time-frequency-based methods improved the performance of shock outcome prediction when compared to currently available alternative methods.

ACKNOWLEDGEMENT

There are many people whom the author would like to thank for their support through the course of this research. Firstly, I wish to express my gratitude to Professor Paul Addison, thesis supervisor, for his helpful recommendations and constructive discussions.

I would like to thank Dr James Watson who advised me on the wavelet transform. I also would like to express my gratitude to Dr Neil Grubb and Dr Gareth Clegg for their medical guidance.

I would like to acknowledge the support of the School of the Built Environment, Napier University and Thammasat University who supported this work through research studentship awards.

Special thank to my colleagues at Napier University and Cardiodigtal Ltd with whom I have shared many memorable times.

Finally, I would like to thank my parents for their continued support during the production of this thesis.

DECLARATION

This thesis is submitted to Napier University for the degree of Doctor of Philosophy. The work described herein was carried out under the supervision of Professor Paul Addison. The work was undertaken within the School of the Built Environment, Napier University. Except where stated otherwise, this thesis is the result of my own work and in accordance with the Napier University regulations governing the degree of Doctor of Philosophy. This thesis has not been submitted in whole or in part for any degree or diploma at this or any other university.

During the period of research the following papers have been published and/or presented at conference:

1. Addison P S, Uchaipichat N, Watson J N, Clegg G R, Robertson C E, Steen P A, and Eftestol T (2001), *"Wavelet power spectrum-based prediction of successful defibrillation from ventricular fibrillation"*, Proceeding of The 23rd Annual International Conference of the IEEE Engineering in Medicine and Biology Society, October 25-28, 2001 in Istanbul, Turkey.

2. Uchaipichat N, Watson J N, Addison P S, Clegg G R, Robertson C E, Steen P A, and Eftestol T (2001), *"Wavelet power spectrum analysis of cardiac arrhythmias: ventricular fibrillation"*, Proceeding of The 24th Electrical Engineering Conference, Thailand.

3. Uchaipichat N, Watson J N, Addison P S, Clegg G R, Robertson C E, Steen P A, and Eftestol T (2002), *"Optimal pre-shock signal length for time-frequency classification used in the prediction of successful defibrillation"* Proceeding of International Congress on Biological and Medical Engineering in Singapore.

4. Addison P S, Uchaipichat N, Watson J N, Clegg G R, Robertson C E, Steen P A, and Eftestol T (2002), *"Positional dependence of time-frequency information in the ECG used for the prediction of defibrillation success"* Proceeding of 2nd European Medical & Biological Engineering Conference in Vienna.

5. Uchaipichat N, Addison P S, G R, Robertson C E, Steen P A, Eftestol T and Watson J N (2003), "*Wavelet transform-based methods to assess pre-shock probability of successful defibrillation in patients with ventricular fibrillation*", Proceeding of 2nd IEEE EMBS UK&RoI Postgraduate Conference on Biomedical Engineering & Medical Physics, Birmingham, UK.

6. Watson J N, Uchaipichat N, Addison P S, Clegg G R, Robertson C E, Eftestol T, and Steen P A (2004), "*Improved prediction of defibrillation success for out-of-hospital VF cardiac arrest using wavelet transform methods*", Resuscitation, Vol. 63, pp. 269-275.

These publications are reproduced in appendix C

Nopadol Uchipichat
Napier University, Edinburgh

CONTENTS

CHAPTER 3 METHODOLOGY

CHAPTER 4 SHOCK OUTCOME PREDICTION

LIST OF TABLES

CHAPTER 1

There are no tables associated with Chapter 1

CHAPTER 2

There are no tables associated with Chapter 2

CHAPTER 3

CHAPTER 4

CHAPTER 5

CHAPTER 6

There are no tables associated with Chapter 6

List of Figures

CHAPTER 1

There are no figures associated with Chapter 1

CHAPTER 2

CHAPTER 3

CHAPTER 4

CHAPTER 5

CHAPTER 6

NOMENCLATURE

Letters

BI	bisector frequency
C	loss matrix
C_g	admissibility constant
E	1) energy 2) expectation
FM	median frequency
FP	peak frequency
FT	flatness
$Im(\cdot)$	imaginary part
KT	kutosis
N	cross validation number
N_b	number of bins
N_w	Gaussian width
$P(\omega_j)$	*a priori* probability for class ω_j
$P(\omega_j/v_i)$	*a posteriori* probability for class ω_j on feature v_i
R	1) risk function 2) ratio
$Re(\cdot)$	real part
SH	Shannon entropy
SK	skewness
STD	standard deviation
$T(a,b)$	wavelet transform
V	feature vector
a	wavelet scale
b	location parameter
f	frequency
f_c	passband centre of the mother wavelet
i	row
j	column
$p(v_i/\omega_j)$	class conditional density function
t	time
v_i	member of feature vector
w_i	shock outcome

Greek symbols

Σ	1) summation 2) covariance matrix
Ψ	Fourier transform of wavelet function
$\Psi_{a,b}$	Fourier transform of scaling wavelet function
β	risk value
α	learning rate
σ^2	variance
ρ	correlation coefficient
τ	time shifting

μ	mean
ψ	wavelet function
$\psi_{a,b}$	scaling wavelet function
ω	radial frequency
ω_i	decision class
ω_o	wavelet central frequency

Acronyms

1D	one-dimensional
2D	two-dimensional
AF	atrial fibrillation
AMSA	amplitude spectrum area
ALS	advanced life support
AUC	area under (ROC) curve
AV	atrioventricular
AVFV	absolute VF voltage
BLS	basic life support
CPP	coronary perfusion pressure
CPR	cardiopulmonary resuscitation
CWT	continuous wavelet transform
DC	direct current
ECG	electrocardiogram
EMD	electromechanical disassociation
ERC	European Resuscitation Council
FFT	fast Fourier transform
GP	genetic programming
IQR	interquartile range
LDA	linear discriminant analysis
MCG	magnetocardiogram
MCM	medical control module
NN	neural network
NOROSC	no return of spontaneous circulation
OS	operation system
PCA	principal component analysis
PCG	phonocardiogram
PDF	probability distribution function
PEA	pulseless electrical activity
RBN	radial basis function
ROC	receiving operator characteristic
ROSC	return of spontaneous circulation
PROSC	probability of successful defibrillation
STFT	short time Fourier transform
STFT1	short time Fourier transform using 1 second window width
STFT2	short time Fourier transform using 2 second window width
STFT3	short time Fourier transform using 3 second window width
SVT	supraventricular tachycardia
WRST	Wilcoxon rank sum test
WT	wavelet transform
VLP	ventricular late potential

VF	ventricular fibrillation
VT	ventricular tachycardia

CHAPTER 1
INTRODUCTION

1.1 Cardiac arrhythmias

1.2 Scope of the research

1.3 Thesis outline

CHAPTER 1
INTRODUCTION

1.1 Cardiac arrhythmias

Cardiac arrhythmias can be catastrophic and life threatening. Ventricular tachyarrhythmias, in particular ventricular fibrillation (VF), are the primary arrhythmic events in the majority of patients who present with sudden cardiac death (Goldstein et al, 1981; Jacobs and Oxer, 1990). VF is the most common arrhythmic cause of sudden cardiac death since the heart fails to pump blood effectively. VF is a disordered electrical activity causing the ventricles to contract in a rapid, unsynchronized, uncoordinated fashion. The quivering ventricles are unable to contract or pump blood to the body. This is a medical emergency that must be treated with cardiopulmonary resuscitation (CPR) and defibrillation as soon as possible. The administration of a defibrillation shock using an electrical defibrillator is the only known therapy for the treatment of VF. However, an unsuccessful defibrillation causes tissue damage during the shock period (Xie et al, 1997).

Considerable interest has focused upon these particular rhythms as it is recognised that prompt therapy can lead to a successful outcome. For these reasons there has been considerable interest in analysis of the VF waveform in order to predict the shock outcome of defibrillation shock. Over recent years, three main techniques have been employed in the prediction of defibrillation outcome; these are:

- Waveform amplitude-based methods (Weaver et al, 1985; Monsieurs et al, 1998; Amann et al, 2001; Callaway et al, 2001)

- Fourier transform-based methods (Brown et al, 1991; Stewart et al, 1992; Strohmenger et al, 1994; Eftestol et al, 2000; Hamprecht et al, 2001)

- Combined frequency and amplitude-based method (Brown and Dzwonczyk, 1996; Strohmenger et al, 1997 and 2001; Noc et al, 1999; Marn-Pernat et al, 2001; Amann et al, 2002; Povoas et al, 2002)

However, it is interesting to note that, to date, none of these techniques have proven reliable enough for clinical application.

Until recently, the surface electrocardiogram (ECG) recorded during VF was thought to represent disorganised and unstructured electrical activity of the heart. This is in stark contrast to the information rich ECG in other states of health and disease (Rude et al, 1983; Brush et al, 1985). However, recent work by Addison et al (2001) and Watson et al (2000) has shown that rich structure may be found in the VF waveform. This structure was made visible using signal analysis techniques based on the wavelet transform.

1.2 Scope of the research

The aim of this research was to improve shock outcome prediction from the VF signal through the use of wavelet transform (WT) and short time Fourier transform (STFT) based time-frequency analysis methods.

This aim was accomplished by achieving the following objectives:

- To review the applications of time-frequency methods, in particular the wavelet transform, in the analysis of biomedical signals

- To review the literature concerning the analysis of shock outcome prediction

- To develop a power spectrum analysis based on continuous wavelet transform (CWT) and STFT time-frequency decompositions

- To employ a classification method to discriminate between successful and unsuccessful shock outcomes based on features extracted from the time-frequency power spectra

- To investigate the effect of principal component analysis (PCA) on classifier performance

- To determine the optimal length of pre-shock VF signal for shock outcome prediction

- To study the effect of central frequency of wavelet function on the shock outcome prediction

- To investigate the probability of successful defibrillation (PROSC) for expressing multivariable features

1.3 Thesis outline

This thesis is structured as follows:

Chapter 2 presents a brief background of the relevant cardiology including an overview of the cardiovascular system, electrocardiogram, and cardiac arrhythmias. In addition, this chapter presents the techniques of signal analysis using time-frequency transforms. In this report, the short time Fourier transform and the wavelet transform are applied to a number of example signals. A review of the literature concerning the use of WT's in the analysis of cardiac signals is then presented followed by a review of shock outcome prediction work by other research groups.

Chapter 3 describes the methodology of the research. This includes the ECG data set used and the analysis techniques employed in the study. The methodology can be separated into three parts: i.e. feature extraction, data pre-processing, and data classification. The computer implementation of the methodology is also explained in this chapter.

Chapter 4 details the results of the research. This is split into three parts:

1. Experiments using original characteristic feature sets
2. Experiments using normalised feature sets
3. The use of feature sets based on principal component analysis (PCA)

Chapter 5 describes supplemental studies involving the use of wavelet analysis in the prediction of defibrillation outcome. In the first study, the probability of successful defibrillation (PROSC) is studied as a variable for monitoring CPR efficiency. The second study considers the effect of changing wavelet central frequency on the shock outcome prediction.

Finally, chapter 6 contains a discussion of the work detailed in this thesis together with conclusions and recommendations for future work.

CHAPTER 2
LITERATURE REVIEW

CHAPTER 2
LITERATURE REVIEW

2.1 Introduction

This chapter introduces and reviews the background of research undertaken by other groups related to the work detailed in this thesis. The chapter begins with a brief review of cardiology describing the cardiovascular system and cardiac arrhythmias. The concept of time-frequency analysis is then explained in section 2.3, focusing on the short time Fourier transform (STFT) and the wavelet transform (WT). Both transforms are introduced in terms of their mathematics and illustrations are used to convey the key concepts. Time-frequency analyses of example signals are employed in this section to achieve this. Section 2.4 reviews cardiology papers where wavelet transform analysis has been employed. A review of defibrillation prediction is covered in section 2.5 and, finally, a chapter summary is provided in section 2.6.

2.2 Background material in cardiology

2.2.1 Overview of the cardiovascular system

The cardiovascular system is illustrated in the closed loop diagram shown in figure 2-1. This loop consists of two pumps (the left heart and the right heart) and two vascular systems (the pulmonary circulation and the systemic circulation). As shown

in figure 2-1, there are two independent pumps from a physiologic perspective, even though there is only one heart from an anatomical perspective. Since the left and right heart pumps are both mechanically and electrically interdependent, these pumps can be independently visualised in the blood circulation system. Blood flows through the pumps (the left and right heart) and the vascular system (the pulmonary and systemic circulation) in sequence. The blood flows through the lungs via the pulmonary circulation where oxygen is added and carbon dioxide is removed. The oxygenated blood from the pulmonary circulation flows through the left heart, and then the blood flows via the system circulation (all cells of the body) extracting oxygen and adding carbon dioxide to the blood and the cycle repeats.

As stated above, the heart consists of two functionally distinct pumps: the left heart and the right heart. Each pump contains two chambers: an atrium and a ventricle. The atria are thin-walled chambers receiving blood from the pulmonary and systemic circulation. Figure 2-2 shows schematically the direction of blood flow indicated by the arrows through the chambers of the heart and the major vessels leading into and out of the heart. The atrium of the right heart receives blood from the vena cavae and the atrium of the left heart receives blood from the pulmonary veins. Blood is then pumped from each atrium into the associated ventricle via the tricuspid valve in the right heart and the mitral valve in the left heart. The ventricles, in particular the left ventricle, have thicker muscular walls capable of pumping blood out of the heart at higher pressures. The blood leaves the right ventricle and the left ventricle by way of the pulmonary artery and aorta respectively. Then, blood from the right ventricle flows through the pulmonary circulation and blood from the left ventricle flows through the systemic circulation.

2.2.2 Electrocardiogram (ECG)

The electrocardiogram (ECG) is a recording from the body surface of the electrical changes that occur within the heart during the cardiac cycle. The ECG is one of the most widely used and helpful investigations in contemporary medicine. It is essential for the identification of disorders of the cardiac rhythm, extremely useful for the diagnosis of abnormalities of the heart, and offers a helpful clue to the presence of

generalised disorders (Houghton and Gray, 1997). The ECG is useful in various cardiac areas for:

- the analysis of abnormal rhythms
- the detection and localisation of changes in the myocardium due to coronary artery disease
- the detection of hypertrophy of the walls of the atria and ventricles
- the detection of changes in electrical activity due to pericardial disease
- the detection of changes in electrical activity of the heart consequent to general metabolic changes

Figure 2-3 shows a schematic diagram of a typical electrocardiograph recording. The principle features of the recording are denoted P, Q, R, S, and T. The normal activation of the heart is initiated by the sinus node. In turn the atria depolarise, and during this time the atrioventricular (AV) node is also depolarised. The P wave represents atrial depolarisation. The QRS complex represents ventricular depolarisation. At the completion of ventricular depolarisation all electrical activity within the heart ceases, and during this period the ECG shows a horizontal straight line called the ST segment. The ST segment begins at the termination of the S wave and continues to the onset of the T wave. The T wave represents ventricular repolarisation.

The electrical cardiac cycle consists of three phases: depolarisation, repolarisation, and resting. The resting myocardial cell is negatively charged to –90 mV. This negative charge is maintained until the cell is activated or activates itself. Depolarisation is the process by which a resting cell becomes more positive. A myocardial cell that is activated by an impulse from the sinus node instantly switches from its resting negative charge of –90 mV to a positive charge that momentarily reaches +30 mV. Repolarisation is the process by which a depolarised cell is restored to its resting state. The repolarisation process begins immediately after rapid depolarisation. A complicated interaction of current flow maintains the membrane at a plateau of approximately 0 mV and then rapidly restores the membrane to its resting state of –90 mV.

The heart rate for normal sinus rhythm is between 50 and 100 beats per minute for healthy adults. An ECG exhibiting normal sinus rhythm obtained from a typical healthy subject is shown in figure 2-4.

2.2.3 Cardiac arrhythmias

An arrhythmia is an irregular or abnormal heartbeat. There are two main types of arrhythmias. These are bradycardia and tachycardia. Bradycardia denotes heart rates lower than 60 beats per minute. Tachycardia denotes heart rates faster than 100 beats per minute. Cardiac arrhythmias can occur in a wide variety of circumstances in patients with no evidence of heart disease or in those with heart disease due to any cause. Arrhythmias can be categorised into either a supraventricular arrhythmia or a ventricular arrhythmia depending on their origin within the heart. Supraventricular rhythms are generated at any myocardial structure above the ventricles including the atrial and the AV junction. Ventricular rhythms are generated within the ventricular myocardium.

2.2.3.1 Supraventricular arrhythmias

Supraventricular rhythms are generated at any structure above the ventricles including the atrial and the AV junction. Supraventricular arrhythmias include the following:

- **Supraventricular premature beat**

Supraventricular premature beats occur when there is atrial or conduction system disease such as left atrial enlargement in mitral stenosis. Beats occurring in these conditions may become atrial fibrillation. After atrial fibrillation is converted to sinus rhythm, reappearance of atrial premature beats often indicates that atrial fibrillation will soon recur. An example of the ECG exhibiting a supraventricular premature beat is shown in figure 2-5(a). It can be seen from the figure that the P waves have a different shape from regular sinus P waves. These P waves are premature and may be associated with an aberrant QRS complex that usually has a right bundle branch block configuration.

- **Supraventricular tachycardia**

Supraventricular tachycardia (SVT) is a general term describing any rapid heart rate originating above the ventricles. Supraventricular tachycardia generally begins and ends quickly. Many people experience short periods of supraventricular tachycardia and have no symptoms. However, supraventricular tachycardia becomes a problem when it occurs frequently or lasts for long periods of time and produces symptoms. Supraventricular tachycardia may also cause confusion or loss of consciousness. Figure 2-5(b) shows the ECG exhibiting supraventricular tachycardia. It can be seen from the figure that the QRS complexes follow the P waves at an interval between 0.12 and 0.20 seconds. The PR interval is shorter than the PR interval in normal sinus rhythm. The heart rate is between 100 and 260 beats per minute.

- **Atrial fibrillation**

Atrial fibrillation is an arrhythmia associated with the upper chambers of the heart: the atria. Atrial fibrillation can cause fast heart rates and a patient may lose consciousness. Atrial fibrillation is not a life threatening heart rhythm. In fact, as people get older, their chances of exhibiting this rhythm are quite high. Many people stay in this rhythm for years without suffering any ill effects from it. As illustrated in figure 2-5(c), there are no noticeable P-waves, and the overall rhythm is irregular.

2.2.3.2 Ventricular arrhythmias

The ventricular rhythms are generated within the ventricular myocardium. The ventricular arrhythmias include the following:

- **Ventricular premature beat**

The most common type of ventricular arrhythmia in both healthy and diseased individuals is the ventricular premature beat. The incidence of this condition increases with age. A premature beat occurs when there is an extra contraction of the ventricles

midway between two normal contractions or shortly after a normal contraction. Ventricular premature beats are not harmful by themselves, but they can be a precursor to two more serious types of ventricular arrhythmias: ventricular tachycardia and ventricular fibrillation. The ECG containing a ventricular premature beat is shown in figure 2-5(d). The irregular rhythm due to the premature beats occurs randomly, and the P-wave is retrograde or absent, hidden in the QRS complex. The PR interval is irregular if present, or absent, hidden in the QRS complex. The QRS complex shape looks extraordinary. The duration of QRS complex can be longer than 0.12 seconds. The T-wave is opposite to the QRS deflection.

- **Ventricular tachycardia**

Ventricular tachycardia is the rapid heartbeat that arises from the lower chambers of the heart, whereby the heart rate is in the region of 160 to 240 beats per minute. Ventricular tachycardia is a rapid dysrhythmia in which the ventricles depolarise very quickly and without regard for the atria. This arrhythmia commonly occurs in healthy people, particularly those who are frightened or excited. Ventricular tachycardia can degenerate into ventricular fibrillation causing a heart attack. Normally, there are no P-waves visible, and the QRS complexes are wider than 0.12 second in the ECG of ventricular tachycardia as shown in figure 2-5(e).

- **Ventricular fibrillation**

Ventricular fibrillation (VF) is the most common arrhythmic cause of sudden cardiac death. VF is a disordered electrical activity causing the ventricles to contract in a rapid, unsynchronized, uncoordinated fashion. The quivering ventricles are unable to contract or pump blood to the body. This is a medical emergency that must be treated with cardiopulmonary resuscitation (CPR) and defibrillation as soon as possible.

The characteristics of VF ECG is broad, unstructured, undulating complexes of varying amplitude and rate as shown in the figure 2-5(f). There are neither P waves nor QRS complexes visible in ventricular fibrillation. There is instead an irregular electric activity with a rate usually between 150 and 500 waves per minute

2.3 Time-frequency transforms

2.3.1 Introduction

In the 18th century, the French mathematician Joseph Fourier developed the Fourier transform to determine the frequency components of stationary signals. This technique is still popular for the analysis of a diverse range of signals where the Fourier transform maps the information within the time domain signal into the frequency domain. The Fourier transform was invented specifically for the analysis of stationary signals. However, most practical signals such as speech signals, turbulent fluid flows, the electrocardiogram (ECG), blood flow, etc. are non-stationary. Hence, Fourier analysis of these signals usually faces the problem of time localisation. This limitation of the Fourier transform is described in detail in this chapter. Several time-frequency analysis methods have been developed to overcome this problem including the short time Fourier transform (STFT), short time harmonic transform, Wigner-Ville transform, S transform, and wavelet transform (WT). Time-frequency transforms, in particular the WT, have become very popular in the last two decades. The number of applications of the WT is rapidly increasing in a variety of subject areas covering science, engineering, finance, and medicine. Wavelet transform analysis has been applied to a variety of biomedical signals including the electroencephalogram, electromyogram, acoustic signals, blood pressure, the phonocardiogram (PCG), the photoplethysmogram (pulse oximeter signal) and the ECG. In this thesis, both the STFT and WT are employed to characterise VF waveforms in order to facilitate the prediction of defibrillation shock outcome.

2.3.2 The Fourier transform

The concept of the Fourier technique is to map a function from the time domain into the frequency domain. The Fourier transform can be represented as the inner product between the analysed signal and a complex sinusoidal function, given by

$$F(f) = \left\langle f(t), e^{i2\pi ft} \right\rangle = \int_{-\infty}^{+\infty} f(t) e^{-i2\pi ft} dt \tag{2-1}$$

where *F(f)* is the Fourier transform of the function *f(t)*. The Fourier transform expands the original function in terms of orthonormal basis functions of sine and cosine waves of infinite duration. The Fourier coefficients of the transformation represent the contribution of each sine and cosine wave at each frequency. The Fourier transform operates under the assumption that the original signal is periodic in the time domain. Hence, the Fourier transform is limited in its application to non-stationary signals. Moreover, the Fourier transform is not efficient in the representation of time-localised signal features since the basis function is of infinite extent.

To overcome these limitations time-frequency methods were developed. These allow for a degree of temporal and spectral localisation simultaneously. As stated above, many time-frequency methods are currently available. The STFT and the continuous Wavelet transform (CWT) are reviewed in detail in the following two sections.

2.3.3 The short time Fourier transform (STFT)

As stated above, non-stationary signals are not properly represented by the Fourier transform because of the limitation of time localisation. A modified version of the Fourier transform called the short time Fourier transform (STFT) was introduced by Gabor to solve this limitation. The main concept of the STFT is to consider a non-stationary signal as a stationary signal over short periods of time within a window function (Gade et al, 1997; Rioul et al, 1991). The STFT is defined as

$$F(\tau, f) = \int f(t) g(t-\tau) e^{-i2\pi ft} dt \tag{2-2}$$

where $g(t-\tau)$ is the window function. According to equation 2-2, the STFT maps a signal into a two-dimensional function in time, τ, and frequency, f. The energy surface distribution derived from the STFT is called the spectrogram. This is defined as:

$$E(\tau, f) = |F(\tau, f)|^2 \tag{2-3}$$

The computation of the STFT is illustrated schematically in figure 2-6. The information from the signal within the window function, $g(t-\tau)$, located at τ is extracted using the standard Fourier transform. A sliding window containing a complex sinusoid is repeatedly shifted along the time axis (τ increasing) and the spectrum of the signal within the window is computed at each localisation until the end of signal.

An example of the STFT of a non-stationary signal is shown in figure 2-8. The window function used in this example is a Gaussian function defined as:

$$g(t) = \frac{e^{(-t^2/2\sigma^2)}}{\sigma\sqrt{2\pi}} \tag{2-4}$$

where σ^2 is variance of the function. The width of the window is defined as being equal to 6σ. Figure 2-7 illustrates the Gaussian window used. The window width defines, for practical implementation, the point at which the Gaussian function is near zero.

Figures 2-8(b) and 2-8(c) illustrate the STFT spectrogram corresponding to the signal in figure 2-8(a). The Gaussian window function in this example is of half second width. The time localisation of the frequency change in the original signal is clearly seen at 5 seconds in the spectrogram shown in figure 2-8(b). This example shows the efficiency of STFT in time localisation. However, the frequency resolution is not good for this example (as can be seen by the broadness of the bands in the time-frequency plane). The frequency resolution can be improved by using a wider Gaussian window. Figure 2-8(c) illustrates the STFT spectrogram computed using a Gaussian window function of three-second width. In this example, the frequency resolution is clearly better than the STFT obtained from the half-second window. However, the temporal location of the frequency change of the signal is not as clearly seen in this spectrogram. From this example it can be seen that the time resolution for the wider window is poorer than that for the narrower window.

From the above it can be seen that the STFT can, to some degree, solve the problem of non-stationary signals. However, there is an inherent resolution problem associated with the STFT. Since a fixed window is used in the computation, the STFT has the implicit problem of resolution. The use of narrow windows produces good time resolution but poor frequency resolution. In contrast, STFTs associated with wide windows have good frequency resolution but poor time resolution.

2.3.4 The wavelet transform

2.3.4.1 Introduction

The wavelet transform is a valuable signal analysis tool that can simultaneously elucidate spectral and temporal information from complex signals. It overcomes the limitations of the Fourier transform, which only contains globally averaged information, and has the potential to lose specific features within the signal. In addition, by employing a window of variable width it overcomes the problem of the fixed window width associated with the STFT as described in the previous section. This chapter briefly introduces the mathematics of the wavelet transform and a variety of example signals are used as illustration.

2.3.4.2 Mathematics

The wavelet transform of a continuous real-valued time signal, *x(t)*, with respect to the real valued wavelet function, ψ, is defined as

$$T(a,b) = \frac{1}{\sqrt{a}} \int_{-\infty}^{\infty} \psi^* \left(\frac{t-b}{a} \right) x(t) dt \qquad (2\text{-}5)$$

where $\psi^*((t-b)/a)$ is the complex conjugate of the analysing wavelet used in the convolution (Vetterli and Kovacevic 1995). The wavelet transform can therefore be thought of as the cross-correlation of the analysed signal with a wavelet function that has been translated by a value b and dilated by a factor a. These values are often referred to as the location and dilation parameters respectively.

A wavelet function must satisfy a number of conditions, these are:

A wavelet must have finite energy:

$$E = \int_{-\infty}^{\infty} |\psi(t)|^2 \, dt < \infty \tag{2-6}$$

where E is the energy of the wavelet function.

A wavelet must satisfy the admissibility condition:

$$C_g = \int_{-\infty}^{\infty} \frac{|\Psi(f)|^2}{f} df < \infty \tag{2-7}$$

where $\Psi(f)$ is the Fourier transform of $\psi(t)$. The C_g term in equation 2-7 is known as the admissibility constant. This implies that the wavelet has no component at zero frequency and thus the wavelet must have a zero mean, i.e.:

$$\int_{-\infty}^{\infty} \psi(t) dt = \Psi(0) = 0 \tag{2-8}$$

The total energy contained in a signal, $x(t)$, is defined as the integration of its squared magnitude, i.e.:

$$E = \int_{-\infty}^{\infty} |x(t)|^2 \, dt = \|x(t)\|^2 \tag{2-9}$$

The relative contribution of the signal energy contained at a specific a scale and b location is given by the two-dimensional wavelet energy density function as

$$E(a,b) = |T(a,b)|^2 \tag{2-10}$$

The plot of $E(a,b)$ representing the energy density surface of the wavelet transform is known as a scalogram. The total energy in the original signal can be determined from the scalogram by integrating across a and b as follows

$$E = \frac{1}{C_g} \int_{-\infty}^{\infty} \int_{0}^{\infty} |T(a,b)|^2 \frac{da}{a^2} db \tag{2-11}$$

In addition, the relative contribution of total energy contained within a specific a scale can be represented in terms of the scale dependent energy distribution:

$$E(a) = \frac{1}{C_g} \int_{-\infty}^{\infty} |T(a,b)|^2 db \tag{2-12}$$

The scale dependent energy distribution, $E(a)$ can be converted to a frequency dependent wavelet energy spectrum $E(f)$ (Addison 2002). To do this, the wavelet scale a must be converted to a characteristic frequency of the wavelet. The passband centre of the wavelet's power spectrum, f_c, is commonly used in this conversion. Hence, the characteristic frequency associated with a wavelet of arbitrary a scale is given by:

$$f = \frac{f_c}{a} \tag{2-13}$$

where the passband centre of the mother wavelet, f_c, becomes a scaling constant and f represents the characteristic frequency of the wavelet at scale a. From equations 2-12 and 2-13, it can be shown that the frequency dependent wavelet energy spectrum is given by:

$$E(f) = \frac{1}{f_c C_g} \int_{-\infty}^{\infty} |T(f,b)|^2 db \tag{2-14}$$

The scalogram plot, representing the energy density surface in the time-frequency plane, is defined by:

$$E(f,b) = \frac{|T(f,b)|^2}{f_c C_g} \tag{2-15}$$

Hence, the total energy in the signal is given by:

$$E = \int_{-\infty}^{\infty}\int_{0}^{\infty} E(f,b)\,df\,db \tag{2-16}$$

or

$$E = \frac{1}{f_c C_g}\int_{-\infty}^{\infty}\int_{0}^{\infty} |T(f,b)|^2\,df\,db \tag{2-17}$$

The original signal can be reconstructed from the inverse wavelet transform as

$$x(t) = \frac{1}{C_g}\int_{-\infty}^{\infty}\int_{0}^{\infty} T(a,b)\psi_{a,b}(t)\frac{da\,db}{a^2} \tag{2-18}$$

This equation reconstructs the original function from its wavelet transform by the integrating over all scales, a, and locations, b (Vetterli and Kovacevic, 1995; Mallat, 1998; Addison, 2002).

Figure 2-9 and figure 2-10 illustrate the mechanics of the wavelet transform. Figure 2-9 shows the wavelet function moving along the time axis e.g. from b_1 to b_2 to b_3, etc. The scale of wavelet width is then altered, as shown in figure 2-10. The correlation between the raw signal and wavelet function is computed over a range of scales and locations. In practice the convolution of the wavelet and signal is computed over a range of scales which cover the spectral characteristics of the signal features of interest.

2.3.4.3 The computation of the wavelet transform using Fourier methods

As mentioned previously, the wavelet transform is the convolution of a signal with a wavelet function (equation 2-5). The wavelet function can be written compactly as:

$$\psi_{a,b}(t) = \frac{1}{\sqrt{a}}\psi(\frac{t-b}{a}) \tag{2-19}$$

where the normalisation is in the sense of wavelet energy. Therefore, the wavelet transform of equation 2-5 can be written as:

$$T(a,b) = \int_{-\infty}^{\infty} x(t)\psi^{*}_{a,b}(t)dt \tag{2- 20}$$

where $\psi^{*}_{a,b}(t)$ is the complex conjugate of the wavelet function. According to the convolution theorem, the wavelet transform can be expressed in terms of the Fourier transform of the raw signal and the wavelet as follows

$$T(a,b) = \int_{-\infty}^{\infty} X(f)\Psi^{*}_{a,b}(f)df \tag{2-21}$$

where $X(f)$ and $\Psi^{*}_{a,b}(f)$ represent the Fourier transform of $x(t)$ and $\psi^{*}_{a,b}(t)$ respectively. The Fourier transform of the dilated and translated wavelet, $\Psi_{a,b}(f)$, can be expanded as follow

$$\Psi_{a,b}(f) = \int_{-\infty}^{\infty} \frac{1}{\sqrt{a}}\psi(\frac{t-b}{a})e^{-i(2\pi f)t}dt \tag{2-22}$$

Substituting $t' = \frac{t-b}{a}$ into equation 2-22 we obtain

$$\begin{aligned}\Psi_{a,b}(f) &= \frac{1}{\sqrt{a}}\int_{-\infty}^{\infty}\psi(t')e^{-i(2\pi f)(at'-b)}d(at'-b) \\ &= \sqrt{a}\int_{-\infty}^{\infty}\psi(t')e^{-i(2\pi f)(at'-b)}dt' \\ &= \sqrt{a}e^{-i(2\pi f)b}\int_{-\infty}^{\infty}\psi(t')e^{-i(2\pi af)t'}dt'\end{aligned} \tag{2-23}$$

Dropping prime from t' in the above, we get

$$\begin{aligned}\Psi_{a,b}(f) &= \sqrt{a}e^{-i(2\pi f)b}\int_{-\infty}^{\infty}\psi(t)e^{-i(2\pi af)t}dt \\ &= \sqrt{a}e^{-1(2\pi f)b}\Psi(af)\end{aligned} \tag{2-24}$$

hence, equation 2-21 can be written in expanded form as

$$T(a,b) = \sqrt{a}\int_{-\infty}^{\infty}X(f)\Psi^{*}(af)e^{i(2\pi f)b}df \tag{2-25}$$

Equation 2-25 shows that the wavelet transform can be described in the form of an inverse Fourier transform (Addison 2002). This form is very useful for the fast implementation of the CWT in computer programs. In addition, the wavelet transform in the terms of the Fourier transform presents the concept of the wavelet transform as a multi-frequency-band analysis.

2.3.4.4 Complex wavelets: the Morlet wavelet

The objective of this section is to introduce complex wavelets which have both real and imaginary parts. In this research, the Morlet wavelet was employed in the analysis. It is defined as

$$\psi(t) = \pi^{-1/4}\left(e^{i2\pi f_0 t} - e^{-(2\pi f_0)^2/2}\right)e^{-t^2/2} \tag{2-26}$$

where f_0 is the central frequency of the mother wavelet. The second term in the brackets is known as the correction term. This term corrects for the non-zero mean of the complex sinusoid of the first term. In practice the correction term can be ignored for values of $f_0 >> 0$ and the Morlet wavelet can be written as

$$\psi(t) = \pi^{-1/4}e^{i2\pi f_0 t}e^{-t^2/2} \tag{2-27}$$

This simple form of the Morlet wavelet is well known as the standard Morlet wavelet. From equation 2-27, it can be seen that the standard Morlet wavelet is comprised of three terms: the normalisation factor ($\pi^{-1/4}$), a complex sinusoid ($e^{i2\pi f_0 t}$), and a Gaussian envelope ($e^{-t^2/2}$). Figure 2-11 shows the standard Morlet wavelet with f_0 = 0.894 Hz: a value which is often used in practice. This figure shows the components of the standard Morlet wavelet: the complex sinusoid within the Gaussian envelope. The scaled Morlet wavelet is defined as

$$\psi(at) = \pi^{-1/4} e^{i2\pi f_0 at} e^{-(at)^2/2} \tag{2-28}$$

Figure 2-12 shows the standard Morlet wavelet at various a scales. The Morlet functions in figures 2-12(a)-(c) are scaled with a equal to 1, 2, and 3 respectively. All these functions have the same central frequency f_0 = 0.894 Hz. The wavelet stretches when the scale increases, hence the corresponding frequency bandwidths are reduced. This is shown in figure 2-12(d). The energy spectrum of the wavelet moves to the left-hand side of the plot (i.e. lower frequencies) when the scale of the wavelet increases. In addition, the bandwidth of the wavelet is narrower while the temporal scale of the wavelet is wider. This is the limitation of resolution in the wavelet transform. The frequency resolution at high frequency is worse than the frequency resolution at low frequency. Conversely, the time resolution at high frequency is better than the time resolution at low frequency.

Figure 2-13 illustrates the use of the Morlet wavelet in the analysis of an example signal. The signal is composed of a two-frequency component waveform as shown in figure 2-13(a). The central frequency of the Morlet used in this example is 5 rad/sec (f_0= 0.8 Hz). The results of the complex Morlet wavelet analysis may be displayed in many ways. The real part of $T(a,b)$ is shown in figure 2-13(b). The plot shows the frequency components of the time-frequency components of the waveform during the 5 Hz and 2 Hz regions. Similarly, the imaginary part of $T(a,b)$ is shown in figure 2-13(c). Notice that the imaginary plot is phase-shifted, lagging behind the real part by one quarter of a cycle. The phase plot of the transform is illustrated in figure 2-13(d). The phase plot varies cyclically between - π and π. A phase of -π and π corresponds to the minima of the real plot in figure 2-13(b). Figure 2-13(e) contains a modulus plot of the wavelet transform. The modulus is defined as

$$|T(a,b)| = \sqrt{[\mathrm{Re}(T(a,b))]^2 + [\mathrm{Im}(T(a,b))]^2} \quad (2\text{-}29)$$

In figure 2-18(e), the maximum and minimum values of the modulus are represented in white and black respectively. Bands at 5 Hz and 2 Hz can be seen in the modulus plot.

2.3.4.5 The wavelet transform of example signals

This section illustrates the analysis for example test signals using the wavelet transform. These illustrate: (1) stationary signal analysis, (2) non-stationary signal analysis, (3) noise reduction, and (4) transient detection.

- **Stationary signal**

This example presents the analysis of a stationary signal. Figure 2-14(a) shows the test signal composed of two combined sinusoidal waveforms at 1 Hz and 2 Hz. These two frequencies occur over the whole time period of the signal. The result of the wavelet analysis is represented as the scalogram shown in figure 2-14(b). Two major frequency bands can clearly be seen at 1 Hz and 2 Hz. The results of the continuous wavelet transform can be also represented as a 3D-plot as shown in figure 2-14(c). In the 3-D plot, there are two separated ridges that have characteristic frequencies centred at 1 Hz and 2 Hz. This example shows the ability of the wavelet transform to elucidate stationary signals by partitioning the individual frequency components within the time-frequency plane.

- **Non-stationary signal**

The analysis of a non-stationary signal using the wavelet transform is illustrated in this example. Figure 2-15(a) shows a chirp signal defined as:

$$x(t) = \sin(t^2) \quad (2\text{-}30)$$

The chirp signal comprises a sinusoid with a time dependent frequency. Figure 2-15(b) shows the CWT scalogram associated with the signal. It is clearly seen that the frequency band of chirp increases from bottom left to top right: i.e. increasing in frequency with time. This example illustrates the wavelet transform's ability to localise the pertinent information of a non-stationary signal in both time and frequency.

- **Noise reduction**

This example illustrates the technique of noise reduction using the CWT. Figure 2-16(a) shows the test signal containing a section with added high frequency noise. The original signal comprises two sinusoidal waveforms at 20 Hz and 100 Hz. High frequency noise is added in the segment between 0.1 sec and 0.2 sec. The scalogram of this signal is shown in figure 2-16(b). It can be seen from the scalogram that the high frequency noise is obviously separated from the main components of signal. It is simple to remove this noise by removing the CWT component from this region before performing the inverse transform. Figure 2-16(c) illustrates the filtered signal after removing the noise from the transformed signal in this way.

- **Transient detection**

This example shows the use of the CWT in the detection of signal transients. Figure 2-17(a) shows a stationary signal composed of two frequency components at 20 Hz and 100 Hz. The small transient spike, shown in figure 2-17(b), was then added to this stationary signal to give the test signal shown in figure 2-17(c). The Fourier power spectrum of the signal is shown in figure 2-18(a) where two dominant spectral components (at frequencies 20 Hz and 100 Hz) can be observed. However, Fourier analysis cannot detect the transient. The CWT scalogram of the same signal is shown in figure 2-18(b). The transient is obviously apparent in the scalogram at a temporal location of at 0.5 seconds. This example shows the advantage of CWT analysis for use in the detection of subtle temporally localised signal transients.

2.4 The uses of wavelet transform methods in cardiology

Over recent years, wavelet analysis has been applied to a range of biomedical data including the electroencephalogram, electromyogram, acoustic signals and the ECG (Sahambi et al, 1997; Ivanov et al, 1996; Wiklund et al, 1997; Thurner et al, 1998). Wavelet-based studies of ECG signals have either examined heart rate variability, classified ECG waveforms, or have been used for ECG data compression. Our group has focused on the analysis of complex waveforms during ventricular fibrillation (VF) (Addison et al, 2000 and 2001; Watson et al, 2000) as well as other medical and engineering signals (Addison, 1999; Addison et al, 2001; Watson et al, 1999).

The wavelet transform is now widely used in the analysis of cardiac signals. Several research groups have applied the wavelet transform to analyse various cardiac signals such as the ECG, blood pressure, the phonocardiogram (PCG), and the photoplethysmogram (pulse oximeter signal). This section reviews the analysis of these cardiac signals using the wavelet transform.

Wavelet-based studies of ECG signals have examined the constituent components of ECG waveforms. Bahoura et al (1997) have developed a real time implementation of the wavelet transform to distinguish pertinent ECG components including QRS complexes, P waves, and T waves from noise, baseline drift and interference. Sahambi et al (1997) also studied the errors due to power line interference and baseline drift using wavelets. The same group (Sahambi et al, 1998) used the wavelet transform for detecting ST segments and implemented their algorithm on a DSP card for on-line analysis. Park et al (1998) applied the combination of a wavelet transform and adaptive filter to eliminate ECG baseline wandering and reduce signal distortion. Lemire et al (2000) have employed a wavelet time-entropy measure to characterise the morphology of T waves in pig ECGs. Recently, Link et al (2001) used the Morlet wavelet to analyse the beat-to-beat variability of QRS signals in both magnetocardiagrams (MCGs) and ECGs.

The wavelet transform is very useful for biomedical data compression and in particular the compression of the ECG signal. Crowe et al (1992) used the wavelet transform as a tool for the compression of ECG data. Chen et al (1993) introduced the

orthogonal discrete wavelet transform for ECG compression. Thakor et al (1993) proposed 'the Multiwave Algorithm' based on the wavelet transform for ECG compression. Lu et al (2000) have proposed the set partitioning in hierarchical tree (SPIHT) coding technique to ECG compression. This algorithm includes partial ordering of the dyadic wavelet coefficients of ECG signals by magnitude with a set partitioning sorting algorithm, ordered bit plane transmission and exploitation of self-similarity across different layers. Ahmeda et al (2000) applied the discrete wavelet for ECG compression and, a year later, Ahmeda and Abo-Zahhad (2001) combined a non-orthogonal discrete wavelet transform and linear predictor for ECG compression.

In addition, the wavelet transform is a powerful tool for detecting and classifying heart disease. Khadra et al (1993) applied the wavelet transform to the detection of ventricular late potentials (VLP) from patients with sustained ventricular tachycardia. Five years later Rakotomamonjy et al (1998) used a combination of neural networks and the wavelet transform to detect VLPs. Khadra et al (1997) employed the wavelet transform to detect the characteristics of VF, VT, and AF arrhythmias. Mojsilovic et al (1997) analysed and classified the texture of myocardial infarction from the wavelet image extension. Wavelet image extension involves the decomposition of the studied image with an orthonormal wavelet based filter bank to form an image approximation with higher resolution. Masson and Rieu (1998) used the Morlet wavelet to investigate the noise generated from mechanical artificial heart valves. Al-Fahoum et al (1999) have combined the wavelet transform and neural network to classify the cardiac arrhythmias.

Others cardiac signals have also been analysed using wavelet transform. For example Khadra et al (1991) compared the characteristics of normal and abnormal heartbeat sounds in phonocardiogram signals using the Morlet wavelet. Obaidat (1993) has applied the wavelet transform to the analysis of characteristic components in the phonocardiogram signal. And, Stefanovska et al (1999) have analysed low frequency oscillation present in peripheral blood circulation using the Morlet-based wavelet transform.

2.5 A review of papers concerning prediction of shock outcome

Cardiac arrhythmias (the irregular beating of the heart) can be catastrophic and life threatening. Ventricular Fibrillation (VF) is considered to be the most life threatening arrhythmia since the heart fails to pump blood effectively. VF is the primary arrhythmic event in the majority of patients who present with sudden cardiac death (Goldstein et al, 1981, Jacobs and Oxer, 1990). The patient with VF may die within a few minutes without the restoration of a pulse-giving rhythm. During VF, a degree of myocardial electrical organisation exists and is reflected in the surface ECG (Clayton et al, 1992). In the frequency spectrum of VF, the mean frequency of the dominant peak can be measured accurately using either the fast Fourier transform (FFT) or maximum entropy methods (Clayton and Murray, 1993). The frequency bands become narrower as the arrhythmia develops during the onset and early stages of VF (Clayton et al, 1995). Addison et al (2000 and 2001) found that a rich underlying coherent structure of VF can be made visible using the CWT.

The administration of a defibrillation shock using an electrical defibrillator is the only known therapy for the treatment of VF. However, refibrillation frequently appears after defibrillation (White et al, 2002). Moreover, an unsuccessful defibrillation causes tissue damage during the shock period (Xie et al, 1997). The defibrillation threshold has an effect on the probability of successful defibrillation (Singer and Lang, 1992). Carlisle et al (1998) studied the effectiveness of synchronised defibrillator shocks with measurements for unsynchronised shocks. This study showed that the minimum threshold-delivered energy or the minimum threshold-delivered current giving the successful shock is not significantly different between synchronised shock and unsynchronised shock.

Considerable interest has focused upon VF as it is recognised that prompt therapy can lead to a successful outcome. For these reasons there has been considerable interest in analysis of the VF waveform. Until recently, the surface electrocardiogram recorded during VF was thought to represent disorganised and unstructured electrical activity of the heart. This is in stark contrast to the information rich ECG in other states of health and disease (Rude et al, 1983; Brush et al, 1985). Over the past two decades, numerous research groups have attempted a number of alternative methodologies for

the analysis of the prediction of defibrillation outcome. The methodologies are based upon:

- Amplitude of ventricular fibrillation methods
- Fourier power spectrum methods
- Short time Fourier transform methods
- Combined frequency and amplitude methods
- Other methods

These are considered in detail in the following subsections.

2.5.1 Amplitude of ventricular fibrillation-based methods

Weaver et al (1985) found that the amplitude of ventricular fibrillation has an effect on the survival rate of the resuscitated patient. They analysed the amplitude of ventricular fibrillation ECGs for 394 patients. The survival rate of patients exhibiting fine fibrillation associated with very low amplitude (less than 0.2 mV) was only 6 %. However, coarse fibrillation, associated with high amplitude (more than 0.2 mV), corresponded to a survival rate of 36 %.

Monsieurs et al (1998) proposed the development of a scoring system for outcome classification at the start of pre-hospital resuscitation for patients with cardiac arrest exhibiting VF. The first 100 consecutive patients with cardiac arrest with VF were analysed in this study. Fisher's linear discrimination analysis was employed to classify between survivors and non-survivors using these variables: amplitude of VF in mV (VF_a), the number of base-line crossing of VF per second (VF_blc) and age. The classification result using VF_a and VF_blc achieved the correct classification for 79% of survivors and 70% of non-survivors. Adding the age variable, the survival index increased to 86% of survivors and 73% of non-survivors.

Amann et al (2001) studied the behaviour of ECGs during VF in 25 pigs using $N(\alpha)$ histogram analysis. In this study, the data were grouped into two sets: vaso-data (pigs receiving vasopressin alone) and placebo-data (pigs receiving physiologic saline alone). The defibrillation outcome with vasopressin was 100% successful whereas the

defibrillation without vasopressin was 0% successful. The width of N(α) histogram obtained from the ECG amplitudes was used as a parameter for predicting the defibrillation success. The results showed that the defibrillation success correlated with small width N(α) histograms. However, the width of N(α) histogram did not significantly separate the vaso-data from placebo-data. A year later, this group suggested a new parameter from the N(α) histogram analysis to replace the width of N(α) histogram (Amann et al, 2001). The parameter used in this study was the quotient of the start of the histogram to its width (histogramstart/ histogramwidth). The results showed that the quotient histogramstart/histogramwidth was superior to mean fibrillation frequency for predicting defibrillation success during CPR. The N(α) parameter histogramstart/histogramwidth distinguished between the effect of vasopressin (successful defibrillation) and epinephrine (unsuccessful defibrillation).

Callaway et al (2001) examined the prediction of defibrillation success using fractal analysis. ECG waveform recordings from automated external defibrillator were obtained for 75 VF adult patients. A scaling exponent estimating the fractal self-similarity was used as the parameter to predict the probability of first-shock defibrillation and survival to hospital discharge. A lower mean value of scaling exponent was observed for a variety of successful outcomes.

2.5.2 Fourier power spectrum-based methods

Brown et al (1991) proposed a methodology to predict the result of defibrillation using Fourier spectrum analysis. This study experimented with twenty two mixed-breed swine weighing more than 15 kg. The ventricular fibrillation ECG signals acquired during the 20 seconds before defibrillation were analysed using the fast Fourier transform (FFT). The median frequency of the resulting power spectra served as a parameter for the prediction of defibrillation outcome. In this methodology, a sensitivity of 100% and a specificity of 92.31%, corresponding to a median frequency of 9.14 Hz was achieved in predicting the result of defibrillation. However, a severe limitation of this study was the insufficient number of ECG data sets used.

Stewart et al (1992) studied the relationship between successful resuscitation and dominant VF frequency. The study data were collected from the 56 patients in a

mobile coronary care unit. The results showed that low frequency VF indicates a poor chance of successful resuscitation.

Strohmenger et al (1994) studied defibrillation success in patients during cardiac surgery using frequency analysis. Data were collected from 20 patients undergoing aortocoronary bypass grafting. The median frequency of those ECGs which resulted in supraventricular rhythm was 4.7±0.17 Hz. This was higher than the median frequency of VF signals resulting in unsuccessful defibrillation. The probability of success was 100% at a frequency of ≥ 5.5 Hz. In a later study involving closed-chest CPR after vasopressin treatment in a porcine model of VF, this group suggested that the median frequency of VF reflected myocardial blood flow and the chance of successful defibrillation (Strohmenger et al, 1996).

Eftestol et al (2000 and 2001) analysed an 821-trace data set collected from 156 patients with out-of-hospital cardiac arrest using Fourier methods. The ECG of the VF, signal 4 seconds prior to shock, was analysed to predict defibrillation outcome. A number of power spectrum-based features were employed including centroid frequency, peak power frequency, spectral flatness, and energy. A second decorrelated features set was produced using coefficients generated using principle component analysis (PCA). The combination of centroid frequency and peak power frequency achieved a mean± SD sensitivity of 92± 2% and specificity of 27± 2% in testing. The highest performance of classifier testing corresponded to the combination of PCA decorrelated spectral features was a sensitivity of 92±1% at a specificity of 42± 1%.

Hamprecht et al (2001) considered the prediction of successful countershock in porcine models (from 25 pigs) of VF using parameters obtained from logarithmic power spectral densities. The experiments showed that fibrillation power was slightly better for predicting success than mean fibrillation frequency and peak-trough amplitude. In the experiment, the prediction of successful defibrillation corresponding to the fibrillation power feature with a threshold ≥ 79 dB achieved a sensitivity, specificity, positive predictive value, and negative predictive value of 98%, 98%, 99%, and 97% respectively.

2.5.3 Short time Fourier transform-based methods

The downtime is the duration of time between the onset of ventricular fibrillation and the application of defibrillation. An estimate of downtime was determined from the changes in median frequency during VF by Brown et al (1989). In the study, the VF ECG signals from 11 swine were recorded for 10 minutes. Each four-second epoch of data was transformed into the frequency domain using a fast Fourier transform. Estimated downtime was determined from the median frequency data at two, four, six, and eight minutes after VF induction. The downtime-estimating algorithm was tested to determine the success rate for predicting known downtimes of less than or more than five minutes for each animal at all observed downtimes. Of the 1,360 total predictions made, the algorithm correctly predicted 1,128 times when the downtime was less than or more than five minutes.

Martin et al (1991) have studied the variation of median frequency (FM) with time during VF. This work studied the characteristics during VF in human and swine models using the STFT. The results showed that the FM against time curve of a human model gradually decreased whereas the FM curves in swine model decreased initially then increased to a peak followed by a gradual decline.

2.5.4 Combined frequency and amplitude-based methods

Brown and Dzwonczyk (1995) compared the probability of defibrillation outcome between frequency and amplitude parameters. Data acquired from 55 patients exhibiting VF were used in this study. The frequency parameters, centroid and peak power frequencies used were determined from the Fourier power spectrum. The amplitude parameters, average segment amplitude and average wave amplitude, were extracted from the temporal ECG traces. The study found that the probability of predicting countershock outcome using centriod frequency, peak power frequency, average segment amplitude, and average wave amplitude were found to be 0.72, 0.70, 0.52, and 0.53, respectively.

Strohmenger et al (1997) studied the VF signals from 26 patients. Frequency parameters were extracted from the Fourier power spectrum including the median

frequency, dominant frequency and edge frequency. In addition a measurement of amplitude was determined from the original time domain ECG signal. Their study showed that median frequency, dominant frequency and amplitude are predictive of countershock success. The best result achieved was 100% sensitivity at 46.27% specificity using dominant frequency and a 12-second epoch.

Noc et al (1999) studied data collected from 66 pigs. The studied parameters were coronary perfusion pressure, maximum VF amplitude, mean VF amplitude, and dominant VF frequency. They found that predicting of the success of defibrillation with mean VF amplitude alone or in combination with dominant VF frequency was effective and on a par with coronary perfusion pressure (CPP).

Strohmenger et al (2001) investigated shock outcome prediction during human VF episodes using frequency and amplitude variables. An 821-trace data set collected from 156 patients with out-of-hospital cardiac arrest was analysed in the study. The frequency variables employed were median frequency, dominant frequency and edge frequency. The amplitude measure was determined from the time domain ECG signal by calculating the difference between the maximum and the minimum amplitude for each segment of pre-shock signal. The best result achieved was 73% sensitivity and 67% specificity and using the amplitude variable over a 3000 ms length of pre-shock signal.

Marn-Pernat et al (2001) investigated the potential of the amplitude spectrum area (AMSA) correlated with coronary perfusion pressure (CPP) in the prediction of defibrillation success. AMSA is the area under the curve calculated from the resulting amplitude frequency spectrum. AMSA is defined as follows:

$$AMSA = \sum A_i F_i \tag{2-31}$$

where A_i is the amplitude at the i th frequency F_i. In this study, the data were obtained from 31 electrical shocks delivered to 10 domestic pigs. The results showed that an AMSA value of 21 mV·Hz gave an optimum prediction of restoration of perfusing rhythm after shock with a sensitivity of 88% and specificity of 91% achieved.

Amann et al (2002) reported on the prediction of defibrillation outcome using a combination of mean frequency and amplitude variable. They examined VF signals of 64 pigs from 4 different cardiac arrest models with different durations of untreated VF, different durations of CPR, and the use of various drugs. The length of 10-second epochs between 20 and 10 seconds before the first defibrillation shock were examined to predict the shock outcome. Three variables were considered for the prediction of defibrillation, there were: mean frequency (FREQ), mean peak-to-trough amplitude (AMP) and a survival index (SI). The SI was obtained from a linear equation derived from the mean frequency and mean peak-to-trough amplitude variables. This study showed that the four different models of cardiac arrest were not significantly different FREQ, AMP, and SI values ($P > 0.5$). In addition, SI improved the predictive power compared with using FREQ and AMP alone. The best result achieved 89% sensitivity and 86% specificity using this survival index variable.

Povoas et al (2002) used the AMSA method for predicting the shock outcome. In this study, 34 defibrillation attempts were obtained from 10 domestic pigs. An AMSA value of 21 mV•Hz resulted in a negative predictive value of 0.96 and a positive predictive value of 0.78.

2.5.5 Other methods

Patwardhan et al (1999) have investigated the degree of phase coupling among orthogonal ECGs collected from ten adult mongrel dogs. The bispectra were estimated from orthogonal ECGs in the X, Y, and Z direction. The bispectral energies of VF ECGs during the last 4 seconds before shock were integrated within the 8.7-11.7 Hz range in both frequency axes. The results showed that that the degree of phase coupling at the dominant frequency (≈9 Hz in both frequency axes) of unsuccessful trials were larger than from the successful trials. The average bispectral energies between 200 and 1000 ms before defibrillation shock from the unsuccessful trails were significantly greater than that from the successful trials ($p<0.05$).

Podbregar et al (2003) proposed genetic programming (GP) for the prediction of defibrillation outcome. This research studied 203 ECG recordings in 47 patients with out-of-hospital cardiac arrest. The predictive model was developed using GP with

four variables. These were two time domain variables (time delay and amplitude), a frequency domain variable (total energy) and a variable from non-linear dynamics (the Hurst exponent). Data from 100 VF signals from the database were used to develop a GP model. When applied to the test data containing 32 successful and 71 unsuccessful shocks the method achieved 100% sensitivity and 97% specificity. The positive predictive value and negative predictive value were 94.1% and 100% respectively. The likelihood ratios for positive and negative test result were 35.50 and 0.00 respectively. However, this study has a major limitation in that a low number of defibrillations were studied.

2.6 Chapter summary

This chapter has described the background to this research. Three main sections were provided in this review. In the first section, a brief overview of the relevant cardiology was described including the cardiovascular system, the ECG, and cardiac arrhythmias. The second section covered the concept of time-frequency analysis where the STFT and the wavelet transform were explained in terms of their mathematics and illustrations were used to convey the concepts. The next section reviewed the use of wavelet methods in cardiology including the analysis of cardiac signals such as the ECG, PCG, and blood circulation. Finally, a literature review of the work of other groups in producing a shock outcome prediction tool was described. The wavelet and STFT techniques described in this chapter form the basis of the analysis techniques developed by the author for his programme of research. These are described in detail in the following chapter.

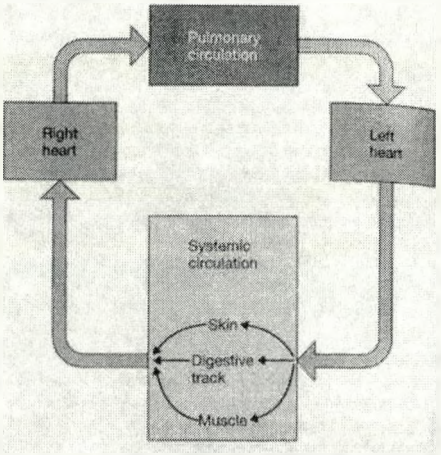

Figure 2-1: The closed loop diagram of the cardiovascular system

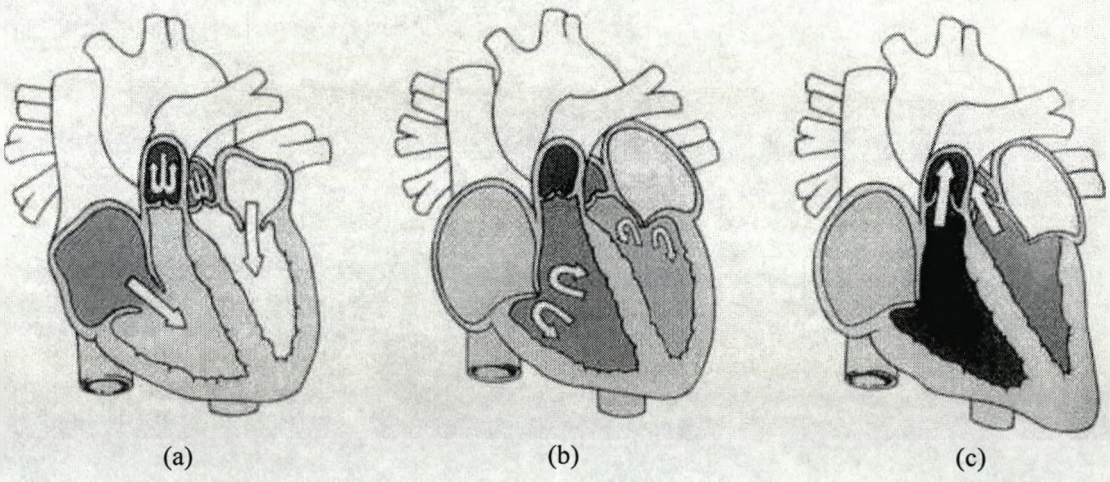

Figure 2-2: The direction of blood flow

(a) blood is pumped from atrium into the associated ventricle; (b) The ventricle chambers is pumping blood at high pressure; (c) the blood from the right and left ventricles flows through the pulmonary circulation and systemic circulation, respectively.

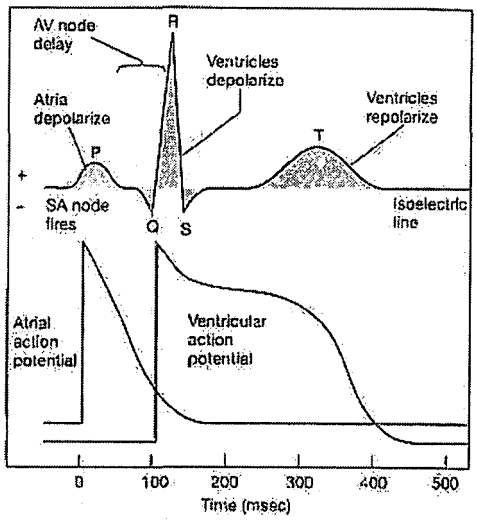

Figure 2-3: The components of ECG including the relationship between cellular action potentials and the surface ECG

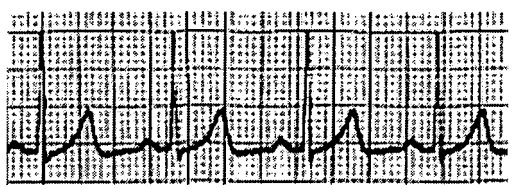

Figure 2-4: Normal sinus rhythm

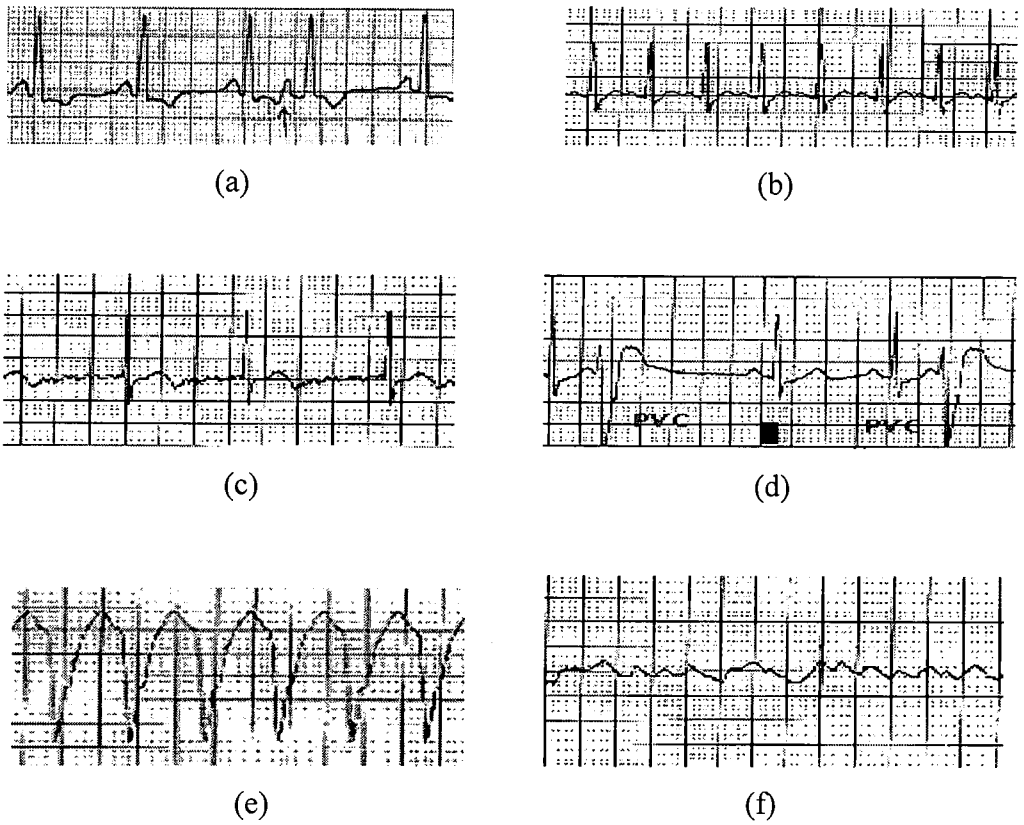

Figure 2-5: The ECGs of cardiac arrhythmias

(a) The ECG of a supraventricular premature beat; (b) The ECG of a supraventricular tachycardia; (c) The ECG of atrial fibrillation; (d) The ECG of ventricular premature beat; (e) The ECG of ventricular tachycardia; (f) The ECG of ventricular fibrillation

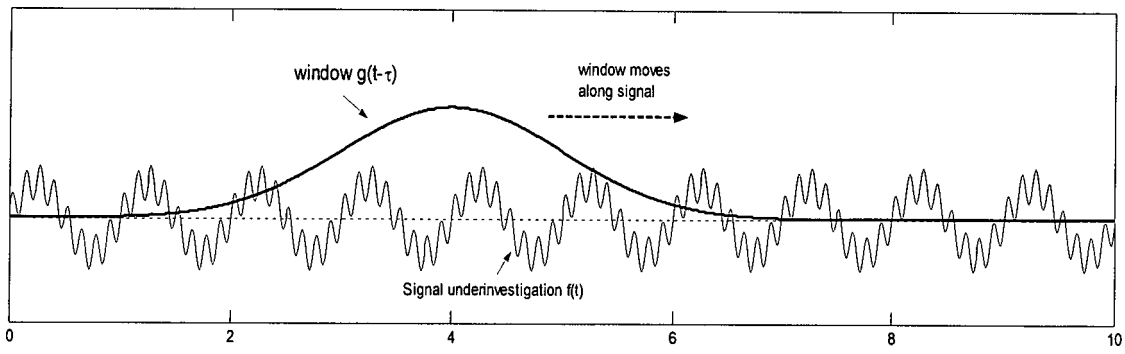

Figure 2-6: An illustration of STFT computation

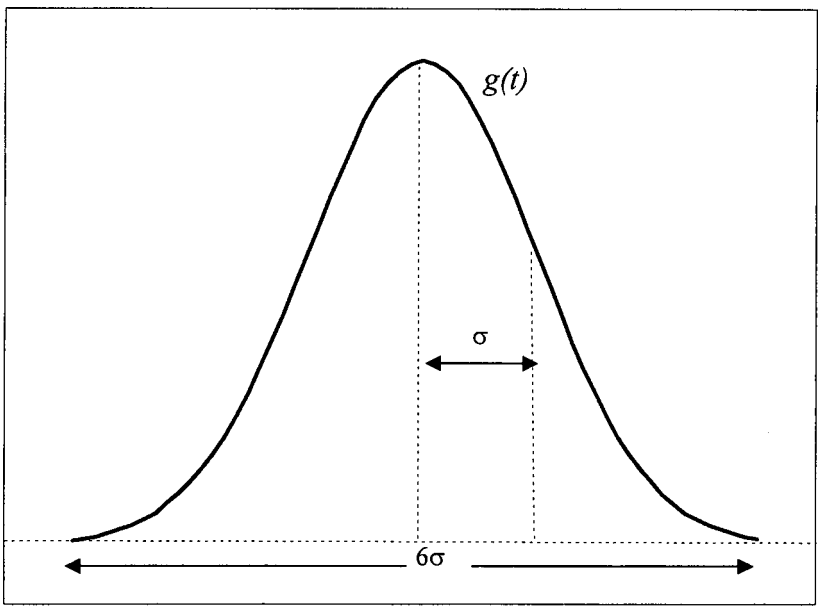

Figure 2-7: Gaussian window function

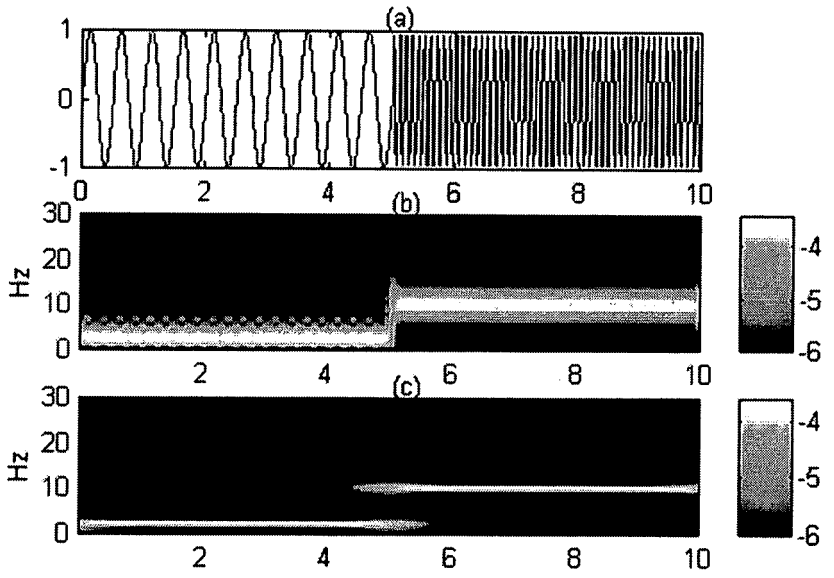

Figure 2-8: Example of STFT analysis

(a) Original signal; (b) Spectrogram generated using a 0.5-second wide Gaussian window; (c) Spectrogram generated using a 3-second wide Gaussian window

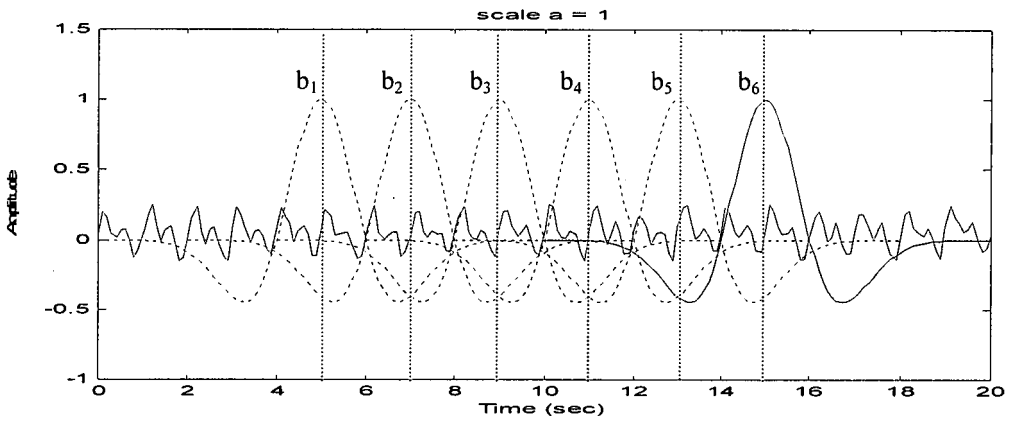

Figure 2-9: The wavelet function at scale a = 1 at various locations on the signal

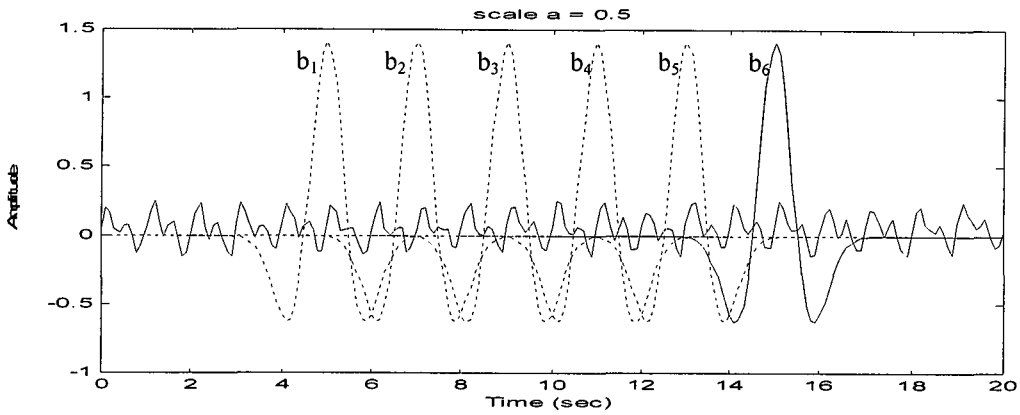

Figure 2-10: The wavelet function at scale a = 0.5 at various locations on the signal

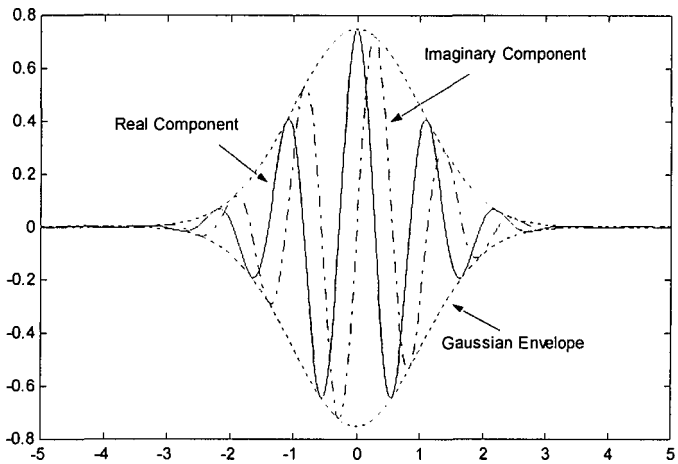

Figure 2-11: The Morlet wavelet function

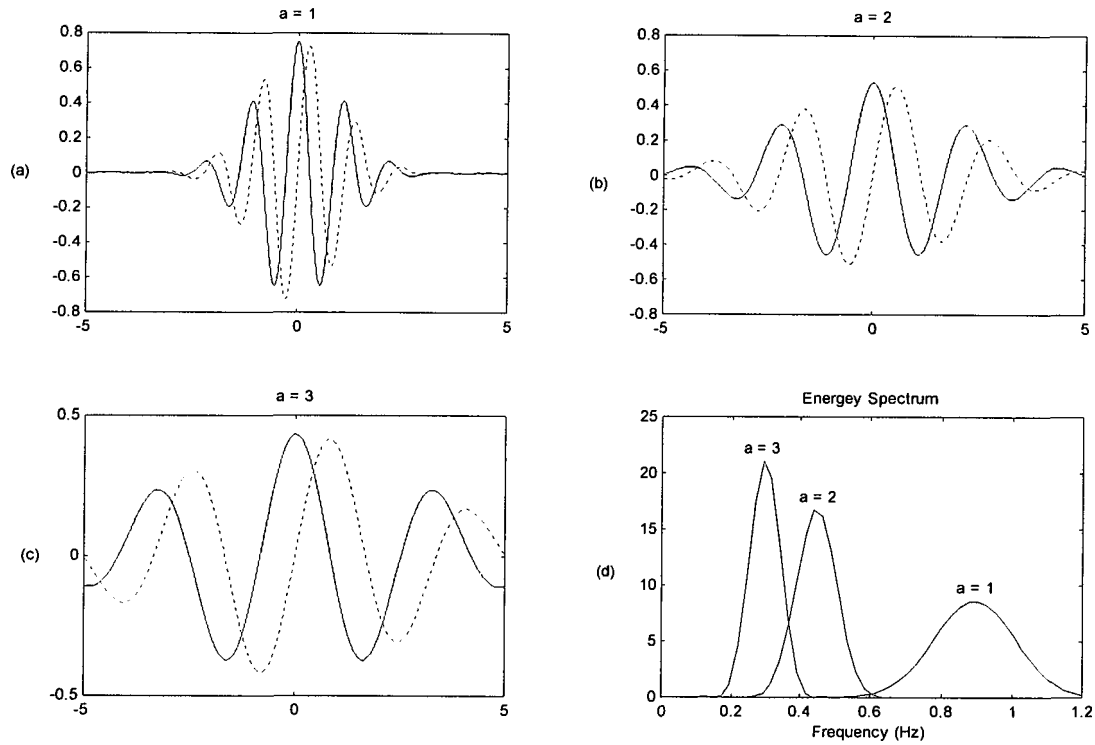

Figure 2-12: The Morlet function at various scales

(a) $a = 1$; (b) $a = 2$; (c) $a = 3$; (d) the energy spectrums

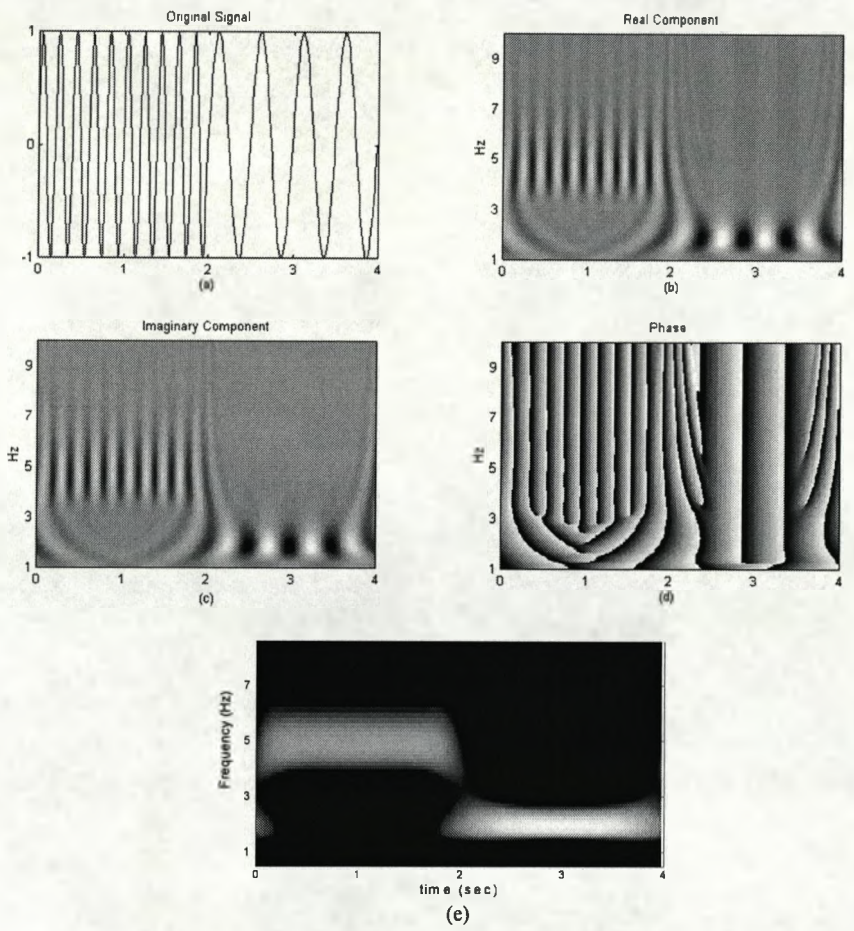

Figure 2-13: The wavelet transform using the Morlet wavelet
(a) original signal; (b) a real component plot of the result; (c) an imaginary component plot of the result; (d) phase plot of the result; (e) a modulus plot

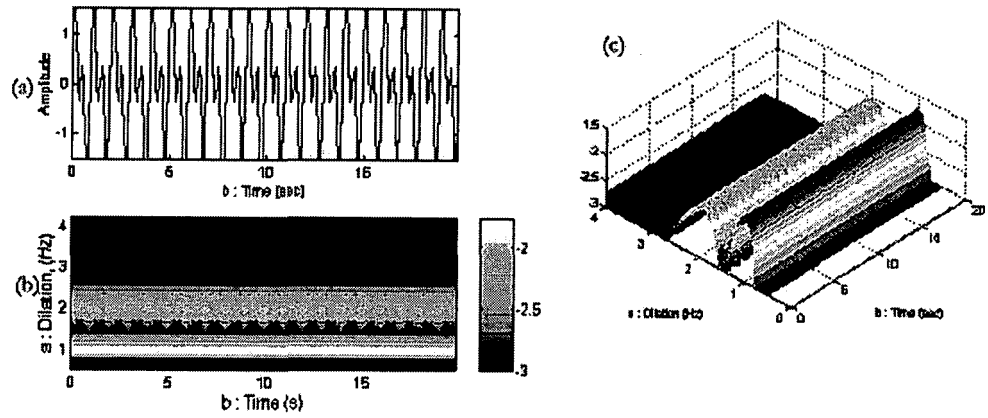

Figure 2-14: Example of wavelet transform
(a) original signal; (b) scalogram; (c) 3-D plot of the result

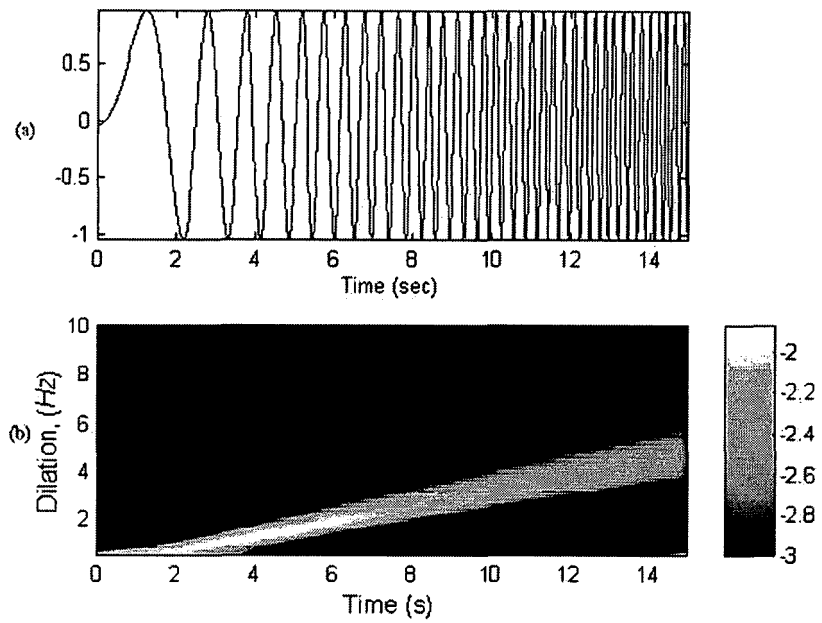

Figure 2-15: The wavelet transform of a chirp signal
(a) original signal; (b) scalogram plot of the wavelet transform

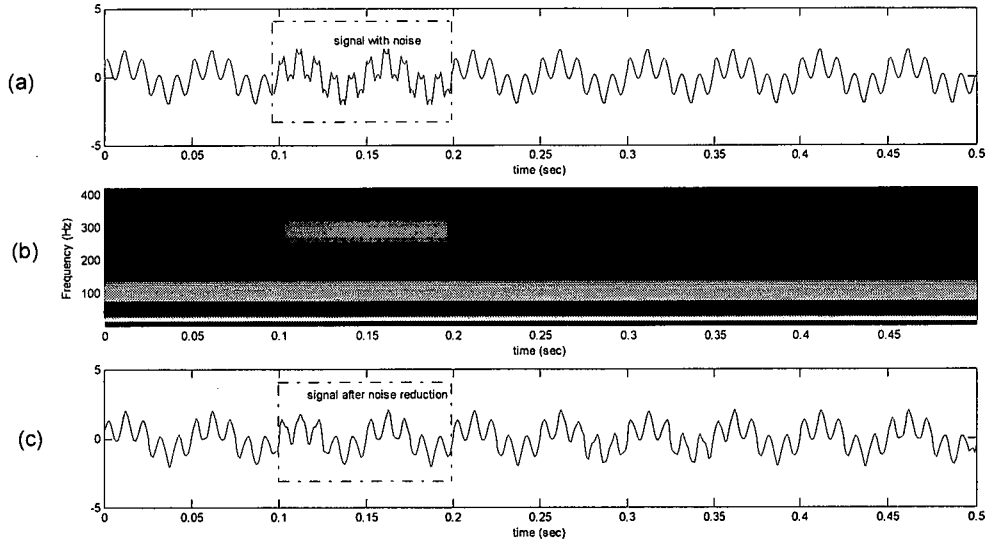

Figure 2-16: Noise reduction

(a) original signal including high frequency noise; (b) scalogram plot of wavelet transform; (c) the denoised signal

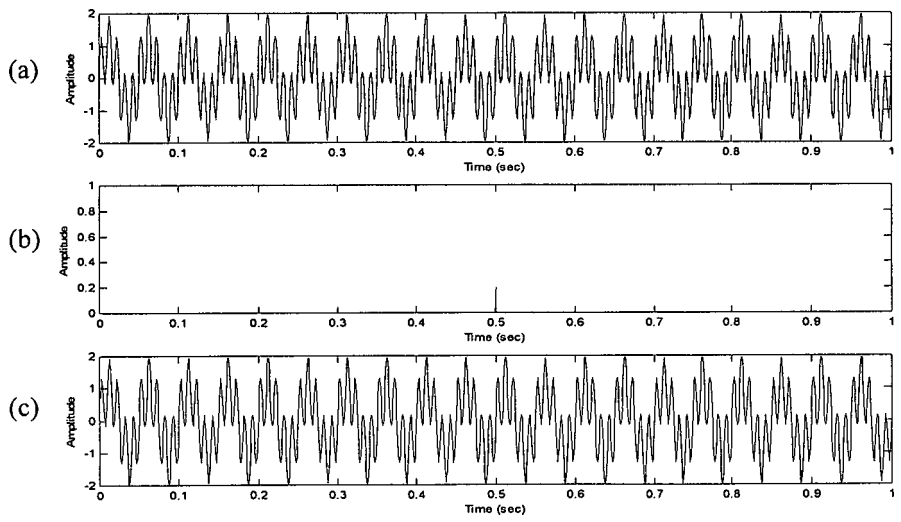

Figure 2-17: The composite signal used in the demonstration of CWT-based transient detection

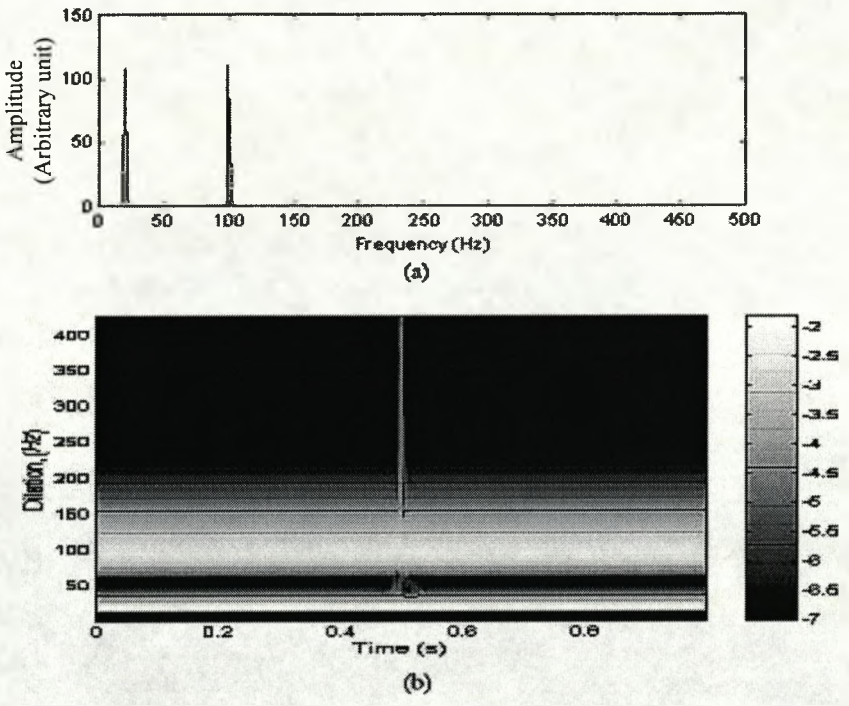

Figure 2-18: The results of transient detection using the CWT

(a) the power spectrum using Fourier transform;

(b) scalogram plot of wavelet transform

CHAPTER 3
METHODOLOGY

CHAPTER 3
METHODOLOGY

3.1 Introduction

This chapter describes the details of the data and analysis methods employed in the research. The ECG data sets used in the analysis are described in section 3.2. Sections 3.3 to 3.5 cover the research methodology, shown schematically in the simple box diagram of figure 3-1. Three main stages are illustrated: feature extraction, data pre-processing, and data classification. The feature extraction procedure is described in section 3.3 where an explanation is given of the time-frequency-based power spectral analysis used for extracting characteristic features of the pre-shock ECGs. Section 3.4 describes the data pre-processing stage which prepares the characterising features before feeding into the classifier. In section 3.4, feature normalisation and principal component analysis (PCA) are investigated as alternative feature formats for use in the study of shock outcome prediction. Section 3.5 provides details of the Bayesian's classifier used for predicting defibrillation outcome in this study. Sections 3.6 to 3.9 then go on to describe the software implementation of the developed research methodology. Section 3.6 details coding of the computer program. Software validation is described in section 3.7, and an investigation of the optimal number of cross validations required in the analysis is presented in section 3.8. Finally, section 3.9 contains a summary of the contents of the chapter.

3.2 Study data

The study undertaken by the author is based on an 821-trace ECG data set of VF immediately prior to countershock. This data set was obtained from 156 patients with out-of hospital cardiac arrest of cardiac etiology. The data was acquired by the Medical Control Module (MCM) of the 'Heartstart 3000' defibrillator and supplied by Professor Petter Steen of Ullevaal University Hospital, Department of Anesthesiology, Oslo, Norway. Approval for this study was obtained through the Regional Committee for Research Ethics, health region III (Norway), and the Norwegian Data Inspectorate (Eftestol et al, 2000).

Each trace is composed of three segments: (1) 20 seconds of ECG containing pre-shock VF, (2) the shock itself, and (3) 20 seconds of ECG immediately post-shock. A typical time trace is shown in figure 3-2. This shows pre-shock ventricular fibrillation (VF) with the shock administered half way through the trace. The subsequent trace contains the defibrillation outcome signal.

The signals were grouped according to shock outcome as shown in table 3-1 (Eftestol et al, 2000). In the first group, the outcome was defined as Return Of Spontaneous Circulation (ROSC) if a palpable pulse was presented in the post-shock period. In the second group, the outcome was defined as electromechanical disassociation (EMD) or pulseless electrical activity (PEA) when the heart continues to work electrically but fails to provide a circulation (Houghton and Gray, 1997). The outcome was defined as asystole if there is no spontaneous electrical cardiac activity (Houghton and Gray, 1997). The outcome was defined as VF where the VF started after 5 seconds from the shock. Finally, the outcome was defined as non-reset if the VF continued immediately after shock (less than 5 seconds post-shock). Figures 3-3 to 3-7 show five typical ECG traces including the pre-shock VF, the shock itself, and the post-shock traces. Both the ECG time series and corresponding wavelet transform scalogram are shown for each case. The outcomes are ROSC for figure 3-3, EMD for figure 3-4, Asystole for figure 3-5, VF for figure 3-6, and non-reset shock for figure 3-7. In the study conducted by the author, the outcomes were further sub-categorised as ROSC and NOROSC (NO Return Of Spontaneous Circulation) where NOROSC includes all non-ROSC signals, i.e. EMD, asystole, VF, and non-reset.

3.3 Feature extraction

In this study, the characteristic features were extracted from the power spectrum of the time-frequency transform. The wavelet power spectrum was defined previously in chapter 2, equation 2-14. From the STFT (see equation 2-3), the power spectrum can be expressed as:

$$E(f) = \sum_{\tau=0}^{\infty} E(\tau, f) \tag{3-1}$$

where τ is the location of the window function used in the STFT computation.

Figure 3-8 illustrates the relationship between information in the time-frequency domain and the power spectrum. The power spectrum shown on the right of the figure was computed by summing the component in the scalogram along the time domain. The power spectra derived from the STFT and CWT are smoother than that obtained using the Fourier transform. This is shown in figure 3-9. In this example, the window function used in the STFT analysis was a Gaussian function of 2 seconds width. For the CWT analysis, the Morlet function was employed as the mother wavelet.

Several characterising features computed from the power spectrum were examined as potential markers for shock outcome prediction. These were: median frequency (FM), peak frequency (FP), standard deviation (STD), skewness (SK), kurtosis (KT), and flatness (FT). These features are defined as follows:

median frequency:
$$FM = \frac{\sum_{f=0}^{\infty} f\, E(f)}{\sum_{f=0}^{\infty} E(f)} \tag{3-2}$$

peak frequency:
$$FP = \arg\max_{f}(E(f)) \tag{3-3}$$

standard deviation:
$$STD = \sqrt{\sum_{f=0}^{\infty} (f - FM)^2 E(f)} \tag{3-4}$$

skewness:

$$SK = \frac{\sum_{f=0}^{\infty}(f - FM)^3 E(f)}{\left(\sum_{f=0}^{\infty}(f - FM)^2 E(f)\right)^{3/2}} \tag{3-5}$$

kurtosis:

$$KT = \frac{\sum_{f=0}^{\infty}(f - FM)^4 E(f)}{\left(\sum_{f=0}^{\infty}(f - FM)^2 E(f)\right)^{2}} \tag{3-6}$$

flatness:

$$FT = \frac{\sum_{f=0}^{\infty}\log(E(f))}{\sum_{f=0}^{\infty}E(f)} \tag{3-7}$$

3.4 Data pre-processing

Data pre-processing is an optional stage before feeding features into the classifier. This study employed two pre-processing methods: feature normalisation and principal component analysis (PCA). The feature normalisation method maps the original feature distribution into the unit interval between zero and one. The PCA technique creates new variables which are linear combinations of the original variables. These methods are described in more detail in the following two sub-sections.

3.4.1 Feature normalisation

The objective of feature normalisation is to standardise the characteristic feature sets (equation 3-2 to 3-7) before feeding into the classifier. The value range of the modified feature sets is between zero and one. The mapping method is based on the boxplot representation of the data.

A boxplot (or Whisker plot) is a useful statistical plot representing much of the important information on data distribution. The boxplot displays the overall distribution of the data set using a rectangular box with whiskers. The box may be aligned either horizontally or vertically. The boxplot shown in figure 3-10 provides a visual display of pertinent statistical information including the three quartiles and the minimum and the maximum values of the data.

The main box in the boxplot indicates an interquartile range (IQR) of the data set with the bottom edge indicating the location of the first quartile and the upper edge indicating the location of the third quartile. The line within the box represents the second quartile or median. Lines spread from the end of the box are known as whiskers. The upper whisker extends to the highest valued data point within 1.5 IQR from the third quartile. The lower whisker extends to the lowest valued data point within 1.5 IQR from the first quartile. The points lying outwith the whisker ranges are called outliers and are each shown separately.

Feature normalisation changes the raw PDFs obtained from the features (equation 3-2 to 3-7) to lie within the unit interval. In order to achieve this, first the characterising feature PDFs are truncated by relocating the outliers to the end of the furthest outlying whiskers. This is shown schematically in figure 3-11. The lower and upper whiskers in the boxplots are then set to zero and one respectively. The equation for this data mapping can be expressed as

$$y = \frac{x - lower}{upper - lower} \tag{3-8}$$

where *lower* is the lower whisker value; and *upper* is the upper whisker value. Note that two boxplots are shown in figure 3-11. These correspond to the two feature sets ROSC and NOROSC used in the study (see section 3.2). The normalised feature mapping uses the highest and lowest value of the whiskers from either boxplot. The minimum and maximum values of new feature range are zero and one respectively, as shown on the right hand side of figure 3-11. The two outliers at the top and bottom of the original features set shown in the boxplot are moved to the new limits (zero and one) of the normalised feature range (right boxplot).

3.4.2 Principal component analysis (PCA)

Principal components analysis (PCA) is a technique used to form new variables which are linear combinations of the original variables. PCA is concerned with expressing the variance-covariance structure of variables through a few linear combinations of these variables. This technique is very useful in data reduction and data interpretation. This chapter describes the concept and application of PCA as used in the data classification described in this thesis.

In this study, the PCA method was employed in the prediction of the defibrillation outcome. The PCA was used to generate new variables from the original features (equation 3-2 to 3-7). The PCA variables were then fed into the classifier for predicting the defibrillation outcome of the VF signal.

3.4.2.1 The mathematics of PCA (Chatfield and Collins, 1980, Johnson and Wichern, 1998)

Algebraically, principal components are particular linear combinations of p random variables. Suppose $X^T = [X_1, X2,.., Xp]$ is a p-dimensional set of random variables with covariance matrix Σ. Each linear combination of the random variables X is

$$\begin{aligned} Y_1 &= a_1'X = a_{11}X1 + a_{21}X2 + \ldots + a_{p1}X_p \\ Y_2 &= a_2'X = a_{12}X1 + a_{22}X2 + \ldots + a_{p2}X_p \\ &\vdots \\ Y_p &= a_p'X = a_{1p}X1 + a_{2p}X2 + \ldots + a_{pp}X_p \end{aligned} \qquad \text{(3-9a)}$$

or

$$Y_j = a_j^T X \qquad j = 1, 2, \ldots, p \qquad \text{(3-9b)}$$

where $a_j^T = [a_{1j}, \ldots, a_{pj}]$ is a vector of constants. Thus the variance and variance-covariance matrix of Y_j is

$$\mathrm{Var}(Y_j) = a_j^T \Sigma a_j \qquad j = 1,2, \ldots ,p \tag{3-10}$$

$$\mathrm{Cov}(Y_j, Y_k) = a_j^T \Sigma a_k \qquad j, k = 1,2, \ldots ,p \tag{3-11}$$

The principal components are uncorrelated linear combinations Y_1, Y_2, ..., Y_p whose variances in equation (3-10) are as large as possible.

The first principal component is the linear combination with maximum variance: that is, it maximises Var (Y_1) subject to the constraint that $a_1^T a_1 = 1$. This approach was originally proposed by Harold Hotelling to find the line in p-space such that the total sum of squared perpendicular distances from the points to the line is maximised.

The second principal component is the linear combination Y_2 which has the maximum variance subject to $a_2^T a_2 = 1$. This component is uncorrelated with Y_1 (i.e. Cov(Y_1 , Y_2) = 0). Similarly, the latter components Y_3, Y_4, ..., Y_p can be derived to be uncorrelated and to have decreasing variance.

3.4.2.2 The use of PCA pre-processing in data classification

This section introduces the application of PCA as a pre-processing method in data classification. Two illustrative examples of the use of PCA in 2-class data classification are considered in this section (As we will see later the work of this thesis is based on a 2-class system: ROSC and NOROSC). The PCA technique produces new features according to equation 3-9a or 3-9b. Figure 3-12 illustrates the data distributions of two test data groups (group1 and group2) in the X1-X2 plane. The data of group1 and group2 are symbolised using circles and crosses respectively. The PDFs of these two data sets along the X1 axis are shown in the bottom plot and the PDFs of the two data sets along the X2 axis are shown in the right hand plot. The two PCA axes, (PCA1 and PCA2) determined using equation 3-10, are shown in figure 3-12. PCA1, representing the first component, is the linear combination of the data with maximum variance. PCA2 representing the second component, is orthogonal to PCA1. The PDFs of the two data sets projected on PCA1 and PCA2 axis are showed in figures 3-13(a) and 3-13(b) respectively. Compared to the original variables (X1 and X2), the PDFs of these two sets are better separated on PCA1 axis

but exhibit poorer separation on the PCA2 axis. Therefore, PCA1 is the most effective projection with which to discriminate group1 from group2. PCA2 is a significantly worse projection than the original axis projections for classification purposes.

The above example illustrates how the use of the first PCA can provide better separated data groups. This is not always the case. The following example will illustrate a poor case of classification using the first PCA. Figure 3-14 shows another example of two groups data in the X1-X2 plane. The PDFs of these two data sets along the X1 axis are shown at the bottom of the plot and the PDFs of the two data sets along the X2 axis are shown at the right hand side of the plot. The projections of the data onto the PCA1 and PCA2 axes are shown in figure 3-15(a) and 3-15(b) respectively. In this case, the data on the PCA1 axis gives the worst separation of group1 and group 2. In contrast the data of group1 and group2 were completely discriminated when projected on to the PCA2 axis. Hence, it can be seen from this example that great care must be taken when using PCA analysis as a pre-processing tool as the major principal component does not necessarily allow best separation of the data groups.

3.5 Data classification

3.5.1 Probability distribution function estimation

The probability distribution function (PDF) estimates used in this work are computed using the multidimensional histogram technique and Gaussian kernel smoothing (Eftestol et al, 2000). Each feature set is sorted into a series of bins on the feature axis, and the resulting histogram smoothed using an elliptic Gaussian kernel function. Histogram bin number and Gaussian kernel width are the controlling parameters in the PDF estimation. Each feature axis was divided into N_b intervals. The width of the Gaussian kernel function controls the smoothness. The one-dimensional histogram is smoothed by the one-dimensional Gaussian kernel function given by

$$h(i) = \frac{e^{\frac{-(i-t)^2}{2\sigma}}}{\sigma\sqrt{2\pi}} \tag{3-12}$$

where t is the centre of the bin. The Gaussian kernel width was limited to 6σ in the study.

One-dimensional (1D) PDF estimation is illustrated in the simple example shown in figure 3-16. The data points are located at 1, 4, 6, 11, 12, and 16 on the X1 axis as shown in the top of the plot. In this example, the histogram was generated using 20 bins and each bin smoothed using the one-dimensional Gaussian kernel functions shown in the middle plot. The Gaussian width (6σ) in this example was set equal to 10. The estimated PDF, generated from the sum of the Gaussian kernel functions, is shown in the bottom plot of figure 3-16.

Multidimensional histograms are smoothed using a multivariate Gaussian kernel function given by

$$f(x) = \frac{1}{(2\pi)^{p/2}|\Sigma|^{1/2}} e^{-(x-\mu)'\Sigma^{-1}(x-\mu)/2} \tag{3-13}$$

where $-\infty < x_i < \infty$, $i = 1, 2, \ldots, p$. Equation 3-13 is the generalised p-dimensional Gaussian distribution for a $p \times 1$ vector x of observations with the expected value μ and the variance-covariance matrix Σ (Johnson and Wichern, 1998).

A 2-dimensional bivariate Gaussian distribution can be evaluated in terms of the individual parameters: $\mu_1 = E(X_1)$, $\mu_2 = E(X_2)$, $\sigma_{11} = Var(X_1)$, $\sigma_{22} = Var(X_2)$, and $\rho_{12} = \sigma_{12}/(\sigma_{11}\sigma_{22})^{1/2} = Corr(X_1, X_2)$.

The inverse of the covariance matrix, $\Sigma = \begin{bmatrix} \sigma_{11} & \sigma_{12} \\ \sigma_{12} & \sigma_{22} \end{bmatrix}$, is

$$\Sigma^{-1} = \frac{1}{\sigma_{11}\sigma_{22} - \sigma_{12}^2}\begin{bmatrix} \sigma_{22} & -\sigma_{12} \\ -\sigma_{12} & \sigma_{11} \end{bmatrix} \tag{3-14}$$

Substituting $\sigma_{12} = \rho_{12}(\sigma_{11}\sigma_{22})^{1/2}$, the squared distance become

$$(x-\mu)'\Sigma^{-1}(x-\mu) =$$

$$[x_1-\mu_1, x_2-\mu_2]\frac{1}{\sigma_{11}\sigma_{22}(1-\rho_{12}^2)}\begin{bmatrix} \sigma_{22} & ,-\rho_{12}\sqrt{\sigma_{11}\sigma_{22}} \\ -\rho_{12}\sqrt{\sigma_{11}\sigma_{22}}, & \sigma_{11} \end{bmatrix}\begin{bmatrix} x_1-\mu_1 \\ x_2-\mu_2 \end{bmatrix}$$

$$= \frac{\sigma_{22}(x_1-\mu_1)^2 + \sigma_{11}(x_2-\mu_2)^2 - 2\rho_{12}\sqrt{\sigma_{11}\sigma_{22}}(x_1-\mu_1)(x_2-\mu_2)}{\sigma_{11}\sigma_{22}(1-\rho_{12}^2)}$$

$$= \frac{1}{1-\rho_{12}^2}\left[\left(\frac{x_1-\mu_1}{\sqrt{\sigma_{11}}}\right)^2 + \left(\frac{x_2-\mu_{21}}{\sqrt{\sigma_{22}}}\right)^2 - 2\rho_{12}\left(\frac{x_1-\mu_1}{\sqrt{\sigma_{11}}}\right)\left(\frac{x_2-\mu_{21}}{\sqrt{\sigma_{22}}}\right)\right] \tag{3-15}$$

Since

$$|\Sigma| = \sigma_{11}\sigma_{22} - \sigma_{12}^2 = \sigma_{11}\sigma_{22}(1-\rho_{12}^2) \tag{3-16}$$

we can substitute equation (3-15) and (3-16) to equation (3-13) to get

$$f(x_1,x_2) = \frac{1}{2\pi\sqrt{\sigma_{11}\sigma_{22}(1-\rho_{12}^2)}} e^{\left\{-\frac{1}{2(1-\rho_{12}^2)}\left[\left(\frac{x_1-\mu_1}{\sqrt{\sigma_{11}}}\right)^2 + \left(\frac{x_2-\mu_{21}}{\sqrt{\sigma_{22}}}\right)^2 - 2\rho_{12}\left(\frac{x_1-\mu_1}{\sqrt{\sigma_{11}}}\right)\left(\frac{x_2-\mu_{21}}{\sqrt{\sigma_{22}}}\right)\right]\right\}} \tag{3-17}$$

The 2-dimensional histogram is smoothed using a bivariate Gaussian distribution with $\sigma_{11}=\sigma_{22}=\sigma$ and $\rho_{12}=0$. The symmetic bivariate Gaussian function can be expressed by

$$f(x_1, x_2) = \frac{1}{2\pi\sigma} e^{\left\{-\frac{1}{2\sigma}\left[(x_1-\mu_1)^2+(x_2-\mu_2)^2\right]\right\}} \quad (3\text{-}18)$$

where (μ_1, μ_2) is the centre of each bin and the Gaussian width is limited to 6σ.

Figure 3-17 contains an example of 2D-PDF estimation using the above expressions. The scatter plot of the example data is shown in the top plot. The histogram was produced using 200×200 bins and each bin was smoothed using 2D symmetric bivariate Gaussian functions. The middle plot of figure 3-17 shows the estimated PDF which was smoothed using 2D Gaussian functions with widths (6σ) equal to 5. The bottom plot of figure 3-17 displays the estimated PDF smoothed using wider Gaussian function where the width was set equal to 10. The enhanced spreading of this PDF compared to that generated using narrower Gaussian kernels is obvious when comparing the two plots.

3.5.2 Bayes classifier

As stated in section 3.2, the five outcomes (w_i i=1 , … , 5 shown in table 3-1) were further clustered into two groups: w_1 corresponding to ROSC and w_2, w_3, w_4, and w_5 corresponding to a NOROSC outcome. In this two-class classification, the ROSC group was represented by ω_1 and the NOROSC group was represented by ω_2. The vector V contains the study features which were derived from the spectral characteristics given by equations 3-2 to 3-7. The feature vector used in the study can be expressed as:

$$V = \begin{bmatrix} v_1 \\ v_2 \\ v_3 \\ v_4 \\ v_5 \\ v_6 \\ v_7 \\ v_8 \\ v_9 \end{bmatrix} = \begin{bmatrix} FM \\ FP \\ STD \\ SK \\ KT \\ FT \\ FM-FP \\ FM-FT \\ FP-FT \end{bmatrix}. \quad (3\text{-}19)$$

The probability density functions of each feature v_i with respect to class ω_j, $p(v_i/\omega_j)$, were estimated using the multidimensional histogram technique and Gaussian kernel smoothing as described in the previous section. The *a posteriori* probability for each class conditioned on the feature v_i is calculated using Bayes rule, defined as

$$P(\omega_j / v_i) = \frac{P(\omega_j)p(v_i / \omega_j)}{\sum_{j=1}^{k} P(\omega_i)p(v_i / \omega_i)} \quad ; \quad j = 1,...,k \tag{3-20}$$

and k=2 corresponding to the ROSC and NOROSC cases.

Using these probabilities we split the feature space V into decision regions ω_j where $j = 1, \ldots, k+1$. The extra class ω_{k+1} represents the reject class. This is done by assigning a cost function $c(\omega_i, \omega_j)$, which describes the loss suffered if class ω_j is decided when the true class is in fact ω_i.

3.5.3 Risk function

A cost value is a key rule for decision rule optimisation in the Bayes classifier. Each cost value, $c(\omega_i, \omega_j)$, represents the classified class ω_j as belonging to the true class ω_i. The cost matrix **C** representing K(K+1) cost values for K classes classification is defined as

Reject Column

$$\mathbf{C} = \begin{bmatrix} c(\omega_1,\omega_r) & c(\omega_1,\omega_1), c(\omega_1,\omega_2), \cdots, c(\omega_1,\omega_k) \\ c(\omega_2,\omega_r) & c(\omega_2,\omega_1), c(\omega_2,\omega_2), \cdots, c(\omega_2,\omega_k) \\ \vdots & \vdots \quad \vdots \quad \ddots \quad \vdots \\ c(\omega_k,\omega_r) & c(\omega_k,\omega_1), c(\omega_k,\omega_2), \cdots, c(\omega_k,\omega_k) \end{bmatrix} \tag{3-21}$$

The cost matrix contains 2 components which are:

- The first column of **C** containing the K rejected losses

- The other components, K×K matrix, including the K cases of correct decisions

In general the diagonal of matrix L, representing correct decisions, contains zeros; whereas off diagonals contains positive values. In the general case, the loss matrix can be represented as

$$\mathbf{C} = \begin{bmatrix} c(\omega_1,\omega_r), & 0 & ,c(\omega_1,\omega_2),\cdots,c(\omega_1,\omega_k) \\ c(\omega_2,\omega_r),c(\omega_2,\omega_1), & 0 & ,\cdots,c(\omega_2,\omega_k) \\ \vdots & \vdots & \vdots \quad ,\ddots, \quad \vdots \\ c(\omega_k,\omega_r),c(\omega_k,\omega_1),c(\omega_k,\omega_2),\cdots, & & 0 \end{bmatrix} \tag{3-22}$$

The classifier risk is the expectation of the loss $E\{\mathbf{C}\}$ expressed as

$$\begin{aligned} \mathbf{R} &= E\{\mathbf{C}\} = \mathbf{C}^T\mathbf{P} \\ &= \begin{bmatrix} c(\omega_1,\omega_r),c(\omega_2,\omega_r)\ldots,c(\omega_k,\omega_r) \\ c(\omega_1,\omega_1),c(\omega_2,\omega_1)\ldots,c(\omega_k\omega_1) \\ \vdots \quad \vdots \quad \ddots \quad \vdots \\ c(\omega_1,\omega_k),c(\omega_2,\omega_k)\ldots,c(\omega_k,\omega_k) \end{bmatrix} \begin{bmatrix} P(\omega_1/v) \\ P(\omega_2/v) \\ \vdots \\ P(\omega_k/v) \end{bmatrix} \end{aligned} \tag{3-23}$$

Risk minimisation is the method of optimising classification performance. To find the optimum decision rule, we search for the minimum component.

3.5.4 The two-class classifier

As stated above, for this study the shock outcome was categorised into two groups according to the success of defibrillation shock. The first group, labelled ω_1, is the class of the return of spontaneous circulation (ROSC) containing w_1. The other group, labelled ω_2, is the class of the non return of spontaneous circulation (NOROSC) including w_2, w_3, w_4, and w_5. For the Bayes classifier, we add the reject class (ω_r) for unclassified patterns. The loss matrix, therefore, can be represented as a 2×3 matrix given by

$$\mathbf{C} = \begin{bmatrix} c(\omega_1,\omega_r), c(\omega_1,\omega_1), c(\omega_1,\omega_2) \\ c(\omega_2,\omega_r), c(\omega_2,\omega_1), c(\omega_2,\omega_2) \end{bmatrix} \tag{3-24}$$

The loss matrix can be simplified as

$$c(\omega,\hat{\omega}) = \begin{cases} 0 & for \quad \hat{\omega} = \omega \quad correct \quad decision \\ C_r & for \quad \hat{\omega} = \omega_r \quad reject \\ C_{\omega\hat{\omega}} & otherwise \quad wrong \quad decision \end{cases} \tag{3-25}$$

Therefore, the classifier risk becomes

$$\begin{aligned} \mathbf{R} &= \begin{bmatrix} C_r, C_r \\ 0 \ , C_{\omega_2\omega_1} \\ C_{\omega_1\omega_2}, 0 \end{bmatrix} \begin{bmatrix} P(\omega_1 / v) \\ P(\omega_2 / v) \end{bmatrix} \\ \hat{\mathbf{R}} &= \frac{1}{C_{\omega_1\omega_2}} \mathbf{R} = \begin{bmatrix} C_r / C_{\omega_1\omega_2}, C_r / C_{\omega_1\omega 2} \\ 0 \quad , C_{\omega_2\omega_1} / C_{\omega_1\omega_2} \\ 1 \quad , \quad 0 \end{bmatrix} \begin{bmatrix} P(\omega_1 / v) \\ P(\omega_2 / v) \end{bmatrix} \end{aligned} \tag{3-26}$$

Substituting $\gamma = C_r/C_{\omega 1\omega 2}$ and $\beta = C_{\omega 2\omega 1}/C_{\omega 1\omega 2}$, the classifier risk becomes

$$\hat{\mathbf{R}} = \begin{bmatrix} \gamma, \gamma \\ 0, \beta \\ 1 \ , \ 0 \end{bmatrix} \begin{bmatrix} P(\omega_1 / v) \\ P(\omega_2 / v) \end{bmatrix}$$

$$= \begin{bmatrix} \gamma(P(\omega_1 / v) + P(\omega_2 / v)) \\ \beta P(\omega_2 / v) \\ P(\omega_1 / v) \end{bmatrix} = \begin{bmatrix} \gamma \\ \beta P(\omega_2 / v) \\ P(\omega_1 / v) \end{bmatrix} \tag{3-27}$$

The decision rule of the two-class classifier will select the minimum component of the classification risk $\hat{\mathbf{R}}$. The decision rule can be represented as

$$Decision \ \ for \ \ \hat{\omega} \ : \begin{cases} \omega_r \ \ if \ \ \min \hat{R} = \gamma \\ \omega_1 \ \ if \ \ \min \hat{R} = \beta P(\omega_2 / v) \\ \omega_2 \ \ if \ \ \min \hat{R} = P(\omega_1 / v) \end{cases} \tag{3-28}$$

An example of the risk function is shown schematically in figure 3-18. This example illustrates the decision regions of two-class classifier without a reject class (i.e. only ω_1 and ω_2). The probability distributions, $p(v/\omega_1)$ and $p(v/\omega_2)$, are represented in figure 3-18(a). The *a posterior* probabilities, $P(\omega_1/v)$ and $P(\omega_2/v)$, from Bayes theorem in equation 3-20 are illustrated in figure 3-18(b). A decision boundary obtained from the classifier without risk optimisation is shown in figure 3-18(b) by a dotted line. The risk classifier of this example is defined as

$$\hat{\mathbf{R}} = \begin{bmatrix} \beta P(\omega_2 / v) \\ P(\omega_1 / v) \end{bmatrix} \tag{3-29}$$

and the decision rule is presented as

$$Decide \ \ for \ \ \hat{\omega} \ : \begin{cases} \omega_1 \ \ if \ \ \min \hat{R} = \beta P(\omega_2 / v) \\ \omega_2 \ \ if \ \ \min \hat{R} = P(\omega_1 / v) \end{cases} \tag{3-30}$$

Figure 3-18(c) shows the risk classifier corresponding to different values of β. This plot presents the effect of the risk function on the decision region. The decision boundary moves to the right hand side and the left hand side of the original decision boundary corresponding to values of $\beta = 0.5$ and $\beta = 2$ respectively.

3.5.5 Classifier performances

Classifier performances can be quantified in terms of sensitivity and specificity. The sensitivity quantifies the ability to correctly identify true positives. It is defined as:

$$Sensitivity = \frac{True\ positives}{True\ positives + False\ negatives} \tag{3-31}$$

Sensitivity is assigned as an evaluation criterion. For this research, the sensitivity is the probability of positive prediction of ROSC outcome.

The specificity is the ability to correctly identify true negatives, i.e. the probability of prediction of NOROSC outcome. Specificity is defined as:

$$Specificity = \frac{True\ \ negative}{True\ \ negative + False\ \ positive} \tag{3-32}$$

An illustration of sensitivity and specificity derived from two PDFs is shown schematically in figure 3-19. In the figure, region A represents the true positives: i.e. the number of correct predictions of ROSC outcome. Region C represents the false negatives, corresponding to the number of wrong predictions of ROSC. The regions B and D represent, respectively, the number of wrong and correct decisions of NOROSC outcome.

Sensitivity and specificity are computed from the classifier output where sensitivity is defined for the general case as

$$P_{sens}(\omega_i) = P(R_i|\omega_i) \tag{3-33}$$

and specificity is defined as

$$P_{spec}(\omega_i) = \frac{1}{1-P(\omega_i)} \sum_{j,k \neq i} P(\omega_k) P(R_j|\omega_k) \tag{3-34}$$

In this research, for the two outcomes (ROSC and NOROSC), the sensitivity is given by

$$P_{sens}(\omega_{ROSC}) = P(R_{ROSC} / \omega_{ROSC}) \tag{3-35}$$

and specificity by

$$P_{spec}(\omega_{ROSC}) = \frac{1}{[1-P(\omega_{ROSC})]} P(\omega_{NOROSC}) P(R_{NOROSC} / \omega_{NOROSC}) \tag{3-36-a}$$

since $P(\omega_{NOROSC}) = 1 - P(\omega_{ROSC})$, the specificity can be expressed more compactly as

$$P_{spec}(\omega_{ROSC}) = P(R_{NOROSC} / \omega_{NOROSC}) \tag{3-37-b}$$

The cost function is tuned iteratively to adjust the sensitivity performance to meet the performance criterion (Eftestol et al, 2000).

3.5.6 Decision rule optimisation

The optimisation loop for finding the optimum decision rules is composed of four major parts. A schematic diagram of the decision rule optimisation loop is shown in figure 3-20. The decision rule is updated from each new cost matrix. For simple optimisation, the rejected class is ignored in the classification and the risk classifier can be defined as equation 3-29. Hence only β in the cost matrix is updated in the optimisation. The evaluation system checks the performance of the decision rule. The

cost matrix is updated if the decision rule has a low performance. The procedure updates the cost matrix as follows

$$\beta_{new} = \beta_{old} + \alpha(t - y) \tag{3-38}$$

where t, y, and α are the target value of the evaluation system, the evaluation output, and learning rate, respectively.

3.6 Computer programming

This section details the implementation of the described research methodology in computer code. The experiments were run on a Pentium III 600 MHz laptop computer with 128 MB of RAM. The operation system (OS) used in the experiments was Microsoft Windows version 98. All experiments were conducted using MATLAB version 6.1 incorporating the signal processing and statistics toolbox. Figure 3-21 presents an overview of the research methodology. The source codes used in the work described in this thesis are available in Appendix A.

The cross validation technique was employed to separate the ECG database into training and test sets. In this technique, the data set is divided into N subsets (N is the number of cross validations). One of the N subsets is used as the test set and the remaining N-1 subsets are put together to form the training set. The experiment is repeated N times until each subset is used as the test set. The performance of classification is then computed from the average of N experiments. The subdivision of the data into training and test sets for each experiment is shown schematically in figure 3-22. In this study, the number of cross validations was two (i.e. $N = 2$) as the number of values in the ROSC data set is small. More specifically, the data sets were partitioned into two groups with the first group containing 38 ROSC and 373 NOROSC data and the second group containing 38 ROSC data and 372 NOROSC data.

Each pre-shock VF signal was transformed into the time-frequency plane using either the CWT or STFT. In the CWT, the wavelet transform was computed using the

inverse Fourier transform as described in section 2.3.4.3. A linear frequency range, from 1 Hz to 20 Hz with 200 intervals, was used in the computation of the CWT. In the STFT analysis, the Fourier transform of each window was evaluated from the FFT function in MATLAB with 1024 points concerning the frequency range of 0-50 Hz (i.e. half of the sampling rate). The STFT program *stft_extract.m* is given in Appendix A. A Gaussian window function was employed for the STFT which has set to three widths: these were 1, 2, and 3 seconds. The power spectra were then computed from the CWT scalogram and the three STFT spectrograms. The characteristic features were then computed from the power spectrum as described above. The source codes for the feature extraction (*wt_extract.m* (CWT) and *stft_extract.m* (STFT)) are given in appendix A.

The PDF was estimated using a histogram and Gaussian kernel smoothing technique. The feature set was sorted into N_b bins for generating the histogram. The resulting histogram was smoothed using a Gaussian function of N_w width. The number of bins N_b used in the study were 50, 75, 100, 125, 150, 175, and 200 bins. The width values for the Gaussian function, N_w, used to smooth histogram of original data were 1, 2, 3, 4, 5, 6, 7, 8, 9, and 10. When classifying with normalised features, the width values of the Gaussian function were set to 0.1, 0.2, 0.3, 0.4, 0.5, 0.6, 0.7, 0.8, 0.9, and 1. The 1D-PDF was generated using the program *newsmoothex.m* and the 2D-PDF was generated using the program *newsmooth2ex.m*. Both program codes are provided in Appendix A.

A posterior probability functions were computed from the estimated PDF using the Bayes equation as presented in equation 3-19. *A posterior* probability functions of the training set were trained using the risk optimisation rule until the classifier reached 95% sensitivity. The classifier with the risk value (β) obtained from the training process was then used to test with the posterior probability functions of the test set. The functions of the Bayes classifier programs for 1D and 2D features are called *classify1d_2.m* and *classify2d_2.m*, respectively. These are listed in Appendix A.

3.7 Software validation and classification

This section presents the validation of the classifier which was employed in this thesis. The Bayes classifier detailed in section 3.5 was validated using synthetic test data pior to its use on the main data set. The Bayes classifier was employed to test and train these data sets using the program *classify2d_2.m* listed in Appendix A. In this example, the cross validation number is 2, i.e. each class was equally partitioned into two groups: the training and test sets. The probability distribution function (PDF) of each training set was estimated using the 2D histogram technique and Gaussian kernel smoothing described in 3.5.1. The classifier performances are presented using receiving operator characteristic (ROC) curves. ROC curves are widely used in the medical literature to assess the performance of a diagnostic test. The ROC curve is the plot of the true positive (sensitivity) against the false positive (1-specificity). The area under the ROC curve (AUC) is a summary statistic of diagnostic performance. An AUC value of 1 represents a perfect diagnostic test whereas the AUC value of 0.5 represents a worthless diagnostic test. Both the 1D and 2D Bayes classifiers used in this thesis were validated. In addition, a full parametric study of bin numbers and Gaussian widths were used in the validation for the PDF estimation. In this section, a number of examples of validation of the classifier are provided.

3.7.1 1D classifier validation

Firstly, the 1D classifier was validated using 2 classes of synthetic test data shown as histograms in figure 3-23(a). The number of data for class A and Class B are 120 and 160 respectively. These are randomly distributed within their respective intervals. The data ROC curve illustrated in figure 3-23(b) presents the performance of classification covering the whole sensitivity range. The dashed line shows the theoretical ROC curve associated with increasingly large data sets. Figure 3-24 shows the performances of the 1D classifier obtained from a selection of bin numbers and Gaussian widths. The system ROC curve of each classifier was plotted to allow comparison with the data ROC curve. From the results, it is clearly seen that the use of narrow Gaussian widths produced significant errors in classification compared to the data ROC curve (figure 3-24(a) and 3-24(d)). However, the classifier employing wider Gaussian widths (figure 3-24(b), 3-24(c), and 3-24(d)) produced classification

results much closer to the data ROC curve for the whole range of sensitivity. This validation shows that the 1D classifier used in this thesis achieved good results except when using very narrow Gaussian widths.

3.7.2 2D classifier validation

Figure 3-25(a) shows the test data sets used for the validation of the 2D classifier. The data of class A and class B are symbolised using stars and circles respectively. Based on the linear discriminant analysis technique (LDA), the data ROC curve of the test data in figure 3-25(b) was determined from the classification associated with the decision axis in figure 3-25(a). This data ROC curve was used as a classification reference for the validation of the 2D classification. Figure 3-26 shows the performances of the 2D classifier obtained from a selection of bin numbers and Gaussian widths. The system ROC curve of each classifier was plotted to allow comparison with the data ROC curve. It can be seen from the results that the classification employing very narrow Gaussian width gave poor performances (such as the Gaussian width equal to 0.1 shown in figure 3-26(a) and 3-26(d)). Further, the system employing a large number of bins and very narrow Gaussian widths (e.g. 200×200 bins and Gaussian width set to 0.1) could only classify the test data in a limited sensitivity range between 60% and 80% as shown in figure 3-26(a). However, the classifier employing wider Gaussian widths shown in figure 3-26(b), 3-26(c), and 3-26(e) produced classification results close to the data ROC curve over the whole range of sensitivity. This validation shows that the 2D classifier used in this thesis achieves good results in general except when employing very narrow Gaussian widths.

Figure 3-27 shows decision boundaries of the example classification indicated by the arrow in figure 3-26(e). This example shows non-linear decision boundaries produced by the 2D Gaussian kernel PDF estimation method. For the first validation, the classifier achieved the test performance of 53% specificity at 97% sensitivity as shown in figure 3-27(a). For the second validation, the test performance achieved the classification of 54% specificity at 97% sensitivity as shown in figure 3-27(b). The test performance was defined as the average of the test sensitivities and the test

specificities of both cross-validations. Hence, this example achieved a classification of 53% specificity at 97% sensitivity.

Figure 3-28 shows the scatter plot of two class data with a more random distribution. The data of class A and class B are symbolised using circles and stars respectively. Again, the cross validation number is set equal to 2. The PDF of each training set was estimated using the 2D histogram technique and Gaussian kernel smoothing described in 3.5.1. In these experiments, the example set was classified using a classifier which employed several bin numbers and Gaussian widths.

Figures 3-29 and 3-30 show the boundary decision of the classifier (dashed line) employing 150×150 bins and Gaussian width equal to 0.5. The risk function of the classifier was optimised by updating β in equation 3-29 until an average training sensitivity of 95% was achieved. Figure 3-29 shows the decision boundary of optimised classifier for the training sets of each validation. The boundary decision of the first validation is presented in figure 3-29(a). The training sensitivity and specificity in the first validation were 95% and 98% respectively. Figure 3-29(b) shows the boundary decision of training in the second validation. The training sensitivity and specificity in the second validation were 95% and 93% respectively. The optimised classifier produced an average training sensitivity and average training specificity of 95%. Figure 3-30 illustrates scatter plots of the test sets of each validation including the decision boundaries. For the first validation, the classifier achieved the test performance of 88% specificity at 85% sensitivity as shown in figure 3-30(a). For the second validation, the test performance achieved the classification of 88% specificity at 95% sensitivity as shown in figure 3-30(b). The test performance was defined as the average of the test sensitivities and the test specificities of both validations. Hence, this example achieved a classification of 88% specificity at 90% sensitivity.

Figure 3-31 and 3-32 shows the results of classification between class A and B employing more bins and narrower Gaussian widths in the PDF estimation. The PDF was generated with 200×200 bins and Gaussian width set to 0.2. Figure 3-31(a) presents the scatter plot of training sets including boundary decision for the first validation. The training sensitivity and specificity obtained from optimised system

were 100% and 100% respectively. In the second validation, the training sensitivity and specificity of classifier were 98% and 100% respectively and the boundary decision is as shown in figure 3-31(b). The optimised classifier produced an average training of 100% specificity at 99% sensitivity. Figure 3-32 shows scatter plots of the test sets for each validation including the decision boundary. For the first validation, shown in figure 3-32(a), the classifier achieved the test performance of 90% specificity at 83% sensitivity. For the second validation, shown in figure 3-32(b), the test performance achieved the classification of 88% specificity at 90% sensitivity. The average test sensitivity and test specificity of both validations were 86% and 90% respectively. This classifier under-achieved the test sensitivity criterion since the test sensitivity was not within 5% tolerance of the training sensitivity criterion of 95%. This example shows that the classifier employing a large number of bins and narrow Gaussian widths achieves a good training performance; however, the test sensitivity is poor for this system.

Figure 3-33 and 3-34 display the results obtained from a parametric study employing various bin numbers and widths of the Gaussian smoothing function used in the PDF estimation for the test data shown in figure 3-28. The numbers of bin used in these experiments were 50, 75, 100, 125, 150, 175, and 200. The widths of Gaussian function used for smoothing histograms were 0.1, 0.2, 0.3, 0.4, 0.5, 0.6, 0.7, 0.8, 0.9, and 1. The classifier of each experiment was optimised until the training sensitivity reached 95% as shown in figure 3-33(a). The training specificities corresponding to optimised classifiers are illustrated in figure 3-33(b). The test sensitivity and test specificity of each experiment are illustrated in figure 3-34(a) and 3-34(b) respectively. Figure 3-34(a) shows that classifiers employing very narrow Gaussian widths produced poor sensitivities in testing (e.g. Gaussian width equal to 0.1). The best classification result was chosen from the experiments achieving the test sensitivity within 5% tolerance of the training sensitivity (95%). In this study the best classification performance was achieved using 50×50 bins and a Gaussian width value of 0.5 giving 91% specificity at 90% sensitivity.

3.8 Determination of optimal cross validation number for use in the shock outcome prediction studies

It is important to determine the number of cross validations required because the performance of the classifier is related to it (Burman, 1989). The effect of validation number on the classifier performance was therefore investigated. This was carried out using the experimental data using wavelet power spectra. The VF ECG data detailed in section 3.2 were used in these experiments which covered a range of parameters used in the main study (described in more detail in Chapter 4), e.g. characteristic features, length of pre-shock signal, bin number and Gaussian width. The following three examples show how a suitable cross validation number was determined for the shock outcome prediction work using the ECG data set used in this thesis. Each example was analysed using a Bayes classifier with several cross validation numbers (N): these are $N = 2$, 3, 4, and 5. ROC curves are used to present the performances of the classifier.

Figure 3-35 shows the results from one of these experiments where the length of the pre-shock VF signal used was 10 seconds. The FT extracted from the wavelet power spectra was used as the characteristic feature to classify the shock outcome (ROSC and NOROSC). The values of FT were then mapped into the unit range using the feature normalisation technique described in section 3.4.1.The PDFs of ROSC and NOROSC classes were estimated using 175 bins for generating the histograms and a Gaussian width of 0.2 for smoothing the histograms. The ROC curves present the test sensitivities of the system between 10% and 95%. In addition, error bars are attached to the ROC curves. From the results, the classifier system using a cross validation number of 2 gave the smallest error bars for sensitivity and specificity associated with test sensitivities over 80%.

Figure 3-36 shows a result from one of these experiments where the length of VF pre-shock signal used was 15 seconds. The FP extracted from the wavelet power spectra was used as the characteristic feature to classify the shock outcome (ROSC and NOROSC). The values of FP were then mapped into unit range using the feature normalisation technique. The PDFs of ROSC and NOROSC classes were estimated using 100 bins for generating the histograms and a Gaussian width of 0.2 for

smoothing the histograms. The ROC curves present the test sensitivities of the system between 10% and 95%. The ROC curves of the classifier using a cross validation number of 2 gave the smallest error for both test sensitivity and test specificity associated with sensitivities over 80%.

Figure 3-37 shows a result from one of these experiments where the length of VF pre-shock signal used was 20 seconds. The FM extracted from the wavelet power spectra was used as the characteristic feature to classify the shock outcome (ROSC and NOROSC). The values of FM were then mapped into the unit range using the feature normalisation technique. The PDFs of ROSC and NOROSC classes were estimated using 50 bins for generating the histograms and a Gaussian width of 0.7 for smoothing the histograms. Similar to the above examples, the ROC curves of the classifier using a cross validation number of 2 gave the small error for both test sensitivity and test specificity associated to sensitivities over 80%.

From the above examples it is clear that the cross validation number of 2 gave the best results of classification error in both test sensitivity and test specificity associated with the test sensitivity over 80%. The small error bars show that the system exhibits good repeatability throughout the experiments. The number of test data for each validation decreases as the cross validation number increases. Hence the small number of ROSC data, available for use in the work of this thesis (76 ROSC and 745 NOROSC), causes a large variance in test sensitivity and specificity in the classifier when high cross validation numbers are employed.

In addition, from a practical view point classification using a small number of cross validations is computationally faster than classification using a large number of cross validations. This is especially true for 2D classification. Given all of the above, a cross validation number of 2 was employed in the classification of shock outcome between ROSC and NOROSC in the author's main programme of study outlined in chapter 4.

3.9 Chapter summary

This chapter described the ECG data set study used in the study and detailed the methodology used in the analysis. The feature extraction, data preparation, and data classification methods were then outlined in detail. The computer implementation of the methods was described briefly, with full program listings provided in Appendix A. The problems of software validation and classification issues were then dealt with. These wavelet and STFT-based prediction methods developed by the author and described in this chapter (summarised in figure 3-1) will be employed to perform the shock outcome prediction analysis of the Oslo human out-of-hospital data set. This work is detailed in the following two chapters.

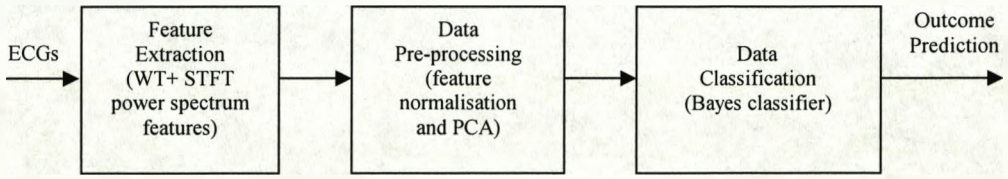

Figure 3-1: Schematic diagram of the methodology

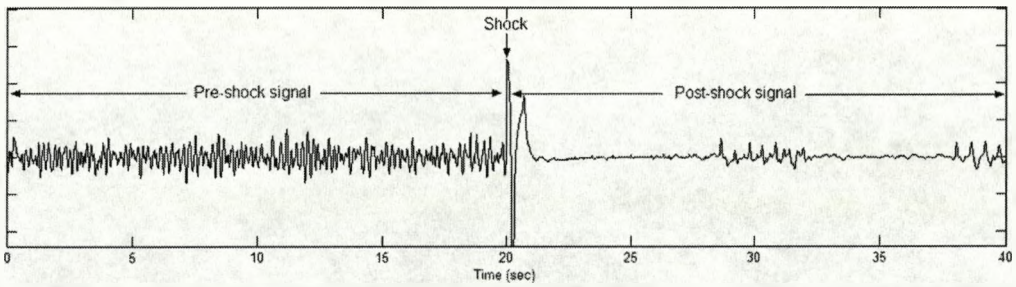

Figure 3-2: An example of an ECG trace from the study data set

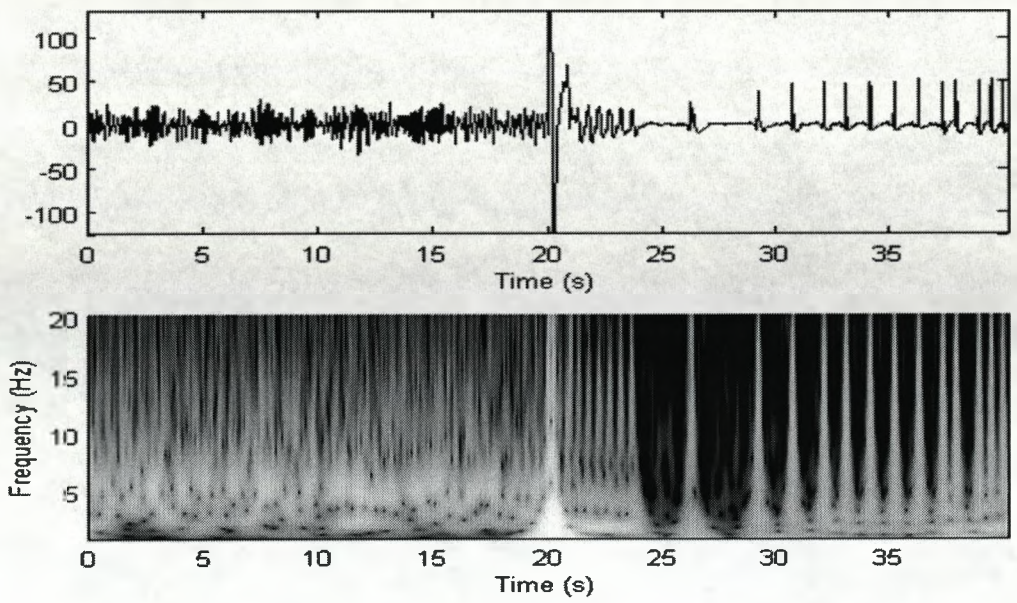

Figure 3-3 Top: a segment of VF trace containing pre-shock VF and post-shock outcome w_1 (i.e. ROSC) Bottom: the corresponding scalogram

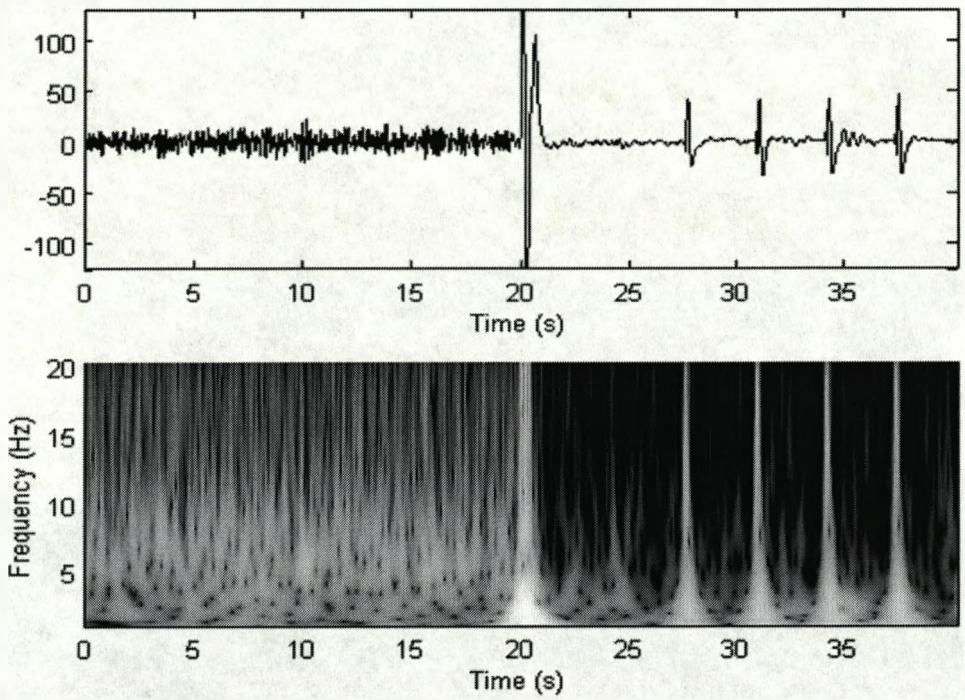

Figure 3-4 Top: a segment of VF trace containing pre-shock VF and post-shock outcome w_2 (i.e. EMD) Bottom: the corresponding scalogram

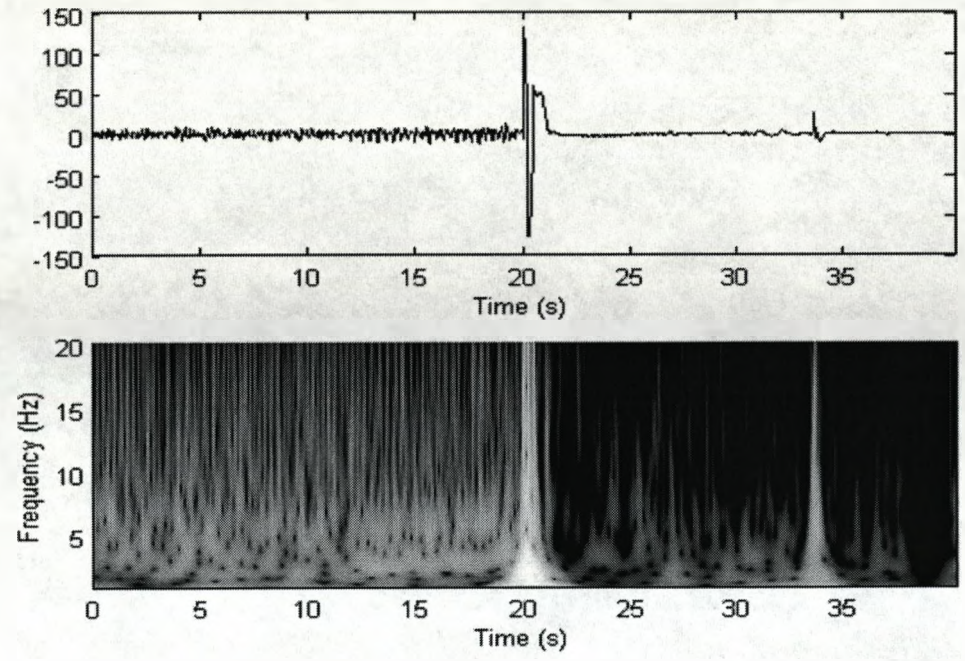

Figure 3-5 Top: a segment of VF trace containing pre-shock VF and post-shock outcome w_3 (i.e. asystole) Bottom: the corresponding scalogram

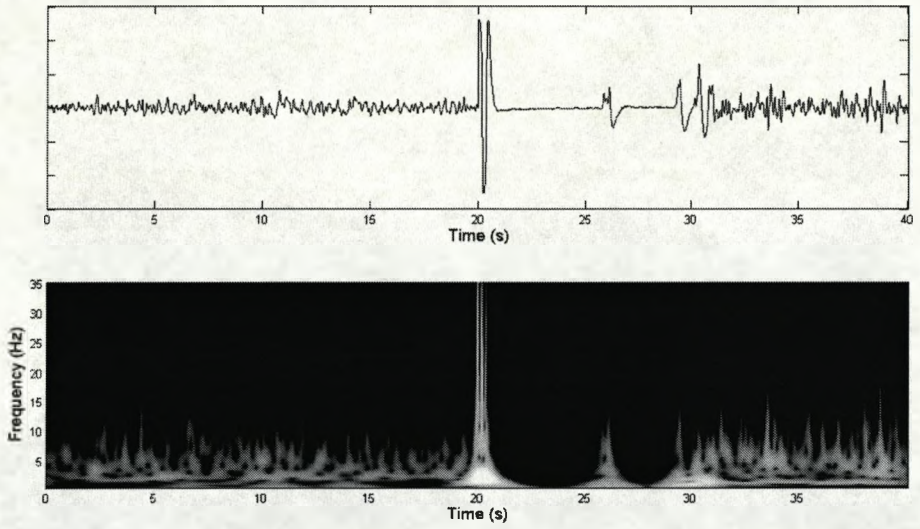

Figure 3-6 Top: a segment of VF trace containing pre-shock VF and post-shock outcome w_4 (i.e. VF) Bottom: the corresponding scalogram

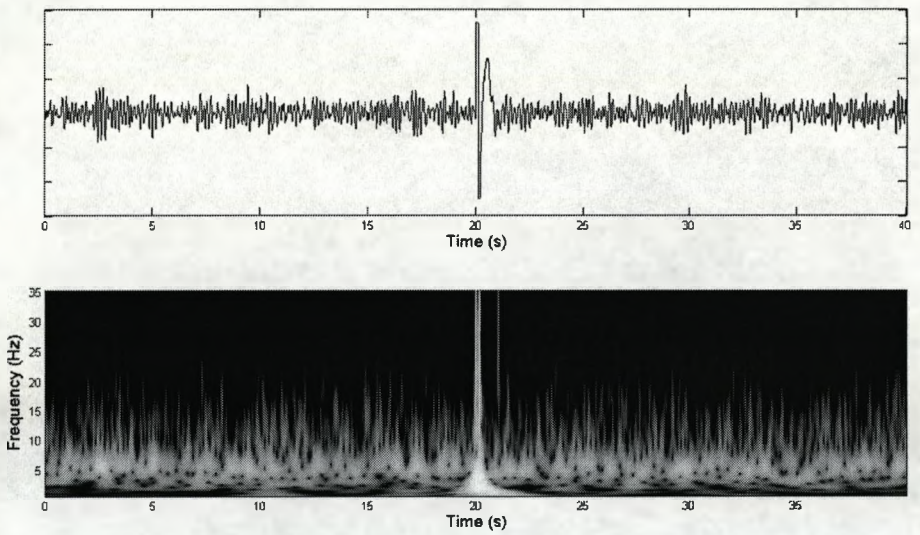

Figure 3-7 Top: a segment of VF trace containing pre-shock VF and post-shock outcome w_5 (i.e. non-reset shock) Bottom: the corresponding scalogram

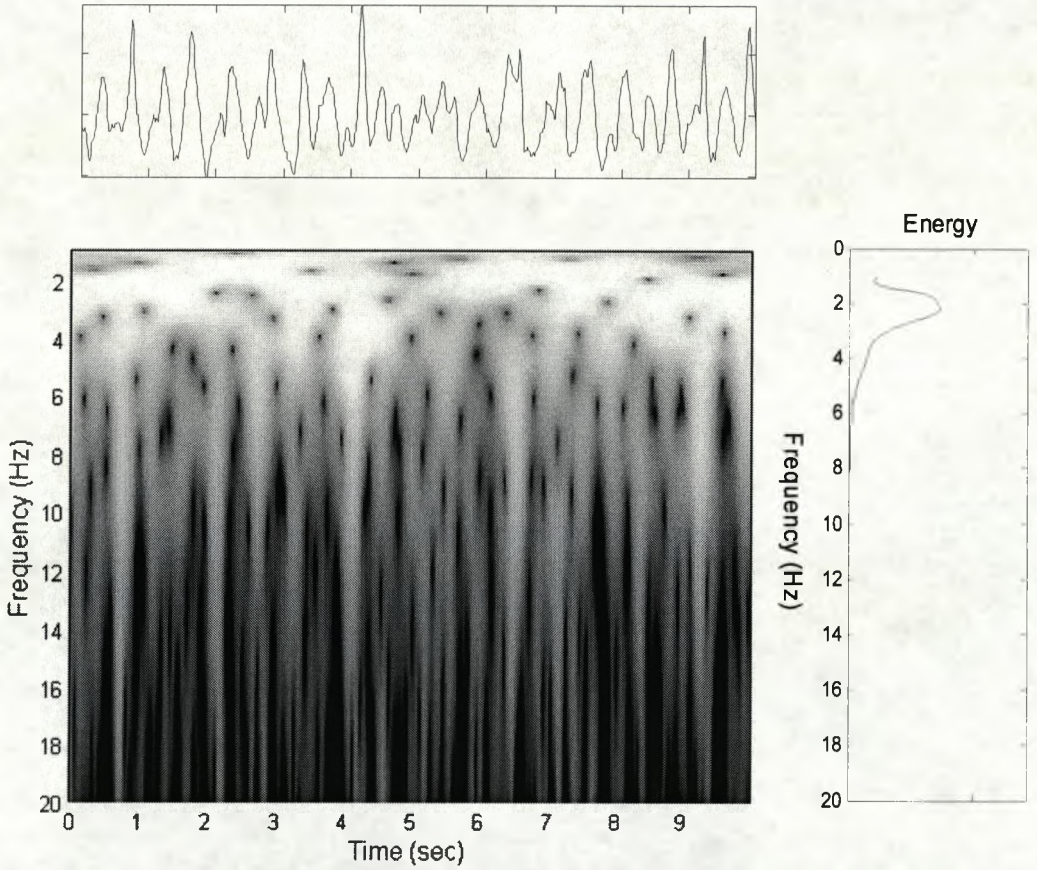

Figure 3-8: The relation between the wavelet scalogram and the wavelet power spectrum: Top left: Original ECG, Bottom left: wavelet scalogram, Right: wavelet frequency spectrum obtained by integrating across the scalogram

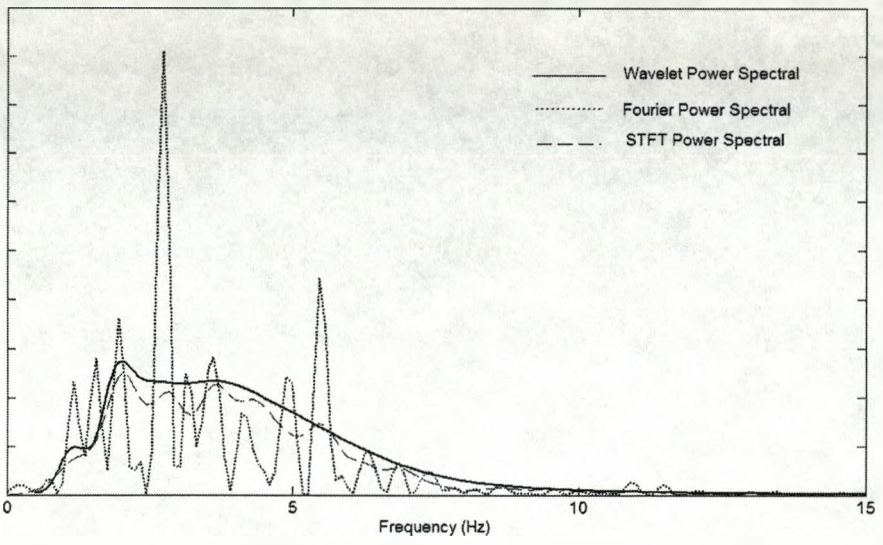

Figure 3-9: Comparing power spectra from the FFT, STFT, and CWT

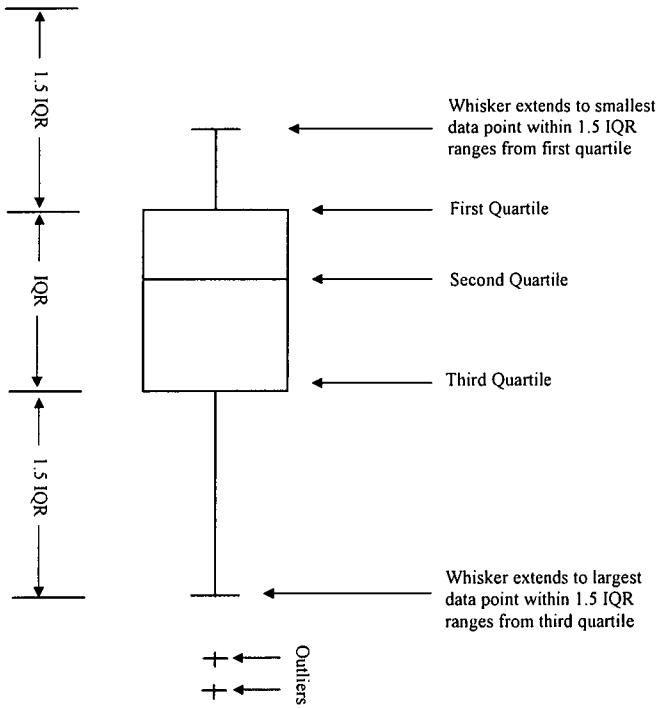

Figure 3-10: Illustration of a boxplot diagram

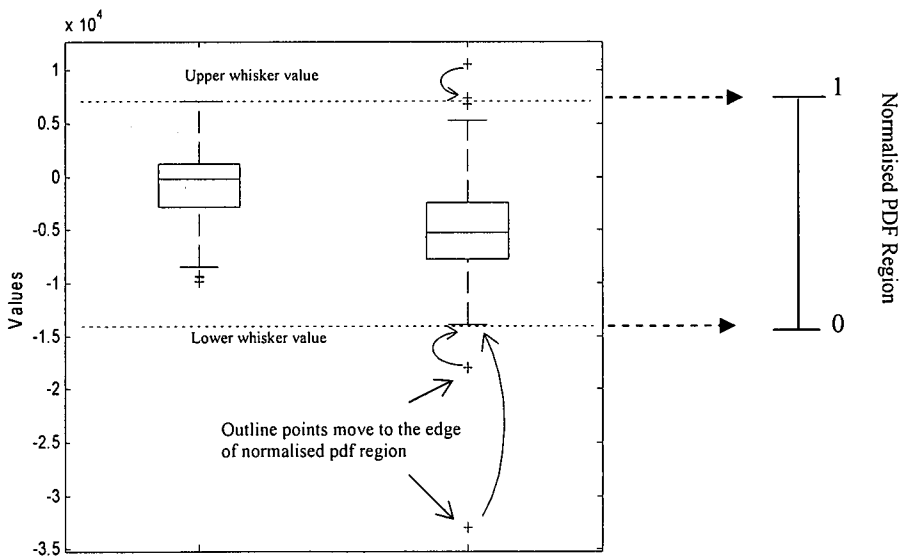

Figure 3-11: The relationship between normalised data and original data

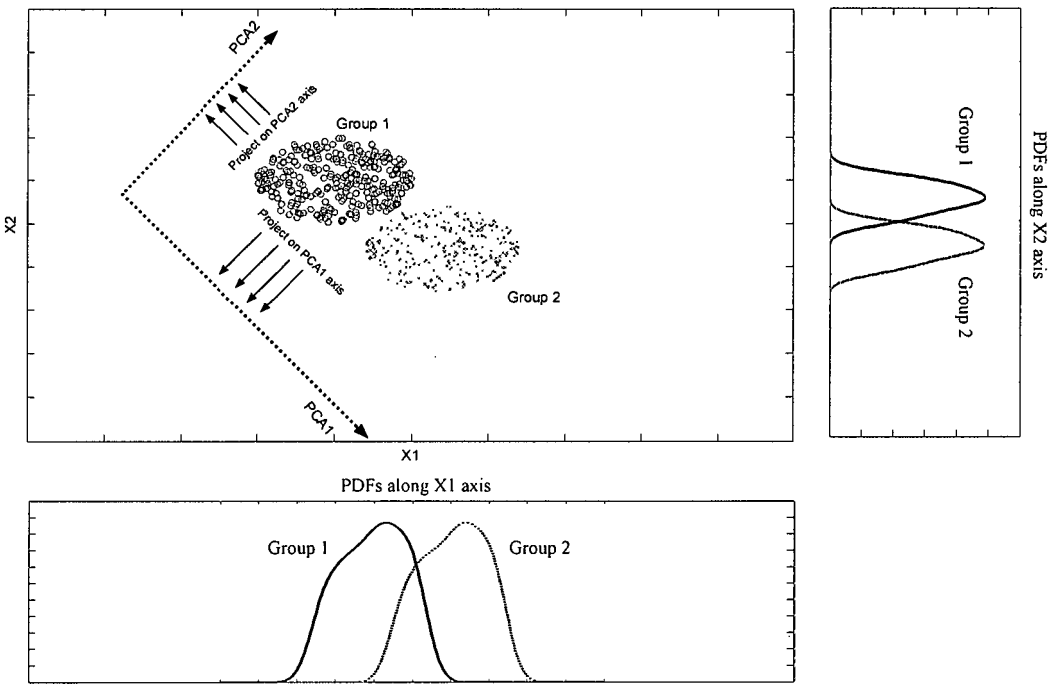

Figure 3-12: Example of PCA with two categories of data classification

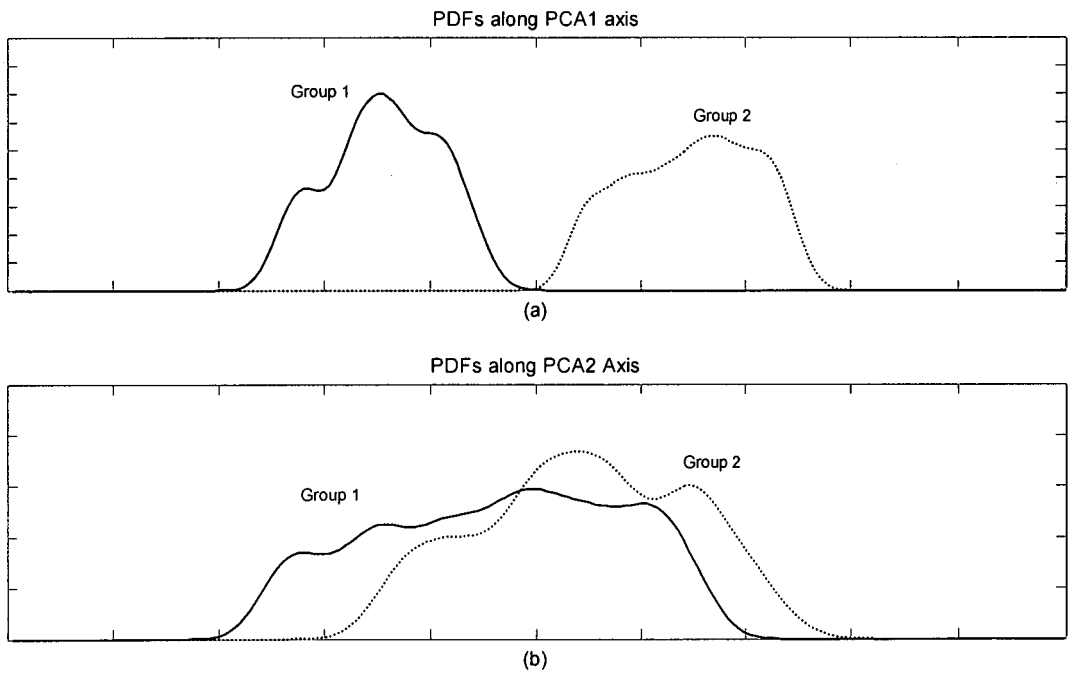

Figure 3-13: PDFs of the two data sets in figure 3-12 projected onto PCA1 and PCA2

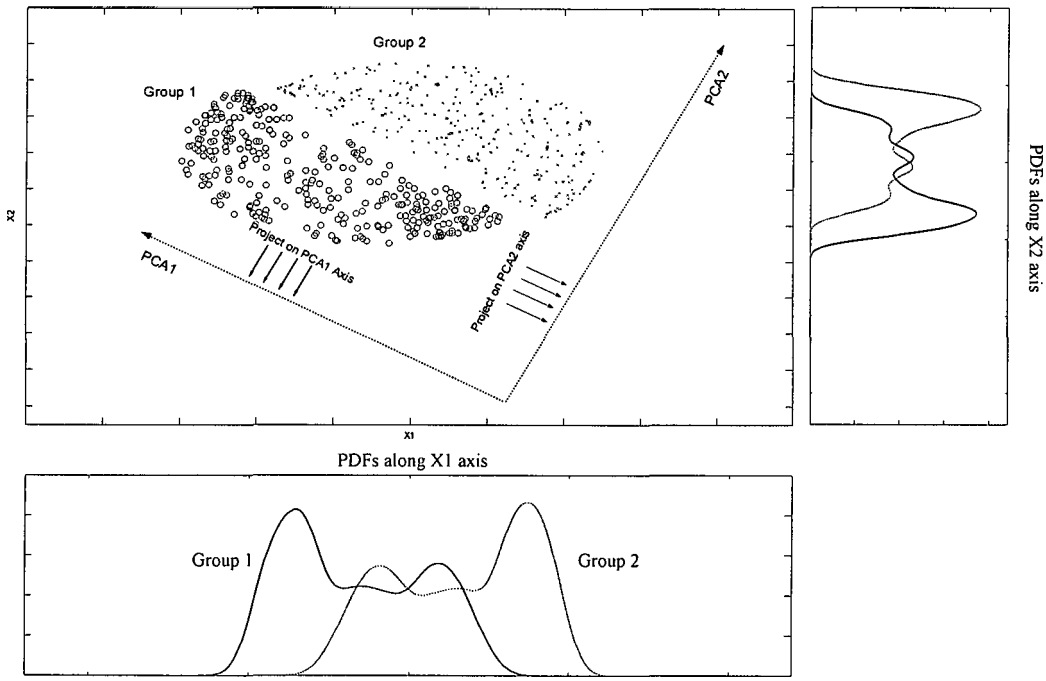

Figure 3-14: Another example of PCA with two categories of data classification

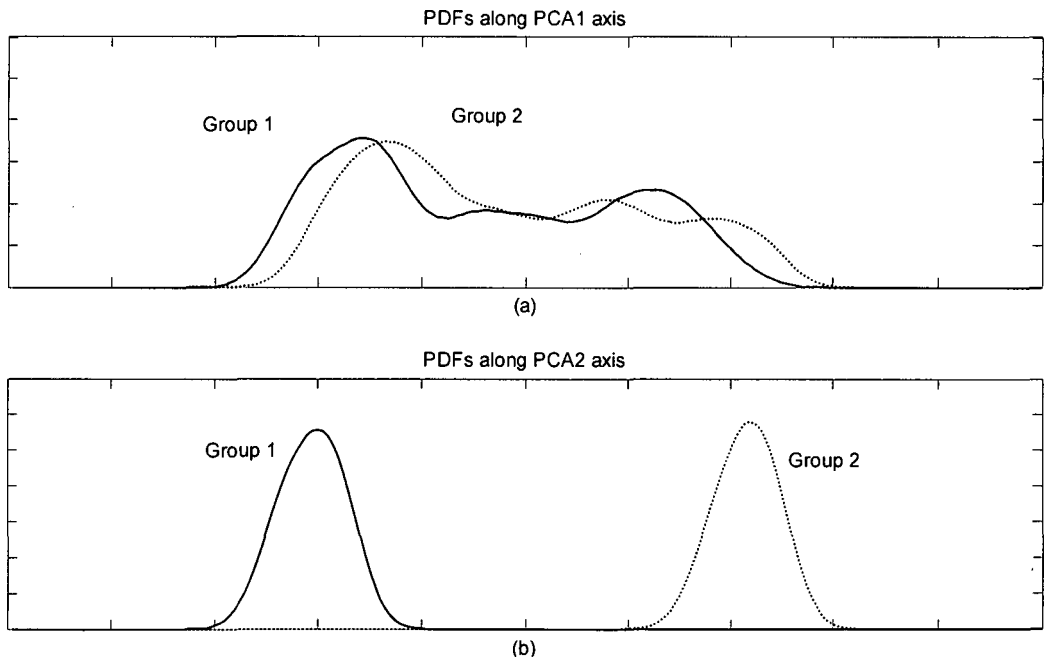

Figure 3-15: PDFs of the two data sets in figure 3-14 projected onto PCA1 and PCA2

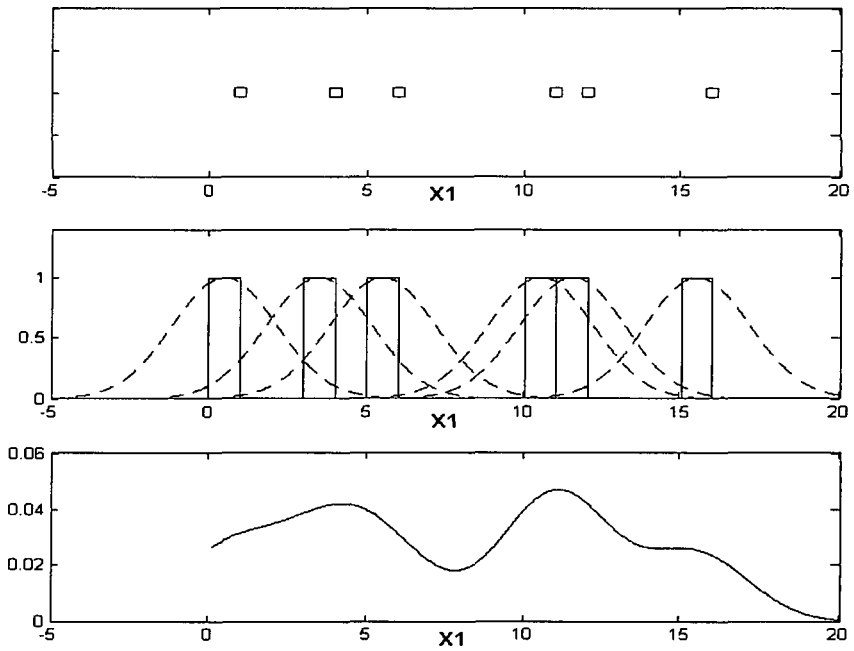

Figure 3-16: An illustration of 1D-PDF estimation

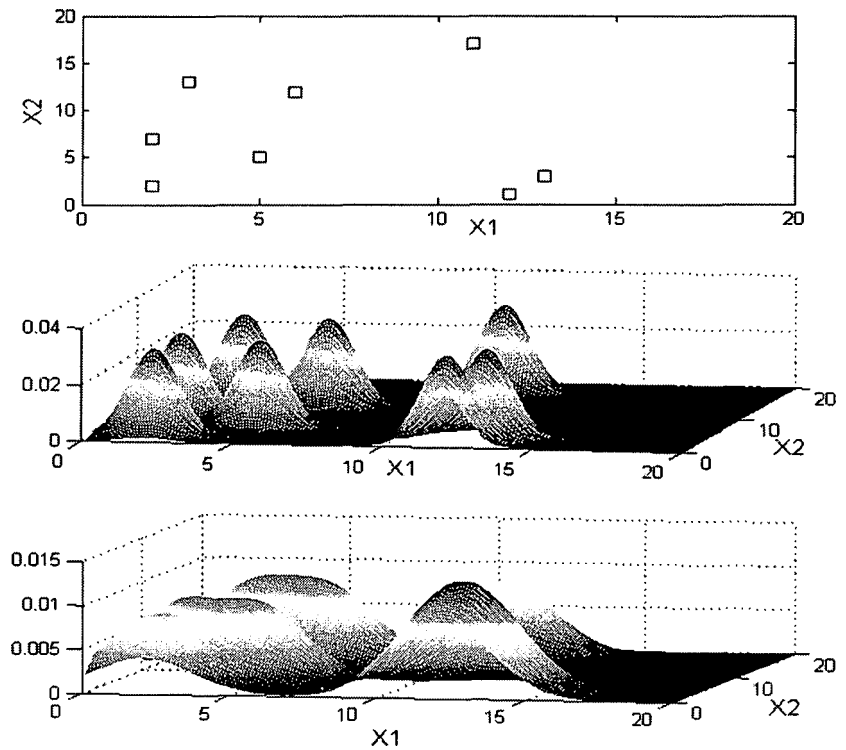

Figure 3-17: Illustrations of 2D-PDF estimation

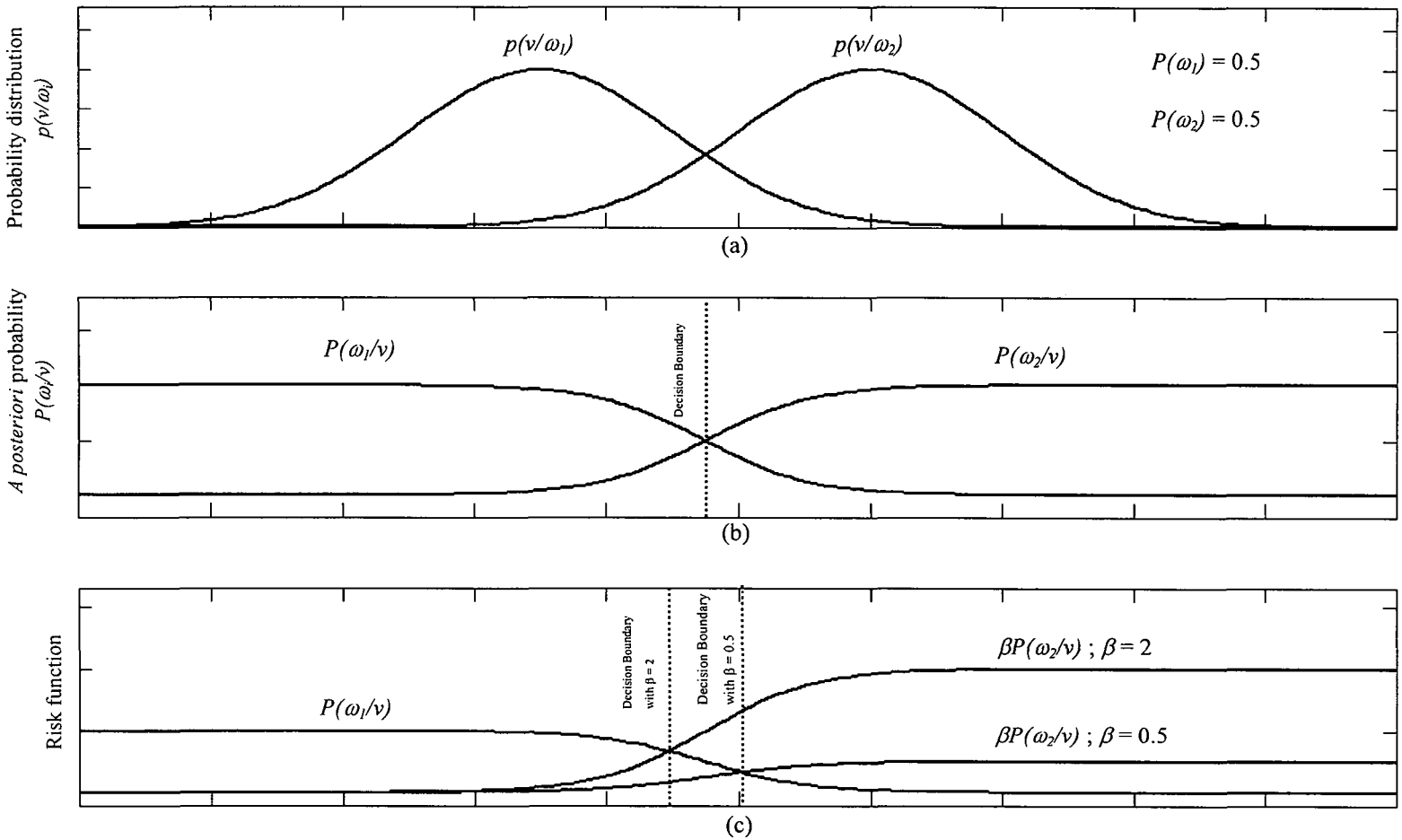

Figure 3-18: Effect of the risk function on the decision region

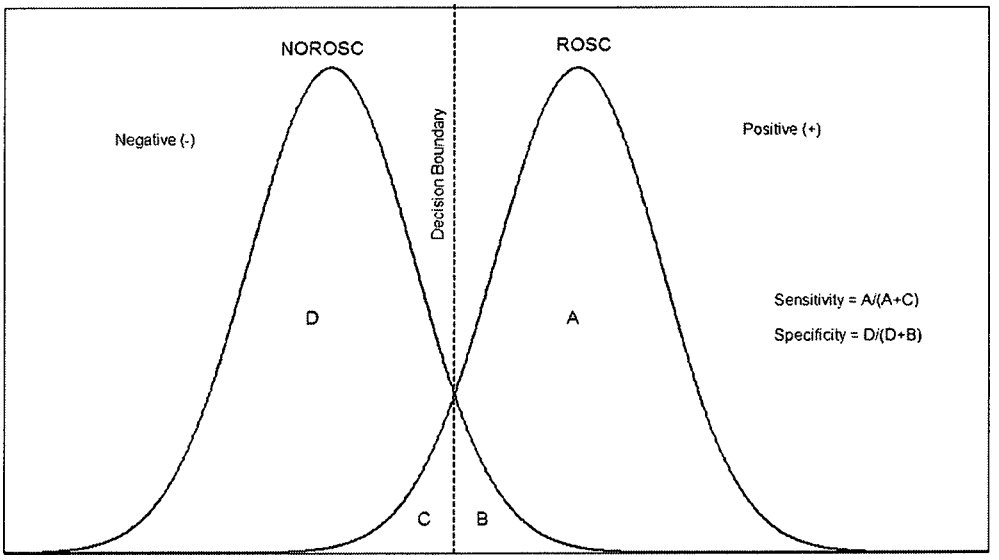

Figure 3-19: An illustration of sensitivity and specificity derived from two PDF's

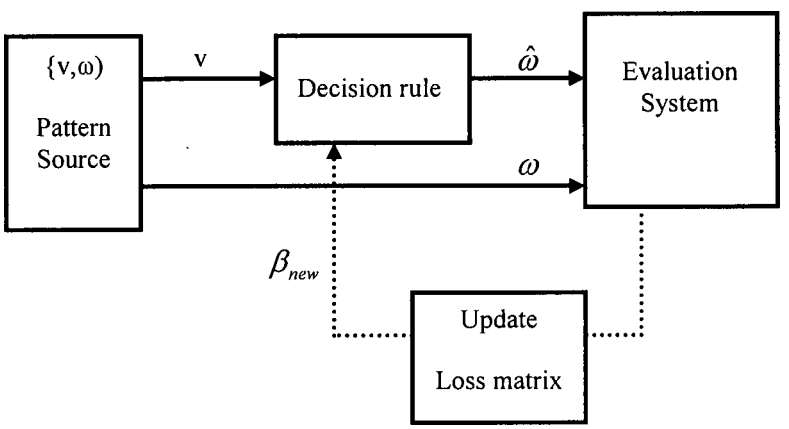

Figure 3-20: The decision rule optimisation loop

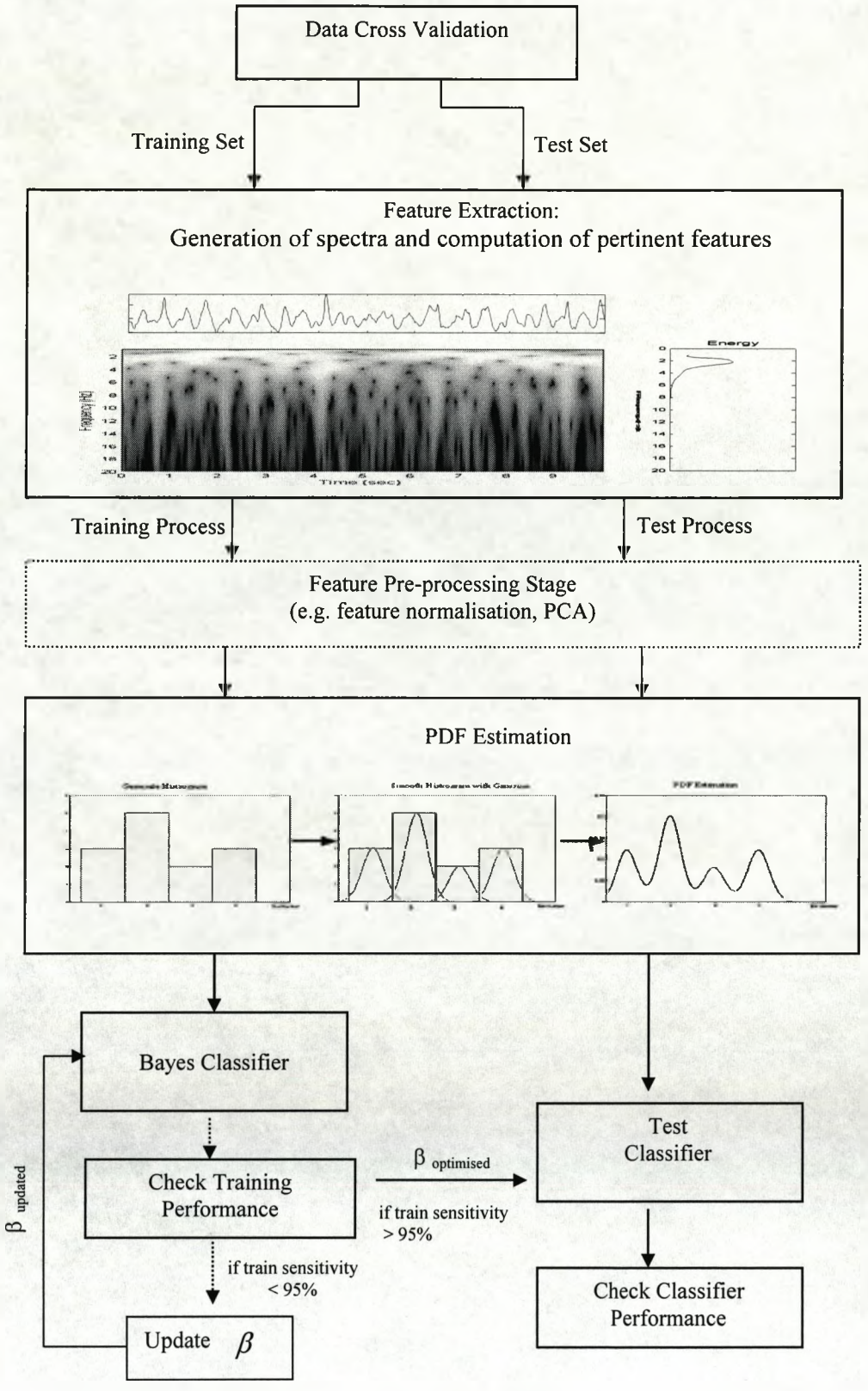

Figure 3-21: Schematic diagram of the research methodology

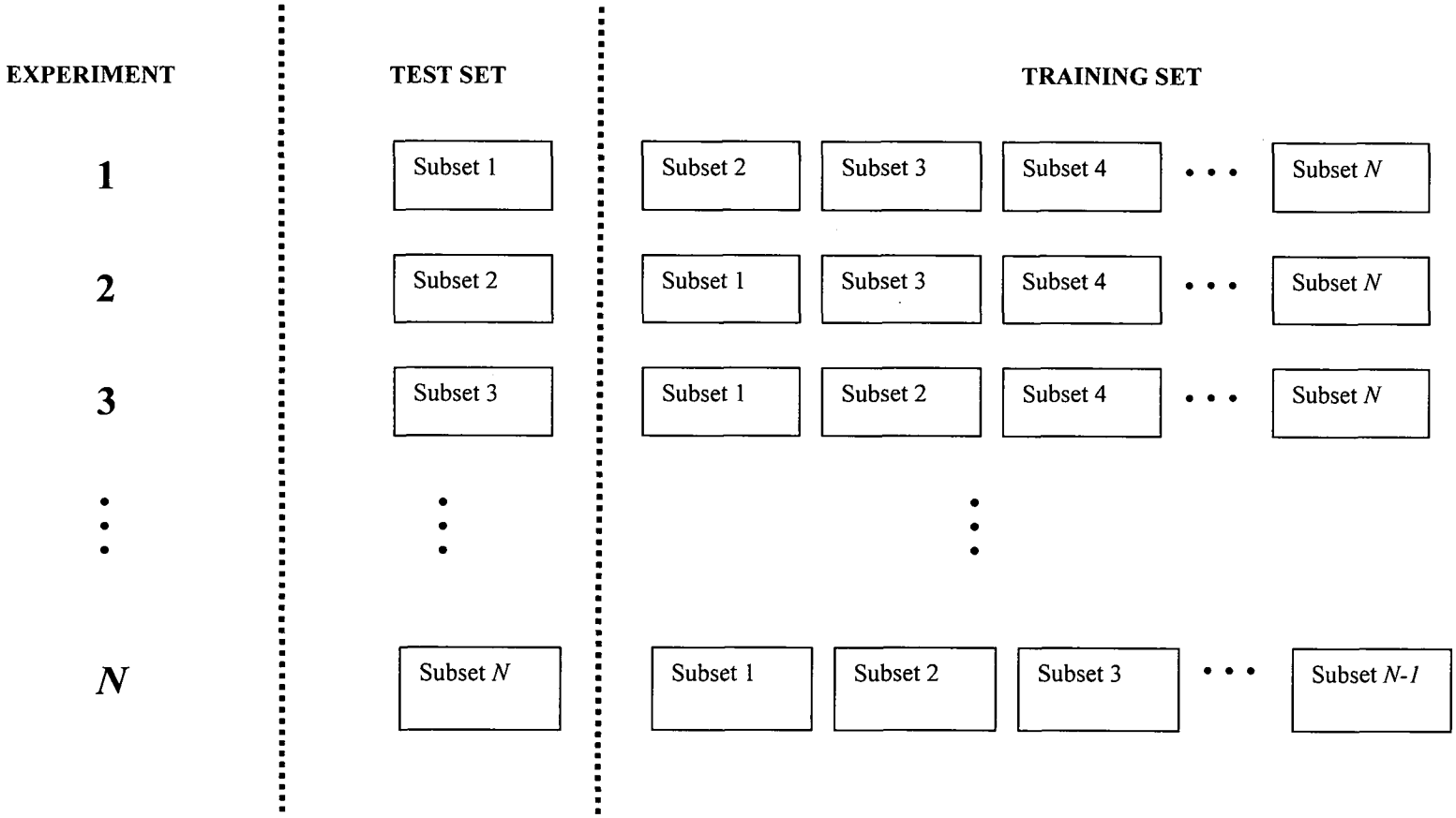

Figure 3-22 The cross validation technique

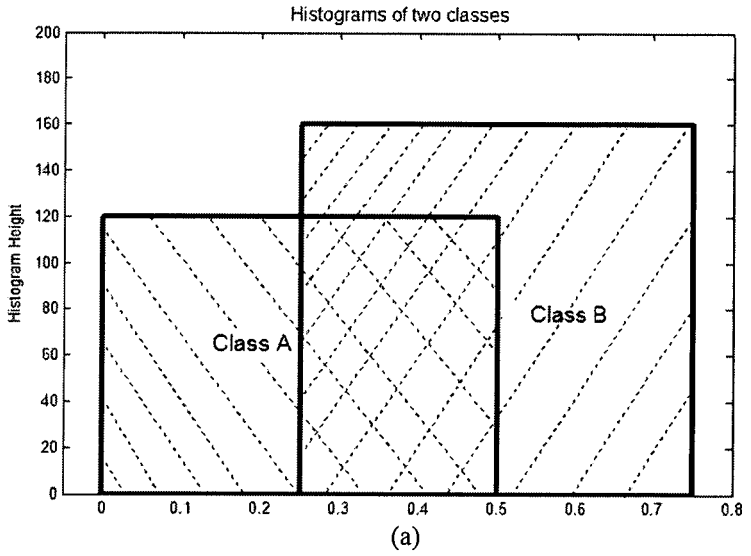

(a)

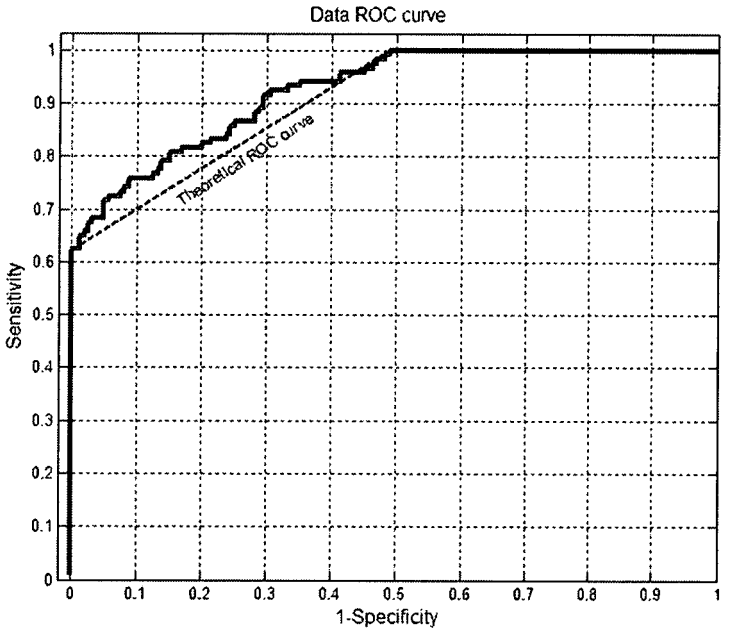

(b)

Figure 3-23: 1D Classification test data

(a) Histograms, (b) Data ROC curve

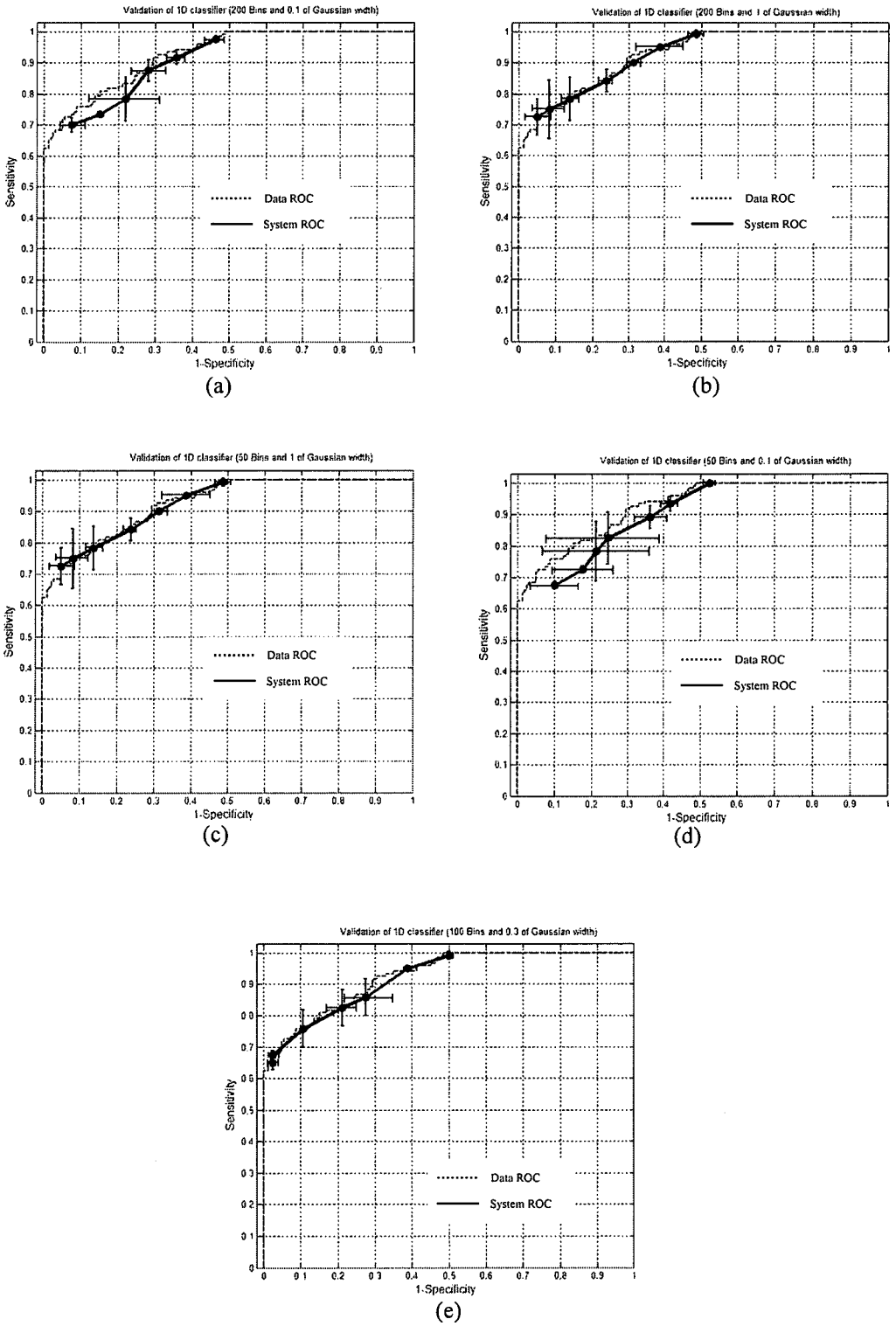

Figure 3-24: Classification performances of the use of various bin numbers and Gaussian widths: (a) 200 bins and a Gaussian width of 0.1, (b) 200 bins and a Gaussian width of 1, (c) 50 bins and a Gaussian width of 1, (d) 50 bins and a Gaussian width of 0.1, and (e) 100 bins and a Gaussian width of 0.3

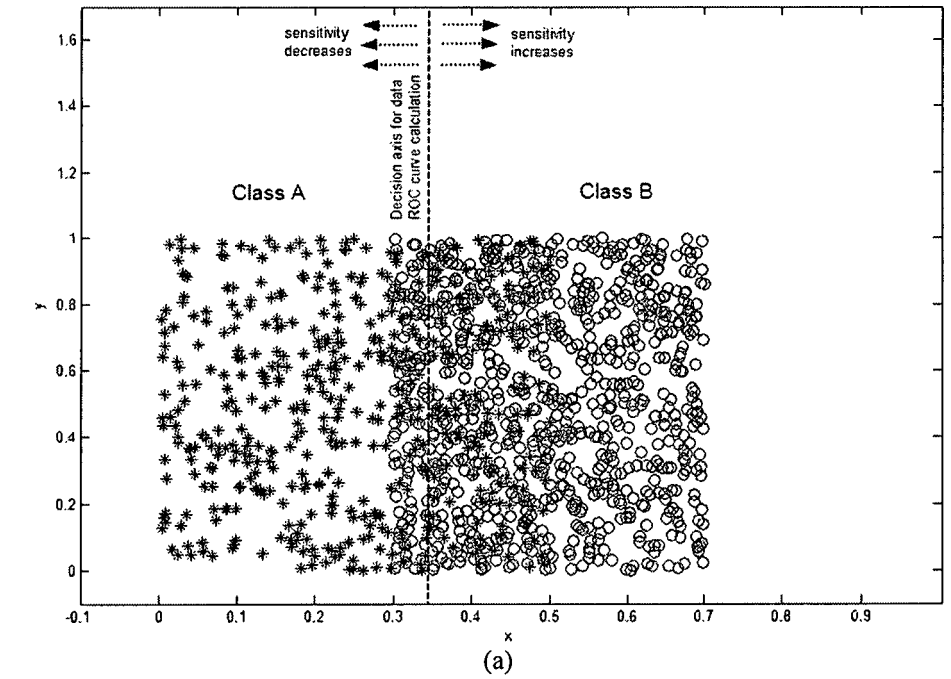

(a)

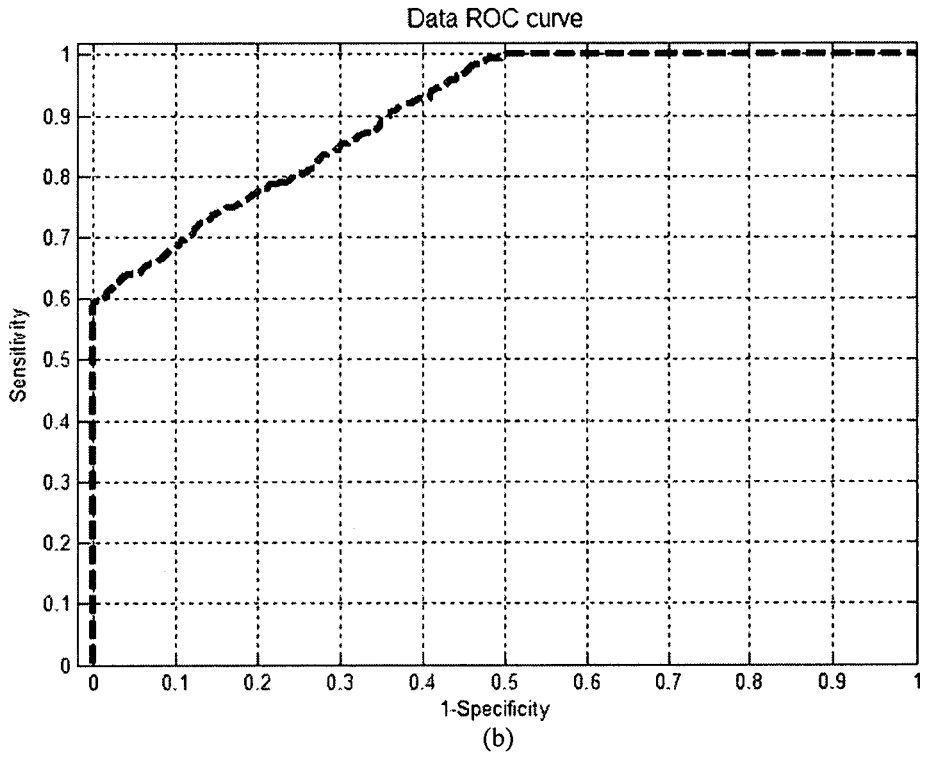

(b)

Figure 3-25: 2D Classification test data

(a) Scatter plots, (b) Data ROC curve

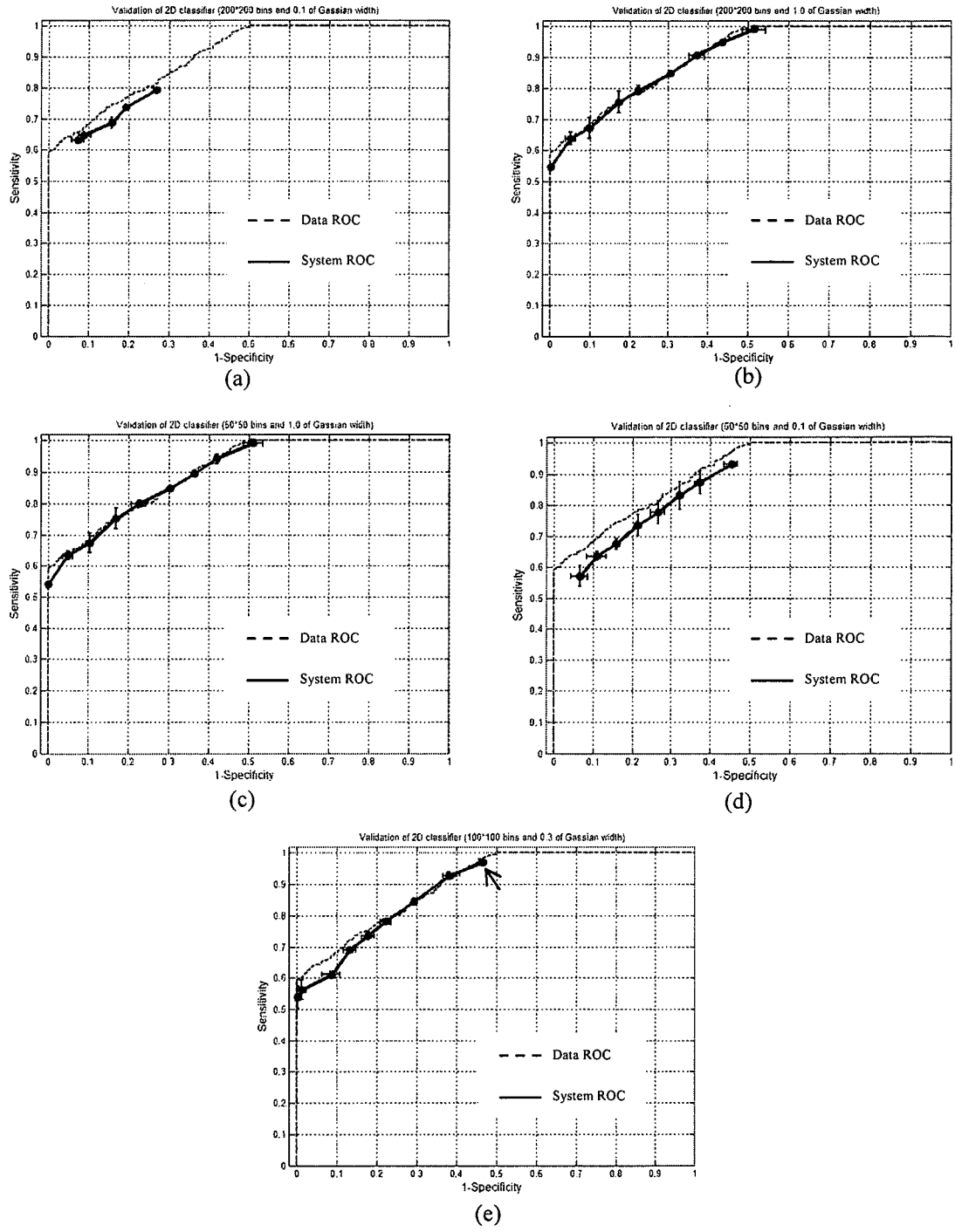

Figure 3-26: Classification performances of the use of various bin numbers and Gaussian widths

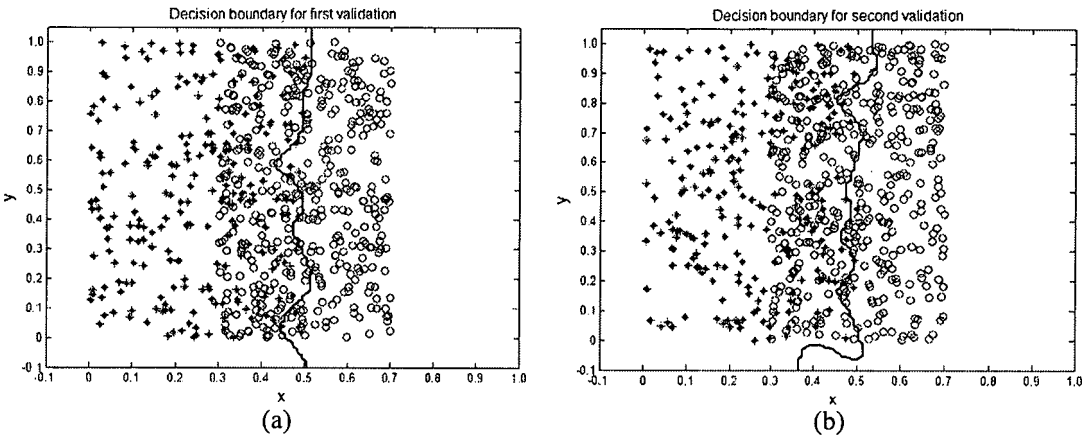

Figure 3-27: The decision boundary for the example in figure 3-26(e)

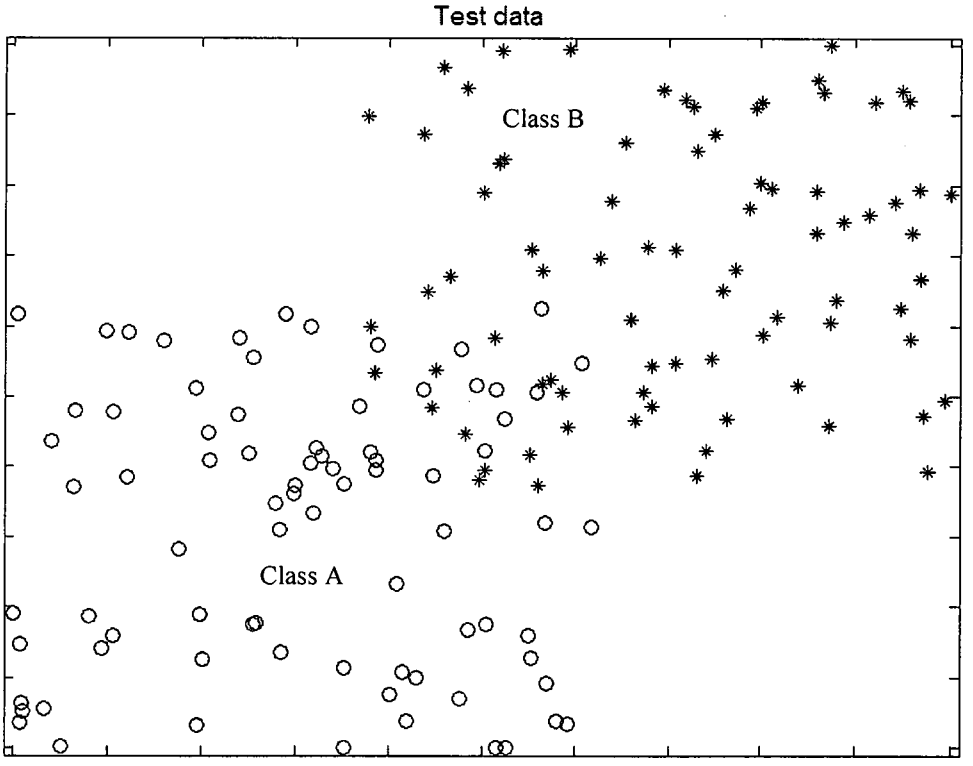

Figure 3-28: The data used in the example of classification

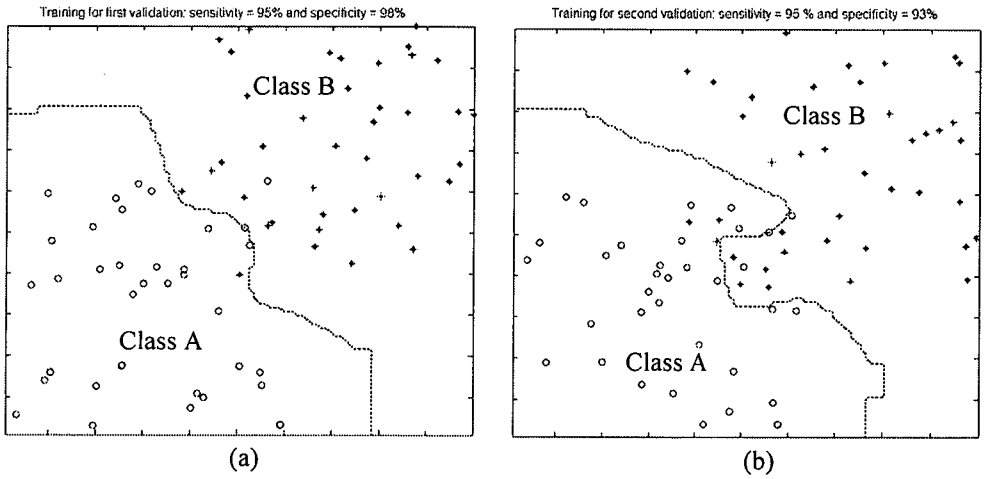

Figure 3-29: The boundary decision on the training sets with 150×150 bins and Gaussian width equal to 0.5; (a) the first validation, (b) the second validation

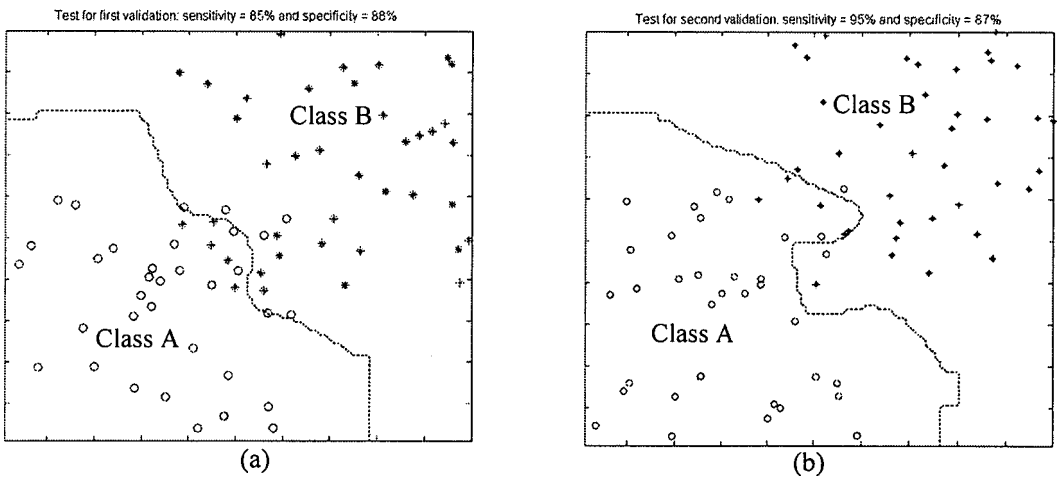

Figure 3-30: The boundary decision on the test sets with 150×150 bins and Gaussian width equal to 0.5; (a) the first validation, (b) the second validation

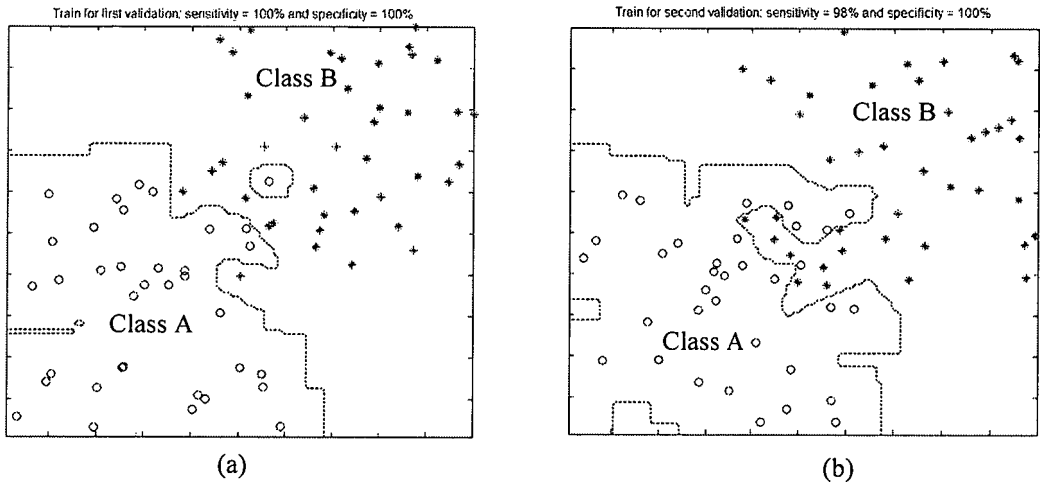

Figure 3-31: The boundary decision on the training sets with 200×200 bins and Gaussian width equal to 0.2; (a) the first validation, (b) the second validation

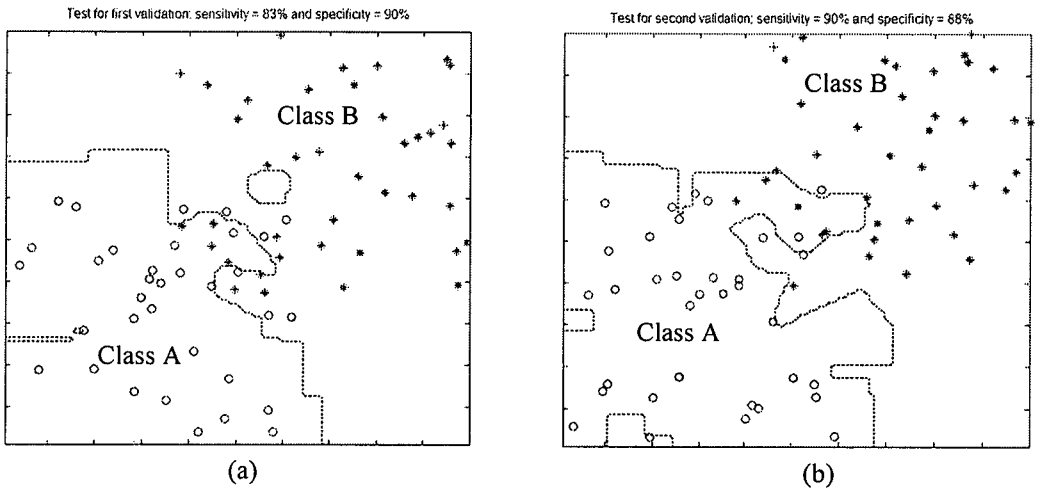

Figure 3-32: The boundary decision on the test sets with 200×200 bins and Gaussian width equal to 0.2; (a) the first validation, (b) the second validation

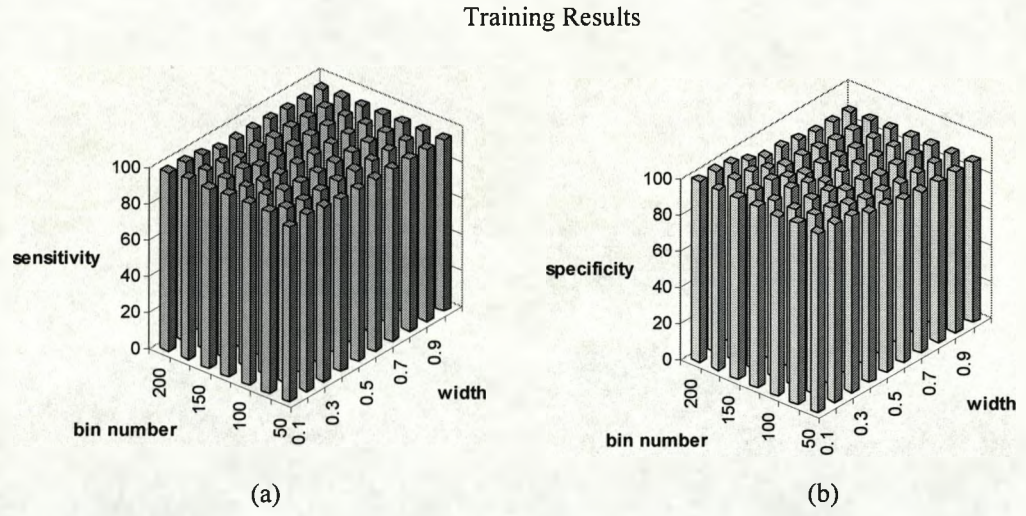

Figure 3-33: The training results obtained using various bin number and Gaussian width: (a) sensitivity, (b) specificity

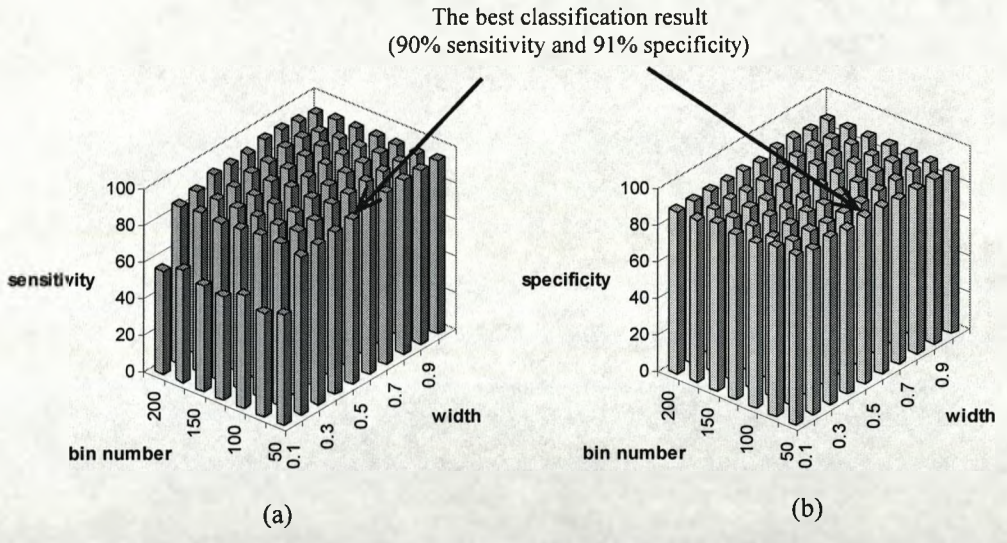

Figure 3-34: The test results obtained using various bin number and Gaussian width: (a) sensitivity, (b) specificity

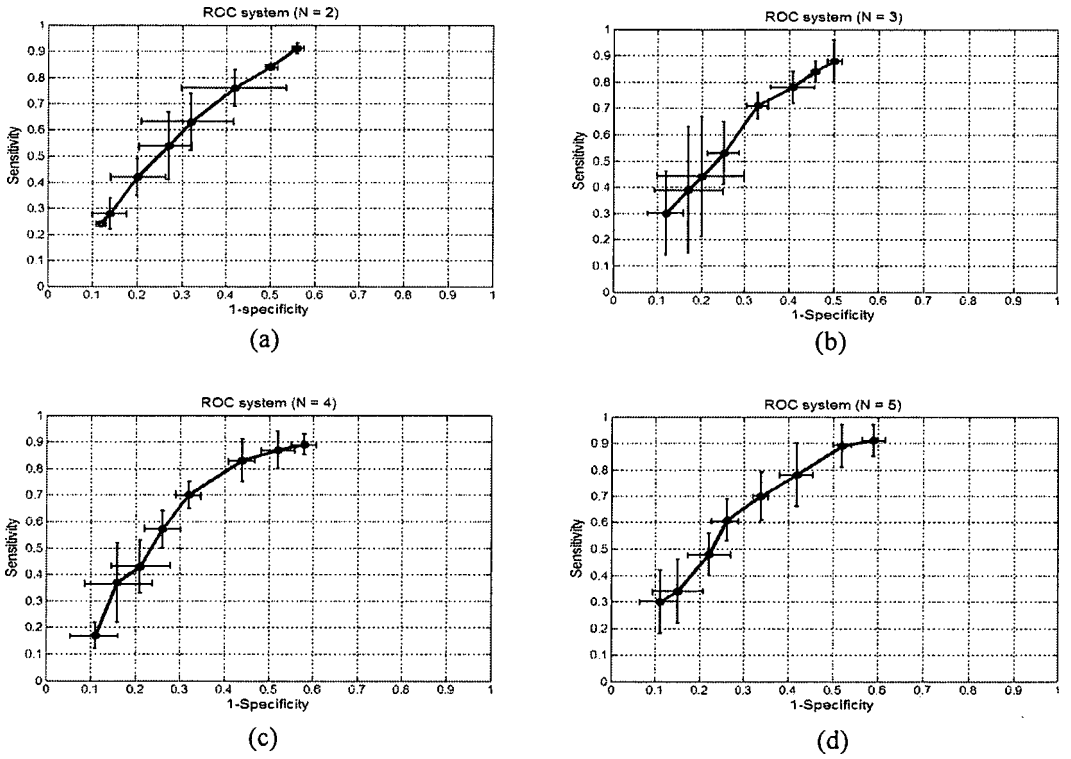

Figure 3-35: The ROC curves with error bars of classifier system using FT feature: (a) $N = 2$, (b) $N = 3$, (c) $N = 4$, and (d) $N = 5$

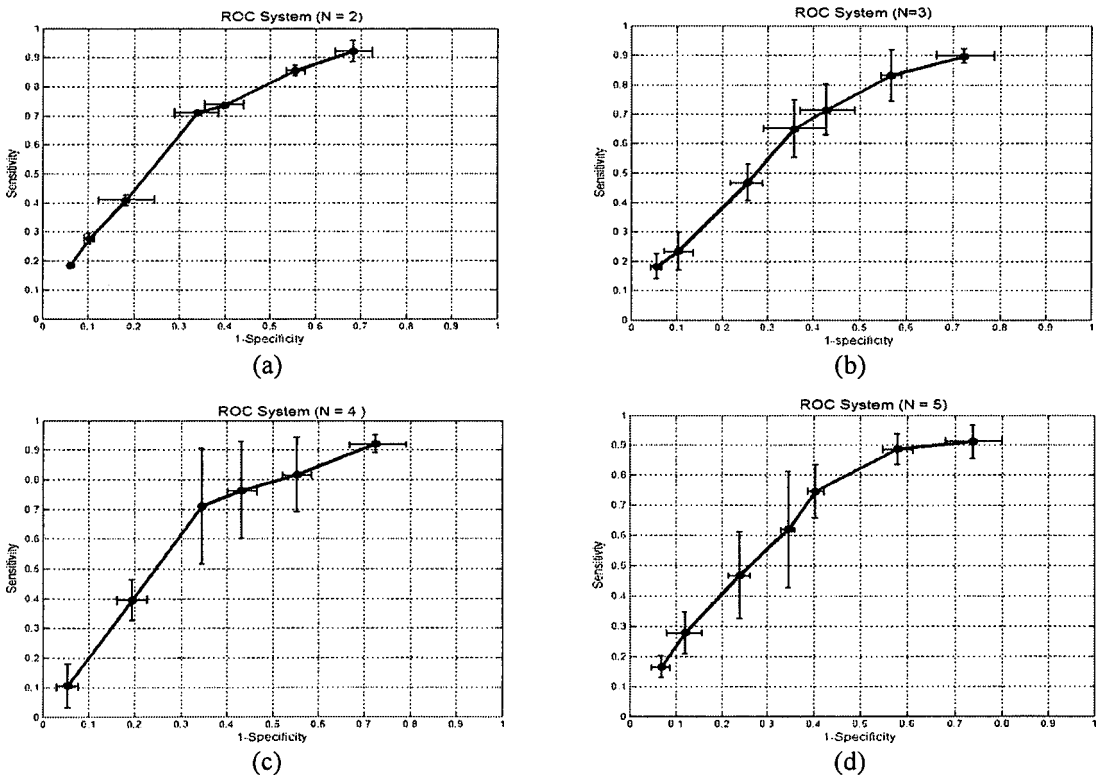

Figure 3-36: The ROC curves with error bars of classifier system using FP feature: $N = 2$, (b) $N = 3$, (c) $N = 4$, and (d) $N = 5$

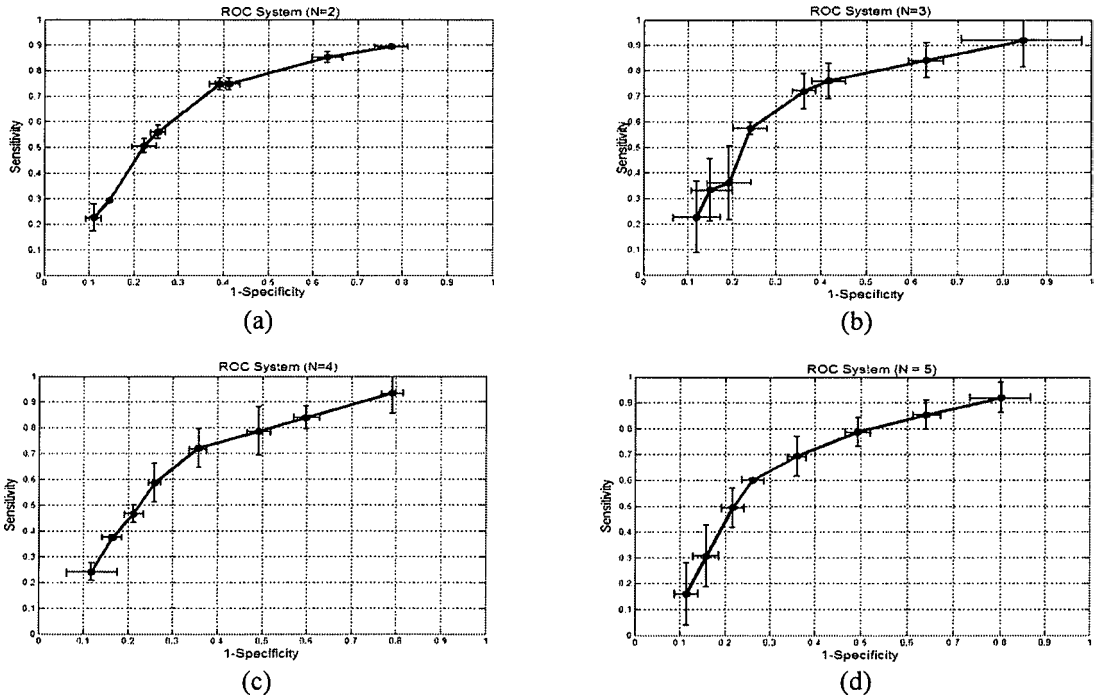

Figure 3-37: The ROC curves with error bars of classifier system using FM feature: (a) $N = 2$, (b) $N = 3$, (c) $N = 4$, and (d) $N = 5$

Class	Shock Outcome	Number of Traces
w_1	ROSC	76
w_2	EMD/PEA	323
w_3	Asystole	86
w_4	VF starting > 5 seconds after shock	35
w_5	Non-reset shock – i.e. no conversion	301
Total		821

Table 3-1: ECG data library

CHAPTER 4
SHOCK OUTCOME PREDICTION

CHAPTER 4
SHOCK OUTCOME PREDICTION

4.1 Introduction

This chapter presents the results of the main shock outcome prediction trials undertaken by the author. The chapter is composed of three main sections relating to each feature format used. Section 4.2 describes the results obtained using the original feature sets extracted directly from the time-frequency power spectra. The results obtained from features normalised within the unit interval are presented in section 4.3. Section 4.4 covers the use of PCA analysis which was employed to generate new feature sets for use in the classification of shock outcome. The analyses undertaken involved an investigation of the optimal length of pre-shock for shock outcome prediction and the optimal temporal location for the pre-shock analysis. A summary of the main results from these analyses is provided in section 4.5.

4.2 Results from the original feature sets

This section contains the results of the classifier using the original feature sets (i.e. non-normalised). The probability density functions of the feature vectors with respect to class ω_j, $p(\mathrm{v}/\omega_j)$ were estimated for the training group data. The sensitivity of ROSC outcome was set, as the criterion for the training classifier, to $P_{sens}(\omega_1) = 95\%$. The cost functions found for each case was then used to test the remaining data. This was carried out for the various bin sizes and Gaussian kernel widths used to generate

the PDF estimate. The bin sizes were adjusted according to the number of bins used (i.e. 50, 75, 100, 125, 150, 175, and 200 bins) to cover the range of the feature data sets (which was set between zero and twenty). This range was used as it encompassed the spectral region of interest, i.e. 1 Hz to 20 Hz. The Gaussian kernel smoothing histograms used to generate the PDFs' were set to 1, 2, 3, 4, 5, 6, 7, 8, and 9 units in width

4.2.1 Determination of an optimal length of pre-shock ECG for use in shock outcome prediction analysis

This section describes the results of the investigation of the performances of shock outcome prediction associated with varying lengths of pre-shock signal. Four pre-shock signal lengths were used in the study. There were 5, 10, 15, and 20 seconds immediately prior to countershock. The analysis employed both 1D and 2D feature sets. The 1D feature sets were: median frequency (FM), peak frequency (FP), standard deviation (STD), skewness (SK), kurtosis (KT), and flatness (FT) of the wavelet and STFT power spectra. The first three features giving the best performances for the 1D analysis were selected for use in combination for the 2D analysis.

4.2.1.1 The 5 second length of pre-shock ECG

This section contains the results from the analysis of 5 second segments of VF signals immediately prior to countershock. The characteristic features in this experiment were computed from the power spectra generated from the summation of the time-frequency scalogram components across the time domain as described in chapter 3, section 3.3. Both the CWT and STFT time-frequency methods were used in the experiments. Three different window lengths were employed for the STFT method. These were 1, 2, and 3 seconds in length.

Figure 4-1 displays the boxplots of each feature set distribution allowing visual comparison between the ROSC and NOROSC groups where each feature was obtained from the WT spectrum of the corresponding signal. The separation of each corresponding ROSC/NOROSC feature set can be quantified using the Wilcoxon

rank sum test (WRST). The WRST values for the feature sets derived from the WT are tabulated in the second column of table 4-1. Figure 4-2 shows the performances of the classifier using 1D and 2D feature sets. The FT feature gave the highest performance for the 1D analysis with 40±9% specificity obtained at 90±11% sensitivity. The combination of the FP and FT features gave the highest performance for the 2D analysis with 47±11% specificity obtained at 90±4% sensitivity.

The WRST values for the feature sets derived from the STFT employing a 1 second window are listed in the third column of table 4-1. The boxplots of these feature distributions are provided in Appendix B, figure B-1. All feature distributions used in the rest of the chapter can be found in Appendix B. Figure 4-3 shows the performances of the classifier using 1D and 2D feature sets. The FP feature gave the highest performance for the 1D analysis with 35±2% specificity obtained at 92±2% sensitivity. The combination of the FM and FT features gave the highest performance for the 2D analysis with 46±3% specificity obtained at 90±4% sensitivity.

The WRST values for the feature sets derived from the STFT employing a 2 second window are listed in the fourth column of table 4-1. Figure 4-4 shows the performances of the classifier using 1D and 2D feature sets. The FT feature gave the highest performance for the 1D analysis with 32±11% specificity obtained at 90±7% sensitivity. The combination of the FM and FT features gave the highest performance for the 2D analysis with 45±4 % specificity obtained at 90±4% sensitivity.

The WRST values for the feature sets derived from the STFT employing a 3 second window are given in the last column of table 4-1. Figure 4-5 shows the performances of the classifier using 1D and 2D feature sets. The FP feature gave the highest performance for the 1D analysis with 30±14% specificity obtained at 90±0% sensitivity. The combination of the FM and FT features gave the highest performance for the 2D analysis with 37±4% specificity obtained at 90±4 % sensitivity.

From the above results, based on a 5 second pre-shock window length, it can be seen that the highest performance of shock outcome prediction for the 1D analysis was obtained from the WT-based FT feature sets. The combination of the FP and FT

features gave the highest performance for the 2D analysis, again using the WT-based feature sets.

4.2.1.2 The 10 second length of pre-shock ECG

This section contains the results from the analysis of 10 second segments of VF signals immediately prior to countershock. The WRST values for the feature sets derived from the WT are listed in the second column of table 4-2. Figure 4-6 shows the performances of the classifier using 1D and 2D feature sets. The FT feature gave the highest performance for the 1D analysis with 43±0% specificity obtained at 91±1.86% sensitivity. The combination of the FM and FT features gave the highest performance for the 2D analysis with 58±2% specificity obtained at 90±4% sensitivity.

The WRST values for the feature sets derived from the STFT employing a 1 second window are listed in the third column of table 4-2. Figure 4-7 shows the performances of the classifier using 1D and 2D feature sets. The FT feature gave the highest performance for the 1D analysis with 40±2% specificity obtained at 90±2% sensitivity. The combination of the FM and FT features gave the highest performance for the 2D analysis with 57±2% specificity obtained at 90±4% sensitivity.

The WRST values for the feature sets derived from the STFT employing a 2 second window are listed in the fourth column of table 4-2. Figure 4-8 shows the performances of the classifier using 1D and 2D feature sets. The FT feature gave the highest performance for the 1D analysis with 38±4% specificity obtained at 91±2% sensitivity. The combination of the FM and FT features gave the highest performance for the 2D analysis with 52±3% specificity obtained at 90±4% sensitivity.

The WRST values for the feature sets derived from the STFT employing a 3 second window are listed in the last column of table 4-2. Figure 4-9 shows the performances of the classifier using 1D and 2D feature sets. The FT feature gave the highest performance for the 1D analysis with 36±0% specificity obtained at 90±4% sensitivity. The combination of the FM and FT features gave the highest performance for the 2D analysis with 53±3% specificity obtained at 90±4% sensitivity.

From the above results, based on a 10 second pre-shock window length, it can be seen that the highest performance of shock outcome prediction for the 1D analysis was obtained from the WT-based FT feature sets. The combination of the FM and FT features gave the highest performance for the 2D analysis, again using the WT-based feature sets.

4.2.1.3 The 15 second length of pre-shock

This section contains the results from the analysis of 15 second segments of VF signals immediately prior to countershock. The WRST values for the feature sets derived from the WT are listed in the second column of table 4-3. Figure 4-10 shows the performances of the classifier using 1D features and 2D feature sets. The FT feature gave the highest performance for the 1D analysis with 39±6% specificity obtained at 91±2% sensitivity. The combination of the FM and FT features gave the highest performance for the 2D analysis with 48±0% specificity obtained at 90±0% sensitivity.

The WRST values for the feature sets derived from the STFT employing a 1 second window are listed in the third column of table 4-3. Figure 4-11 shows the performances of the classifier using 1D and 2D feature sets. The FT feature gave the highest performance for the 1D analysis with 36±10% specificity obtained at 91±2% sensitivity. The combination of the FP and FT features gave the highest performance for the 2D analysis with 38±7% specificity obtained at 91±6% sensitivity.

The WRST values for the feature sets derived from the STFT employing a 2 second window are listed in the fourth column of table 4-3. Figure 4-12 shows the performances of the classifier using 1D and 2D feature sets. The FT feature gave the highest performance for the 1D analysis with 38±6% specificity obtained at 91±2% sensitivity. The combination of the FM and FT features gave the highest performance for the 2D analysis with 42±3% specificity obtained at 90±4% sensitivity.

The WRST values for the feature sets derived from the STFT employing a 3 second window are listed in the last column of table 4-3. Figure 4-13 shows the performances

of the classifier using 1D and 2D feature sets. The FT feature gave the highest performance for the 1D analysis with 38±4% specificity obtained at 91±2% sensitivity. The combination of the FM and FT features gave the highest performance for the 2D analysis with 48±1% specificity obtained at 90±0% sensitivity.

From the above results, based on a 15 second pre-shock window length, it can be seen that the highest performance of shock outcome prediction for the 1D analysis was obtained from the WT-based FT feature sets. The combination of the FM and FT features gave the highest performance for the 2D analysis using the WT and STFT3-based feature sets.

4.2.1.4 The 20 second length of pre-shock

This section contains the results from the analysis of 20 second segments of VF signals immediately prior to countershock. The WRST values for the feature sets derived from the WT are listed in the second column of table 4-4. Figure 4-14 shows the performances of the classifier using 1D features and 2D feature sets. The FM feature gave the highest performance for the 1D analysis with 31±1% specificity obtained at 92±4% sensitivity. The combination of the FM and FT features gave the highest performance for the 2D analysis with 42±9% specificity obtained at 90±2% sensitivity.

The WRST values for the feature sets derived from the STFT employing a 1 second window are listed in the third column of table 4-4. Figure 4-15 shows the performances of the classifier using 1D and 2D feature sets. The FM feature gave the highest performance for the 1D analysis with 37±6% specificity obtained at 90±2% sensitivity. The combination of the FM and FT features gave the highest performance for the 2D analysis with 40±9% specificity obtained at 90±2% sensitivity.

The WRST values for the feature sets derived from the STFT employing a 2 second window are listed in the fourth column of table 4-4. Figure 4-16 shows the performances of the classifier using 1D and 2D feature sets. The FM feature gave the highest performance for the 1D analysis with 35±14% specificity obtained at 90±6%

sensitivity. The combination of the FM and FT features gave the highest performance for the 2D analysis with 38±15% specificity obtained at 90±8% sensitivity.

The WRST values for the feature sets derived from the STFT employing a 3 second window are listed in the last column of table 4-4. Figure 4-17 shows the performances of the classifier using 1D and 2D feature sets. The FM feature gave the highest performance for the 1D analysis with 36±14% specificity obtained at 90±6% sensitivity. The combination of the FM and FT features gave the highest performance for the 2D analysis with 46±9% specificity obtained at 90±6% sensitivity.

From the above results, based on a 20 second pre-shock window length, it can be seen that the highest performance of shock outcome prediction for the 1D analysis was obtained from the STFT1-based FM feature sets. The combination of the FM and FT features gave the highest performance for the 2D analysis, again using the STFT3-based feature sets.

4.2.1.5 Summary of optimal length analysis

This section considers the prediction performances achieved for the various lengths of pre-shock signal used in the analysis. These were 5, 10, 15, and 20 seconds immediately prior to shock. The results reported in section 4.2.1.1- 4.2.1.4 were inspected to determine the optimal length of pre-shock signal required in order to best predict the defibrillation outcome of the VF patient.

Figure 4-18 shows the specificities of all experiments based on the WT power spectra analysis. The test sensitivity was within the generality criterion set. The highest performance achieved was a 58±2% test specificity obtained at 90±4% test sensitivity. This was obtained for the combined feature FM-FT and a 10 second pre-shock signal length. The analysis of 5 seconds of pre-shock signals gave the highest performance for the STD feature set. The analysis of the 10 second pre-shock signal length gave the highest performance for the FP, KT, FT, FM-FP, and FM-FT feature sets. The FP-FT feature set gave the highest performance when using the 15 second pre-shock signal length. Finally, the analysis of the 20 second pre-shock signal length gave the highest performance for the FM and SK feature sets.

Figure 4-19 shows the specificities of all experiments based on the STFT power spectra analysis employing a 1 second window width. The test sensitivity was within the generality criterion set. The highest performance achieved was a 57±2% test specificity obtained at 90±4% test sensitivity. This was obtained for the combined feature FM-FT and a 10 second pre-shock signal length. The analysis of a 5 second pre-shock signal length gave the highest performance for the FP feature set. The analysis of the 10 second pre-shock signal length gave the highest performance for the STD, FT, FM-FT, and FP-FT feature sets. The FM-FP feature set gave the highest performance when using the 15 seconds pre-shock signal length. Finally, the analysis of the 20 second pre-shock signal length gave the highest performance for the FM, SK, and KT feature sets.

Figure 4-20 shows the specificities of all experiments based on the STFT power spectra analysis employing a 2 second window width. The test sensitivity was within the generality criterion set. The highest performance achieved was a 52±3% test specificity obtained at 90±4% test sensitivity. This was obtained for the combined feature FM-FT and a 10 second pre-shock signal length. The analysis of the 10 second pre-shock signal length gave the highest performance for the FP, FT, and FM-FT feature sets. The FM-FP and FP-FT feature sets gave the highest performance when using the 15 second pre-shock signal length. Finally, the analysis of the 20 second pre-shock signal length gave the highest performance for the FM, STD, SK, and KT feature sets.

Figure 4-21 shows the specificities of all experiments based on the STFT power spectra analysis employing a 3 second window width. The test sensitivity was within the generality criterion. The highest performance achieved was a 53±3% test specificity obtained at 90±4% test sensitivity. This was obtained for the combined feature FM-FT and a 10 second pre-shock signal length. The analysis of 5 seconds of pre-shock gave the highest performance for the STD feature set. The analysis of the 10 second pre-shock signal length gave the highest performance for the FP, FM-FP, and FM-FT feature sets. The KT, FT and FP-FT feature sets gave the highest performance when using the 15 second pre-shock signal length. Finally, the analysis

of the 20 second pre-shock signal length gave the highest performance for the FM and SK feature sets.

Considering figures 4-18 to 4-21, it can be seen that there is a general trend in the classification. The 1D classification employing FM, FP, and FT in general gave better results than the classification employing STD, SK and KT. In addition, there was a tendency for the 2D classifier is to improve the performance of prediction. Overall for the analysis of shock outcome prediction employing the original power spectral features, the WT power spectra of 10 second-length of pre-shock ECG achieved the best performance of 58±2% test specificity obtained at 90±4% test sensitivity. This was obtained for the combined feature FM-FT. However, it should be noted that, within error, the 10 second segment FM-FT combined feature for the STFT employing a 1 second window produced a very similar result of 57±2% specificity at 90±4% sensitivity.

4.2.2 Positional dependence of the time-frequency analysis

This section considers the relationship between the predictive value of the pre-shock ECG signal selected for analysis and its temporal distance from the shock event. Selected segments of the ECG trace were examined using two time-frequency decompositions: the WT and the STFT employing a 1-second (Gaussian) window width. The STFT using the 1 second window was chosen as it performed better than the 2 second and 3 second window in the analysis reported in section 4.2.1. Further, it was found from the optimal length analysis that the 10 second pre-shock signal length gave the best performance for the shock outcome prediction, hence this length is used in the analysis of positional dependence of time-frequency information analysis. Three segments of each ECG were considered in the analysis: 0-10 seconds, 5-15 seconds, and 10-20 seconds prior to countershock. Figure 4-22 shows a schematic diagram of the position of pre-shock segments used in this analysis marked A, B, and C respectively. The analysis employed both 1D and 2D feature sets. Similar to the optimal length analysis, the 1D feature sets were FM, FP, STD, SK, KT, and FT. The first three features giving the best performances for 1D analysis were selected for use in combination for the 2D analysis.

4.2.2.1 The 10 seconds length of pre-shock at 0-10 seconds (location A)

This section contains the results from the analysis of 10-second segments of VF immediately prior to countershock. This is shown as section A in figure 4-22. The characteristic features in this experiment were computed from power spectra which were generated from the summation of the time-frequency scalogram components across the time domain. Both the WT and STFT1 time-frequency methods were used in the experiments.

The WRST values for the feature sets derived from the WT are tabulated in the second column of table 4-5. Figure 4-23 shows the performances of the classifier using 1D and 2D feature sets. The FT feature gave the highest performance for the 1D analysis with 43±0% specificity obtained at 91±2% sensitivity. The combination of the FM and FT features gave the highest performance for the 2D analysis with 58±2% specificity obtained at 90±4% sensitivity. (This result has been presented previously in section 4.2.1.2)

The WRST values for the feature sets derived from the STFT employing a 1 second window are listed in the third column of table 4-5. Figure 4-24 shows the performances of the classifier using 1D and 2D feature sets. The FT feature gave the highest performance for the 1D analysis with 40±2% specificity obtained at 91±2% sensitivity. The combination of the FM and FT features gave the highest performance for the 2D analysis with 57±2% specificity obtained at 90±4% sensitivity. (Again, this result has been presented previously in section 4.2.1.2)

4.2.2.2 The 10 seconds length of pre-shock at 5-15 seconds (location B)

This section contains the results from the analysis of 10-second segments of VF at 5 seconds before countershock. This is shown as section B in figure 4-22. The characteristic features in this experiment were computed from power spectra which were generated from the summation of the time-frequency scalogram components across the time domain. Again, both the WT and STFT1 time-frequency methods were used in the experiments.

The WRST values for the feature sets derived from the WT are given in the second column of table 4-6. Figure 4-25 shows the performances of the classifier using 1D and 2D feature sets. The feature FT gave the highest performance for the 1D analysis with 36±1% specificity achieved at 92±0% sensitivity. The combination of the FP and FT features gave the highest performance for the 2D analysis with 54±3% specificity achieved at 90±4% sensitivity.

The WRST values for the feature sets derived from the STFT employing a 1 second window are given in the third column of table 4-6. Figure 4-26 shows the performance results of the classifier using 1D and 2D feature sets. The feature FT gave the highest performance for the 1D analysis with 39±2% specificity achieved at 91±2% sensitivity. The combination of the FM and FT features gave the highest performance for the 2D analysis with 51±0% specificity achieved at 90±0% sensitivity.

4.2.2.3 The 10 second length of pre-shock at 10-20 seconds (location C)

This section contains the results from the analysis of 10-second segments of VF at 10 seconds before countershock. This is shown as section C in figure 4-22. The characteristic features in this experiment were computed from power spectra which were generated from the summation of the time-frequency scalogram components across the time domain. Again, both the WT and STFT1 time-frequency methods were used in the experiments.

The WRST values for the feature sets derived from the WT are given in the second column of table 4-7. Figure 4-27 shows the performances of the classifier using 1D and 2D feature sets. The feature FT gave the highest performance for the 1D analysis with 32±17% specificity achieved at 90±4% sensitivity. The combination of the FM and FT features gave the highest performance for the 2D analysis with 53±7% specificity achieved at 92±6% sensitivity.

The WRST values for the feature sets derived from the STFT employing a 1 second window are given in the third column of 4-7. Figure 4-28 shows the performance results of the classifier using 1D and 2D feature sets. The feature FM gave the highest

performance for the 1D feature analysis with 34±14% specificity achieved at 90±2% sensitivity. The combination of the FP and FT feature gave the highest performance for the 2D analysis with 46±4% specificity achieved at 90±2% sensitivity.

4.2.2.4 Summary of positional dependence of time-frequency analysis

Figure 4-29 shows the results of positional dependence of the WT power spectra analysis using 1D and 2D feature sets. The results show the specificities of all experiments. The test sensitivity was within the generality criterion. The results for the FP, FT, and FM-FT features at position A gave the highest performances. At period B, the performances of classifier with FM-FP and FP-FT were maximised. The classifier gave the highest performance for features FM, STD, SK, and KT over period C.

Figure 4-30 shows the results of positional dependence of the STFT1 power spectra analysis using 1D and 2D feature sets. The results show the specificities of all experiments. The test sensitivity was within the generality criterion. The results for the FP, STD, KT, FT, FM-FP, and FM-FT features at position A gave the highest performances. At period B, the performances of the classifier was maximised for FP-FT. The classifier gave the highest performance for features FM and SK over period C.

Considering figures 4-29 to 4-30, a clear tendency for the 2D classifier to improve the performance of prediction can be observed. It can be seen that the FM-FT 2D feature provides the best result for the 10 second period immediately prior to shock for both the WT and STFT1 methods. Of these, the WT-based method achieved the best performance with 58±2% specificity achieved at 90±4% sensitivity. However, the analysis shows that there is no obvious trend correlating prediction with temporal distance to the shock event.

4.2.3 Summary of the use of original feature sets in shock outcome prediction

The best result of the shock outcome prediction using the original sets of the WT and STFT power spectral features was 58±2% specificity achieved at 90±4% sensitivity.

This performance was achieved from the use of FM-FT features based on WT power spectral analysis for the 10 second pre-shock ECG. Figure 4-31 shows the receiving operator characteristics (ROC) curve of the best classifier associated to 175×175 bins and Gaussian width equal to 3 in 2D-PDF estimation. From the system ROC curve it can be seen that as the test sensitivity increases slightly from 90±4 to 91±2% (indicted by arrows in the plot), the test specificity decreases markedly from 58±2% to 29±8%. Figure 4-32 and 4-33 show the data scatter plots of each validation at 90±4 and 91±2% sensitivity respectively. The decision boundaries of the two test validations achieving an average sensitivity of 90±4% are illustrated in figure 4-32(a) and 4-32(b). The decision boundary associated with 91±2% sensitivity shown in figure 4-33(b) is essentially an expanded version of that in 4-32(b). Inspection of these boundaries show a ROSC data point (arrow in plot) now included within the decision boundary. However, to include this single extra ROSC, a large number of NOROSC's are now included. This causes the dramatic change in specificity associated with a slight change in sensitivity.

4.3 Results from the normalised feature sets

This section presents the results from the normalised feature sets. As described the chapter 3, the characteristic features (equation 3-2 to 3-7) were mapped into the unit range between zero and one. The maximum feature value of one is set to the upper whisker value and the minimum feature value of zero is set equal to the lower whisker value. The bin sizes were adjusted according to the number of bins used (50, 75, 100, 125, 150, 175, or 200) to cover the unit interval range. The Gaussian kernel smoothing histograms were set to 0.1, 0.2, 0.3, 0.4, 0.5, 0.6, 0.7, 0.8, and 0.9 units in width. The sensitivity of ROSC outcome was set to $P_{sens}(w_1)$ = 95% as the criterion for the training classifier. The cost functions found for each case were then used to test the remaining data. In case of the under achieving criterion (i.e. a test sensitivity under 90%), the experiment which gave the highest sensitivity was chosen as the highest performance of the classifier.

The normalised feature sets were subjected to the same analysis as the original sets as described in section 4.2, i.e. optimal length analysis and position analysis. In addition,

it was decided to add three new features to the analysis. These were: bisector frequency (BI), spectrum ratio (R), and spectrum Shannon entropy (SH). These are described below.

The bisector frequency (BI) is the frequency which divides the power spectrum into two parts of equal area. This is illustrated in figure 4-34. In the example shown, the bisector frequency is equal to 4.41 Hz. The ratio of the area A to area B is equal to unity. In addition, figure 4-35 illustrates the location of BI compared to FM and FP. For this case the BI is between the FM and FP.

The spectrum ratio (R) is the ratio of the energy in a selected low frequency band to that in a selected high frequency band. Figure 4-36 shows the average wavelet power spectra between the ROSC and NOROSC data used in the analysis. These plots were computed from the entire datasets of each class using 10 seconds of pre-shock ECG. In the experiment, the low frequency band is set within the range 3.0 to 4.5 Hz and the high frequency is set within the range 4.5-6.0 Hz. This is shown schematically in figure 4-36 the spectrum ratio is equal to the spectrum area A divided by area B. The spectrum ratio can be written as:

$$R = \frac{\sum_{f=3}^{4.5} p(f)}{\sum_{f=4.5}^{6} p(f)} \tag{4-1}$$

From the plots of the average power spectra shown in figure 4-36, it can be seen that the R value from NOROSC data is expected to be higher than the R value from the ROSC data.

Shannon entropy (SH) is a well known measure of uncertainty. Suppose X is a random variable which takes on a finite set of values according to a probability distribution $p(X)$, then Shannon's entropy can be expressed as:

$$SH = -k\sum_{i=1}^{n} p(x_i)\log p(x_i) \tag{4-2}$$

where X takes the values x_i , $1 \leq i \leq n$, n is the number of x's and k is constant value. In the following experiment, SH was used as a parameter presenting the uncertainty of WT and STFT spectra.

Table 4-8 to 4-11 shows the WRST of these three new feature sets for optimal length analysis. The R feature set tends to perform the best for classification. Hence, the R feature was selected for use in the 2D analysis giving three new combinations of features. These are FM-R, FP-R, and FT-R. The lengths of pre-shock signal in the experiments are set to 5, 10, 15, and 20 seconds as was used in the analysis of the original feature sets presented in section 4.2.1.

4.3.1 Determination of an optimal length of pre-shock ECG for use in shock outcome prediction analysis

This section reports on an investigation of the performances of shock outcome prediction associated with varying lengths of pre-shock signal for the normalised feature sets. Four pre-shock signal lengths were investigated in the study: these were 5, 10, 15, and 20 seconds immediately prior to countershock.

4.3.1.1 The 5 second length of pre-shock ECG

This section contains the results from the analysis of 5 second segments of VF signals immediately prior to countershock. The characteristic features in this experiment were computed from the power spectra generated from the summation of the time-frequency scalogram components across the time domain as described in chapter 3, section 3.3. Both the WT and STFT time-frequency methods were used in the experiments. Three different window lengths were employed for the STFT analysis: these were 1, 2, and 3 seconds in length.

Figure 4-37 displays the boxplots of each extra feature set (i.e. BI, R, and SH) distribution allowing visual comparison between the ROSC and NOROSC groups where each feature was obtained from the WT spectrum of the corresponding signal. All other feature distributions used in the rest of the chapter can be found in Appendix B. The WRST values for the feature sets derived from the WT are given in

the second column of table 4-8. Figure 4-38 shows the performances of the classifier using 1D and 2D feature sets. The FP feature gave the highest performance for the 1D analysis with 36±1% specificity obtained at 90±0% sensitivity. The combination of the FP and FT features gave the highest performance for the 2D analysis with 41±2% specificity obtained at 90±4% sensitivity. Higher specificities are observable in figure 4-38 however these are at less than 90% sensitivity.

The WRST values for the feature sets derived from the STFT employing a 1 second window are listed in the third column of table 4-8. Figure 4-39 shows the performances of the classifier using 1D and 2D feature sets. The FT feature gave the highest performance for the 1D analysis with 29±5% specificity obtained at 90±0% sensitivity. The combination of the FM and FT features gave the highest performance for the 2D analysis with 43±2% specificity obtained at 90±4% sensitivity.

The WRST values for the feature sets derived from the STFT employing a 2 second window are listed in the fourth column of table 4-8. Figure 4-40 shows the performances of the classifier using 1D and 2D feature sets. The FT feature gave the highest performance for the 1D analysis with 34±5% specificity obtained at 90±4% sensitivity. The combination of the FM and FT features gave the highest performance for the 2D analysis with 49±4% specificity obtained at 90±4% sensitivity.

The WRST values for the feature sets derived from the STFT employing a 3 second window are listed in the last column of table 4-8. Figure 4-41 shows the performances of the classifier using 1D and 2D feature sets. The FM feature gave the highest performance for the 1D analysis with 34±7% specificity obtained at 90±0% sensitivity. The combination of the FM and FT features gave the highest performance for the 2D analysis with 49±3% specificity obtained at 90±4% sensitivity.

From the above results, based on a 5 second pre-shock window length, it can be seen that the highest performance of shock outcome prediction for the 1D analysis was obtained from the WT-based FP feature sets. The combination of the FM and FT features gave the highest performance for the 2D analysis using the STFT2 and STFT3-based feature sets.

4.3.1.2 The 10 second length of pre-shock ECG

This section contains the results from the analysis of 10 second segments of VF signals immediately prior to countershock. The WRST values for the feature sets derived from the WT are listed in the second column of table 4-9. Figure 4-42 shows the performances of the classifier using 1D and 2D feature sets. The FT feature gave the highest performance for the 1D analysis with 40±2% specificity obtained at 90±4% sensitivity. The combination of the FM and FT features gave the highest performance for the 2D analysis with 55±2% specificity obtained at 90±4% sensitivity.

The WRST values for the feature sets derived from the STFT employing a 1 second window are listed in the third column of table 4-9. Figure 4-43 shows the performances of the classifier using 1D and 2D feature sets. The FT feature gave the highest performance for the 1D analysis with 39±2% specificity obtained at 90±4% sensitivity. The combination of the FM and FT features gave the highest performance for the 2D analysis with 58±4% specificity obtained at 90±4% sensitivity.

The WRST values for the feature sets derived from the STFT employing a 2 second window are listed in the fourth column of table 4-9. Figure 4-44 shows the performances of the classifier using 1D and 2D feature sets. The FT feature gave the highest performance for the 1D analysis with 38±3% specificity obtained at 91±2% sensitivity. The combination of the FM and FT features gave the highest performance for the 2D analysis with 58±4% specificity obtained at 90±4% sensitivity.

The WRST values for the feature sets derived from the STFT employing a 3 second window are listed in the last column of table 4-9. Figure 4-45 shows the performances of the classifier using 1D and 2D feature sets. The FT feature gave the highest performance for the 1D analysis with 40±1% specificity obtained at 90±4% sensitivity. The combination of the FM and FT features gave the highest performance for the 2D analysis with 59±3% specificity obtained at 90±4% sensitivity.

From the above results, based on a 10 second pre-shock window length, it can be seen that the highest performance of shock outcome prediction for the 1D analysis was

obtained from the WT and STFT3-based FT feature sets. The combination of the FM and FT features gave the highest performance for the 2D analysis using the STFT3-based feature sets.

4.3.1.3 The 15 second length of pre-shock ECG

This section contains the results from the analysis of 15 second segments of VF signals immediately prior to countershock. The WRST values for the feature sets derived from the WT are listed in the second column of table 4-10. Figure 4-46 shows the performances of the classifier using 1D and 2D feature sets. The FT feature gave the highest performance for the 1D analysis with 38±4% specificity obtained at 91±2% sensitivity. The combination of the FT and R features gave the highest performance for the 2D analysis with 50±4% specificity obtained at 90±0% sensitivity.

The WRST values for the feature sets derived from the STFT employing a 1 second window are listed in the third column of table 4-10. Figure 4-47 shows the performances of the classifier using 1D and 2D feature sets. The FT feature gave the highest performance for the 1D analysis with 39±7% specificity obtained at 90±2% sensitivity. The combination of the FM and FT features gave the highest performance for the 2D analysis with 53±2% specificity obtained at 90±0% sensitivity.

The WRST values for the feature sets derived from the STFT employing a 2 second window are listed in the fourth column of table 4-10. Figure 4-48 shows the performances of the classifier using 1D and 2D feature sets. The FT feature gave the highest performance for the 1D analysis with 43±1% specificity obtained at 91±2% sensitivity. The combination of the FM and FT features gave the highest performance for the 2D analysis with 51±3% specificity obtained at 90±4% sensitivity.

The WRST values for the feature sets derived from the STFT employing a 3 second window are listed in the last column of table 4-10. Figure 4-49 shows the performances of the classifier using 1D and 2D feature sets. The FT feature gave the highest performance for the 1D analysis with 43±2% specificity obtained at 91±2%

sensitivity. The combination of the FM and FT features gave the highest performance for the 2D analysis with 51±3% specificity obtained at 91±2% sensitivity.

From the above results, based on a 15 second pre-shock window length, it can be seen that the highest performance of shock outcome prediction for the 1D analysis was obtained from the STFT2 and STFT3-based FT feature sets. The combination of the FM and FT features gave the highest performance for the 2D analysis using the STFT1-based feature sets.

4.3.1.4 The 20 second length of pre-shock ECG

This section contains the results from the analysis of 20 second segments of VF signals immediately prior to countershock. The WRST values for the feature sets derived from the WT are listed in the second column of table 4-11. Figure 4-50 shows the performances of the classifier using 1D and 2D feature sets. The R feature gave the highest performance for the 1D analysis with 30±7% specificity obtained at 90±6% sensitivity. The combination of the FT and R features gave the highest performance for the 2D analysis with 54±3% specificity obtained at 90±2% sensitivity.

The WRST values for the feature sets derived from the STFT employing a 1 second window are listed in the third column of table 4-11. Figure 4-51 shows the performances of the classifier using 1D and 2D feature sets. The R feature gave the highest performance for the 1D analysis with 40±2% specificity obtained at 90±2% sensitivity. The combination of the FT and R features gave the highest performance for the 2D analysis with 51±2% specificity obtained at 90±2% sensitivity.

The WRST values for the feature sets derived from the STFT employing a 2 second window are listed in the fourth column of table 4-11. Figure 4-52 shows the performances of the classifier using 1D and 2D feature sets. The FM feature gave the highest performance for the 1D analysis with 37±14% specificity obtained at 90±6% sensitivity. The combination of the FM and FT features gave the highest performance for the 2D analysis with 49±7% specificity obtained at 90±2% sensitivity.

The WRST values for the feature sets derived from the STFT employing a 3 second window are listed in the last column of table 4-11. Figure 4-53 shows the performances of the classifier using 1D and 2D feature sets. The FM feature gave the highest performance for the 1D analysis with 37±14% specificity obtained at 90±6% sensitivity. The combination of the FT and R features gave the highest performance for the 2D analysis with 47±0% specificity obtained at 90±2% sensitivity.

From the above results, based on a 20 second pre-shock window length, it can be seen that the highest performance of shock outcome prediction for the 1D analysis was obtained from the STFT1-based R feature sets. The combination of the FT and R features gave the highest performance for the 2D analysis using the WT-based feature sets.

4.3.1.5 Summary of optimal length analysis for the normalised feature sets

This section considers the prediction performances achieved for the various lengths of pre-shock signal used in the analysis. The normalised features were used in the classification. These were 5, 10, 15, and 20 seconds immediately prior to shock. The results reported in section 4.3.1.1 - 4.3.1.4 were inspected to determine the optimal length of pre-shock signal required in order to best predict the defibrillation outcome of the VF patient.

Figures 4-54(a) and 4-54(b) show the specificities of all experiments based on the WT power spectra analysis for 1D and 2D feature sets respectively. The test sensitivity was within the generality criterion set. The highest performance achieved was a 55±2% test specificity obtained at 90±4% test sensitivity. This was obtained for the combined feature FM-FT and a 10 second pre-shock signal length. The analysis of 5 seconds of pre-shock signals gave the highest performance for the FP and STD feature sets. The analysis of the 10 second pre-shock signal length gave the highest performance for the FM, KT, FT, BI, SH, FM-FP, FM-FT, FM-R, and FP-R feature sets. The R and FP-FT feature sets gave the highest performance when using the 15 second pre-shock signal length. Finally, the analysis of the 20 second pre-shock signal length gave the highest performance for the SK and FT-R feature sets.

Figures 4-55(a) and 4-55(b) show the specificities of all experiments based on STFT power spectra analysis using a 1 second window width for 1D and 2D feature sets respectively. The test sensitivity was within the generality criterion set. The highest performance achieved was a 58±4% test specificity obtained at 90±4% test sensitivity. This was obtained for the combined feature FM-FT and a 10 second pre-shock signal length. The analysis of a 5 second pre-shock signal length gave the highest performance for the STD feature set. The analysis of the 10 second pre-shock signal length gave the highest performance for the FP, BI, SH, and FM-FT feature sets. The FT, FM-FP, FM-R, and FP-R feature sets gave the highest performance when using the 15 seconds pre-shock signal length. Finally, the analysis of the 20 second pre-shock signal length gave the highest performance for the FM, SK, KT, R, FP-FT, and FT-R feature sets.

Figures 4-56(a) and 4-56(b) show the specificities of all experiments based on STFT power spectra analysis using a 2 second window width for 1D and 2D feature sets respectively. The test sensitivity was within the generality criterion set. The highest performance achieved was a 58±4% test sensitivity obtained at 90±4% test sensitivity. This was obtained for the combined feature FM-FT and a 10 second pre-shock signal length. The analysis of a 5 second pre-shock signal length gave the highest performance for the FP feature set. The analysis of the 10 second pre-shock signal length gave the highest performance for the BI and FM-FT feature sets. The STD, FT, R, FM-FP, and FP-FT feature sets gave the highest performance when using the 15 second pre-shock signal length. Finally, the analysis of the 20 second pre-shock signal length gave the highest performance for the FM, SK, KT, SH, FM-R, FP-R, and FT-R feature sets.

Figures 4-57(a) and 4-57(b) show the specificities of all experiments based on STFT power spectra analysis using a 3 second window width for 1D and 2D feature sets respectively. The test sensitivity was within the generality criterion. The highest performance achieved was a 59±3% test specificity obtained at 90±4% test sensitivity. This was obtained for the combined feature FM-FT and a 10 second pre-shock signal length. The analysis of a 5 second pre-shock signal length gave the highest performance for the FP feature set. The analysis of the 10 second pre-shock signal length gave the highest performance for the BI and FM-FT feature sets. The

FT, FM-FP, and FP-FT feature sets gave the highest performance when using the 15 second pre-shock signal length. Finally, the analysis of the 20 second pre-shock signal length gave the highest performance for the FM, STD, SK, KT, R, SH, FM-R, FP-R, and FT-R feature sets.

Consideration of the results in figures 4-54 to 4-57 shows that there is a general trend in the classifications. The 1D classification employing FM, FP, FT, BI, and R gave better results than the classification employing STD, SK, KT and SH. In addition, the tendency for the 2D classifier was to improve the performance of prediction. Overall for the analysis of shock outcome prediction employing the normalised power spectral features, the STFT3 power spectra of 10 second-length of pre-shock ECG achieved the best performance of 59±3% test specificity obtained at 90±4% test sensitivity. This was obtained for the combined feature FM-FT.

4.3.2 Positional dependence of the time-frequency analysis

This section considers the relationship between the predictive value of the pre-shock ECG signal selected for analysis and its temporal distance from the shock event. Selected segments of the ECG trace were examined using two time-frequency decompositions: the WT and the STFT employing a 3-second (Gaussian) window width. The STFT using the 3 second window was chosen as it performed better than the 1 second and 2 second window in the analysis in section 4.3.1. It was found from the optimal length analysis that the 10 second pre-shock signal length gave the best performance for the shock outcome prediction, hence this length is used in the analysis of positional dependence of time-frequency information analysis. Three segments of each ECG were considered in the analysis of 0-10 seconds, 5-15 seconds, and 10-20 seconds prior to countershock. The normalised feature sets were used in this analysis. The analysed time positions used in the experiments are presented in figure 4-22. The analysis employed both 1D and 2D feature sets.

4.3.2.1 The 10 seconds length of pre-shock at 0-10 seconds (location A)

This section contains the results from the analysis of 10-second segments of VF immediately prior to countershock. This is shown as section A in figure 4-22. The

characteristic features in this experiment were computed from power spectra which were generated from the summation of the time-frequency scalogram components across the time domain. Both the WT and STFT3 time-frequency methods were used in the experiments.

The WRST values for the feature sets derived from the WT are tabulated in the second column of table 4-12. Figure 4-58 shows the performances of the classifier using 1D and 2D feature sets. The FT feature gave the highest performance for the 1D analysis with 40±2% specificity obtained at 90±4% sensitivity. The combination of the FM and FT features gave the highest performance for the 2D analysis with 55±2% specificity obtained at 90±4% sensitivity. (This result has been presented previously in section 4.3.1.2)

The WRST values for the feature sets derived from the STFT employing a 3 second window are listed in the third column of table 4-12. Figure 4-59 shows the performances of the classifier using 1D and 2D feature sets. The FT feature gave the highest performance for the 1D analysis with 40±1% specificity obtained at 90±4% sensitivity. The combination of the FM and FT features gave the highest performance for the 2D analysis with 59±3% specificity obtained at 90±4% sensitivity. (This result has been presented previously in section 4.3.1.2)

4.3.2.2 The 10 seconds length of pre-shock at 5-15 seconds (location B)

This section contains the results from the analysis of 10-second segments of VF immediately prior to countershock. This is shown as section B in figure 4-22. The characteristic features in this experiment were computed from power spectra which were generated from the summation of the time-frequency scalogram components across the time domain. Again, both the WT and STFT3 time-frequency methods were used in the experiments.

The WRST values for the feature sets derived from the WT are tabulated in the second column of table 4-13. Figure 4-60 shows the performances of the classifier using 1D and 2D feature sets. The FT feature gave the highest performance for the 1D analysis with 33±0% specificity obtained at 91±2% sensitivity. The combination of

the FM and FT features gave the highest performance for the 2D analysis with 54±2% specificity obtained at 90±4% sensitivity.

The WRST values for the feature sets derived from the STFT employing a 3 second window are listed in the third column of table 4-13. Figure 4-61 shows the performances of the classifier using 1D and 2D feature sets. The FT feature gave the highest performance for the 1D analysis with 40±3% specificity obtained at 92±4% sensitivity. The combination of the FT and R features gave the highest performance for the 2D analysis with 58±2% specificity obtained at 90±0% sensitivity.

4.3.2.3 The 10 seconds length of pre-shock at 5-15 seconds (location C)

This section contains the results from the analysis of 10-second segments of VF immediately prior to countershock. This is shown as section C in figure 4-22. The characteristic features in this experiment were computed from power spectra which were generated from the summation of the time-frequency scalogram components across the time domain. Again, the WT and STFT3 time-frequency methods were used in the experiments.

The WRST values for the feature sets derived from the WT are tabulated in the second column of table 4-14. Figure 4-62 shows the performances of the classifier using 1D and 2D feature sets. The FM feature gave the highest performance for the 1D analysis with 32±18% specificity obtained at 90±6% sensitivity. The combination of the FT and R features gave the highest performance for the 2D analysis with 57±3% specificity obtained at 91±0% sensitivity.

The WRST values for the feature sets derived from the STFT employing a 3 second window are listed in the third column of table 4-14. Figure 4-63 shows the performances of the classifier using 1D and 2D feature sets. The FP feature gave the highest performance for the 1D analysis with 39±8% specificity obtained at 90±2% sensitivity. The combination of the FM and FT features gave the highest performance for the 2D analysis with 49±7% specificity obtained at 90±2% sensitivity.

4.3.2.4 Summary of positional dependence of time-frequency analysis

Figure 4-64 shows the results of positional dependence of the WT power spectra analysis using 1D and 2D feature sets. The results show the specificities of all experiments. The test sensitivity was within the generality criterion. The results for the FP, STD, FT, BI, R, FM-FT, FM-R, and FP-R features at position A gave the highest performances. At period B, the performances of classifier with FM-FP, and FP-FT were maximised. The classifier gave the highest performance for features FM, SK, KT, SH, and FT-R over period C.

Figure 4-65 shows the results of positional dependence of the STFT3 power spectra analysis using 1D and 2D feature sets. The results show the specificities of all experiments. The test sensitivity was within the generality criterion. The results for the FM, STD, FT, BI, FM-FP, and FM-FT features at position A gave the highest performances. At period B, the performances of the classifier was maximised for FM-R, FP-FT, FP-R, and FT-R. The classifier gave the highest performance for features FP, SK, KT, R, and SH over period C.

Considering figure 4-64 to 4-65, the tendency for the 2D classifier is to improve the performance of prediction. It can be seen that the FT-R feature provides the best results at position C for the WT-based method and the FM-FT feature provides the best result at location A for the STFT3 methods. Of these, the STFT3-based method achieved the best performance with 59±3% specificity achieved at 90±4% sensitivity. Again, the analysis shows that there is no obvious trend correlating prediction with temporal distance to the shock event.

4.3.3 Summary of the use of normalised feature sets in shock outcome prediction

The best result of the shock outcome prediction using the original sets of the WT and STFT power spectral features was 59±3% specificity achieved at 90±4% sensitivity. This performance was achieved using the FM-FT feature and STFT3 power spectral analysis for the 10 second pre-shock ECG. Figure 4-66 shows the ROC curve of the best classifier associated with 75×75 bins and a Gaussian width equal to 0.5 in the 2D-PDF estimation. From the system ROC curve it can be seen that the test

sensitivity is constant at 90±4 % (shown by the arrow), and the test specificity decreases markedly from 59±3% to 44±3%. Figure 4-67 shows the decision boundaries of the classifier associated with 95% training sensitivity. The boundaries of the training set for the first and second validations are presented in figures 4-67(a) and 4-67(b) respectively. In testing, the classifier achieved an average sensitivity and specificity of 59±3% and 90±4% respectively. The corresponding decision boundaries are shown in figure 4-67(c) and 4-67(d). Figure 4-68 shows a modified version of the decision boundaries in figure 4-67. For this case, the classifier was trained to 100% sensitivity for both validations. From figures 4-68(a) and 4-68(b), it can be seen that the decision boundaries of the training sets can be seen to expand to cover more ROSC outcomes when compared to those shown in figure 4-67(a) and 4-67(b). The decision boundaries of this system now cover the extra points of the ROSC set (indicated by arrows in the plots). However, these new decision boundaries still do not cover the outliers in the test set (marked by arrows in the plots of figures 4-68(c) and 4-68(d)). As a result, the classifier of figure 4-68 achieves the test sensitivity of 90±4% which is the same as that of the classifier of figure 4-67. On the other hand, the test specificity of the classifier in figure 4-68 decreases to 44±3% (no more ROSCs are included). This causes the change in specificity associated with a constant sensitivity as shown in the ROC curve of figure 4-66.

4.4 The use of principal component analysis (PCA) in the shock outcome prediction analysis

This section describes the use of new variables created using the PCA technique. As described in chapter 3, section 3.4.2, the new variables are linear combinations of the original variables. PCA is concerned with expressing the variance-covariance structure of the data through a few linear combinations of the variables. This section describes the investigation carried out into the performance of the classifier when using the PCA features. Again, pre-shock signals of 5, 10, 15, and 20 seconds in length were used in the study. The PCA features were determined from the original characteristic features described in section 4.3. Once generated, the PCA features were mapped into the normalised format (ranging from zero to one). The four features giving the highest performances were combined together to provide a number of 2D

feature sets. The bin sizes were adjusted according to setting the number of bins equal to 50, 75, 100, 125, 150, 175, and 200 bins to cover the unit interval. The Gaussian kernel smoothing histograms were set to 0.1, 0.2, 0.3, 0.4, 0.5, 0.6, 0.7, 0.8, and 0.9 units in width. The sensitivity of ROSC outcome was set, as the criterion for the training classifier, to $P_{sens}(\omega_1)$ = 95%. The cost functions found for each case was then used to test the remaining data. For cases where the test sensitivity criterion (i.e. less than 90%) was not achieved, the experiment which gave the highest sensitivity was chosen to be the highest performance of the classifier.

4.4.1 Determination of an optimal length of pre-shock ECG for use in shock outcome prediction analysis

This section described the results of the investigation of the performances of shock outcome prediction associated with varying lengths of pre-shock signal. Four pre-shock signal lengths were used in the study. There were 5, 10, 15, and 20 seconds immediately prior to countershock. The analysis employed both 1D and 2D feature sets. The 1D feature sets were PCA1-PCA9 extracted from nine characteristic features in section 4.3. The first four features giving the best performances for 1D analysis were selected to combine for 2D analysis.

4.4.1.1 The 5 second length of pre-shock ECG

This section contains the results from the analysis of 5 second segments of VF signals immediately prior to countershock. The characteristic features in this experiment were computed from the power spectra generated from the summation of the time-frequency scalogram components across the time domain as described in chapter 3, section 3.3. Both the WT and STFT time-frequency methods were used in the experiments. As before, three different window lengths were employed for the STFT analysis: these were 1, 2, and 3 seconds in length.

Figure 4-69 displays the boxplots of each feature set distribution allowing visual comparison between the ROSC and NOROSC groups where each feature was obtained from the WT spectrum of the corresponding signal. The separation of each corresponding ROSC/NOROSC feature set can be quantified using the Wilcoxon

rank sum test (WRST). The WRST values for the feature sets derived from the WT are tabulated in the second column of table 4-15. Figure 4-70 shows the performances of the classifier using 1D and 2D feature sets. The PCA5 feature gave the highest performance for the 1D analysis with 33±6% specificity obtained at 90±0% sensitivity. The combination of the PCA2 and PCA5 features gave the highest performance for the 2D analysis with 48±2% specificity obtained at 90±7% sensitivity.

The WRST values for the feature sets derived from the STFT employing a 1 second window are listed in the third column of table 4-15. The boxplots of these feature distributions are provided in Appendix B, figure B-46. All feature distributions used in the rest of the chapter can be found in Appendix B. Figure 4-71 shows the performances of the classifier using 1D and 2D feature sets. The PCA1 feature gave the highest performance for the 1D analysis with 29±7% specificity obtained at 90±4% sensitivity. The combination of the PCA1 and PCA7 features gave the highest performance for the 2D analysis with 49±3% specificity obtained at 90±4% sensitivity.

The WRST values for the feature sets derived from the STFT employing a 2 second window are listed in the fourth column of table 4-15. Figure 4-72 shows the performances of the classifier using 1D and 2D feature sets. The PCA1 feature gave the highest performance for the 1D analysis with 28±4% specificity obtained at 91±6% sensitivity. The combination of the PCA1 and PCA6 features gave the highest performance for the 2D analysis with 39±0% specificity obtained at 90±4% sensitivity.

The WRST values for the feature sets derived from the STFT employing a 3 second window are given in the last column of table 4-15. Figure 4-73 shows the performances of the classifier using 1D and 2D feature sets. The PCA1 feature gave the highest performance for the 1D analysis with 29±4% specificity obtained at 90±4% sensitivity. The combination of the PCA1 and PCA6 features gave the highest performance for the 2D analysis with 47±0% specificity obtained at 90±7% sensitivity.

From the above results, based on a 5 second pre-shock window length, it can be seen that the highest performance of shock outcome prediction for the 1D analysis was obtained from the WT-based PCA5 feature sets. The combination of the PCA1 and PCA7 features gave the highest performance for the 2D analysis using the STFT1-based feature sets.

4.4.1.2 The 10 second length of pre-shock ECG

This section contains the results from the analysis of 10 second segments of VF signals immediately prior to countershock. The WRST values for the feature sets derived from the WT are listed in the second column of table 4-16. Figure 4-74 shows the performances of the classifier using 1D and 2D feature sets. The PCA2 feature gave the highest performance for the 1D analysis with 43±2% specificity obtained at 91±2% sensitivity. The combination of the PCA2 and PCA4 features gave the highest performance for the 2D analysis with 41±3% specificity obtained at 90±0% sensitivity.

The WRST values for the feature sets derived from the STFT employing a 1 second window are listed in the third column of table 4-16. Figure 4-75 shows the performances of the classifier using 1D and 2D feature sets. The PCA1 feature gave the highest performance for the 1D analysis with 42±6% specificity obtained at 90±4% sensitivity. The combination of the PCA2 and PCA4 features gave the highest performance for the 2D analysis with 28±8% specificity obtained at 90±4% sensitivity.

The WRST values for the feature sets derived from the STFT employing a 2 second window are listed in the fourth column of table 4-16. Figure 4-76 shows the performances of the classifier using 1D and 2D feature sets. The PCA1 feature gave the highest performance for the 1D analysis with 38±3% specificity obtained at 91±2% sensitivity. The combination of the PCA1 and PCA7 features gave the highest performance for the 2D analysis with 44±8% specificity obtained at 90±0% sensitivity.

The WRST values for the feature sets derived from the STFT employing a 3 second window are given in the last column of table 4-16. Figure 4-77 shows the performances of the classifier using 1D and 2D feature sets. The PCA1 feature gave the highest performance for the 1D analysis with 40±1% specificity obtained at 90±4% sensitivity. The combination of the PCA1 and PCA7 features gave the highest performance for the 2D analysis with 42±6% specificity obtained at 90±0% sensitivity.

From the above results, based on a 10 second pre-shock window length, it can be seen that the highest performance of shock outcome prediction for the 1D analysis was obtained from the WT-based PCA2 feature sets. The combination of the PCA1 and PCA7 features gave the highest performance for the 2D analysis using the STFT2-based feature sets.

4.4.1.3 The 15 second length of pre-shock ECG

This section contains the results from the analysis of 15 second segments of VF signals immediately prior to countershock. The WRST values for the feature sets derived from the WT are listed in the second column of table 4-17. Figure 4-78 shows the performances of the classifier using 1D and 2D feature sets. The PCA3 feature gave the highest performance for the 1D analysis with 35±1% specificity obtained at 91±2% sensitivity. The combination of the PCA3 and PCA5 features gave the highest performance for the 2D analysis with 44±1% specificity obtained at 90±0% sensitivity.

The WRST values for the feature sets derived from the STFT employing a 1 second window are listed in the third column of table 4-17. Figure 4-79 shows the performances of the classifier using 1D and 2D feature sets. The PCA1 feature gave the highest performance for the 1D analysis with 44±4% specificity obtained at 91±2% sensitivity. The combination of the PCA1 and PCA3 features gave the highest performance for the 2D analysis with 53±6% specificity obtained at 91±2% sensitivity.

The WRST values for the feature sets derived from the STFT employing a 2 second window are listed in the fourth column of table 4-17. Figure 4-80 shows the performances of the classifier using 1D and 2D feature sets. The PCA1 feature gave the highest performance for the 1D analysis with 43±1% specificity obtained at 91±2% sensitivity. The combination of the PCA1 and PCA5 features gave the highest performance for the 2D analysis with 56±3% specificity obtained at 92±4% sensitivity.

The WRST values for the feature sets derived from the STFT employing a 3 second window are given in the last column of table 4-17. Figure 4-81 shows the performances of the classifier using 1D and 2D feature sets. The PCA1 feature gave the highest performance for the 1D analysis with 43±2% specificity obtained at 91±2% sensitivity. The combination of the PCA1 and PCA5 features gave the highest performance for the 2D analysis with 52±1% specificity obtained at 90±4% sensitivity.

From the above results, based on a 15 second pre-shock window length, it can be seen that the highest performance of shock outcome prediction for the 1D analysis was obtained from the STFT1-based PCA1 feature sets. The combination of the PCA1 and PCA5 features gave the highest performance for the 2D analysis using the STFT2-based feature sets.

4.4.1.4 The 20 second length of pre-shock ECG

This section contains the results from the analysis of 20 second segments of VF signals immediately prior to countershock. The WRST values for the feature sets derived from the WT are listed in the second column of table 4-18. Figure 4-82 shows the performances of the classifier using 1D and 2D feature sets. The PCA4 feature gave the highest performance for the 1D analysis with 27±3% specificity obtained at 90±2% sensitivity. The combination of the PCA4 and PCA5 features gave the highest performance for the 2D analysis with 43±7% specificity obtained at 90±6% sensitivity.

The WRST values for the feature sets derived from the STFT employing a 1 second window are listed in the third column of table 4-18. Figure 4-83 shows the performances of the classifier using 1D and 2D feature sets. The PCA1 feature gave the highest performance for the 1D analysis with 32±2% specificity obtained at 90±2% sensitivity. The combination of the PCA1 and PCA7 features gave the highest performance for the 2D analysis with 44±2% specificity obtained at 90±6% sensitivity.

The WRST values for the feature sets derived from the STFT employing a 2 second window are listed in the fourth column of table 4-18. Figure 4-84 shows the performances of the classifier using 1D and 2D feature sets. The PCA1 feature gave the highest performance for the 1D analysis with 32±3% specificity obtained at 90±2% sensitivity. The combination of the PCA1 and PCA4 features gave the highest performance for the 2D analysis with 39±4% specificity obtained at 90±2% sensitivity.

The WRST values for the feature sets derived from the STFT employing a 3 second window are given in the last column of table 4-18. Figure 4-85 shows the performances of the classifier using 1D and 2D feature sets. The PCA1 feature gave the highest performance for the 1D analysis with 30±10% specificity obtained at 90±6% sensitivity. The combination of the PCA1 and PCA5 features gave the highest performance for the 2D analysis with 46±2% specificity obtained at 90±2% sensitivity.

From the above results, based on a 20 second pre-shock window length, it can be seen that the highest performance of shock outcome prediction for the 1D analysis was obtained from the STFT1 and STFT2-based PCA1 feature sets. The combination of the PCA1 and PCA5 features gave the highest performance for the 2D analysis using the STFT3-based feature sets.

4.4.1.5 Summary of optimal length analysis

The PCA method was employed in the prediction of defibrillation outcome where it was used to generate new variables from the original features. As with the original

and normalised features described in section 4.2 and 4.3, the PCA variables were fed into the classifier to predict the defibrillation outcome of VF signal. This section considers the prediction performances achieved for the various lengths of pre-shock signal used in the analysis. The normalised features were used in the classification. These were 5, 10, 15, and 20 seconds immediately prior to shock. The results reported in section 4.4.1.1- 4.4.1.4 were inspected to determine the optimal length of pre-shock signal required in order to best predict the defibrillation outcome of the VF patient.

Figure 4-86 shows the specificities of all experiments in the optimal length analysis. The test sensitivity was within the generality criterion set. The analysis with 5 second length pre-shock ECG gave the best performance for WT spectra technique with 48±2% specificity obtained at 90±7% specificity. The analysis with 15 second length pre-shock ECG gave the best performance for STFT1 spectra technique with 53±6% specificity obtained at 91±2% sensitivity. The analysis with 15 second length pre-shock ECG gave the best performance for STFT2 spectra technique with 56±3% specificity obtained at 92±4% sensitivity. The analysis with 15 second length pre-shock ECG gave the best performance for STFT3 spectra technique with 52±1% specificity obtained at 90±4% sensitivity. It can be seen that the analysis of 15 second length of pre-shock signals gave the best performances for the STFT2-based method using PCA feature sets.

4.4.2 Positional dependence of the time-frequency analysis

This section considers the relationship between the predictive value of the pre-shock ECG signal selected for analysis and its temporal distance from the shock event. Selected segments of the ECG trace were examined using two time-frequency decompositions: the WT and the STFT employing a 2-second (Gaussian) window width. According to the best results for STFT-based methods in section 4.4.1, the STFT using the 2 second window was used as it performed better than the 1 second and 3 second window in the analysis of 10 second pre-shock signals. Three segments of each ECG were considered in the analysis of 0-10 seconds, 5-15 seconds, and 10-20 seconds prior to countershock. The normalised feature sets were used in this analysis. Figure 4-22 shows a schematic diagram of the position of pre-shock segments used in this analysis marked A, B, and C respectively.

4.4.2.1 The 10 seconds length of pre-shock at 0-10 seconds (location A)

This section contains the results from the analysis of 10-second segments of VF immediately prior to countershock. This is shown as section A in figure 4-22. The characteristic features in this experiment were computed from power spectra which were generated from the summation of the time-frequency scalogram components across the time domain. Both the WT and STFT2 time-frequency methods were used in the experiments.

The WRST values for the feature sets derived from the WT are listed in the second column of table 4-19. Figure 4-87 shows the performances of the classifier using 1D and 2D feature sets. The PCA2 feature gave the highest performance for the 1D analysis with 43±2% specificity obtained at 91±2% sensitivity. The combination of the PCA2 and PCA4 features gave the highest performance for the 2D analysis with 41±3% specificity obtained at 90±0% sensitivity.

The WRST values for the feature sets derived from the STFT employing a 2 second window are listed in the last column of table 4-19. Figure 4-88 shows the performances of the classifier using 1D and 2D feature sets. The PCA1 feature gave the highest performance for the 1D analysis with 38±3% specificity obtained at 91±2% sensitivity. The combination of the PCA1 and PCA7 features gave the highest performance for the 2D analysis with 44±8% specificity obtained at 90±0% sensitivity.

4.4.2.2 The 10 seconds length of pre-shock at 5-15 seconds (location B)

This section contains the results from the analysis of 10-second segments of VF at 5 seconds before countershock. This is shown as section B in figure 4-22. The characteristic features in this experiment were computed from power spectra which were generated from the summation of the time-frequency scalogram components across the time domain. Again, both the WT and STFT2 time-frequency methods were used in the experiments.

The WRST values for the feature sets derived from the WT are listed in the second column of table 4-20. Figure 4-89 shows the performances of the classifier using 1D and 2D feature sets. The PCA5 feature gave the highest performance for the 1D analysis with 37±1% specificity obtained at 91±2% sensitivity. The combination of the PCA2 and PCA5 features gave the highest performance for the 2D analysis with 38±3% specificity obtained at 90±4% sensitivity.

The WRST values for the feature sets derived from the STFT employing a 2 second window are listed in the last column of table 4-20. Figure 4-90 shows the performances of the classifier using 1D and 2D feature sets. The PCA5 feature gave the highest performance for the 1D analysis with 26±1% specificity obtained at 91±2% sensitivity. The combination of the PCA5 and PCA6 features gave the highest performance for the 2D analysis with 39±1% specificity obtained at 90±0% sensitivity.

4.4.2.3 The 10 seconds length of pre-shock at 10-20 seconds (location C)

This section contains the results from the analysis of 10-second segments of VF at 10 seconds before countershock. This is shown as section C in figure 4-22. The characteristic features in this experiment were computed from power spectra which were generated from the summation of the time-frequency scalogram components across the time domain. Again, both the WT and STFT2 time-frequency methods were used in the experiments.

The WRST values for the feature sets derived from the WT are listed in the second column of table 4-21. Figure 4-91 shows the performances of the classifier using 1D and 2D feature sets. The PCA6 feature gave the highest performance for the 1D analysis with 36±1% specificity obtained at 93±2% sensitivity. The combination of the PCA2 and PCA6 features gave the highest performance for the 2D analysis with 47±1% specificity obtained at 90±2% sensitivity.

The WRST values for the feature sets derived from the STFT employing a 2 second window are listed in the last column of table 4-21. Figure 4-92 shows the performances of the classifier using 1D and 2D feature sets. The PCA5 feature gave

the highest performance for the 1D analysis with 39±1% specificity obtained at 90±6% sensitivity. The combination of the PCA1 and PCA7 features gave the highest performance for the 2D analysis with 45±5% specificity obtained at 90±2% sensitivity.

4.4.2.4 Summary of positional dependence of time-frequency analysis

This section studies the relationship between the performances of shock outcome prediction and its temporal distance from the shock event. Figure 4-93 shows the results of positional dependence of the WT and STFT2 power spectra analysis. The results show the specificities of all experiments. The test sensitivity was within the generality criterion. The analysis shows that there is no obvious relationship between the predictive information contained in the ECG and the temporal distance to the shock event for both the WT and STFT-based methods.

4.4.3 Summary of the use of PCA feature sets in shock outcome prediction

The best result of the shock outcome prediction using the original sets of the WT and STFT power spectral features was 56±3% specificity achieved at 92±4% sensitivity. This performance was achieved using PCA1-PCA5 features and a STFT2 power spectral analysis for the 15 second pre-shock ECG. Figure 4.94 shows the ROC curve of the best classifier associated to 75×75 bins and Gaussian width equal to 0.4 in 2D-PDF estimation. The system ROC curve shows that the test sensitivity remains constant at 92±4 % (shown by arrow) as the test specificity decreased markedly from 56±3% to 49±0%. This is similar to the behaviour of the ROC curve derived using the normalised feature sets (figure 4-66). Figure 4-95 shows the decision boundaries of the classifier associated with 95% training sensitivity. The boundaries of the training set for the first and second validations are presented in figures 4-95(a) and 4-95(b) respectively. In testing, the classifier achieved the average sensitivity and specificity at 56±3% and 92±4% respectively. The corresponding decision boundaries are shown in figure 4-95(c) and 4-95(d). Figure 4-96 shows a modified version of the decision boundaries in figure 4-95 where the classifier was trained to 100% sensitivity for both training validations (figure 4-96(a) and 4-96(b)). The decision boundaries of this system now cover extra points of the ROSC set (indicated by arrows in the plots).

However, the decision boundaries still do not cover the outliers of the test set (marked by arrows in the plots). As a result, the classifier of figure 4-96 achieved a test sensitivity of 90±4% which is the same test sensitivity of the classifier of figure 4-95. On the other hand, the test specificity of the classifier in figure 4-96 decreased to 49±0%. This causes the change in specificity associated with a constant sensitivity as shown in the ROC curve of figure 4-94.

4.5 Chapter summary

This chapter presents the main results of the parametric study of shock outcome prediction carried out by the author utilising both the WT and the STFT. Three different feature formats were used in the study. There were: (1) original feature sets, (2) normalised feature sets, and (3) new PCA-based feature sets. Each of these was tested for shock outcome performance based on pre-shock window length (immediately prior to countershock) and the temporal location of the analysis segment prior to the shock. Table 4-22 shows the overall results of shock outcome prediction. For all classifications, the numbers of bin were 50, 75, 100, 125, 150, 175, and 200 bins to cover the range. The Gaussian kernel widths were set to 5%, 10%, 15%, 20%, 25%, 30%, 35%, 40%, and 45% of the PDF range.

Section 4.2 described the results using original features (i.e. non-normalised format) in the classification. For all classifications, the PDFs were estimated using histogram smoothing as described in chapter 3. For the optimal length of pre-shock analysis, the highest performance (58±2% specificity and 90±4% sensitivity) was given by the combination of the FM and FT features obtained from the WT power spectrum using 10 seconds length of pre-shock signal. In the analysis of positional dependence, the successful prediction of post-shock outcome was found not to be correlated to the temporal location of the segment of pre-shock trace.

Section 4.3 described the results using normalised features in the classification. The PDFs were estimated using histogram smoothing as described in chapter 3. For the optimal length of pre-shock analysis, the highest performance (59±3% specificity and 90±4% sensitivity) was again given by the combination of the FM and FT features

this time however obtained from the STFT3 power spectrum using 10 seconds length of pre-shock signal. Similar to the results obtained using the original feature sets, the successful prediction of post-shock does not rely on the position of the segment of pre-shock trace.

Section 4.4 described the results using PCA features in the classification. The PDFs were estimated using histogram smoothing as described in chapter 3. For the optimal length of pre-shock analysis, the highest performance (56±3% specificity and 92±4% sensitivity) was given by the combination of the PCA1 and PCA5 features obtained from the STFT2 power spectrum using 15 seconds length of pre-shock signal. Similar to the results obtained using original and normalised feature sets, the successful prediction of post-shock again does not rely on the position of the segment of pre-shock trace.

From the overall results, it can be seen that the use of normalised feature sets improves the shock outcome prediction when employing the STFT-based methods. The original distributions of FT, using the original features described in section 4.2 (i.e. between zero and twenty), were very localised in the classification. This caused a poor performance of the classifier. However, in the classification using the normalised feature sets (section 4.3), these distributions are expanded to fit in the range between zero and one. This caused a marked improvement in the performance of the classifier. In the analysis of 15 second pre-shock signals, the use of PCA feature sets improved the performance of the shock outcome prediction employing the STFT-based methods.

Figure 4-97(a) compares the system ROC curves of the best performing classifiers associated with different feature formats. These were: the system using the original feature set (solid line) obtained from the use of the FM-FT feature-based WT power spectral analysis for the 10 second pre-shock ECG; the system using the normalised feature set (dotted line) obtained from the use of the FM-FT feature-based STFT3 power spectral analysis for the 10 second pre-shock ECG; and the system using the PCA feature set (dashed line) obtained from the use of PCA1-PCA5 feature-based STFT2 power spectral analysis for the 15 second pre-shock ECG. Overall the system associated with the original feature sets performs best as measured by its largest area

under ROC curve (AUC). The system employing the PCA feature sets gave the worst performance in AUC while achieving the best classification performance for a sensitivity above 90%. The best result for PCA was 56±3% specificity at 92±4% sensitivity. Figure 4-97(b) replots the ROC curves with their original error bars from which we see that, within errors, it is difficult to reach a definitive conclusion concerning the best method given the current data.

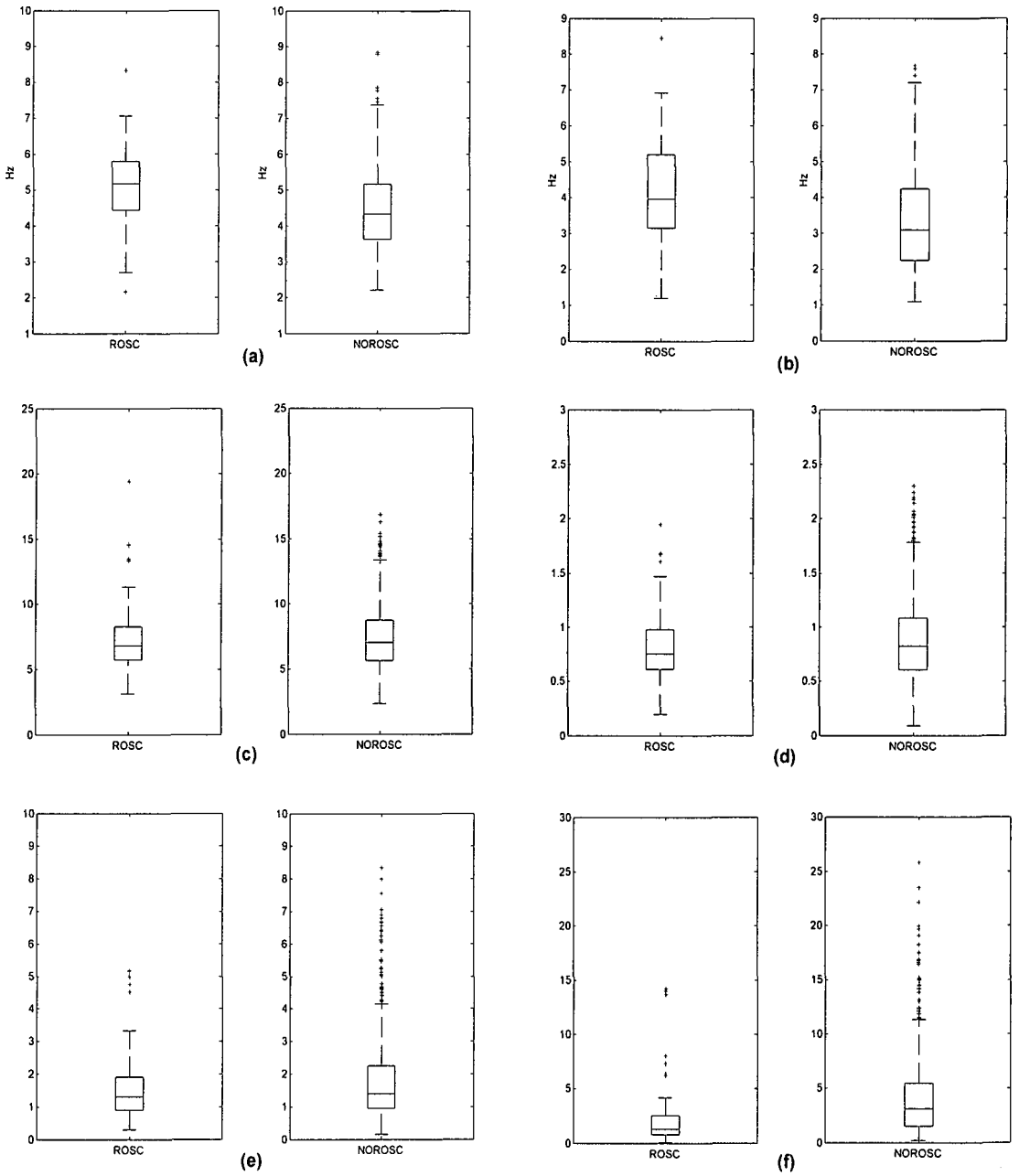

Figure 4-1: Feature boxplots for the ROSC and NOROSC cases: (a) FM feature boxplots, (b) FP feature boxplots, (c) STD feature boxplots, (d) SK feature boxplots, (e) KT feature boxplots, and (f) FT feature boxplots

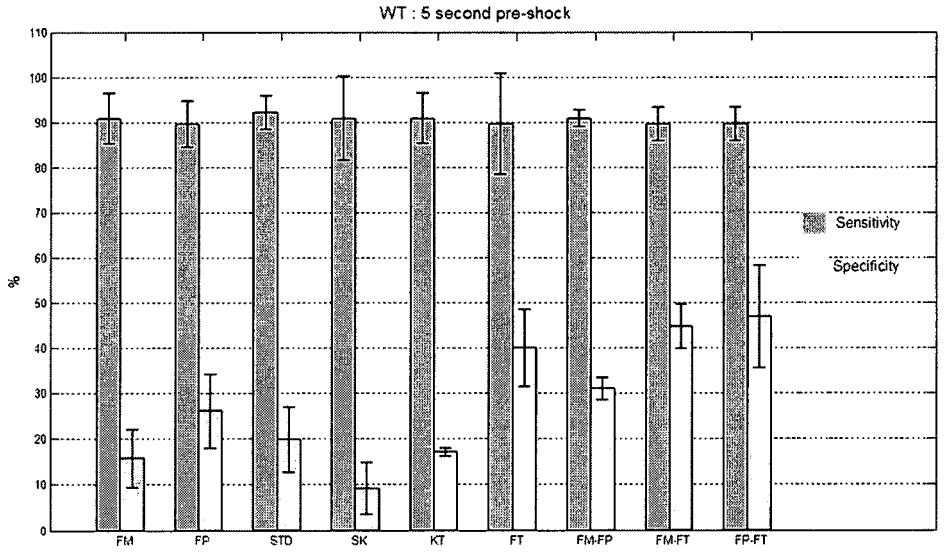

Figure 4-2: The performances of the classifier using the WT power spectrum-based technique (5 second pre-shock)

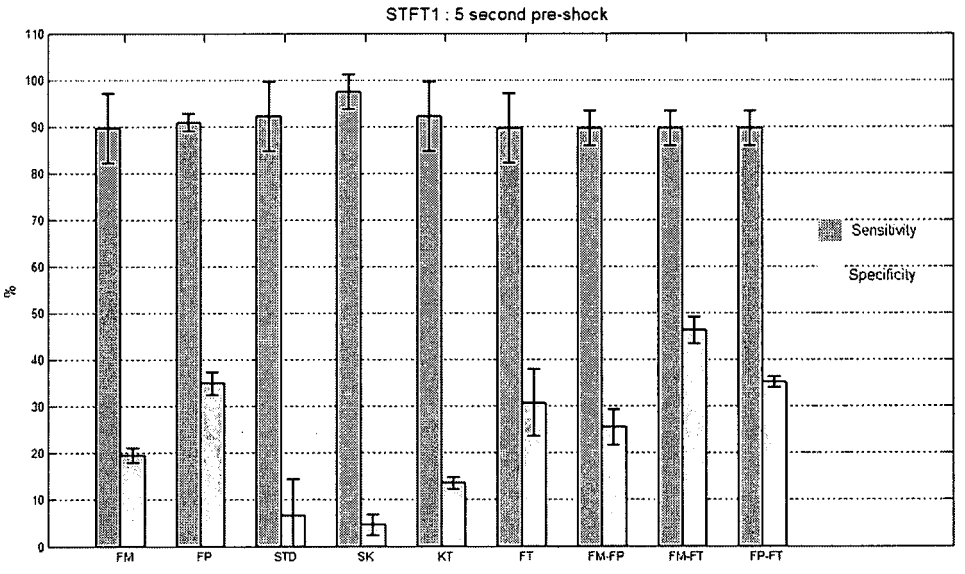

Figure 4-3: The performances of the classifier using the STFT1 power spectrum-based technique (5 second pre-shock)

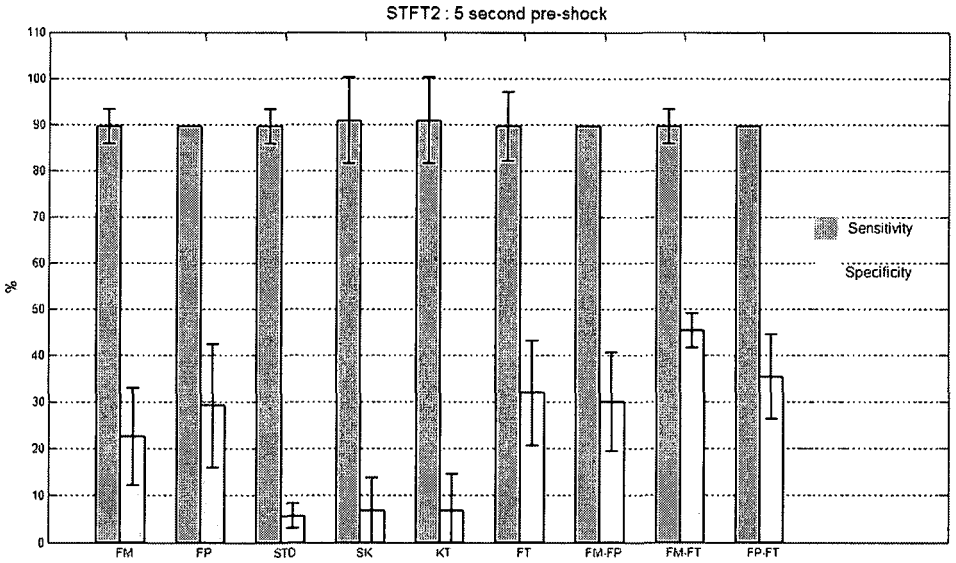

Figure 4-4: The performances of the classifier using the STFT2 power spectrum-based technique (5 second pre-shock)

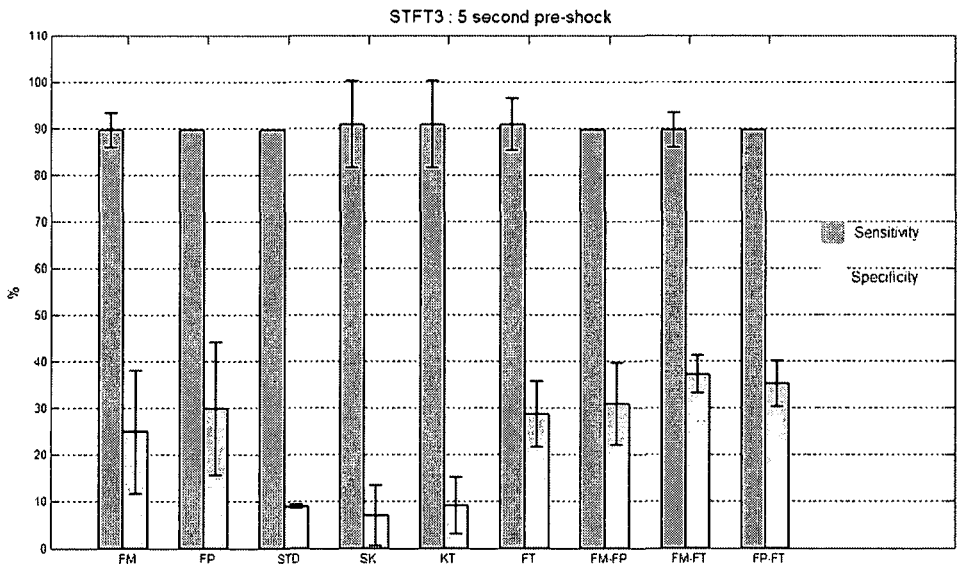

Figure 4-5: The performances of the classifier using the STFT3 power spectrum-based technique (5 second pre-shock)

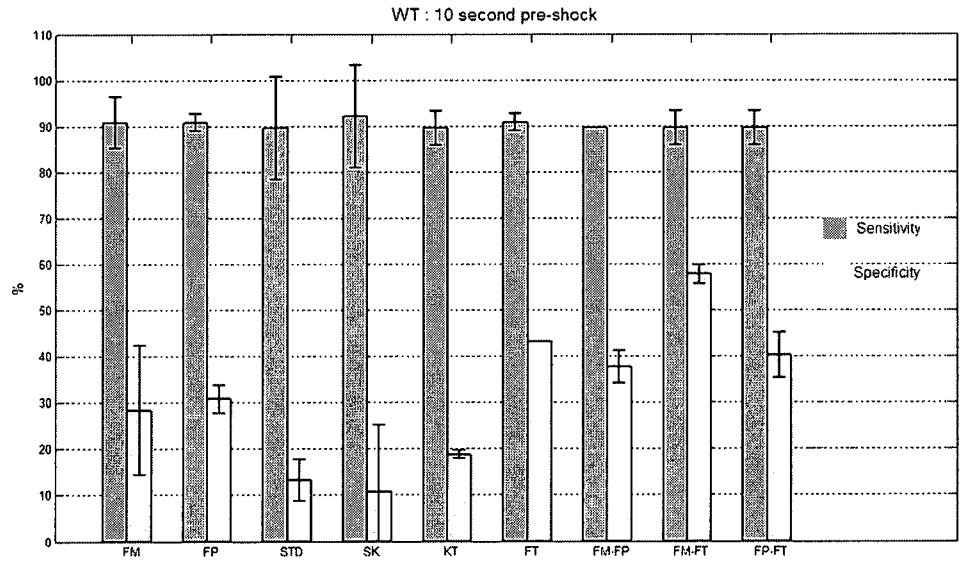

Figure 4-6: The performances of the classifier using the WT power spectrum-based technique (10 second pre-shock)

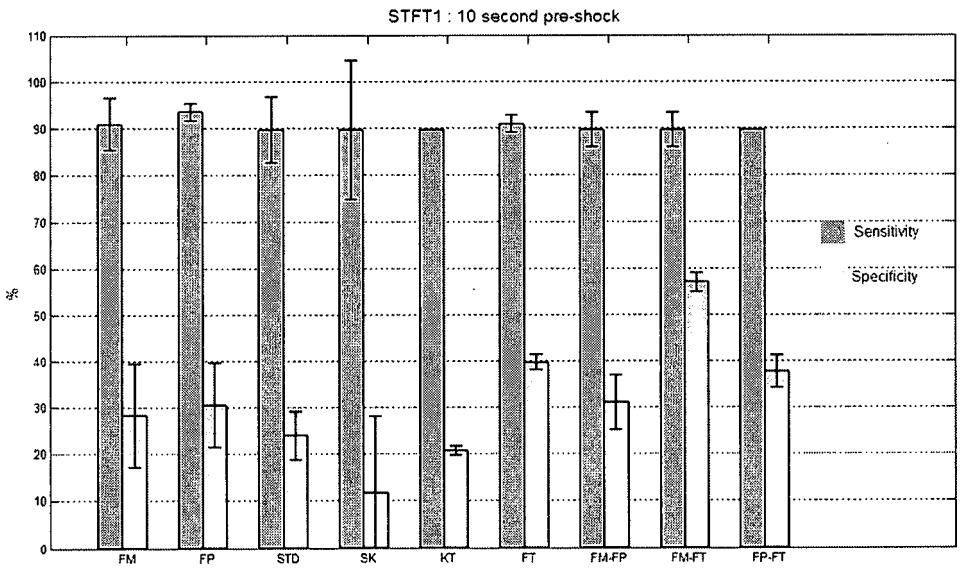

Figure 4-7: The performances of the classifier using the STFT1 power spectrum-based technique (10 second pre-shock)

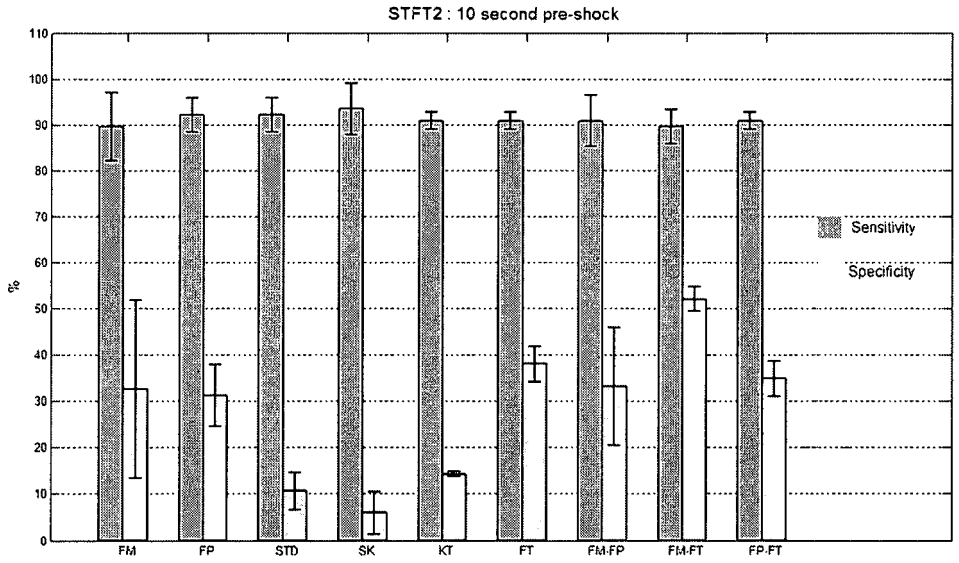

Figure 4-8: The performances of the classifier using the STFT2 power spectrum-based technique (10 second pre-shock)

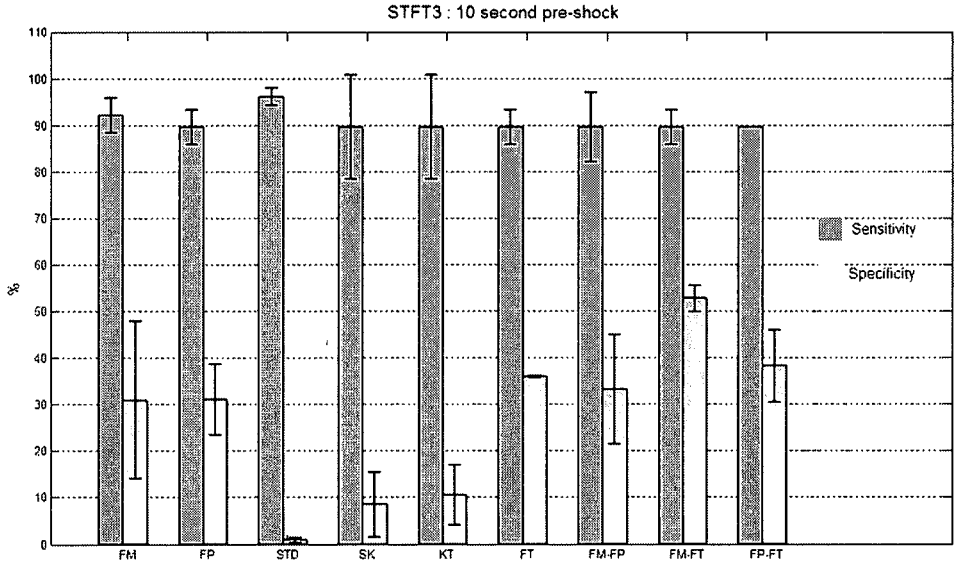

Figure 4-9: The performances of the classifier using the STFT3 power spectrum-based technique (10 second pre-shock)

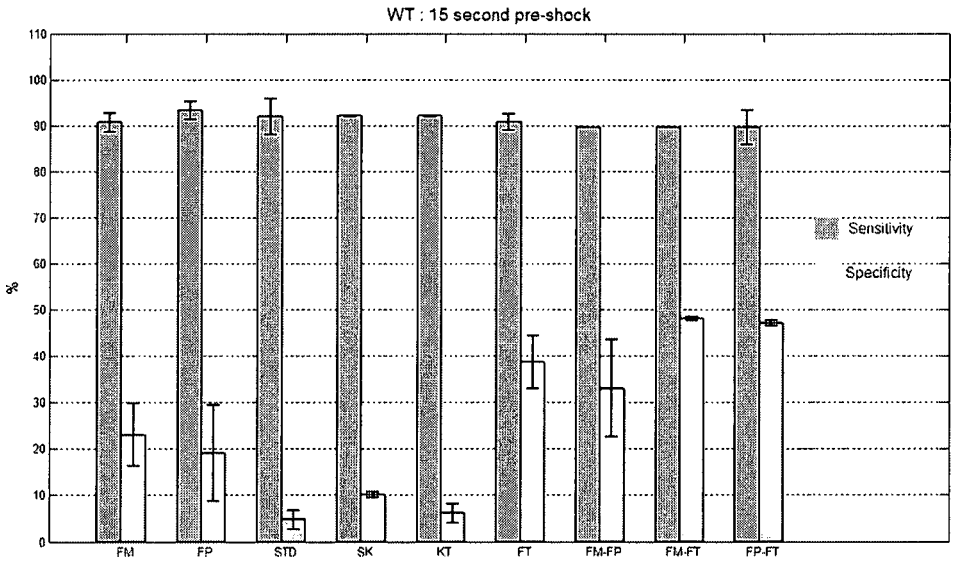

Figure 4-10: The performances of the classifier using the WT power spectrum-based technique (15 second pre-shock)

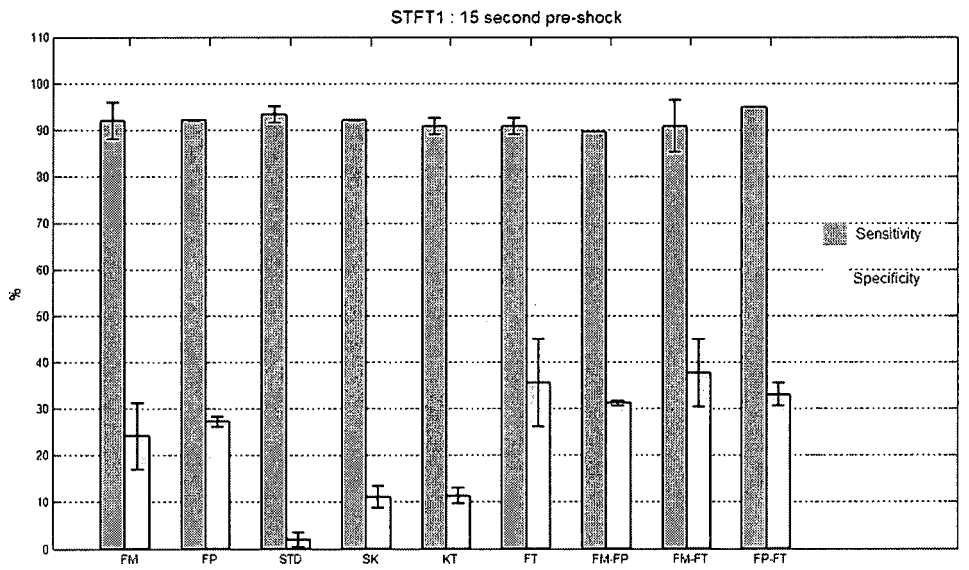

Figure 4-11: The performances of the classifier using the STFT1 power spectrum-based technique (15 second pre-shock)

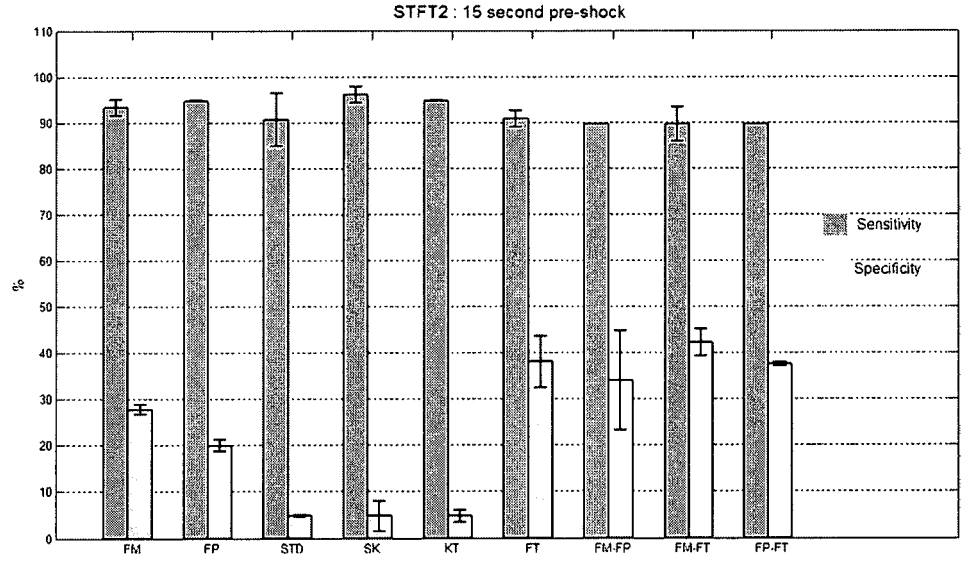

Figure 4-12: The performances of the classifier using the STFT2 power spectrum-based technique (15 second pre-shock)

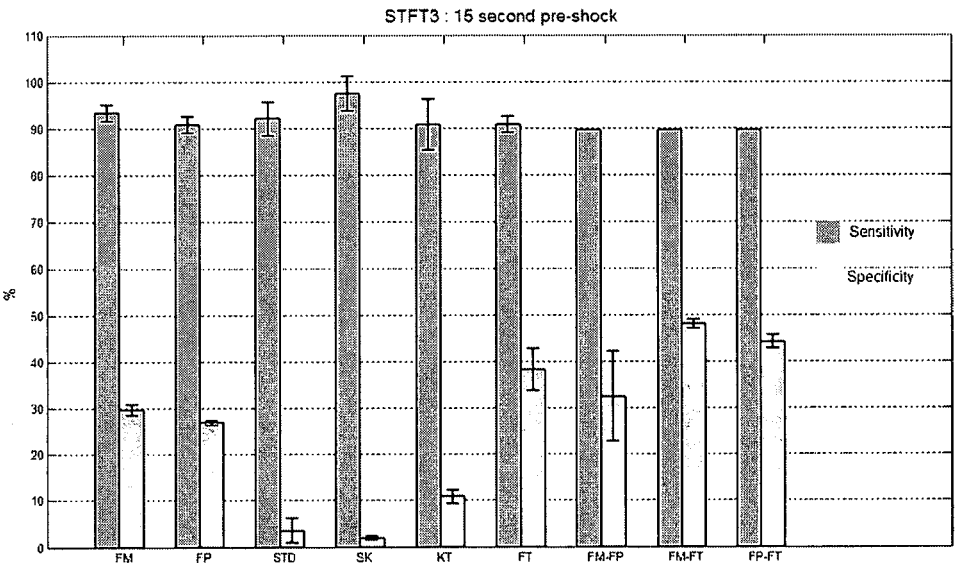

Figure 4-13: The performances of the classifier using the STFT3 power spectrum-based technique (15 second pre-shock)

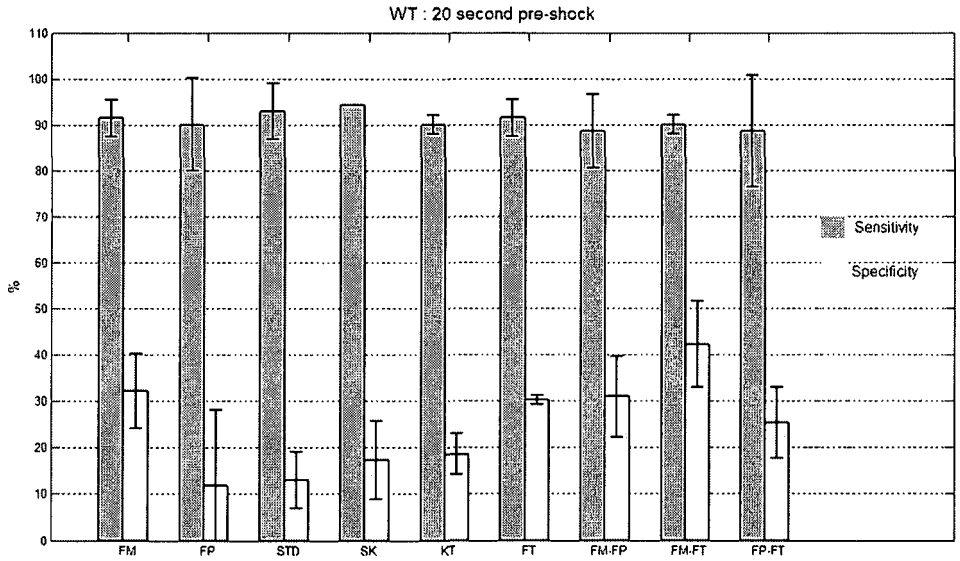

Figure 4-14: The performances of the classifier using the WT power spectrum-based technique (20 second pre-shock)

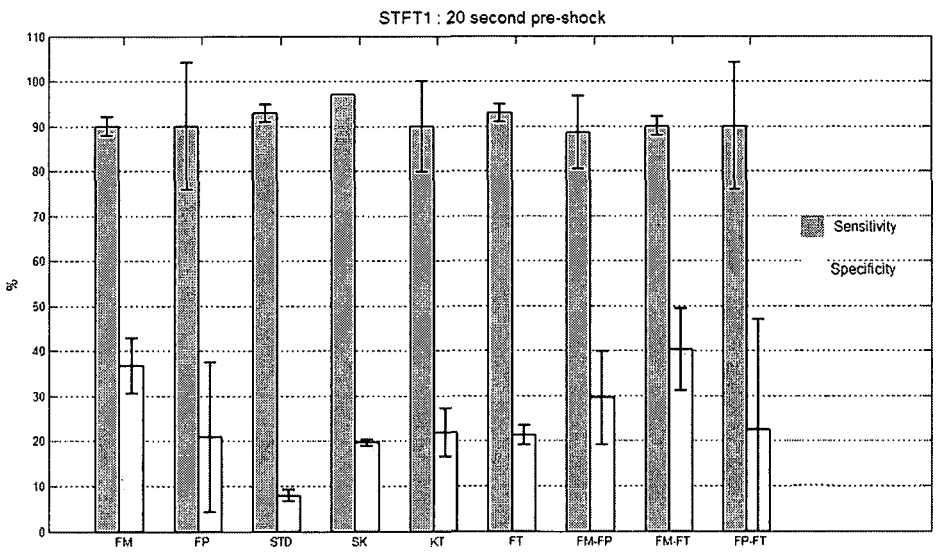

Figure 4-15: The performances of the classifier using the STFT1 power spectrum-based technique (20 second pre-shock)

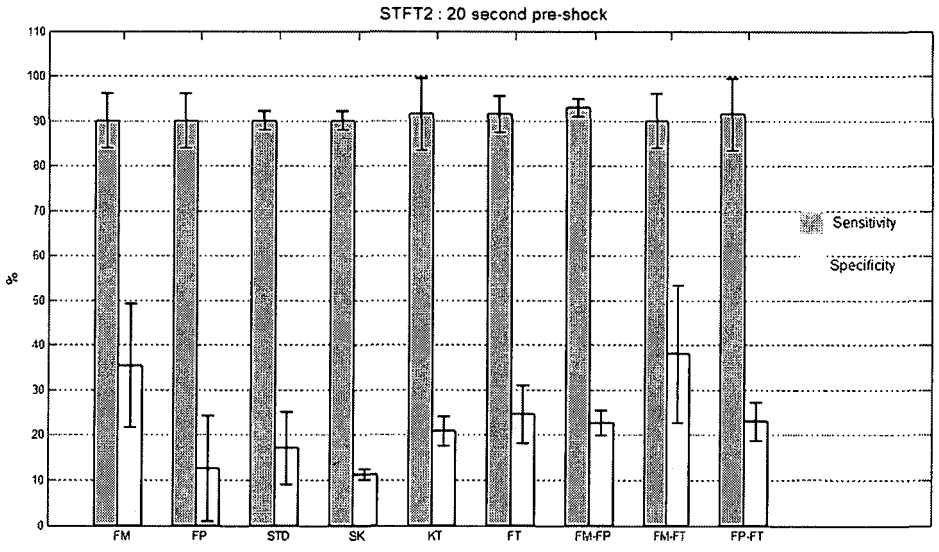

Figure 4-16: The performances of the classifier using the STFT2 power spectrum-based technique (20 second pre-shock)

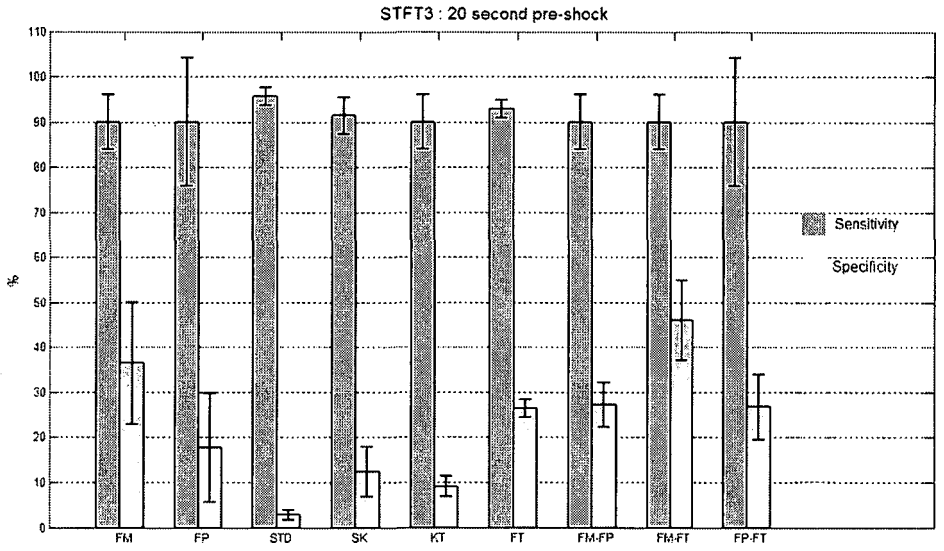

Figure 4-17: The performances of the classifier using the STFT3 power spectrum-based technique (20 second pre-shock)

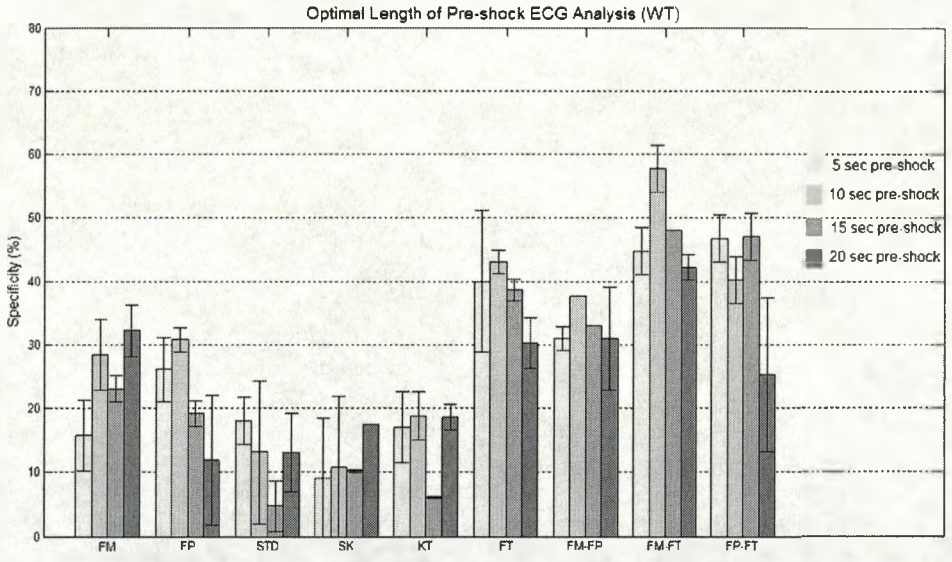

Figure 4-18: The specificities of all experiments based on WT power spectral analysis

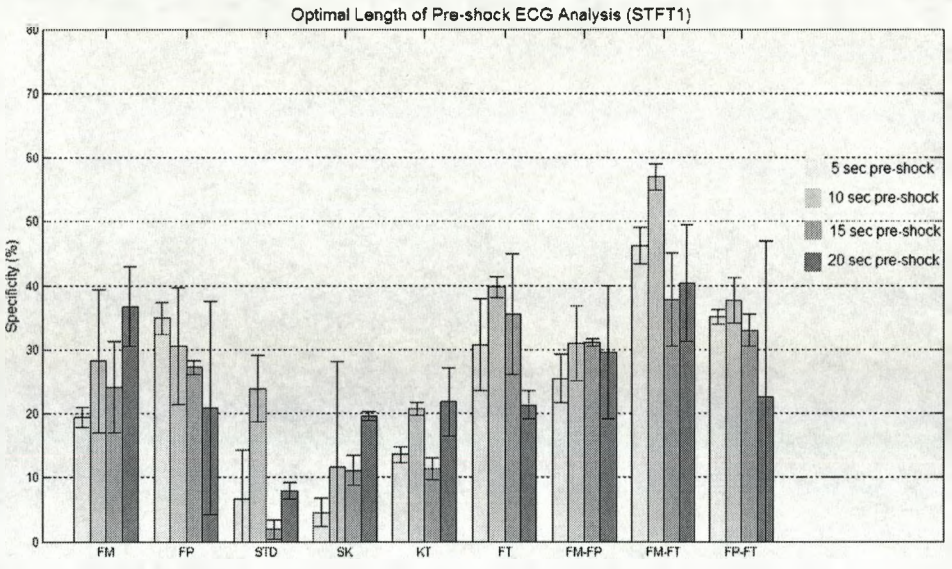

Figure 4-19: The specificities of all experiments based on STFT1 power spectral analysis

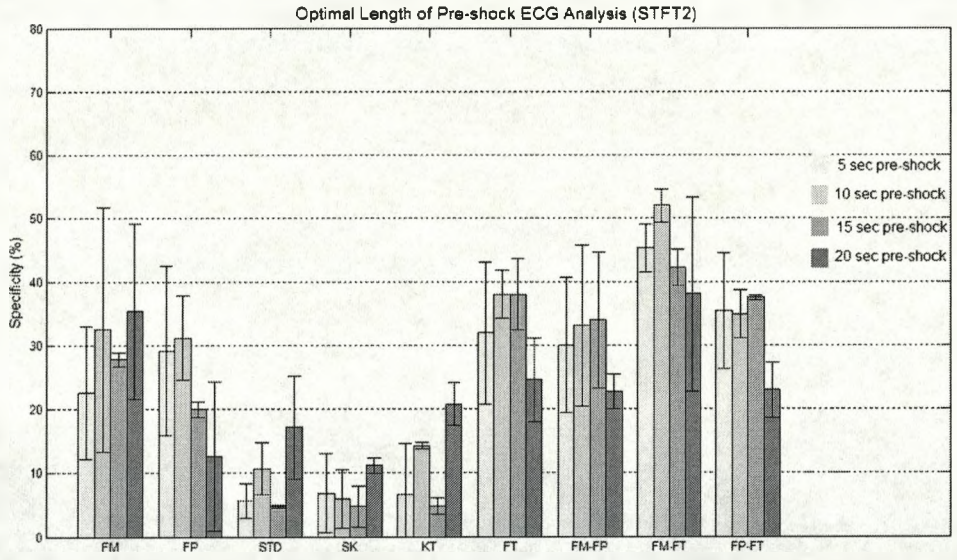

Figure 4-20: The specificities of all experiments based on STFT2 power spectral analysis

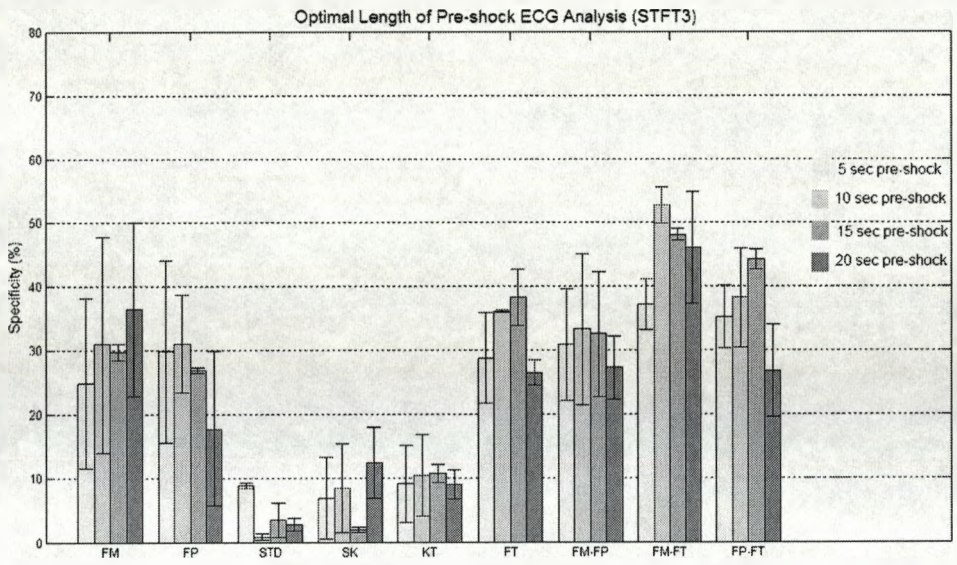

Figure 4-21: The specificities of all experiments based on STFT3 power spectral analysis

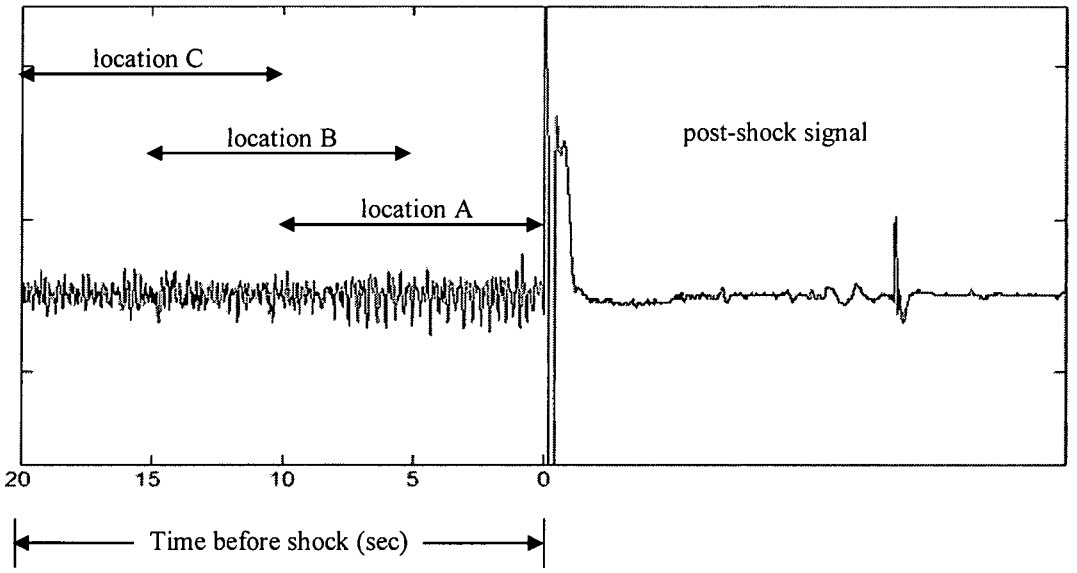

Figure 4-22: The positional of pre-shock segments

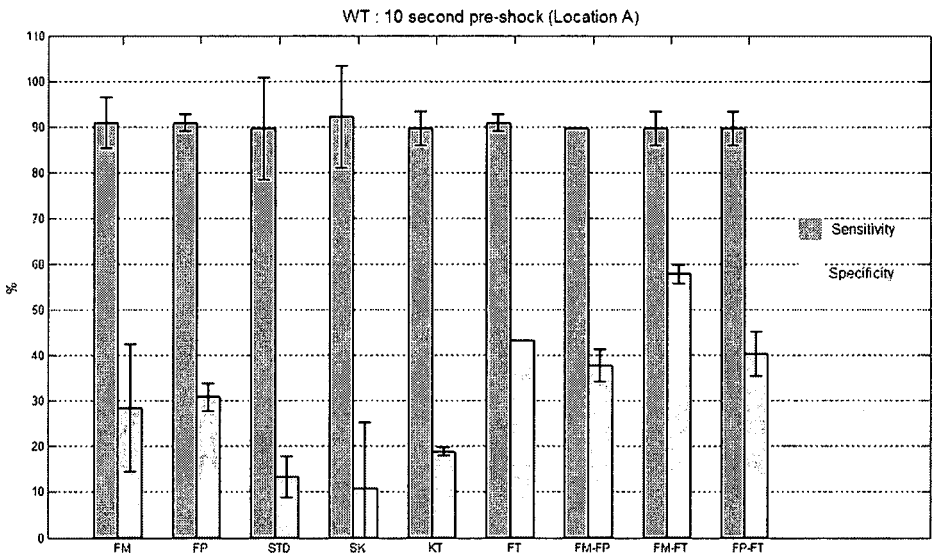

Figure 4-23: The performances of the classifier using the WT power spectrum-based technique (location A)

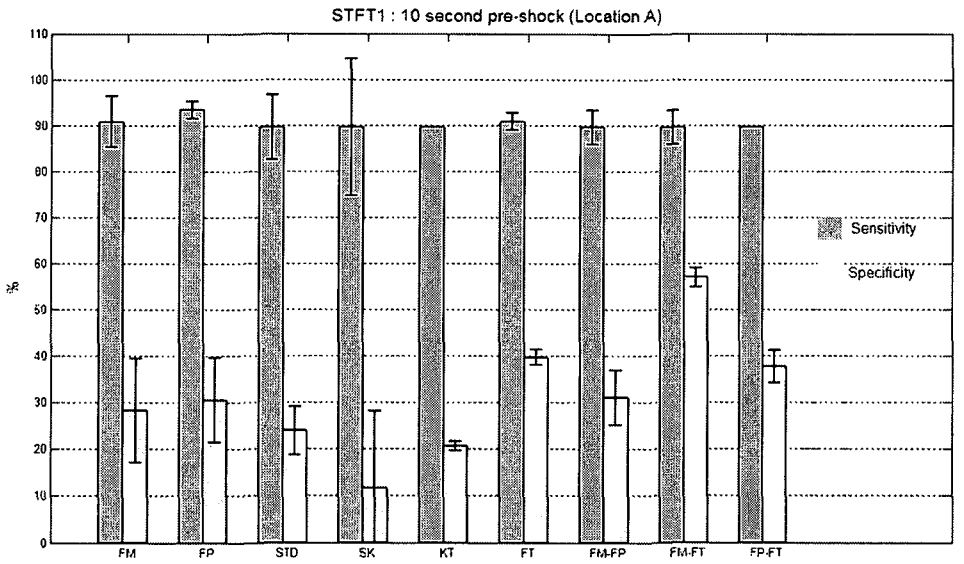

Figure 4-24: The performances of the classifier using the STFT1 power spectrum-based technique (location A)

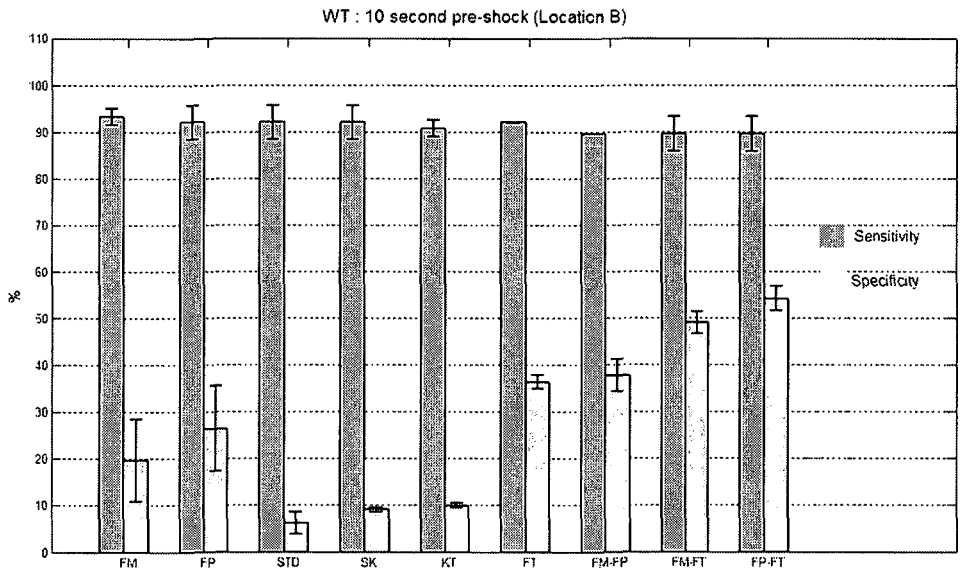

Figure 4-25: The performances of the classifier using the WT power spectrum-based technique (location B)

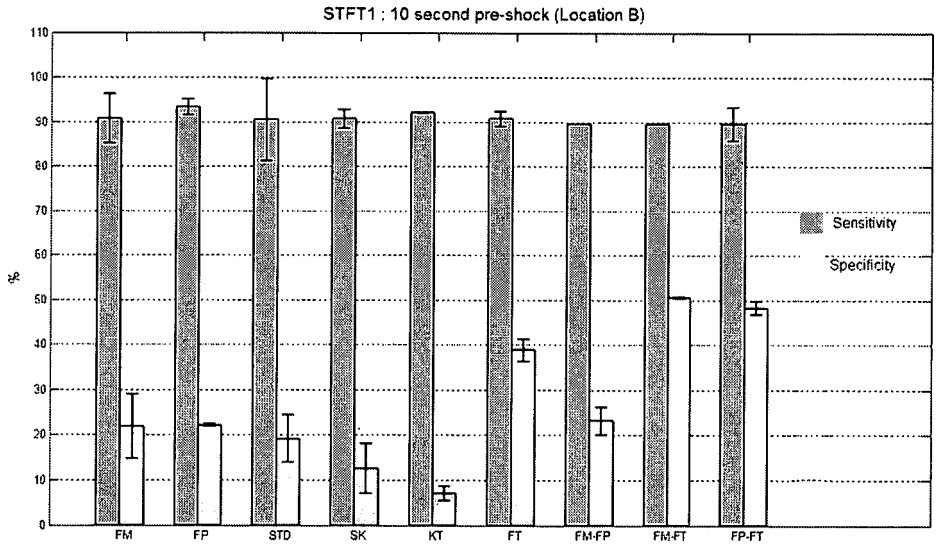

Figure 4-26: The performances of the classifier using the STFT1 power spectrum-based technique (location B)

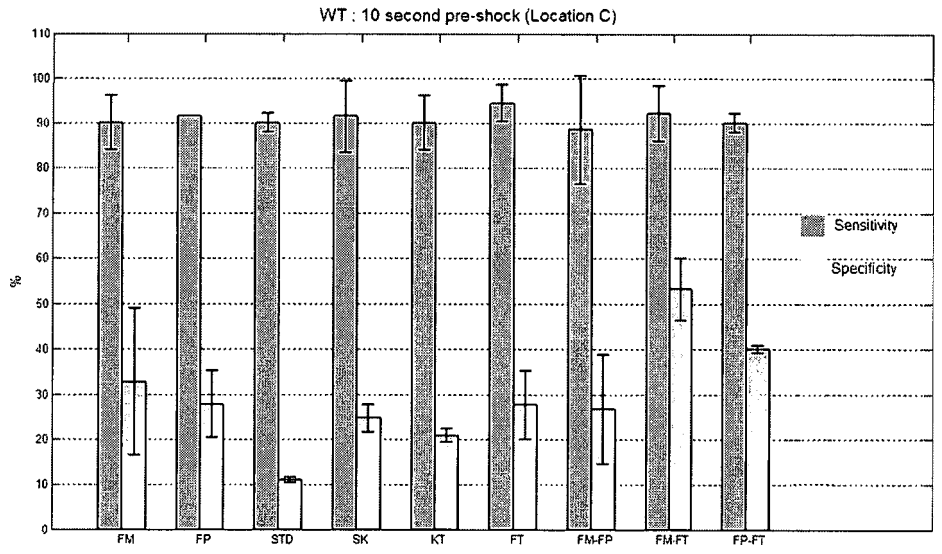

Figure 4-27: The performances of the classifier using the WT power spectrum-based technique (location C)

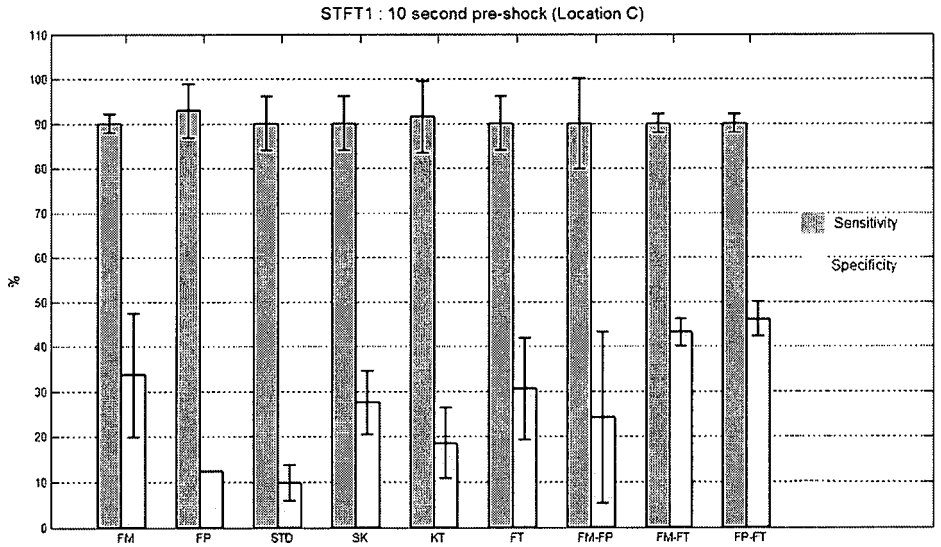

Figure 4-28: The performances of the classifier using the STFT1 power spectrum-based technique (location C)

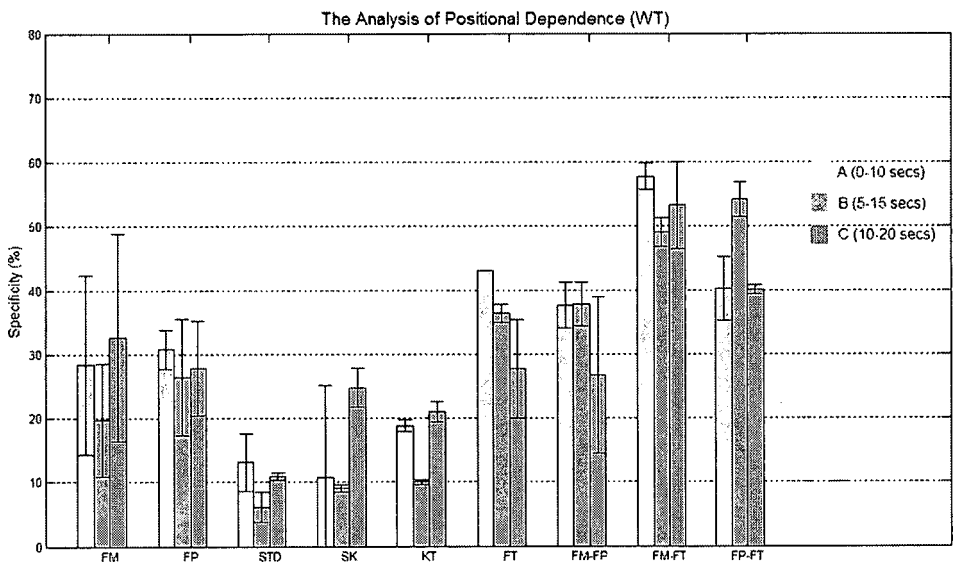

Figure 4-29: The results of positional dependence analysis of WT power spectrum-based technique

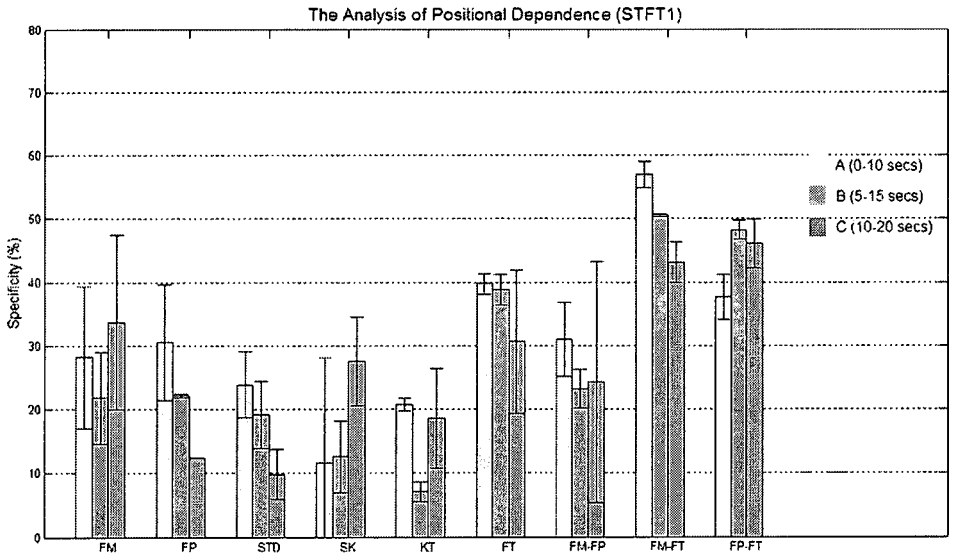

Figure 4-30: The results of positional dependence analysis of STFT1 power spectrum-based technique

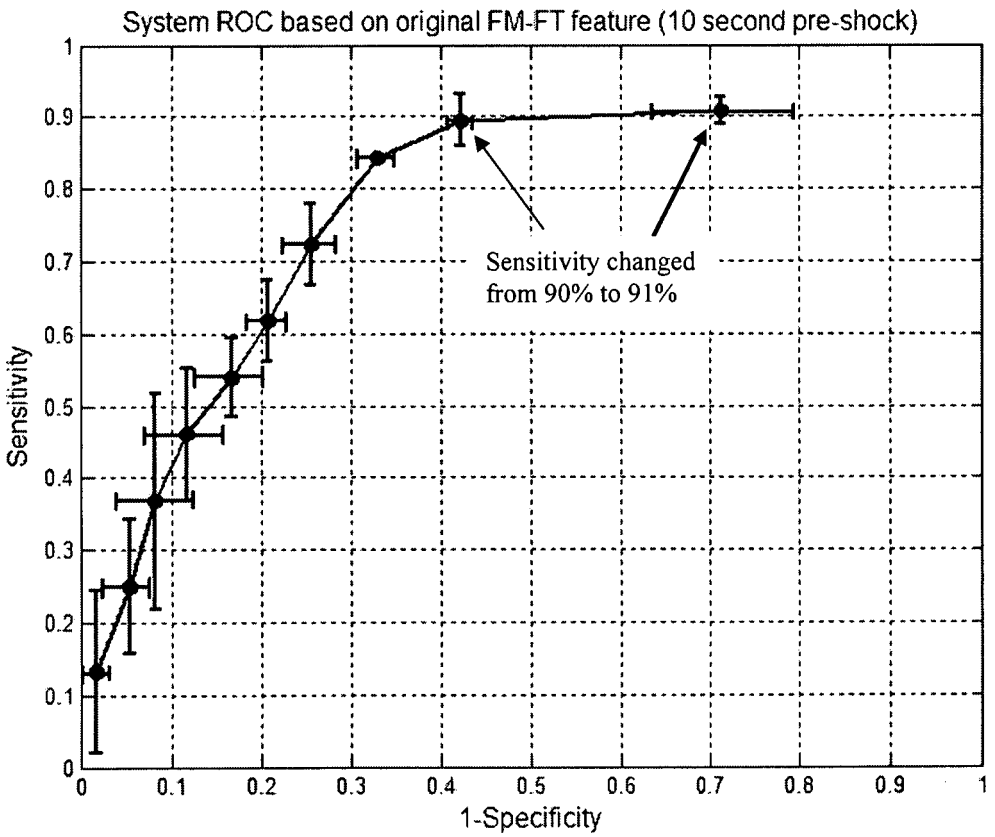

Figure 4-31: The system ROC of the best classifier associated with the original feature sets

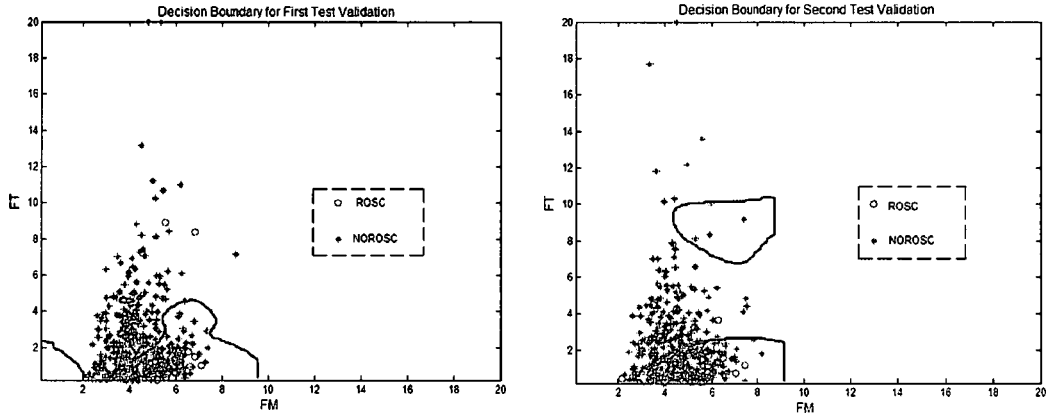

Figure 4-32: The decision boundaries for two test validations associated with 90% test sensitivity: (a) first test validation, (b) second validation

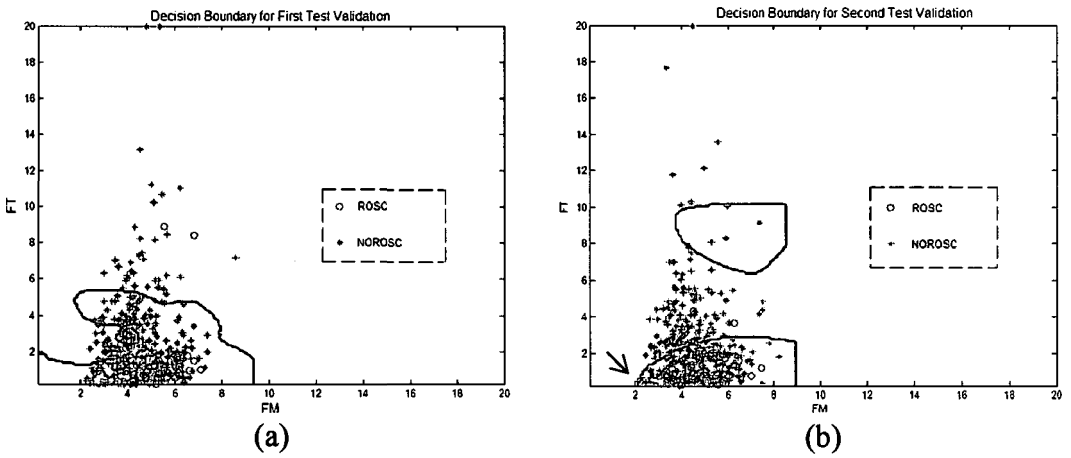

Figure 4-33: The decision boundaries for two test validations associated with 91% test sensitivity: (a) first test validation, (b) second validation

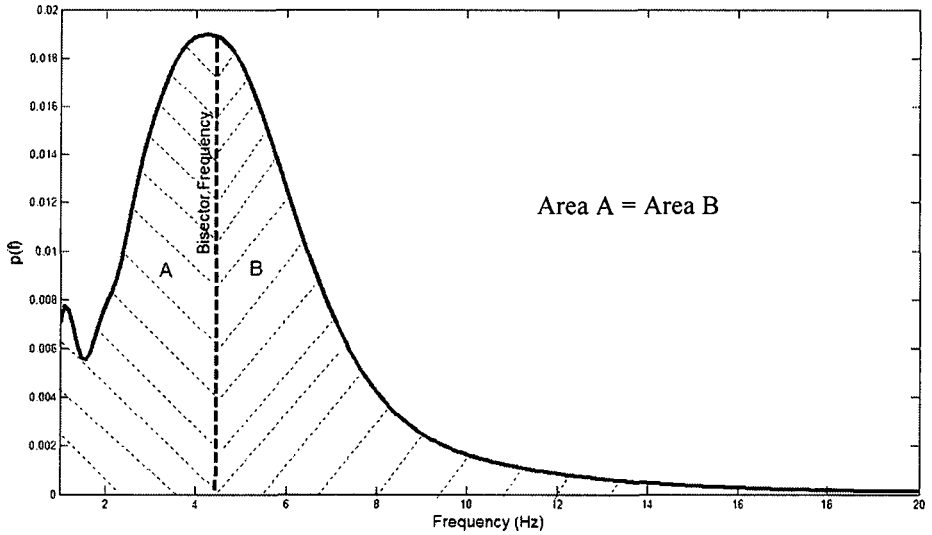

Figure 4-34: An illustration of bisector frequency

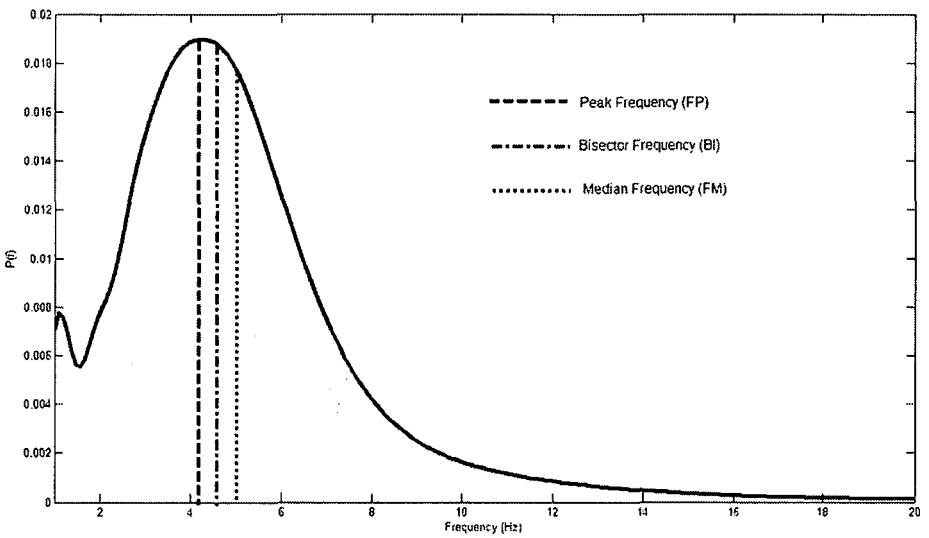

Figure 4-35: The location of the bisector frequency compared to that of peak frequency and median frequency

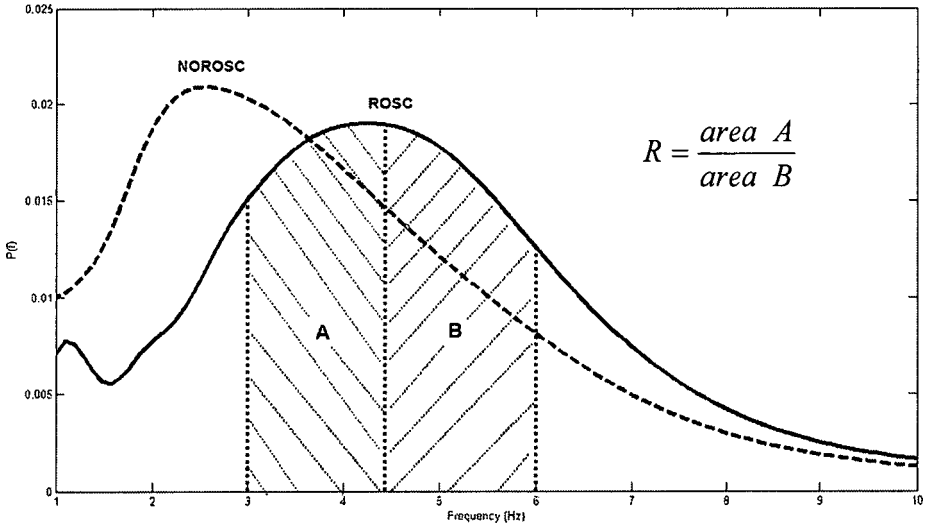

Figure 4-36: The illustration of spectrum ratio (R)

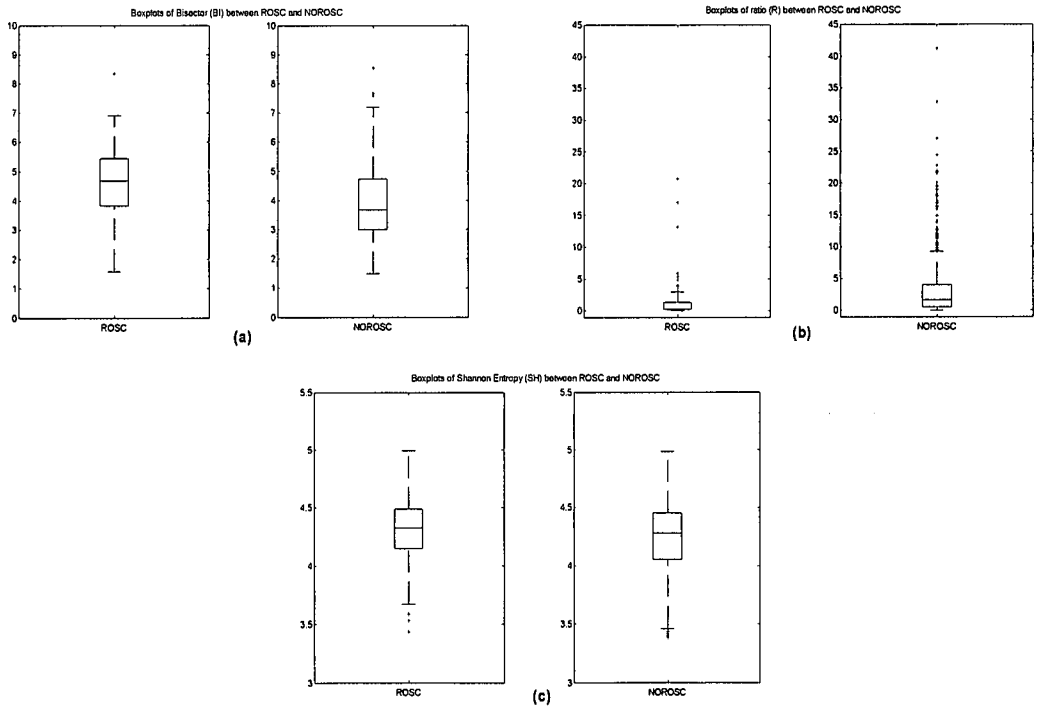

Figure 4-37: The boxplots of BI, R, and SH using WT power spectrum-based technique (5 second pre-shock)

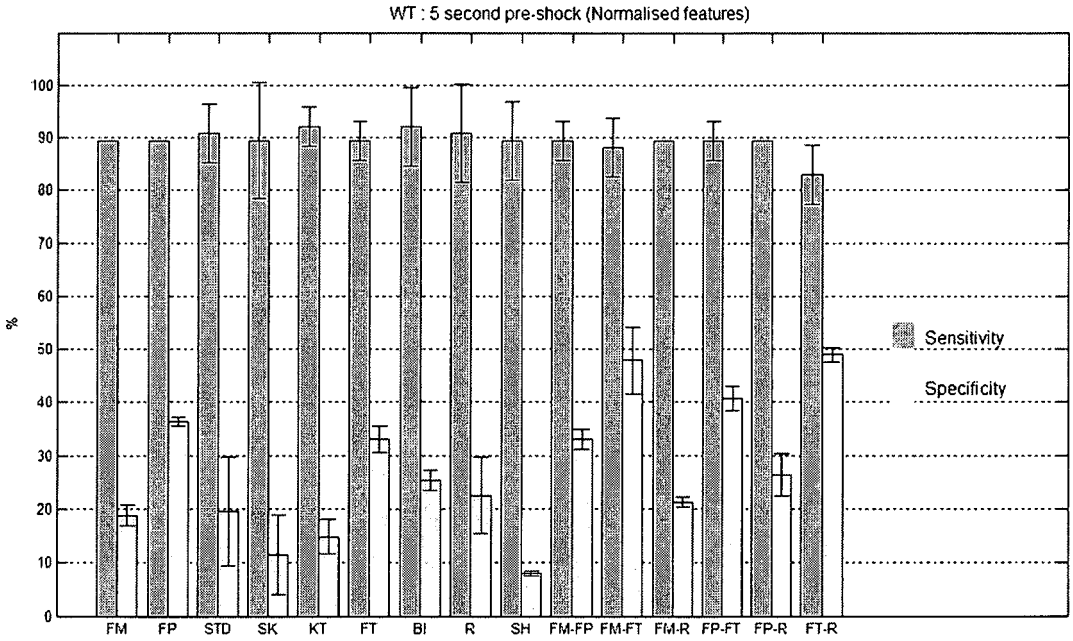

Figure 4-38: The performances of the classifier using WT power spectrum-based technique (5 second pre-shock)

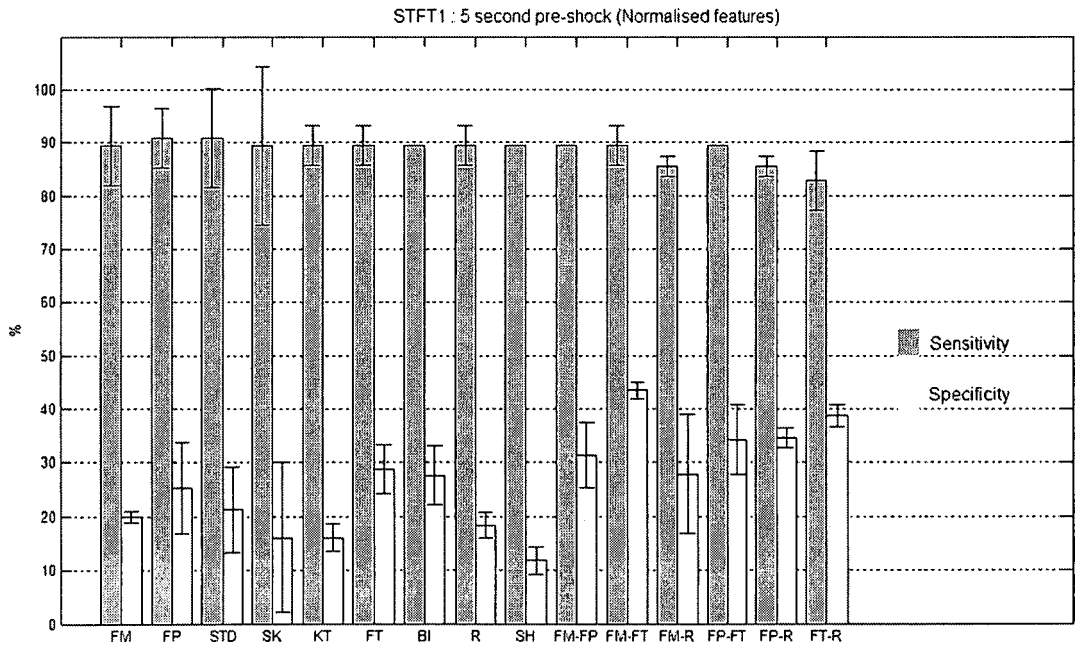

Figure 4-39: The performances of the classifier using STFT1 power spectrum-based technique (5 second pre-shock)

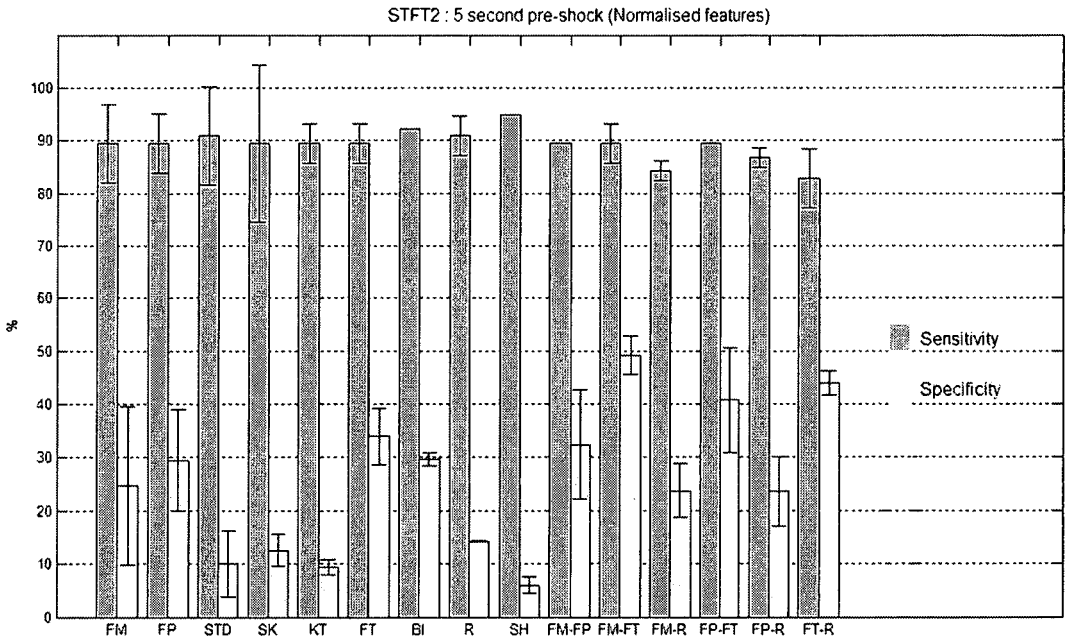

Figure 4-40: The performances of the classifier using STFT2 power spectrum-based technique (5 second pre-shock)

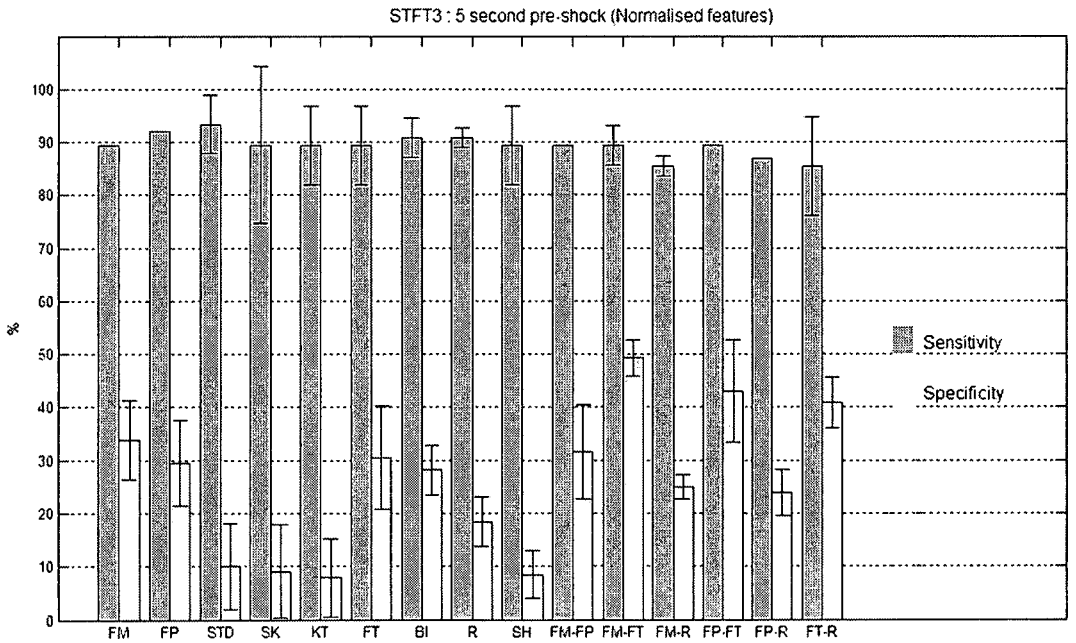

Figure 4-41: The performances of the classifier using STFT3 power spectrum-based technique (5 second pre-shock)

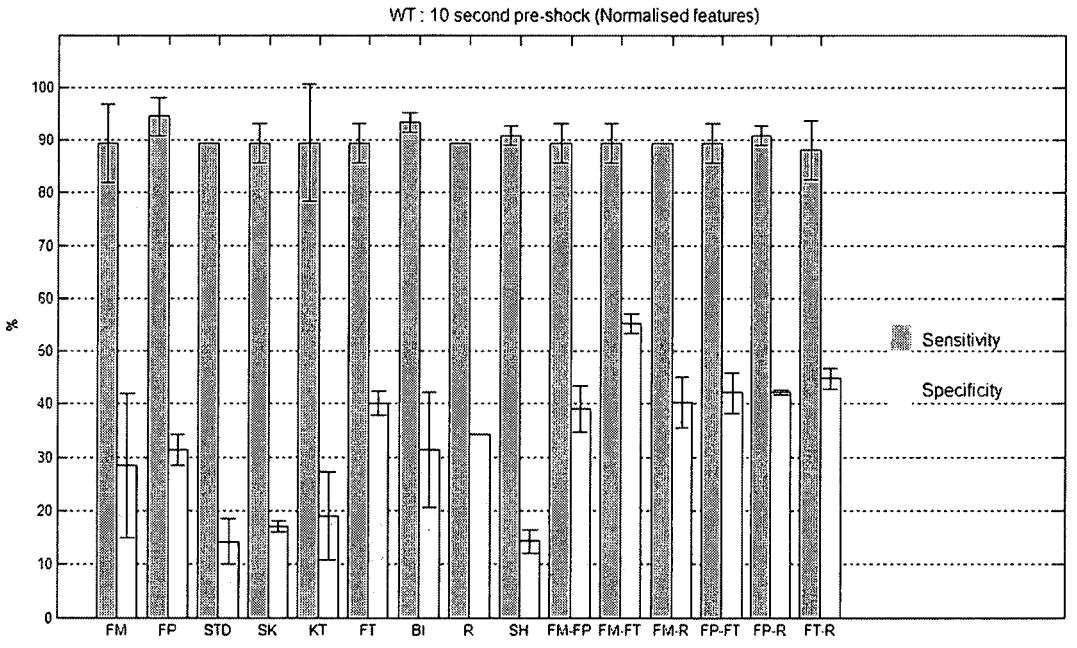

Figure 4-42: The performances of the classifier using WT power spectrum-based technique (10 second pre-shock)

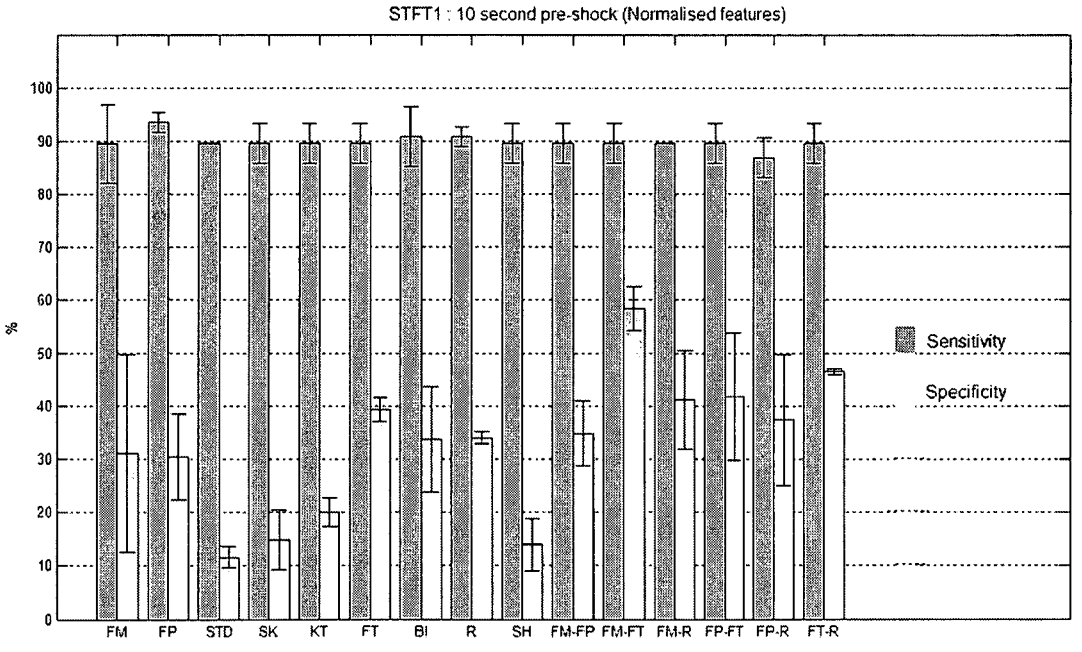

Figure 4-43: The performances of the classifier using STFT1 power spectrum-based technique (10 second pre-shock)

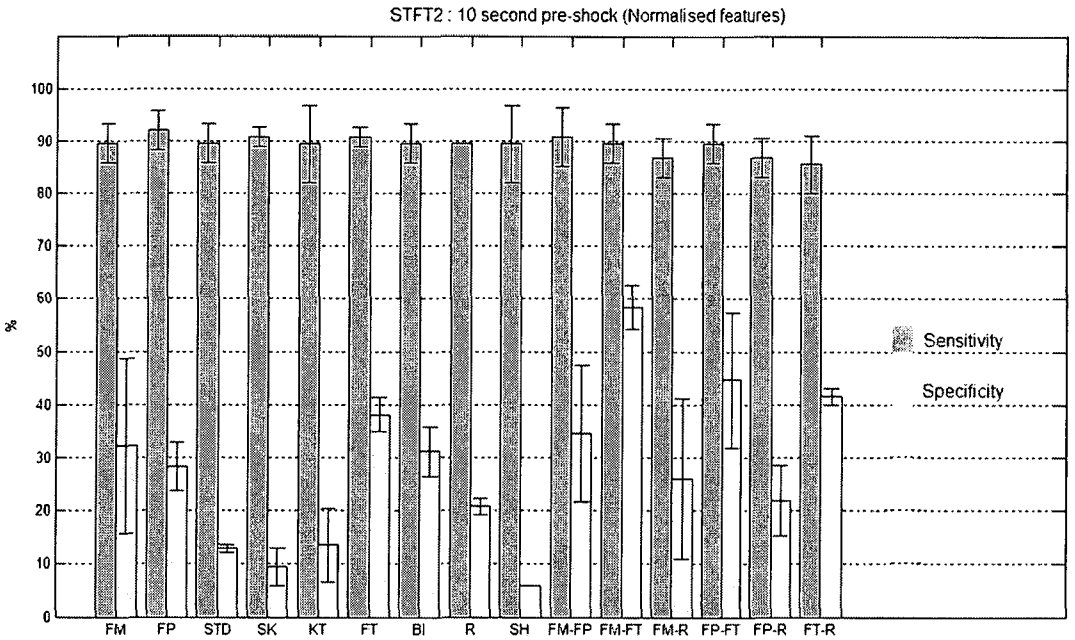

Figure 4-44: The performances of the classifier using STFT2 power spectrum-based technique (10 second pre-shock)

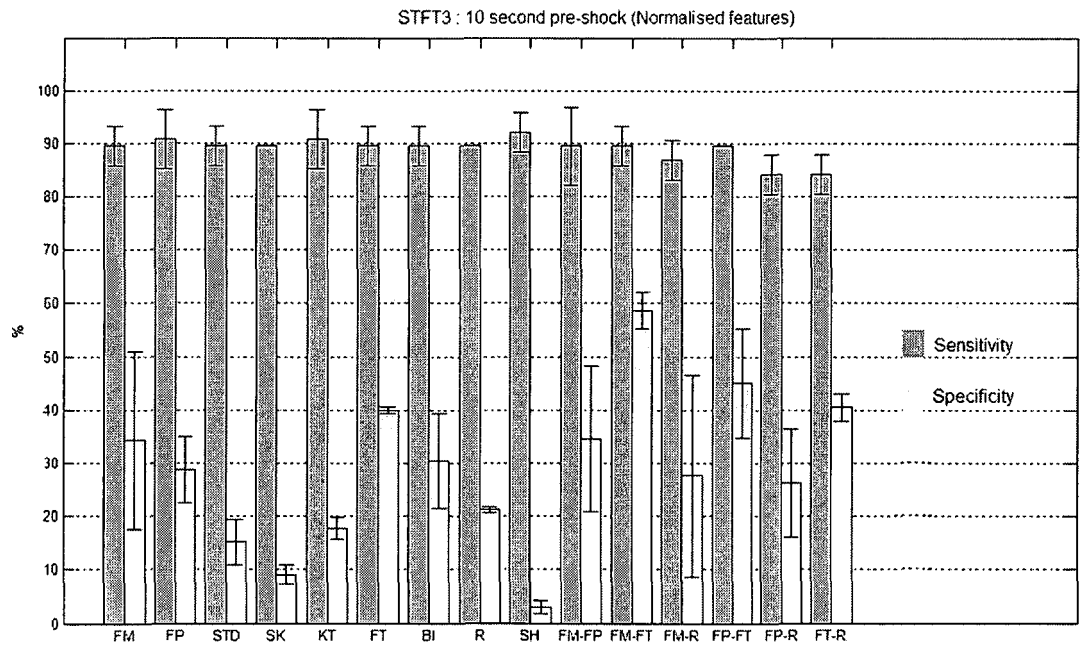

Figure 4-45: The performances of the classifier using STFT3 power spectrum-based technique (10 second pre-shock)

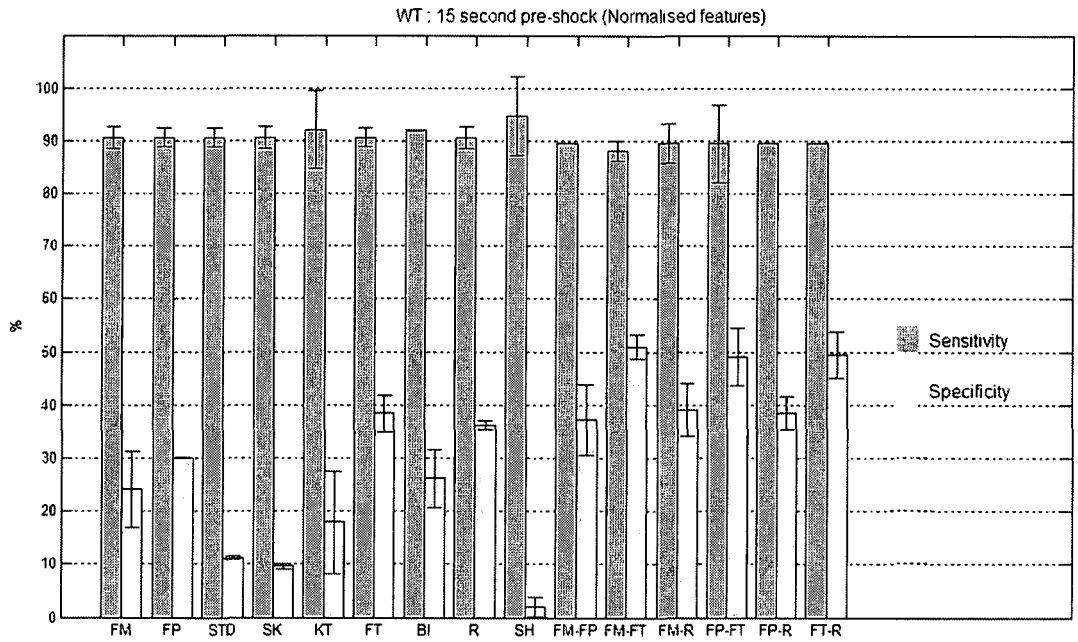

Figure 4-46: The performances of the classifier using WT power spectrum-based technique (15 second pre-shock)

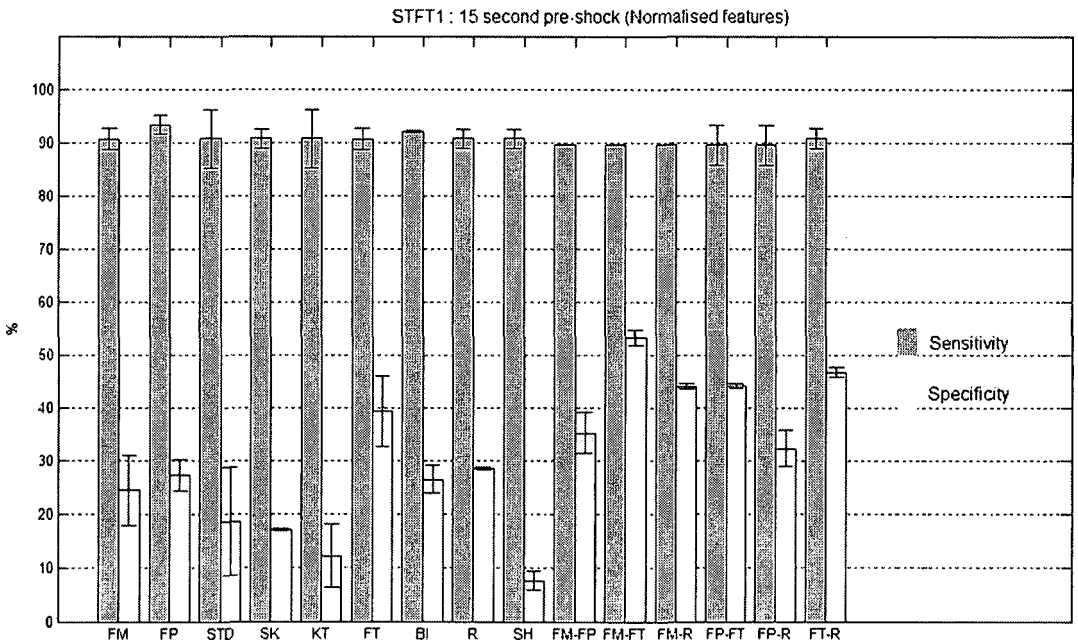

Figure 4-47: The performances of the classifier using STFT1 power spectrum-based technique (15 second pre-shock)

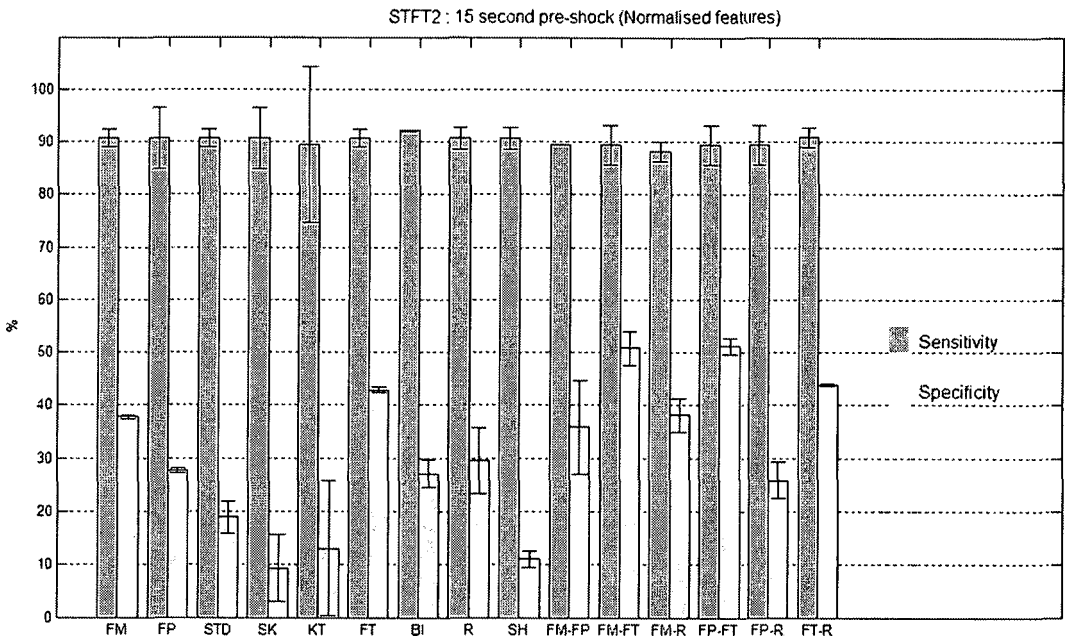

Figure 4-48: The performances of the classifier using STFT2 power spectrum-based technique (15 second pre-shock)

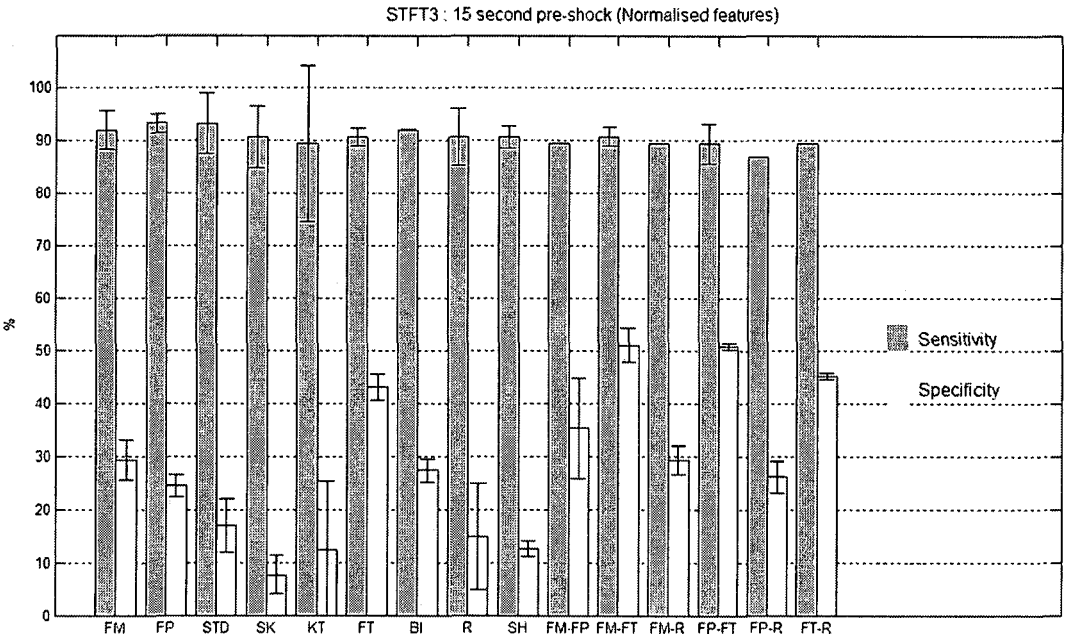

Figure 4-49: The performances of the classifier using STFT3 power spectrum-based technique (15 second pre-shock)

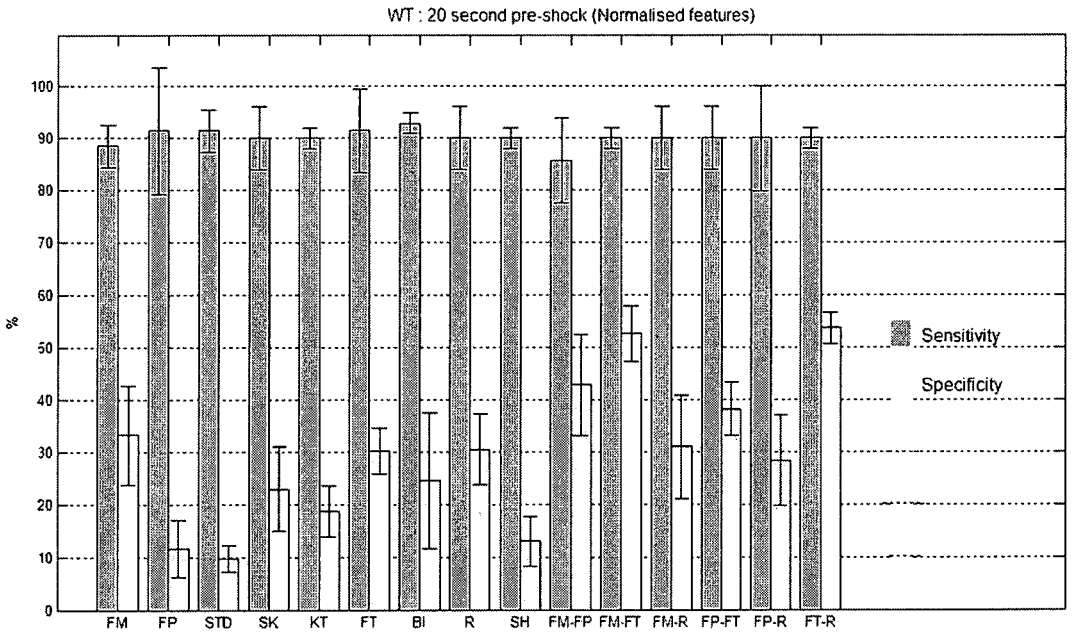

Figure 4-50: The performances of the classifier using WT power spectrum-based technique (20 second pre-shock)

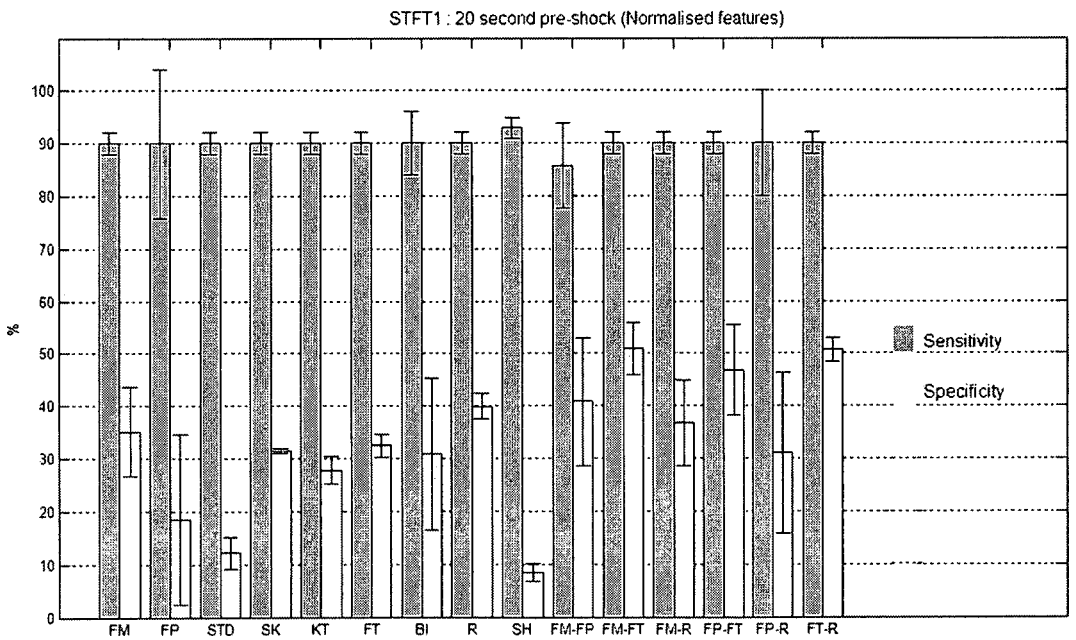

Figure 4-51: The performances of the classifier using STFT1 power spectrum-based technique (20 second pre-shock)

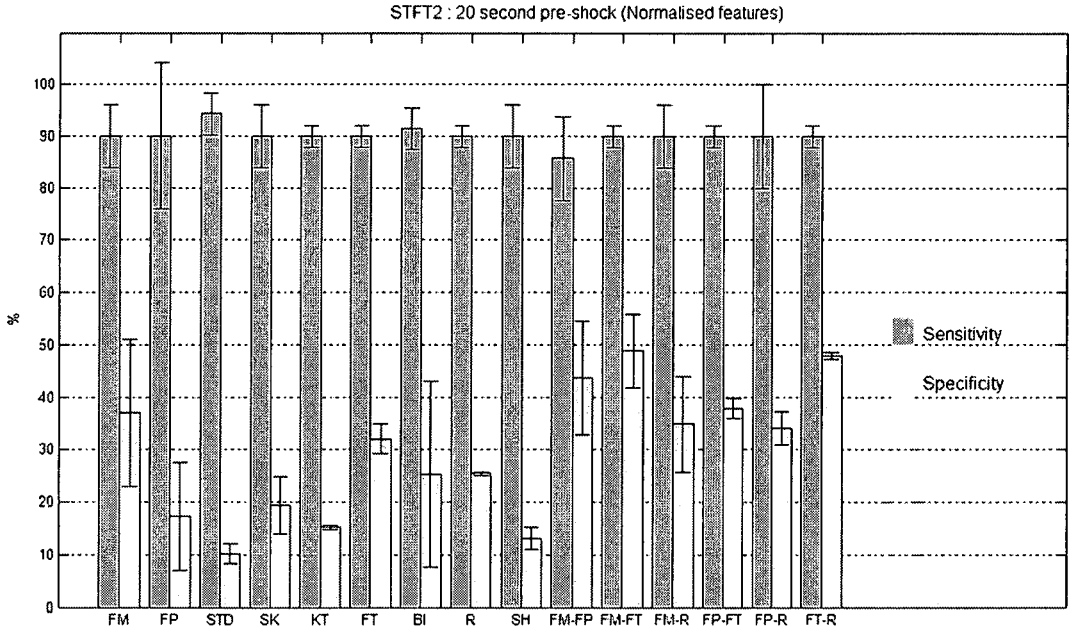

Figure 4-52: The performances of the classifier using STFT2 power spectrum-based technique (20 second pre-shock)

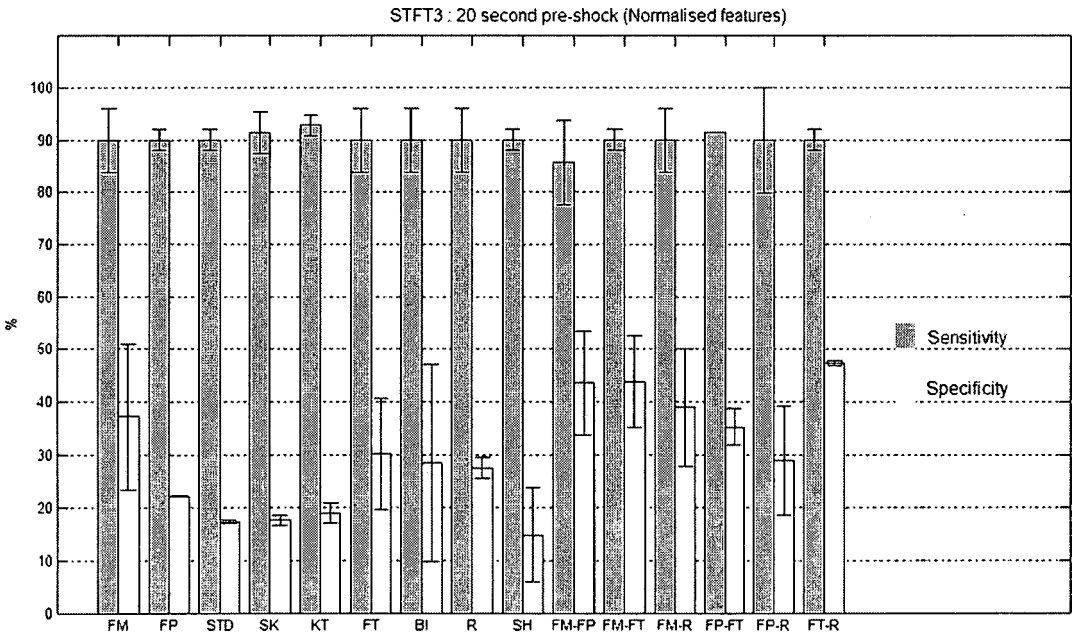

Figure 4-53: The performances of the classifier using STFT3 power spectrum-based technique (20 second pre-shock)

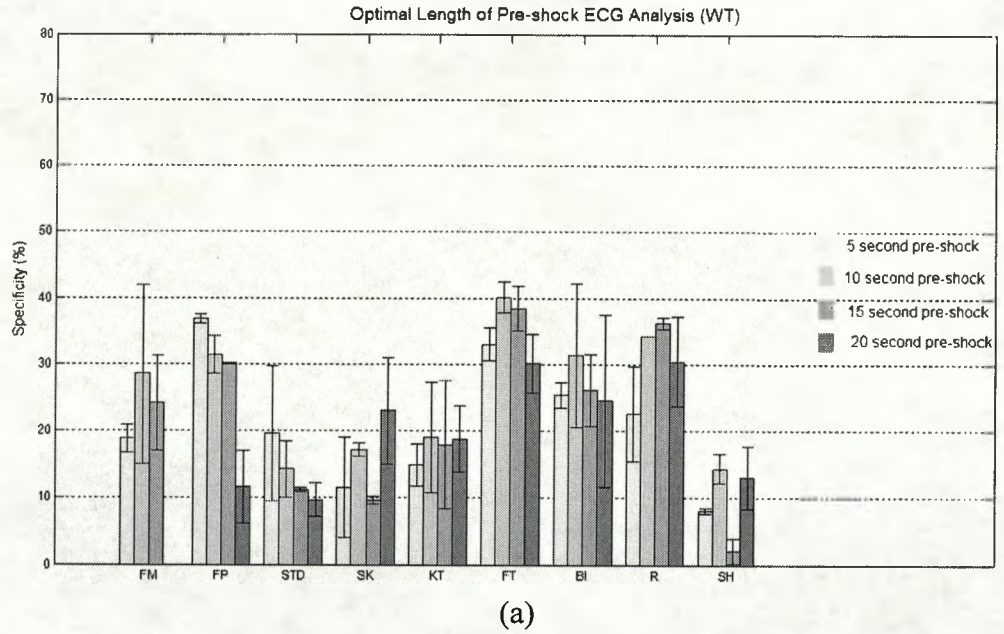

(a)

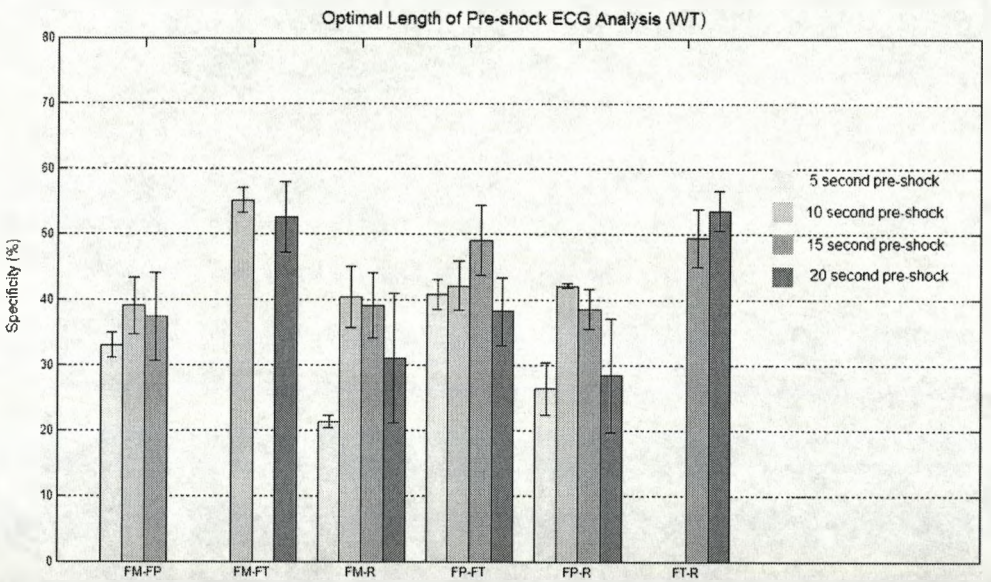

(b)

Figure 4-54: The specificities of all experiments based on WT power spectral analysis: (a) 1D features, (b) 2D features

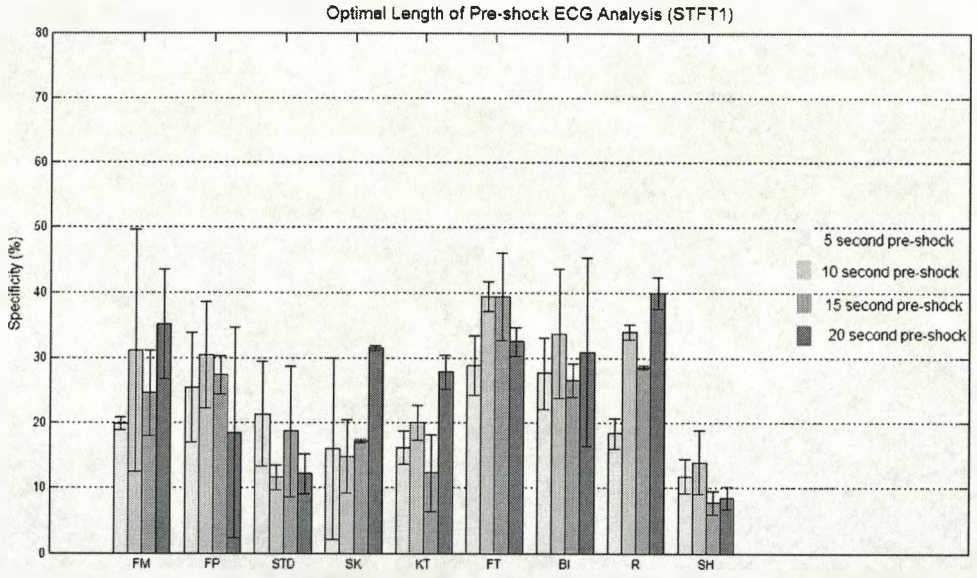

(a)

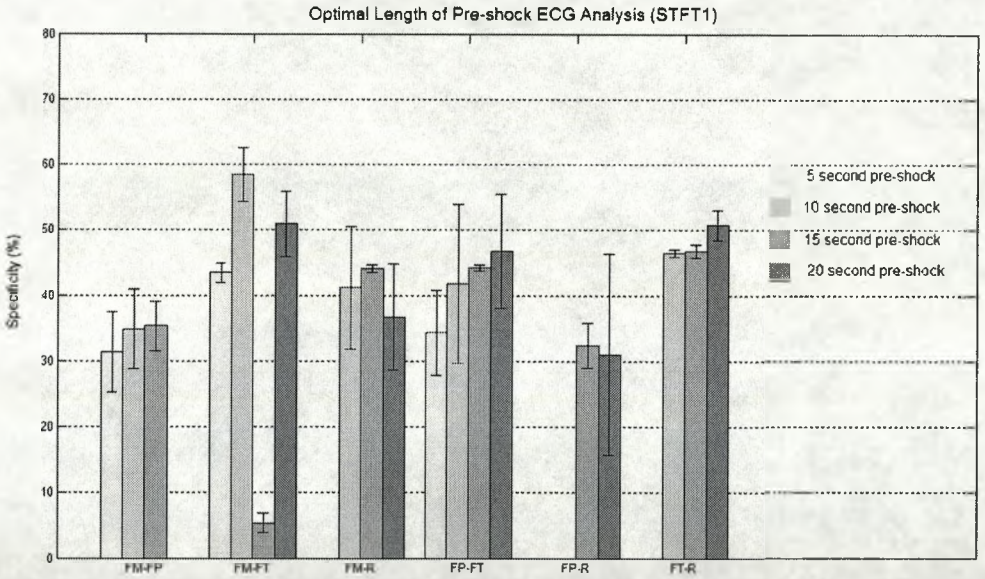

(b)

Figure 4-55: The specificities of all experiments based on STFT1 power spectral analysis: (a) 1D features, (b) 2D features

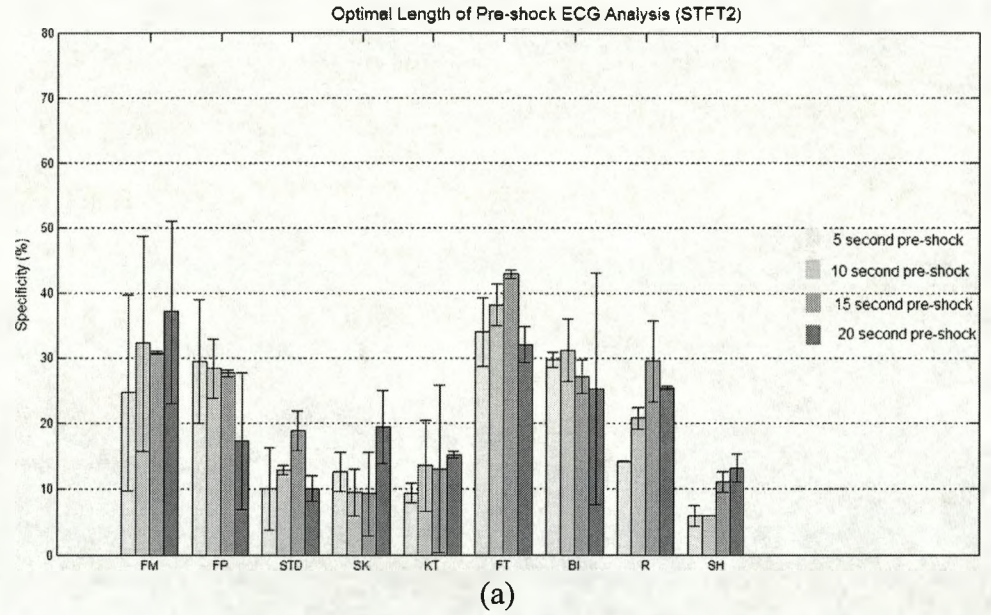

(a)

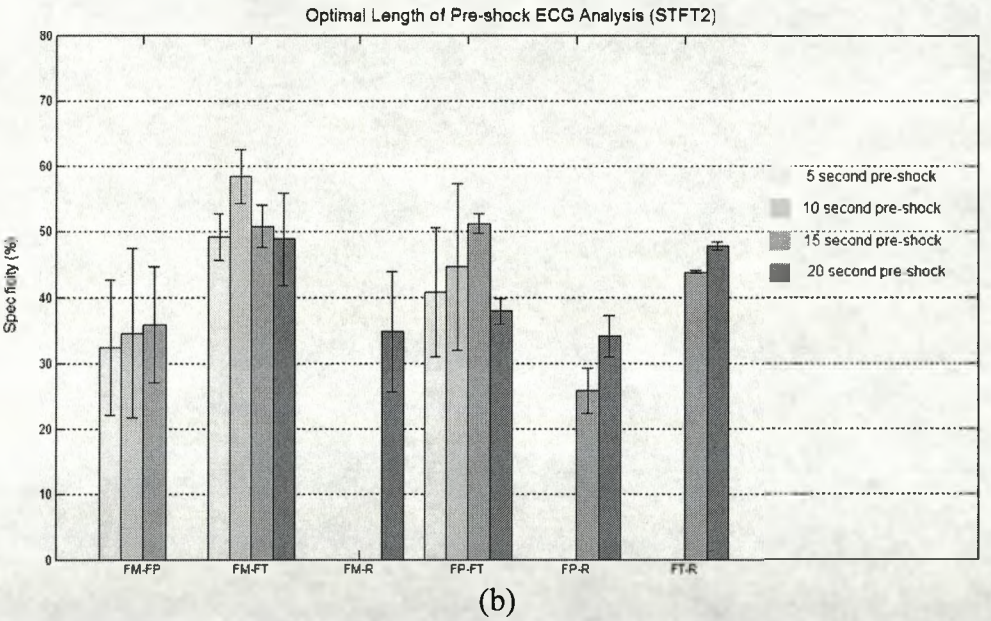

(b)

Figure 4-56: The specificities of all experiments based on STFT2 power spectral analysis: (a) 1D features, (b) 2D features

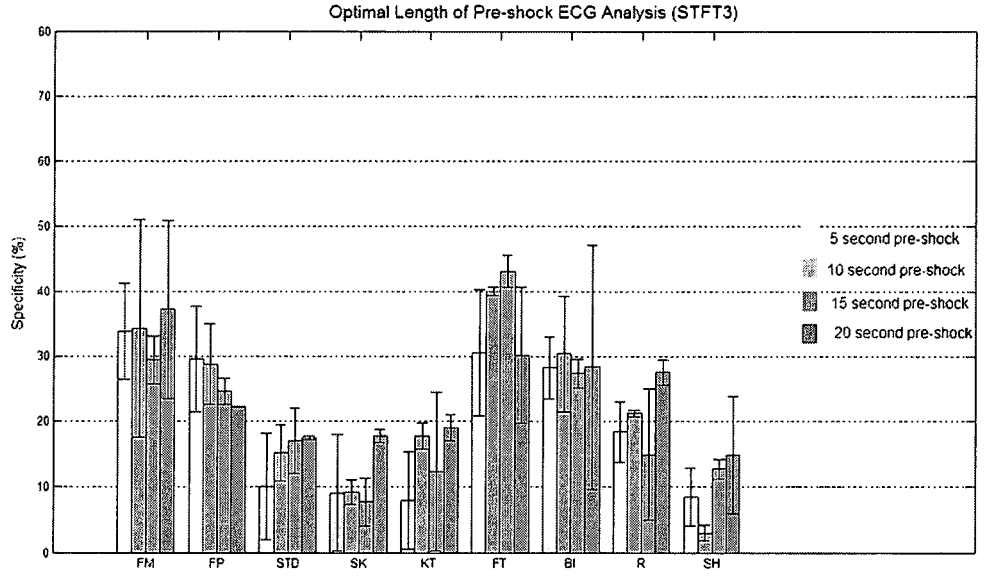

(a)

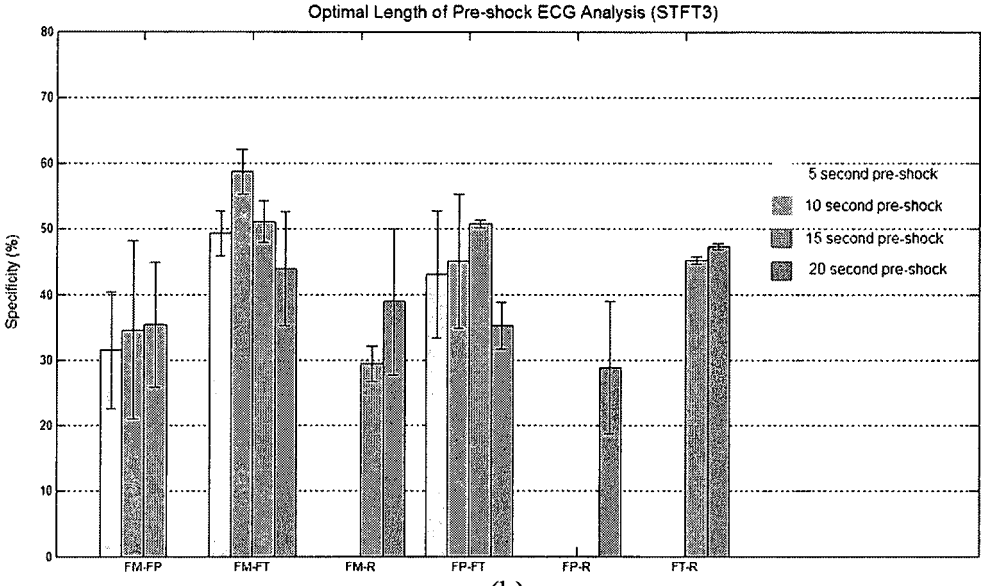

(b)

Figure 4-57: The specificities of all experiments based on STFT3 power spectral analysis: (a) 1D features, (b) 2D features

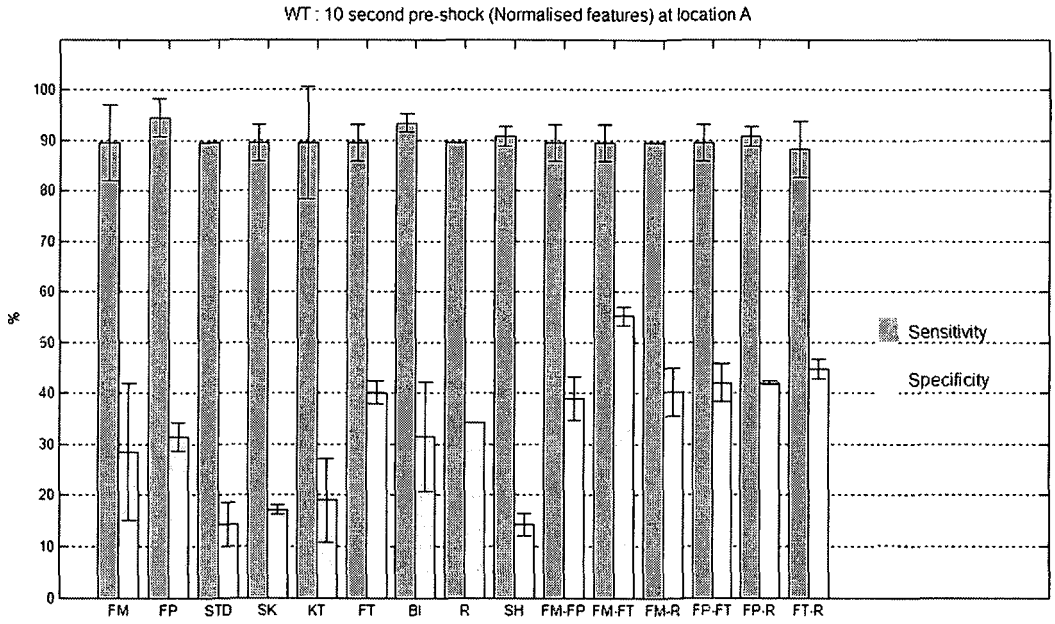

Figure 4-58: The performances of the classifier using the WT power spectrum-based technique (location A)

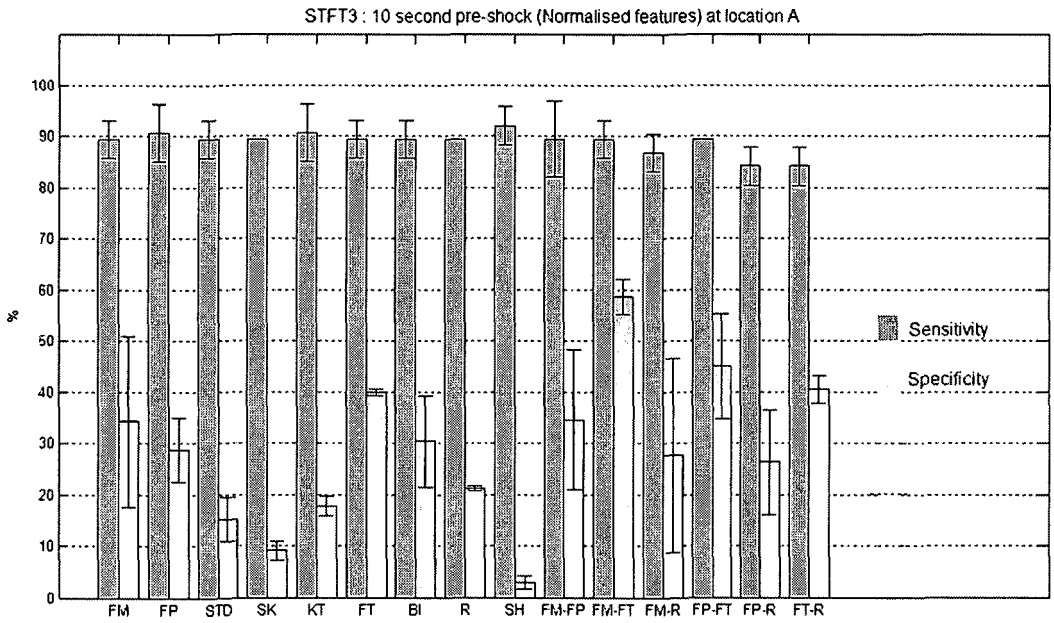

Figure 4-59: The performances of the classifier using the STFT3 power spectrum-based technique (location A)

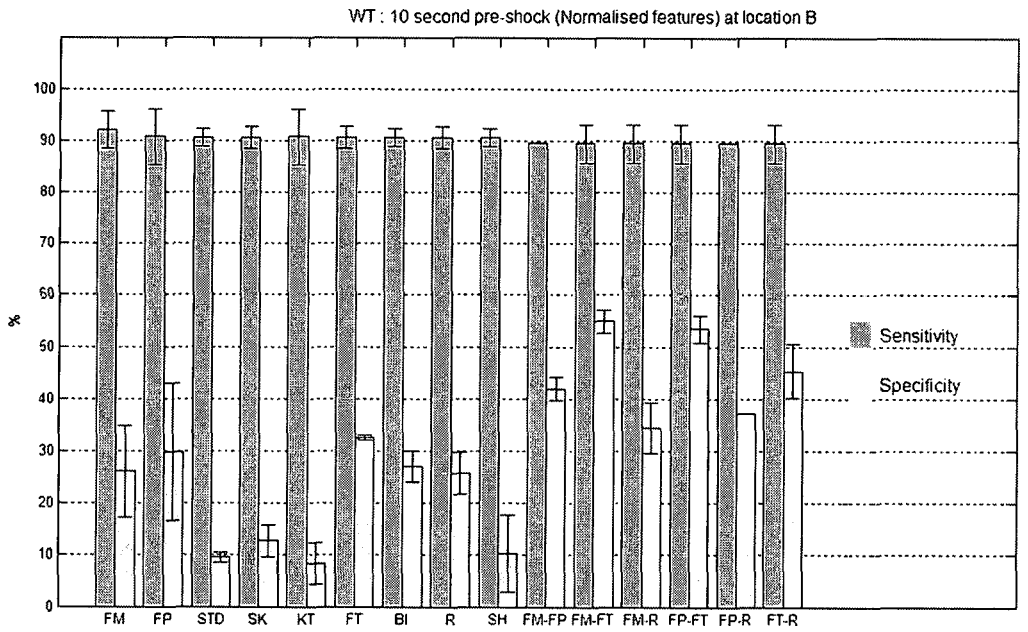

Figure 4-60: The performances of the classifier using the WT power spectrum-based technique (location B)

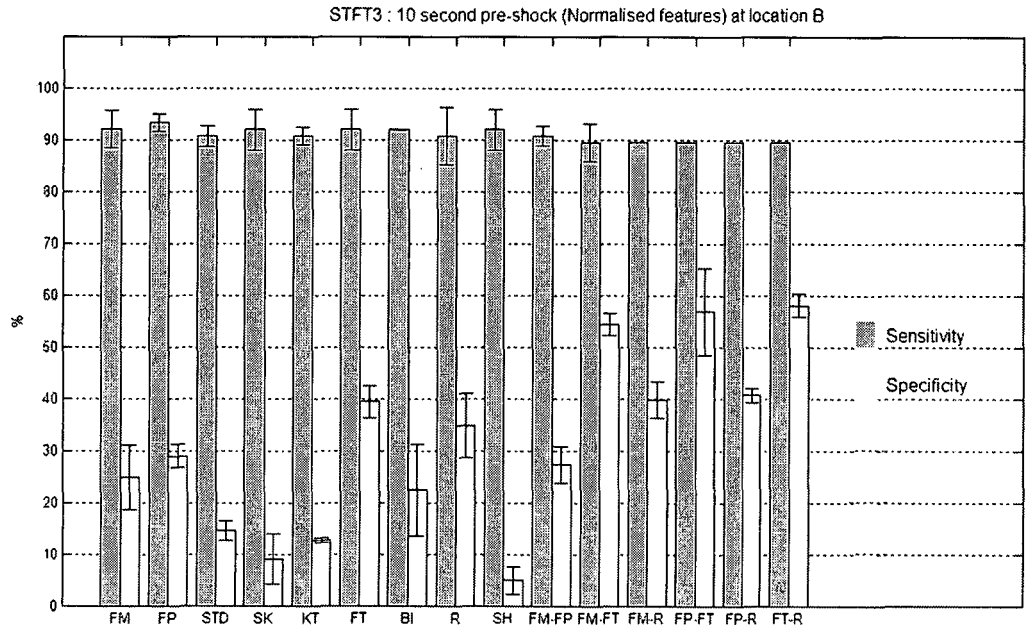

Figure 4-61: The performances of the classifier using the STFT3 power spectrum-based technique (location B)

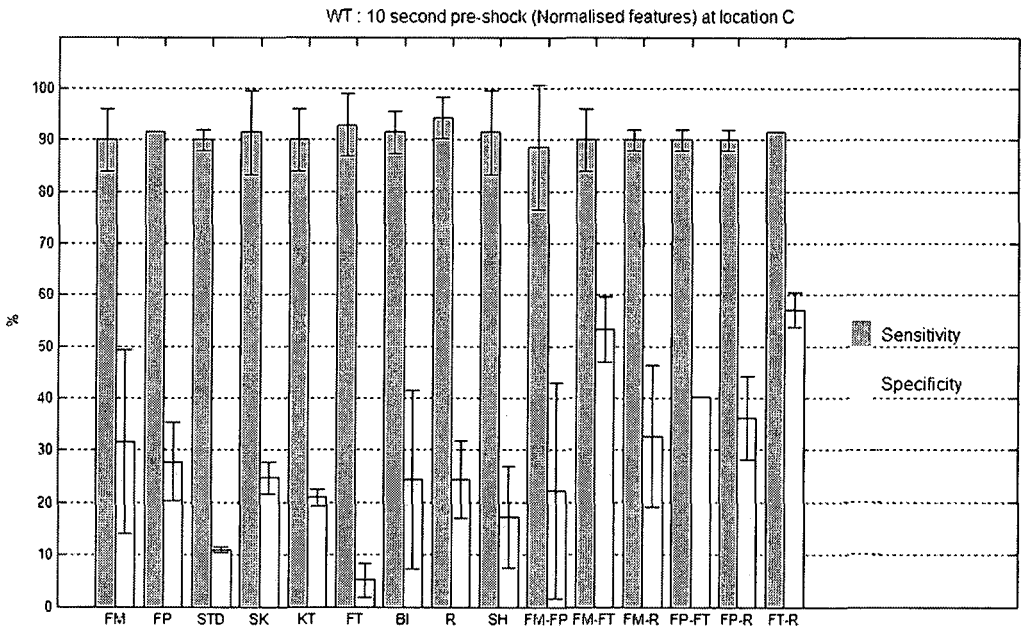

Figure 4-62: The performances of the classifier using the WT power spectrum-based technique (location C)

Figure 4-63: The performances of the classifier using the STFT3 power spectrum-based technique (location C)

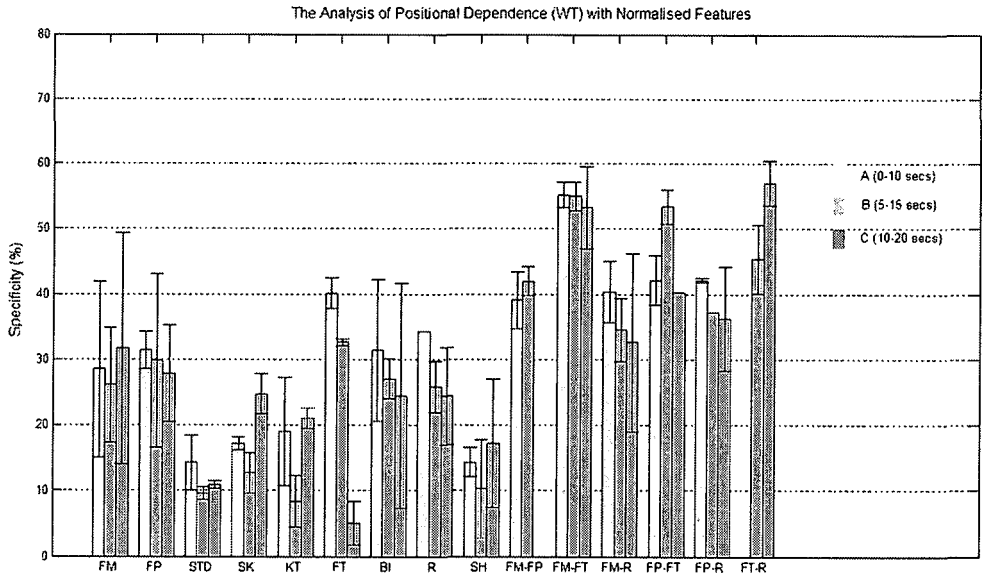

Figure 4-64: The results of positional dependence analysis of WT power spectrum-based technique with normalised features

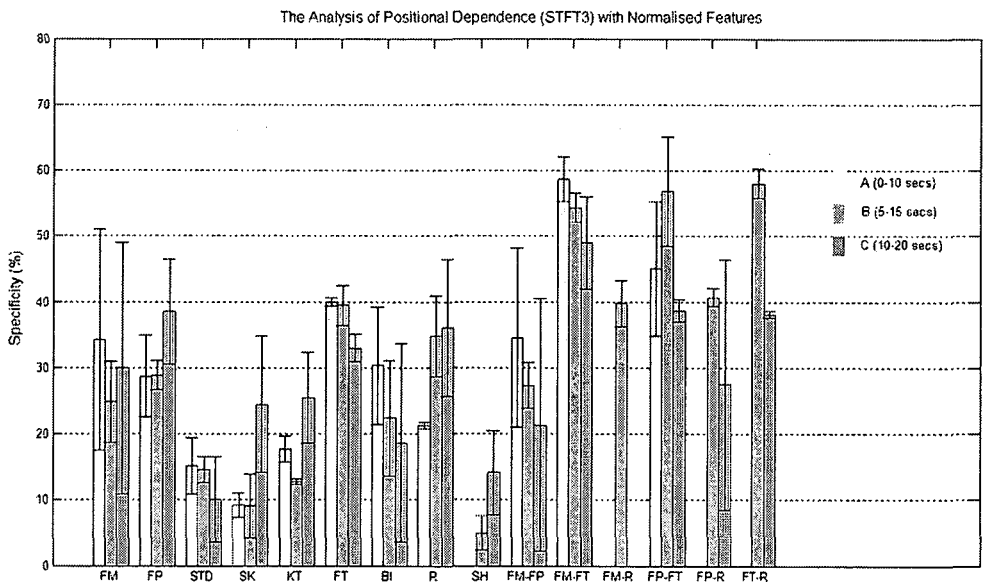

Figure 4-65: The results of positional dependence analysis of STFT3 power spectrum-based technique with normalised features

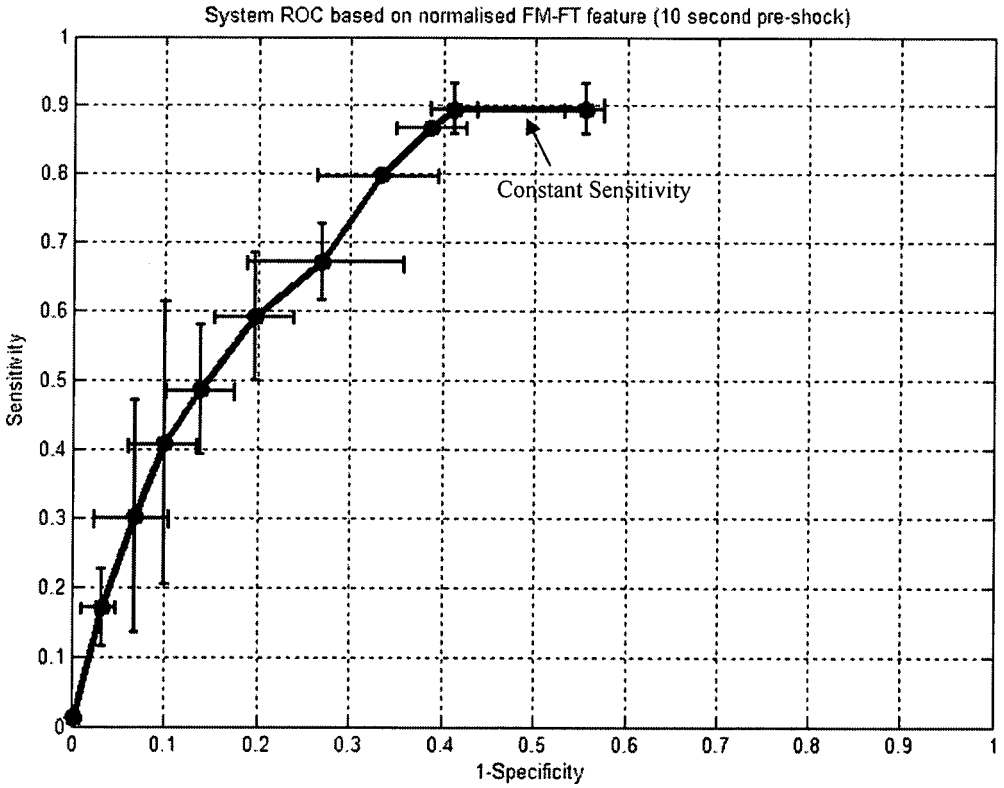

Figure 4-66: The system ROC of the best classifier using normalised feature sets

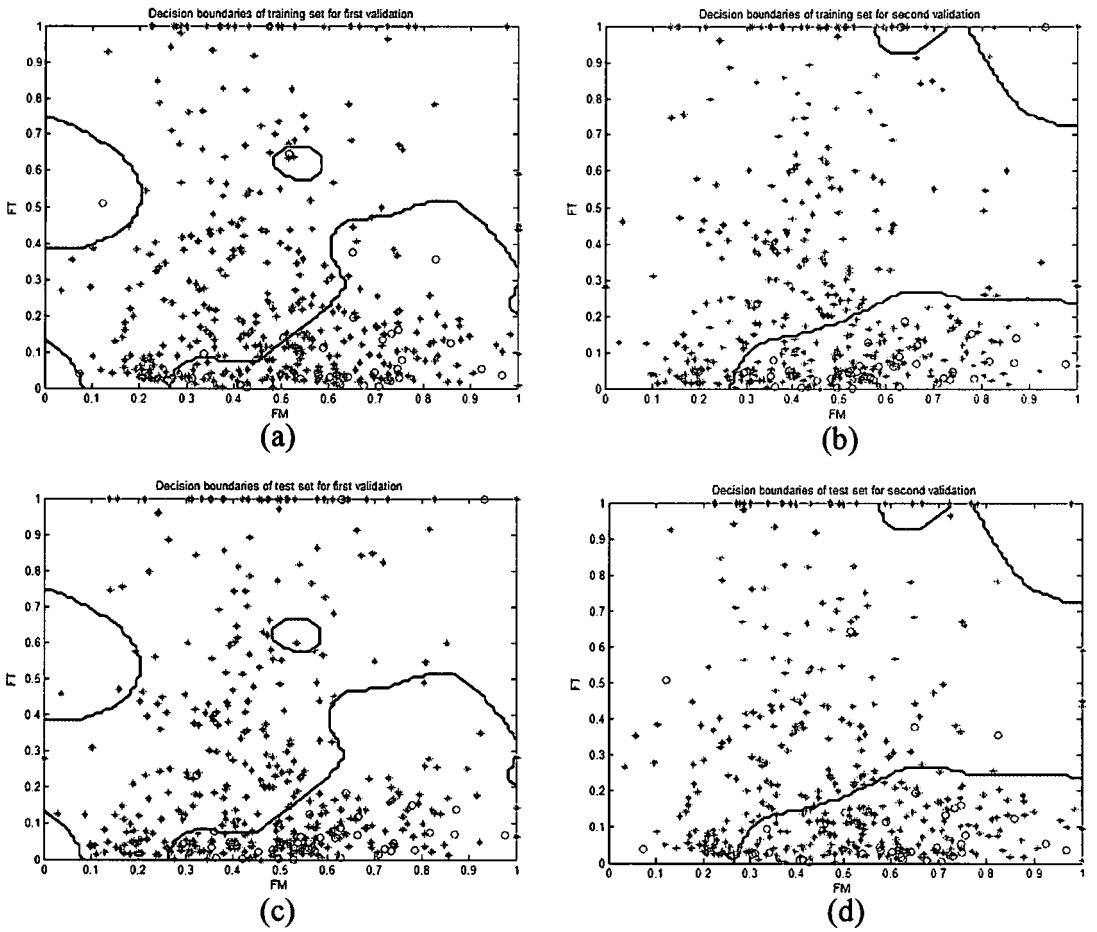

Figure 4-67: The decision boundaries validations associated with the classifier with 95% training sensitivity: (a) training set for first validation, (b) training set for second validation, (c) test set for first validation, (d) test set for second validation

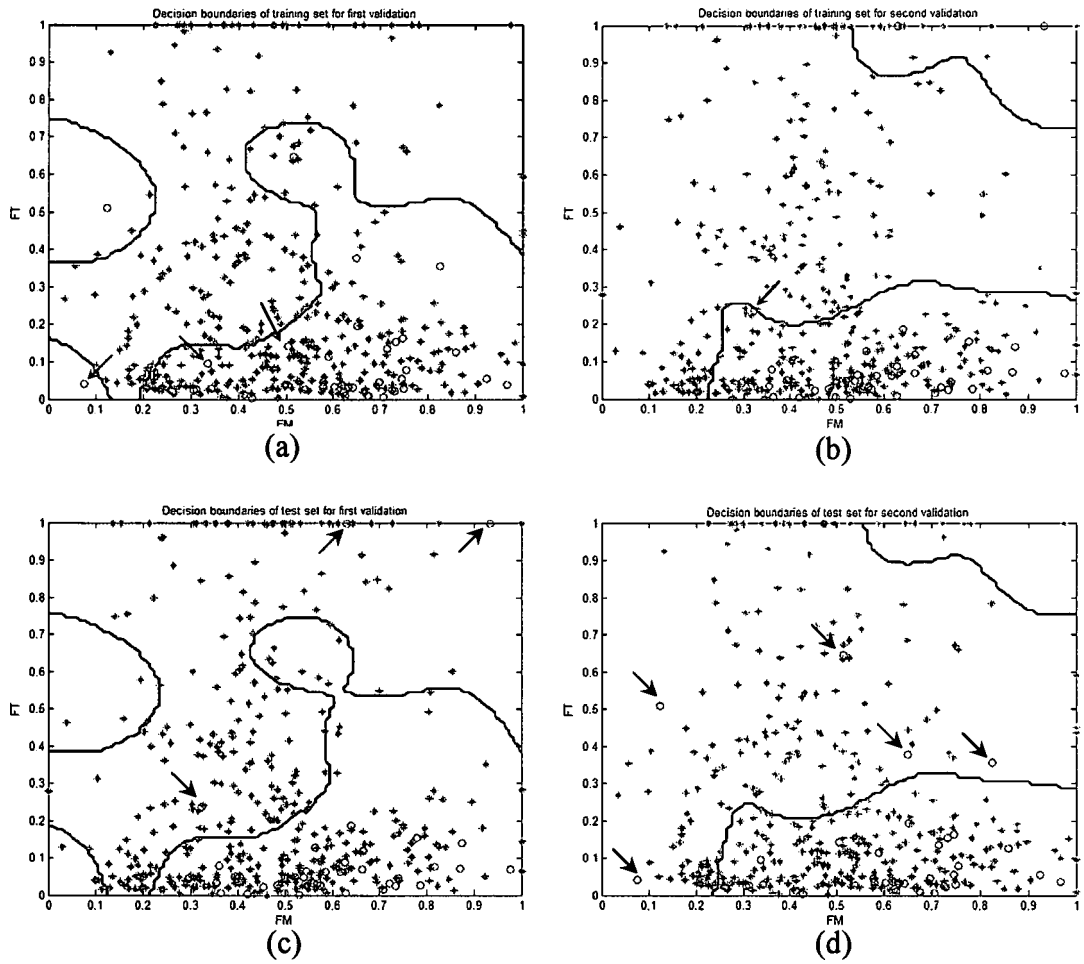

Figure 4-68: The decision boundaries validations associated with the classifier with 100% training sensitivity: (a) training set for first validation, (b) training set for second validation, (c) test set for first validation, (d) test set for second validation

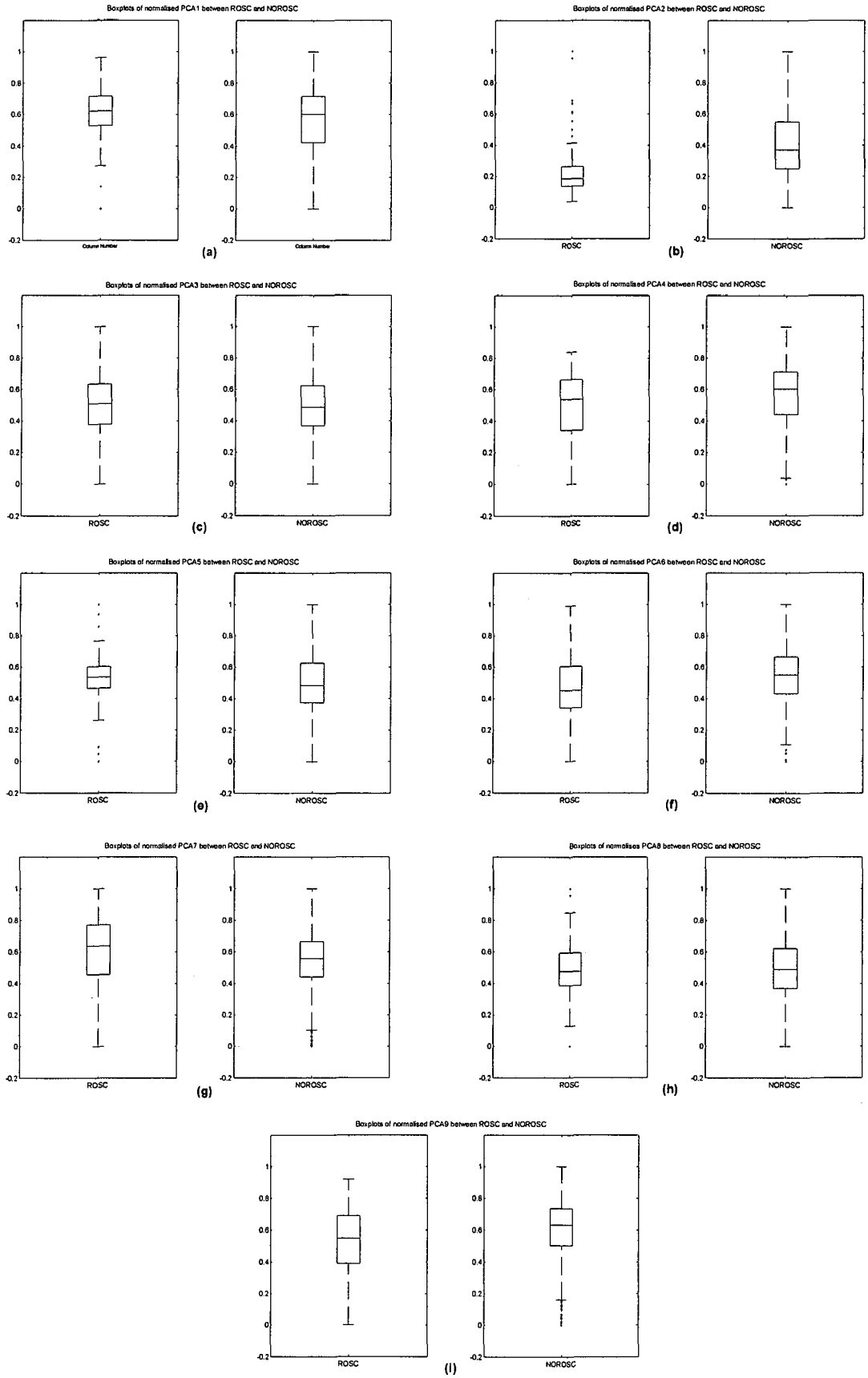

Figure 4-69: Boxplots of normalised PCA between ROSC and NOROSC using the WT power spectrum-based technique (5 second pre-shock)

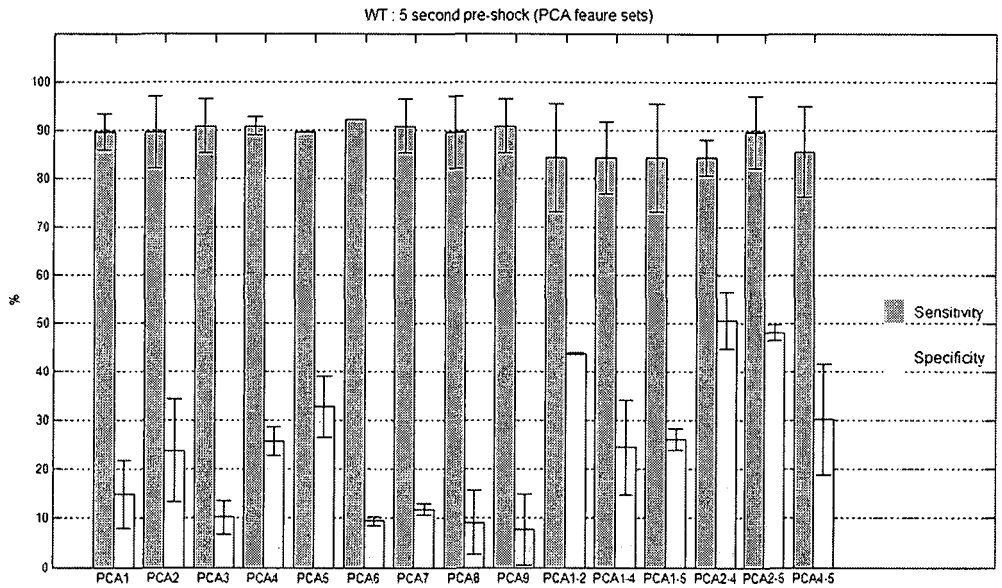

Figure 4-70: The performances of the classifier using the WT power spectrum-based technique (5 second pre-shock)

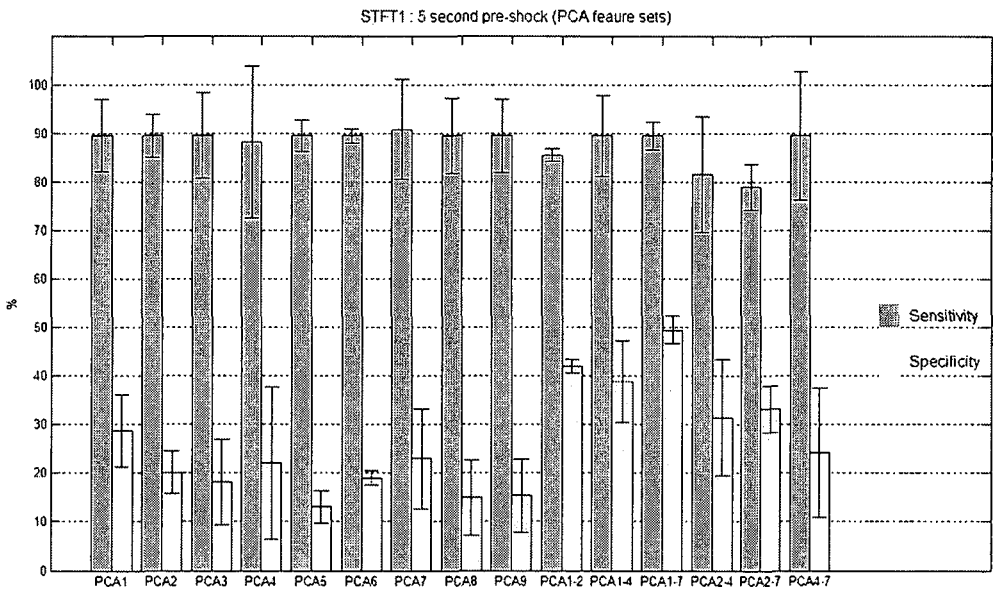

Figure 4-71: The performances of the classifier using the STFT1 power spectrum-based technique (5 second pre-shock)

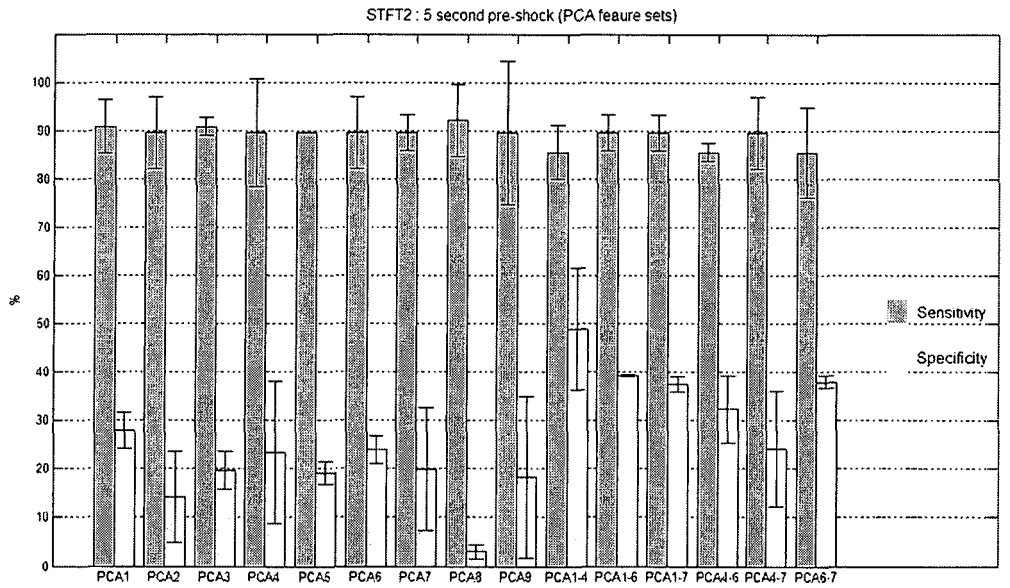

Figure 4-72: The performances of the classifier using the STFT2 power spectrum-based technique (5 second pre-shock)

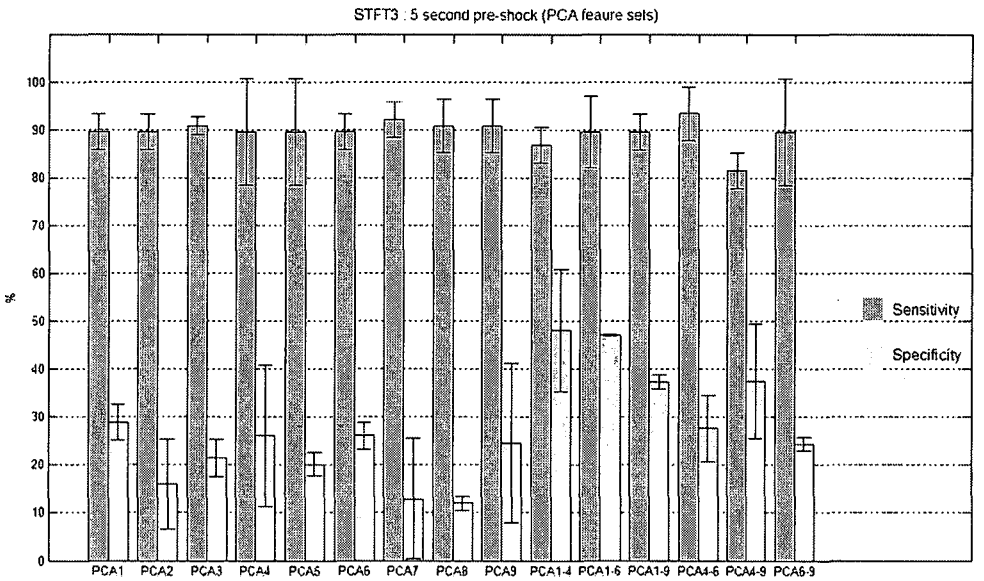

Figure 4-73: The performances of the classifier using the STFT3 power spectrum-based technique (5 second pre-shock)

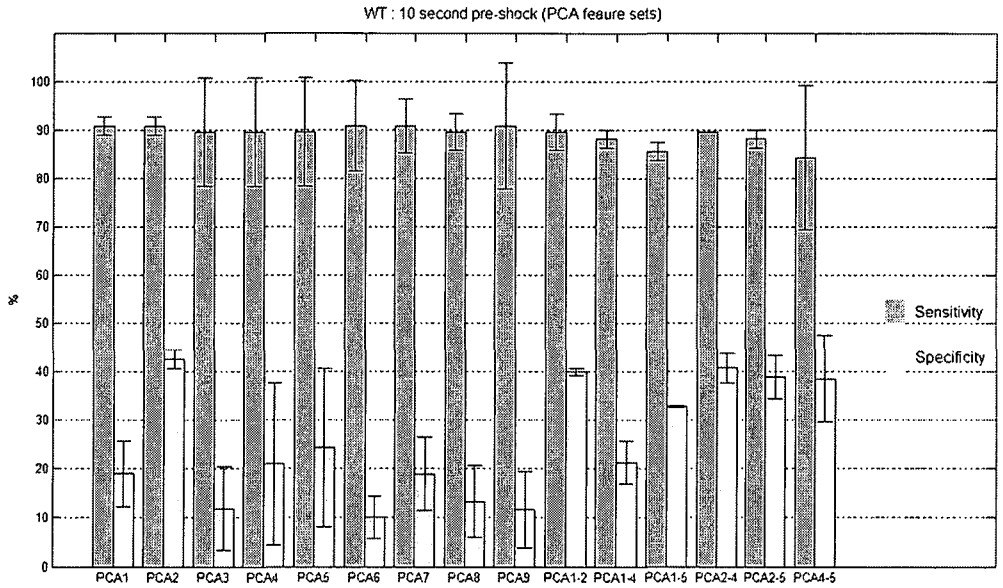

Figure 4-74: The performances of the classifier using the WT power spectrum-based technique (10 second pre-shock)

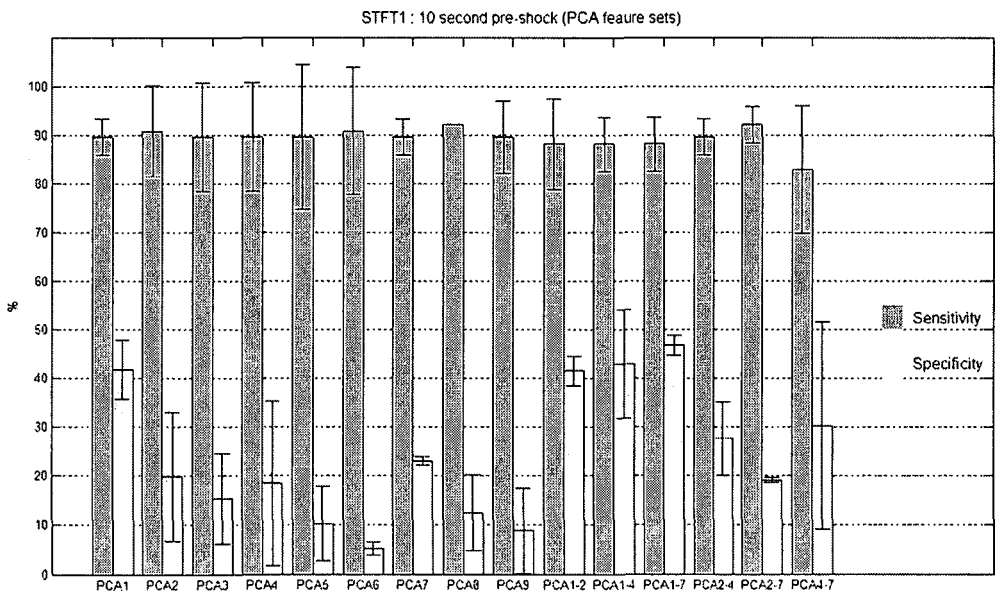

Figure 4-75: The performances of the classifier using the STFT1 power spectrum-based technique (10 second pre-shock)

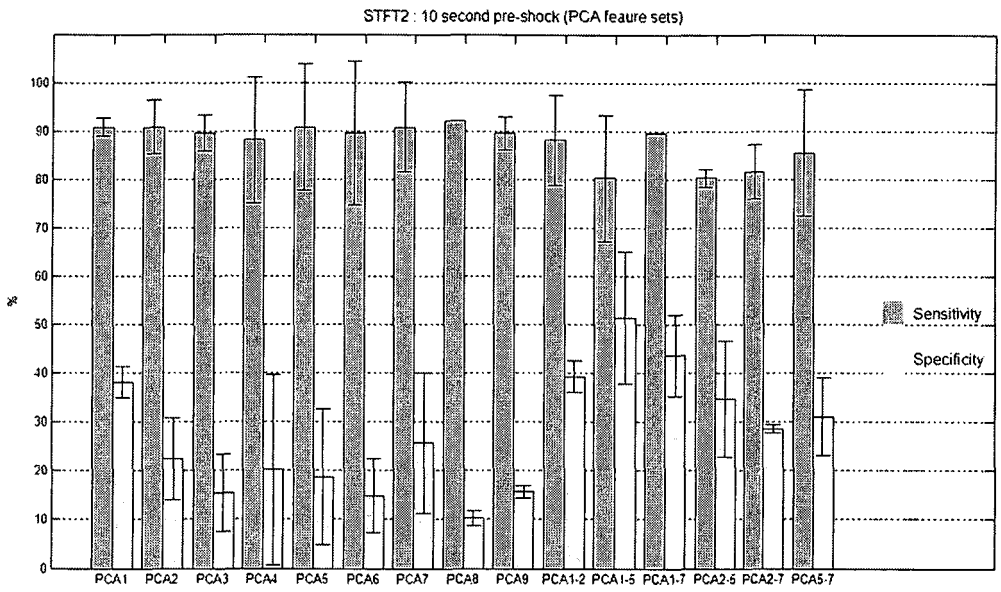

Figure 4-76: The performances of the classifier using the STFT2 power spectrum-based technique (10 second pre-shock)

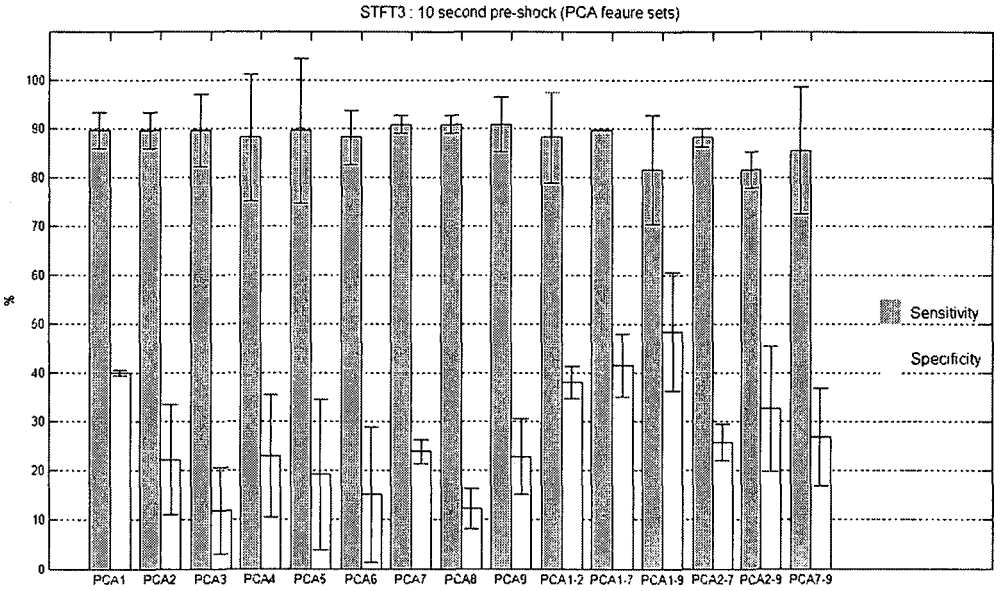

Figure 4-77: The performances of the classifier using the STFT3 power spectrum-based technique (10 second pre-shock)

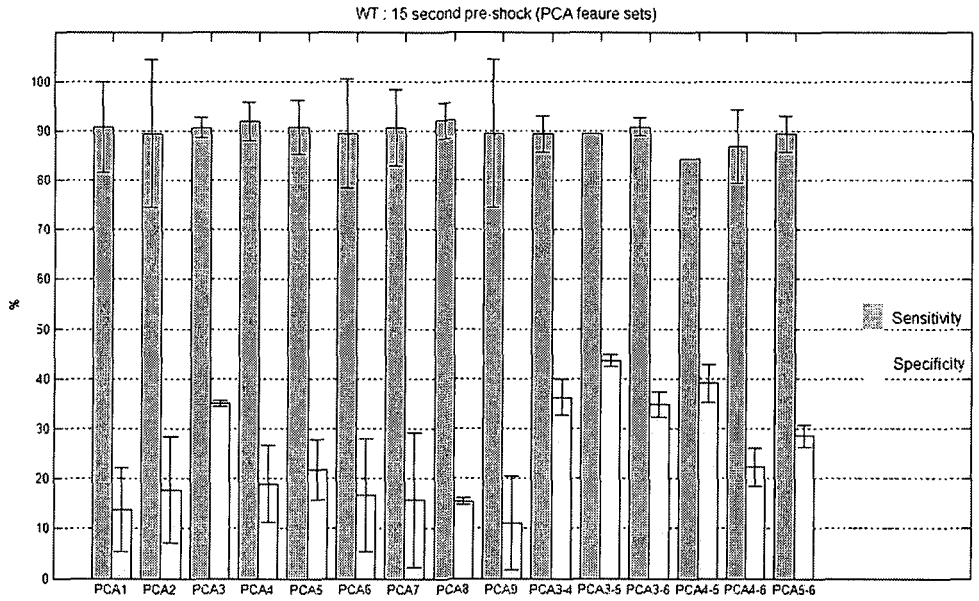

Figure 4-78: The performances of the classifier using the WT power spectrum-based technique (15 second pre-shock)

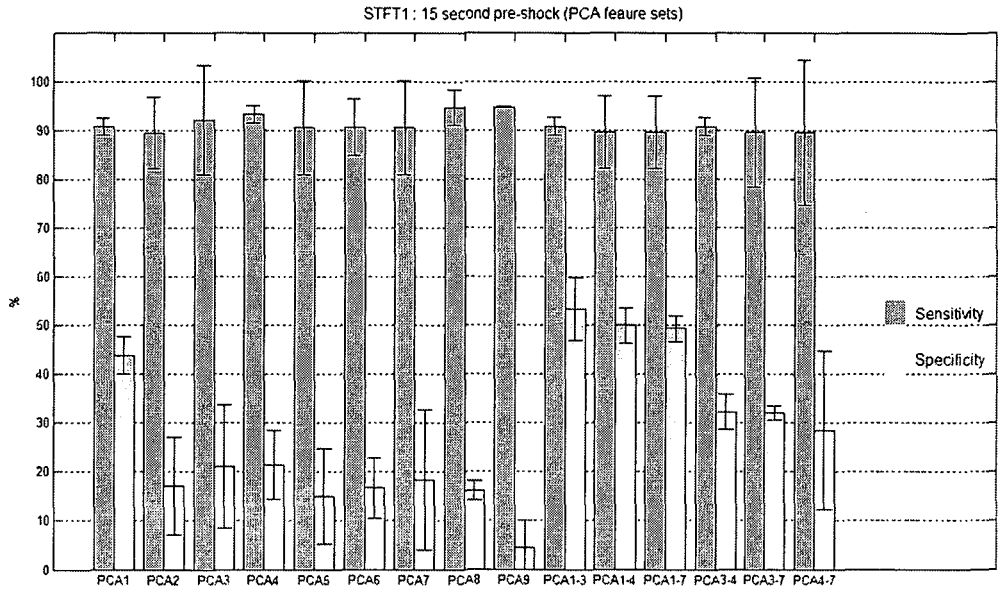

Figure 4-79: The performances of the classifier using the STFT1 power spectrum-based technique (15 second pre-shock)

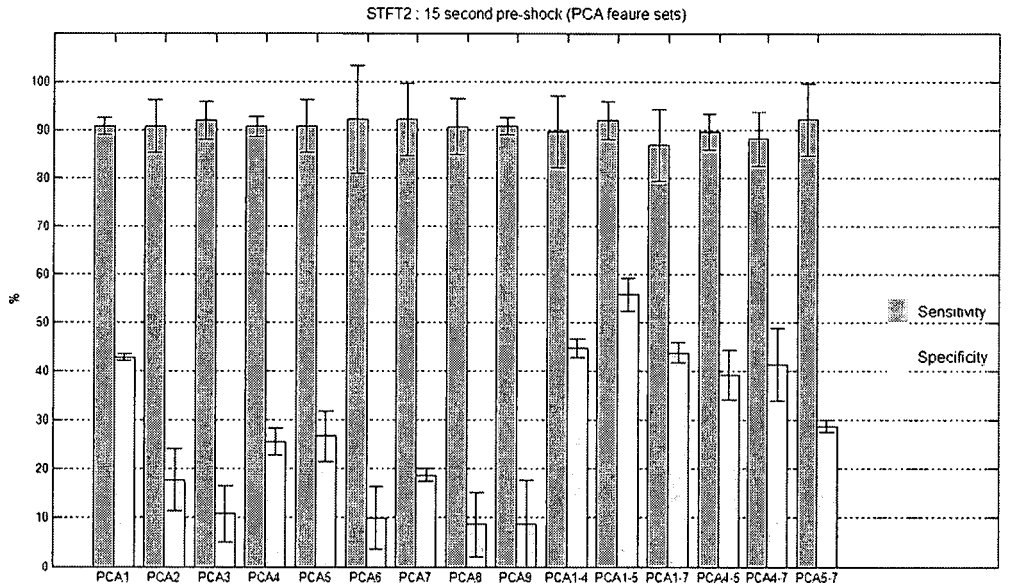

Figure 4-80: The performances of the classifier using the STFT2 power spectrum-based technique (15 second pre-shock)

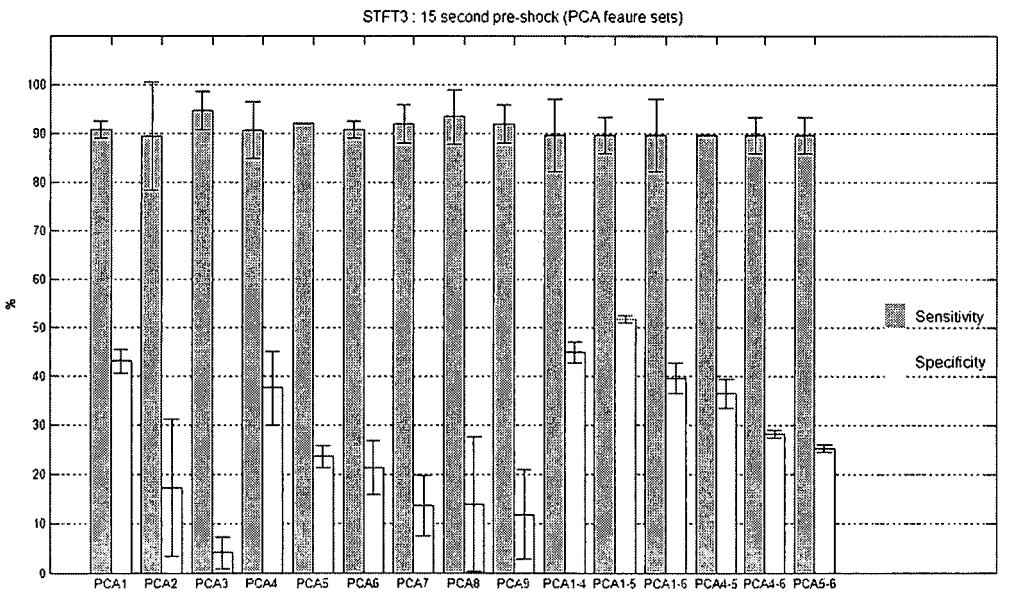

Figure 4-81: The performances of the classifier using the STFT3 power spectrum-based technique (15 second pre-shock)

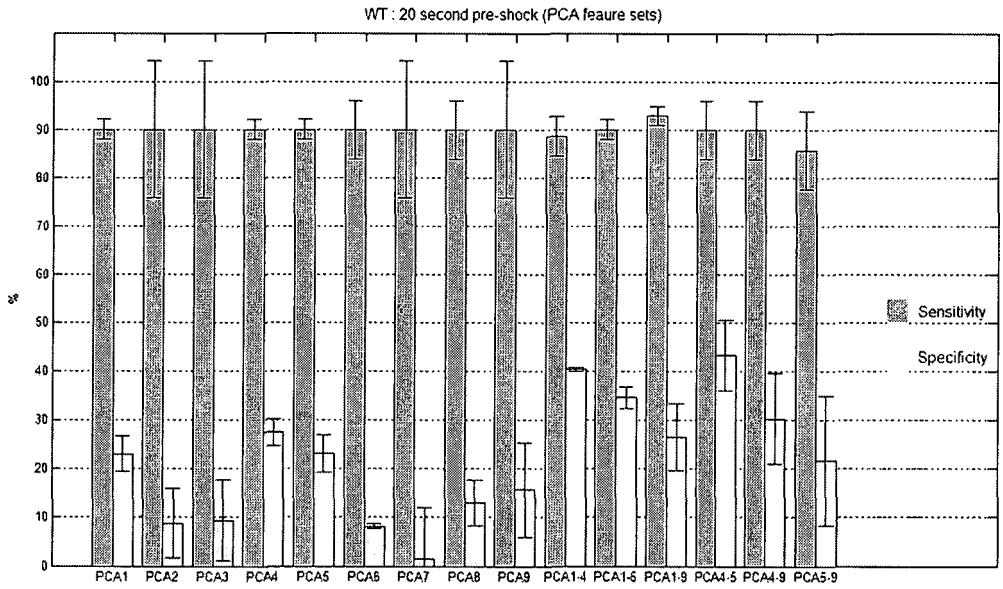

Figure 4-82: The performances of the classifier using the WT power spectrum-based technique (20 second pre-shock)

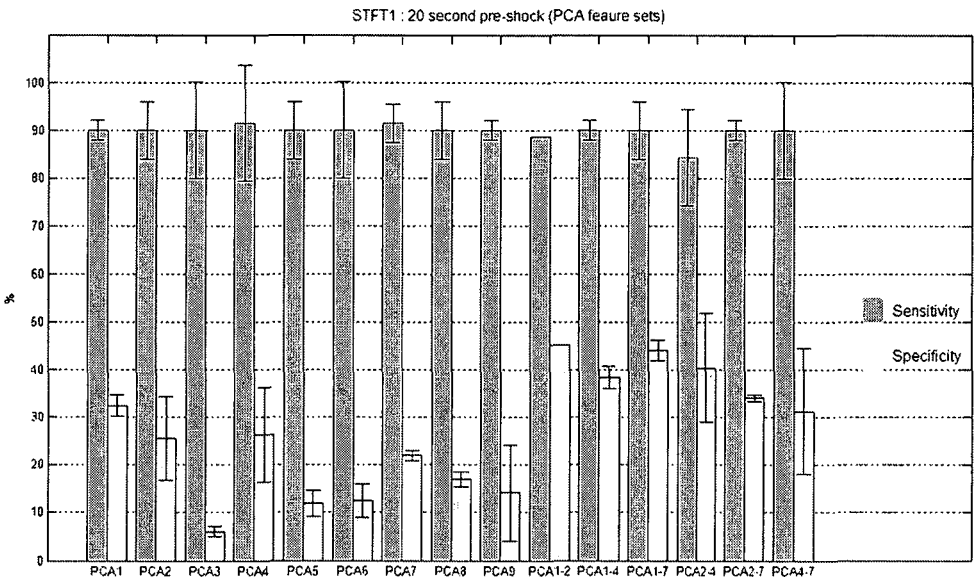

Figure 4-83: The performances of the classifier using the STFT1 power spectrum-based technique (20 second pre-shock)

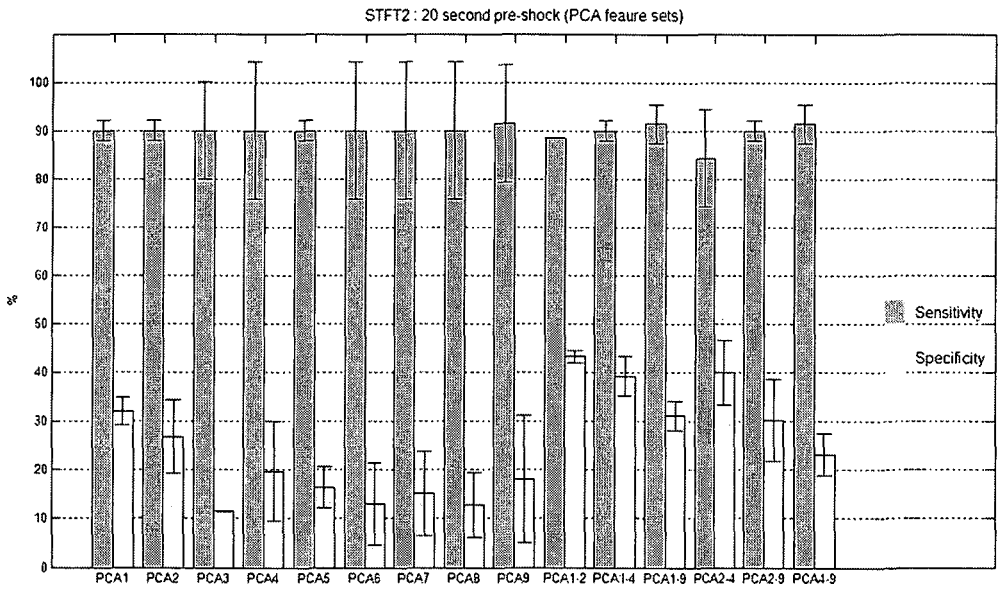

Figure 4-84: The performances of the classifier using the STFT2 power spectrum-based technique (20 second pre-shock)

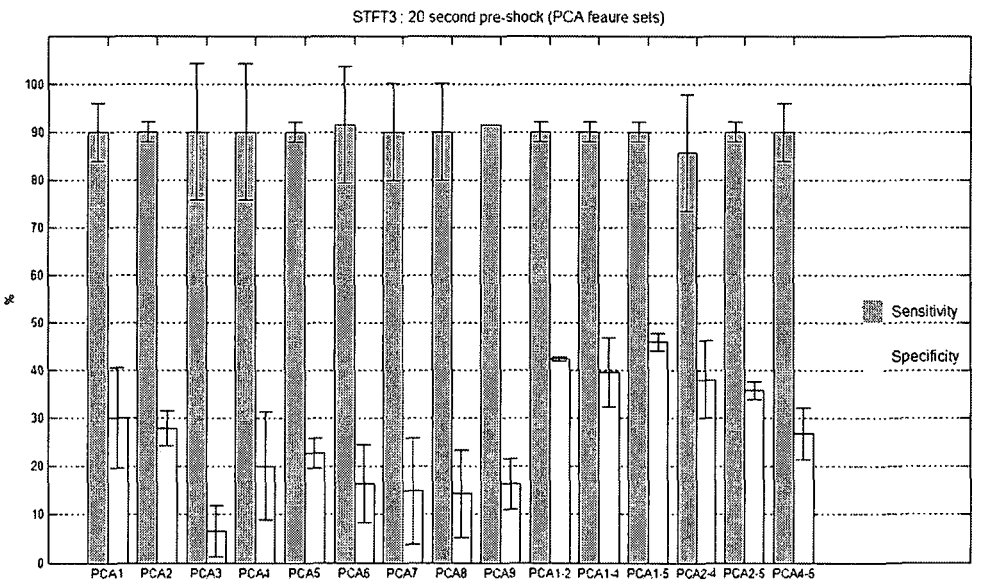

Figure 4-85: The performances of the classifier using the STFT3 power spectrum-based technique (20 second pre-shock)

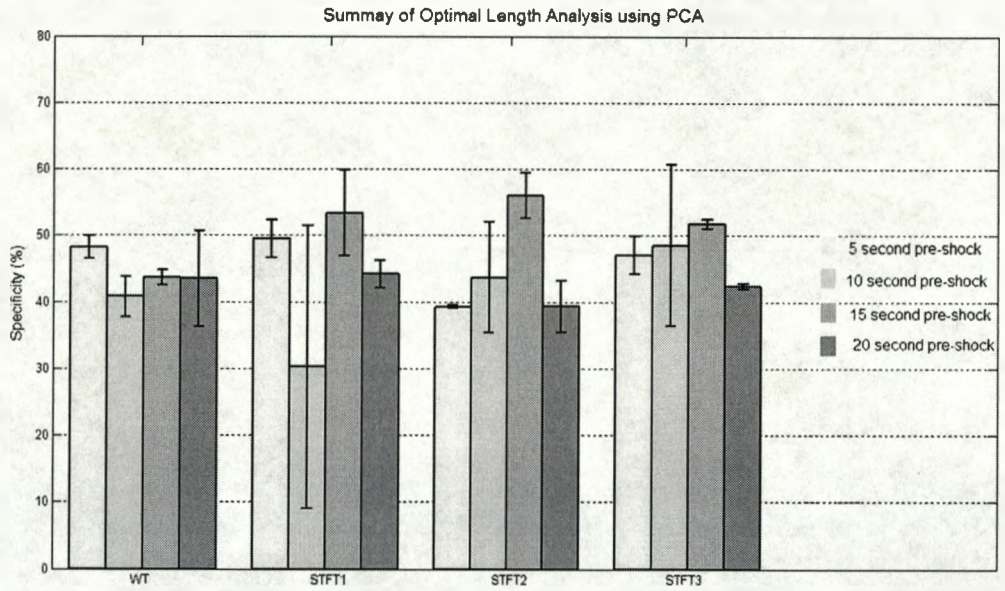

Figure 4-86: Summary of the optimal length analysis with PCA features

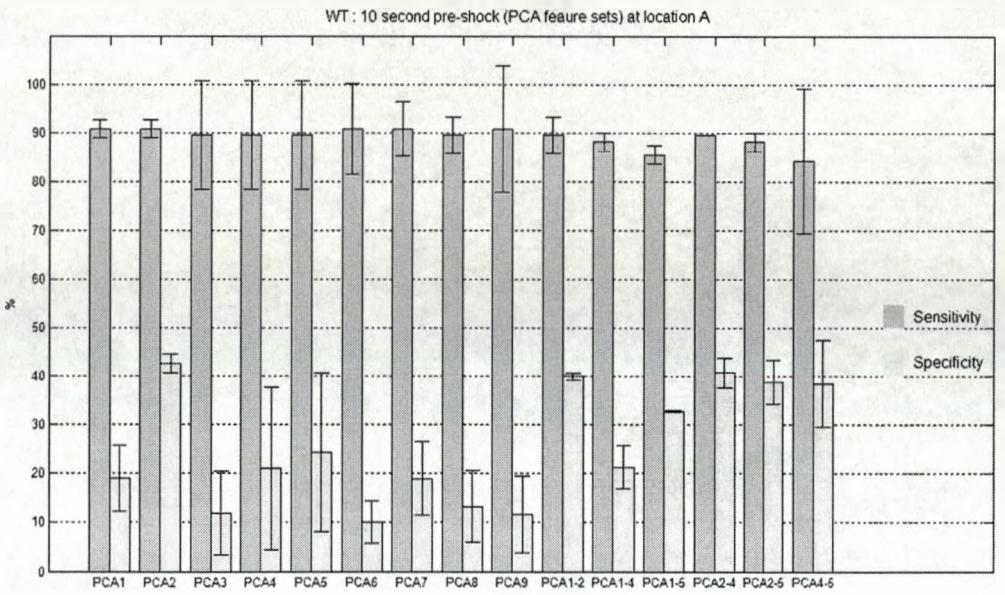

Figure 4-87: The performances of the classifier using the WT power spectrum-based technique (10 second pre-shock) at location A

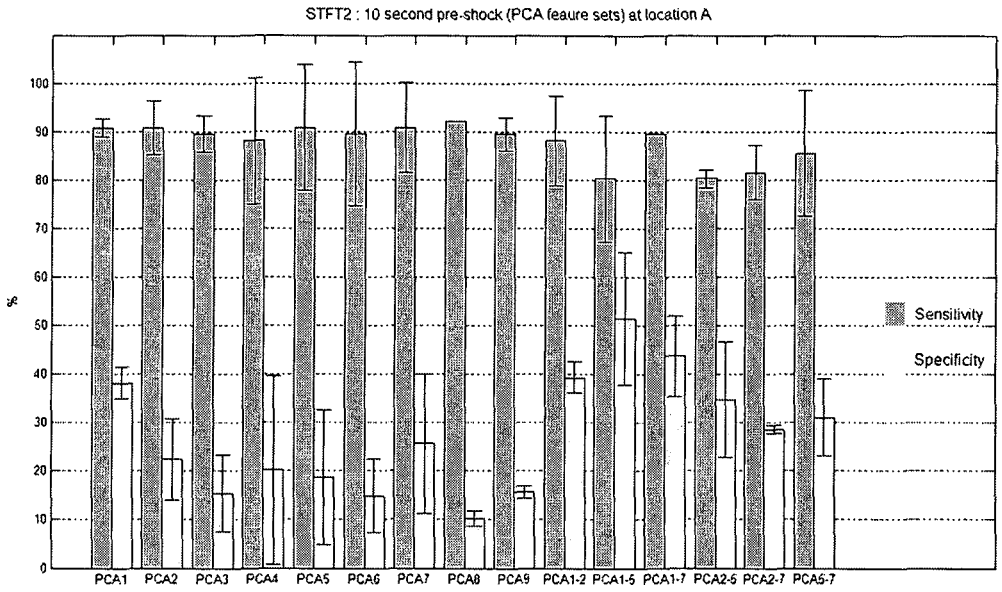

Figure 4-88: The performances of the classifier using the STFT2 power spectrum-based technique (10 second pre-shock) at location A

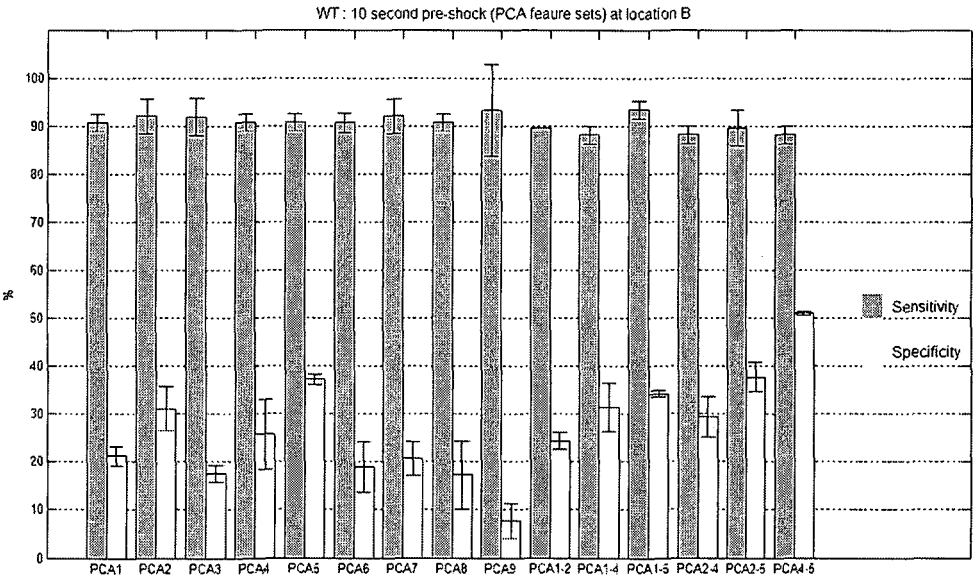

Figure 4-89: The performances of the classifier using the WT power spectrum-based technique (10 second pre-shock) at location B

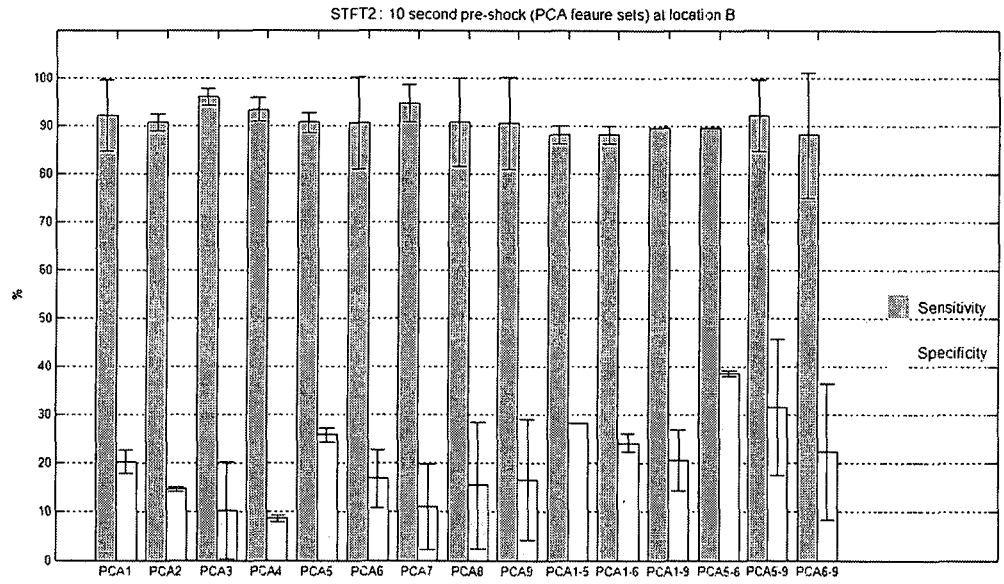

Figure 4-90: The performances of the classifier using the STFT2 power spectrum-based technique (10 second pre-shock) at location B

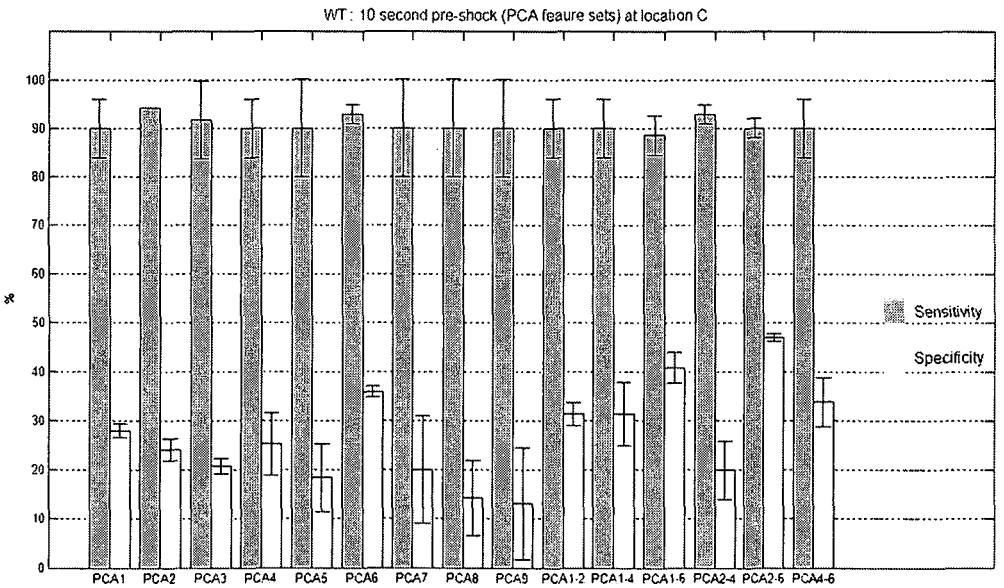

Figure 4-91: The performances of the classifier using the WT power spectrum-based technique (10 second pre-shock) at location C

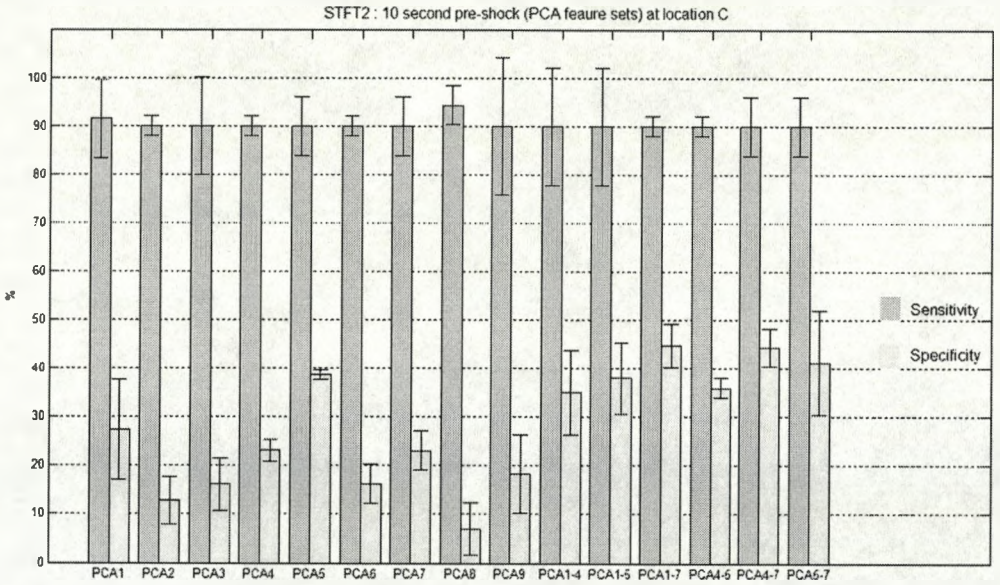

Figure 4-92: The performances of the classifier using the STFT2 power spectrum-based technique (10 second pre-shock) at location C

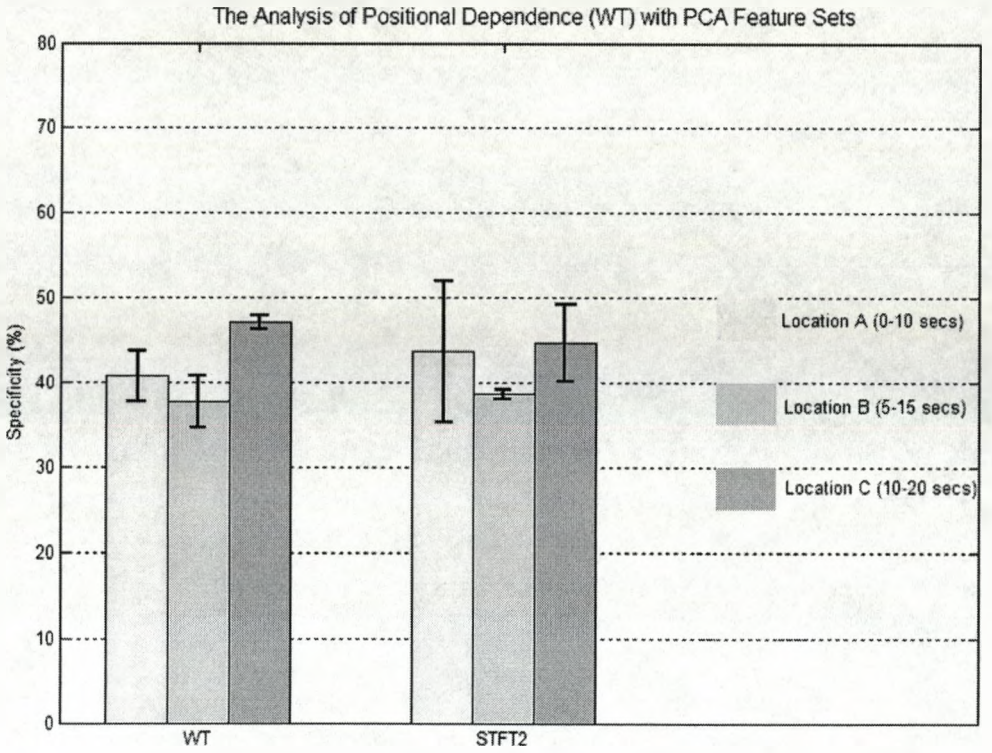

Figure 4-93: Summary of the positional dependence analysis using the PCA features

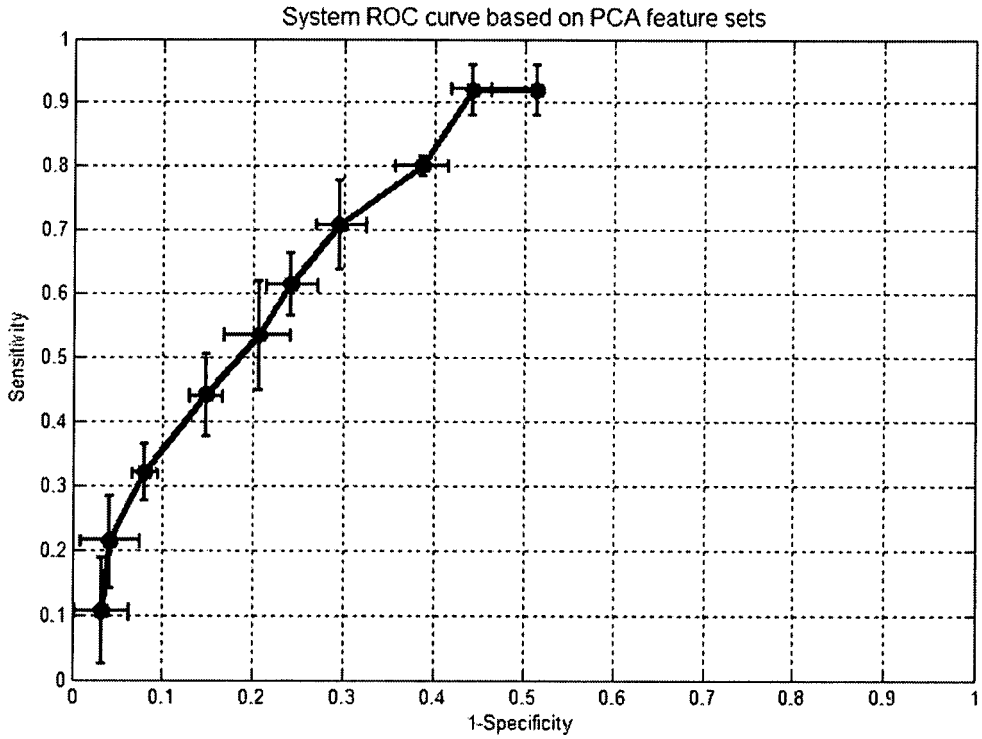

Figure 4-94: The system ROC of the best classifier using the PCA feature sets

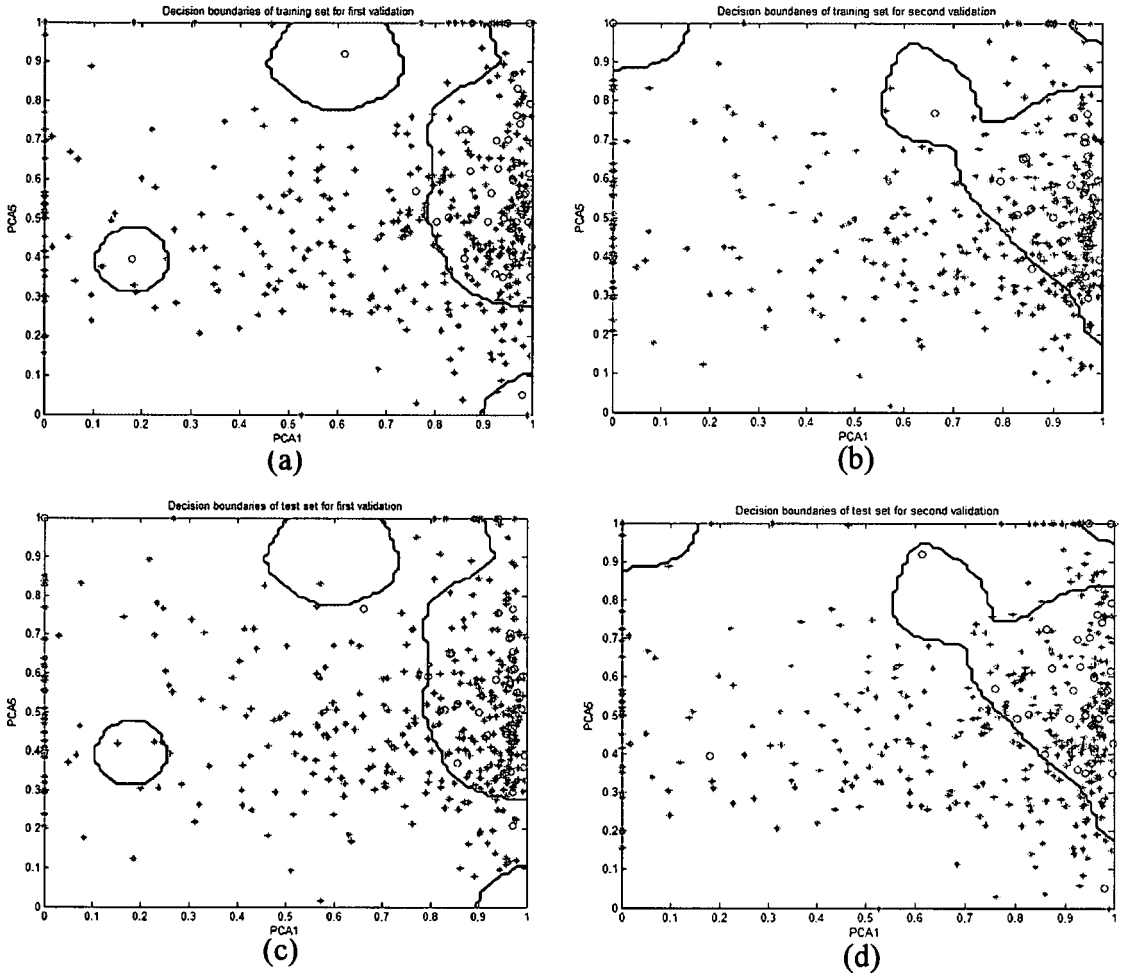

Figure 4-95: The decision boundaries validations associated with the classifier with 95% training sensitivity: (a) training set for first validation, (b) training set for second validation, (c) test set for first validation, (d) test set for second validation

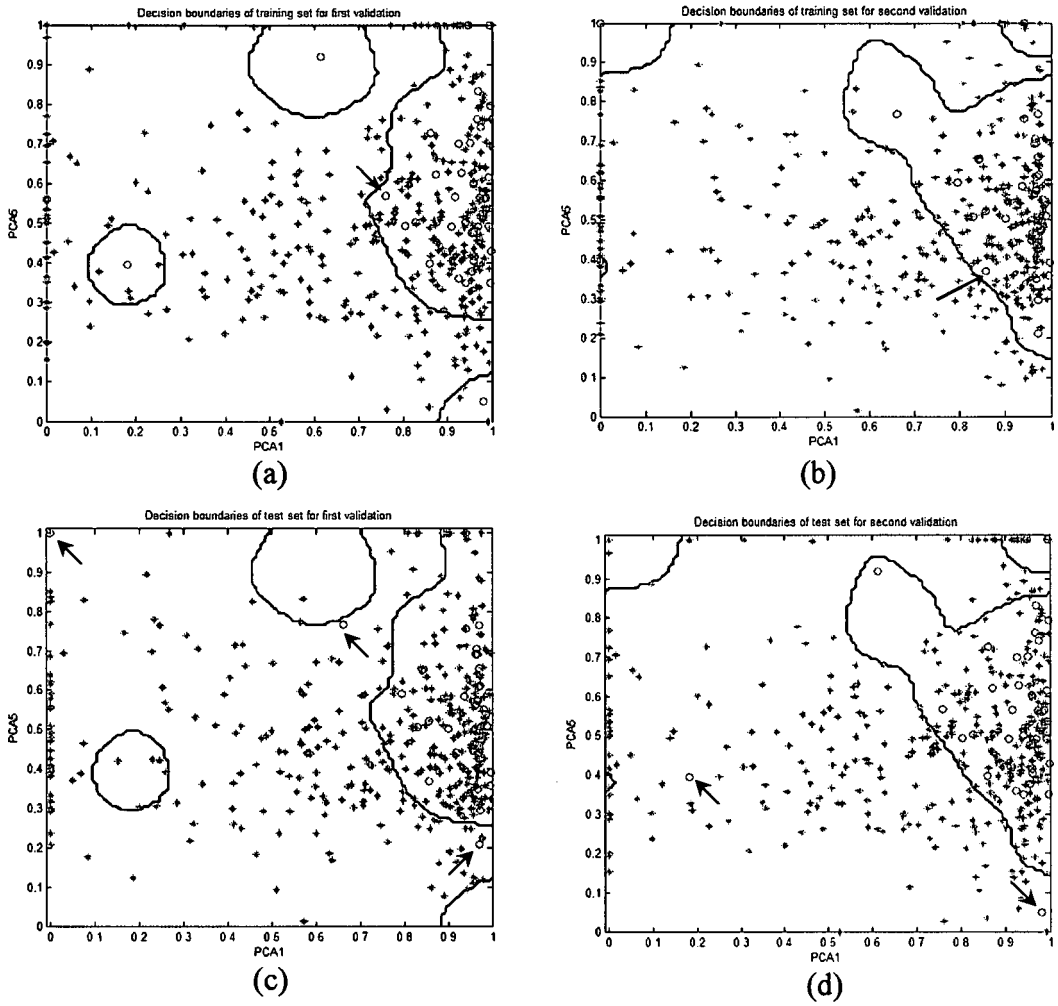

Figure 4-96: The decision boundaries validations associated with the classifier with 100% training sensitivity: (a) training set for first validation, (b) training set for second validation, (c) test set for first validation, (d) test set for second validation

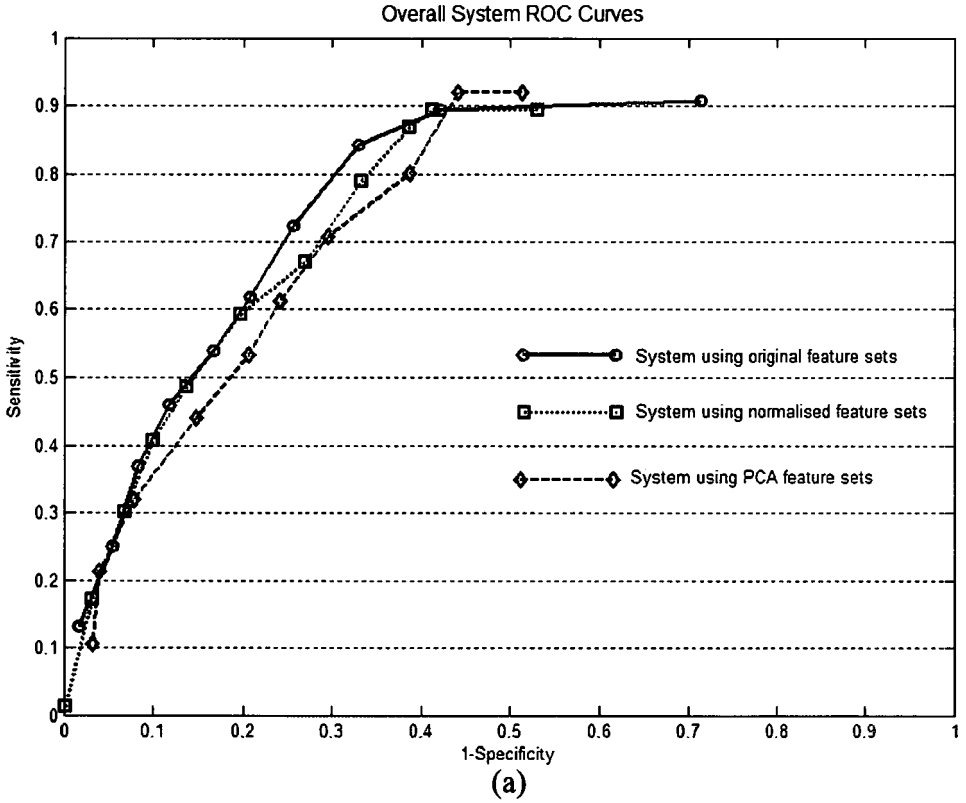

(a)

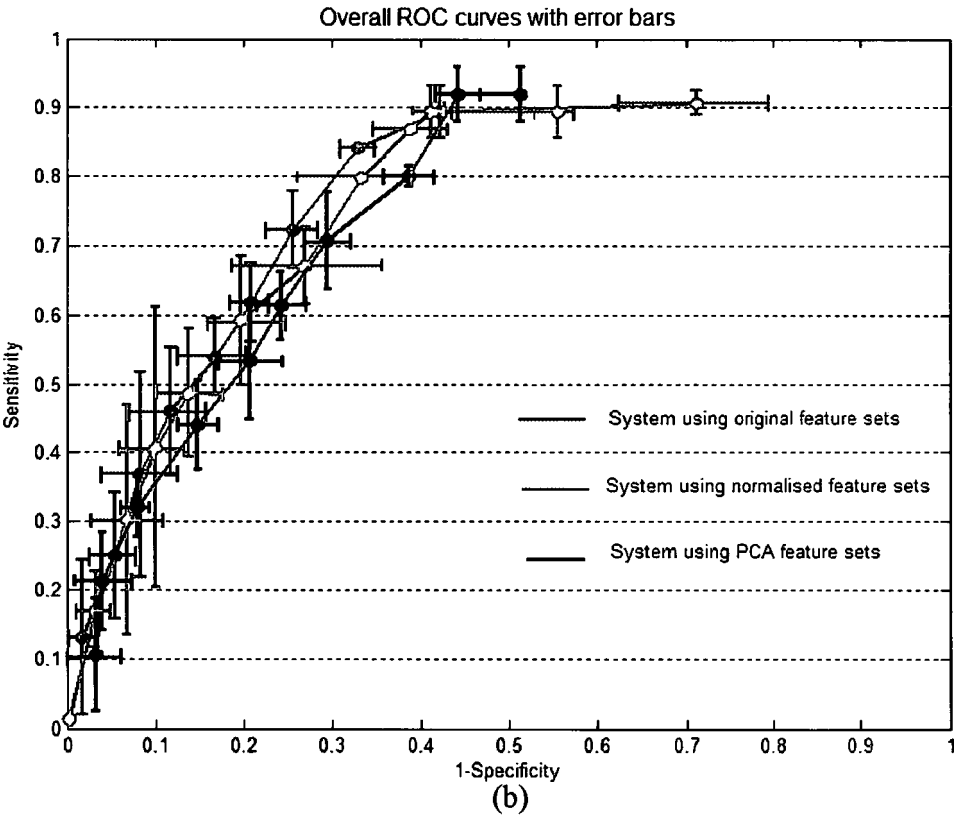

(b)

Figure 4-97: The system ROC curves of the classifiers using original feature sets, normalised features sets, and PCA feature sets

Feature	Wilcoxon Rank Sum Test			
	WT	STFT-1	STFT-2	STFT-3
FM	2.01E-07	2.56E-07	1.92E-07	2.02E-07
FP	3.10E-07	4.06E-07	5.42E-07	6.41E-07
STD	0.5742	0.6744	0.438	0.4528
SK	0.2219	0.1779	0.5077	0.5221
KT	0.3016	0.5231	0.9633	0.9994
FT	2.13E-09	6.32E-09	1.04E-09	1.57E-09

Table 4-1: Wilcoxon rank sum test of each feature in all experiments with 5-second length of pre-shock. The corresponding feature set boxplots can be found in Appendix B, figure B-1, B-2, B-3, and B-4 respectively.

Feature	Wilcoxon Rank Sum Test			
	WT	STFT-1	STFT-2	STFT-3
FM	2.11E-08	1.82E-08	1.82E-08	8.04E-09
FP	4.57E-08	7.73E-08	7.73E-08	1.22E-06
STD	0.5973	0.801	0.801	0.5358
SK	0.105	0.108	0.108	0.379
KT	0.2279	0.4522	0.4522	0.9629
FT	1.72E-10	1.76E-10	1.76E-10	1.46E-08

Table 4-2: Wilcoxon rank sum test of each feature in all experiments with 10-second length of pre-shock. The corresponding feature set boxplots can be found in Appendix B, figure B-5, B-6, B-7, and B-8 respectively.

Feature	Wilcoxon Ranksum Test			
	WT	STFT-1	STFT-2	STFT-3
FM	9.36E-09	2.90E-09	7.11E-08	9.96E-10
FP	5.65E-08	8.88E-08	7.67E-01	1.54E-07
STD	0.7295	0.9621	0.7665	0.7571
SK	0.0749	0.0673	0.2969	0.3481
KT	0.1512	0.2709	0.6358	0.6864
FT	3.93E-11	2.17E-11	5.10E-11	6.85E-11

Table 4-3: Wilcoxon rank sum test of each feature in all experiments with 15-second length of pre-shock. The corresponding feature set boxplots can be found in Appendix B, figure B-9, B-10, B-11, and B-12 respectively.

Feature	Wilcoxon Ranksum Test			
	WT	STFT-1	STFT-2	STFT-3
FM	2.91E-10	3.90E-11	1.08E-11	7.55E-12
FP	6.92E-07	1.01E-09	2.15E-09	5.19E-01
STD	0.3686	0.2207	0.4614	0.5185
SK	0.0033	0.0037	0.0343	0.0494
KT	0.0046	0.0107	0.0689	0.0937
FT	1.30E-06	1.02E-06	2.44E-06	2.96E-06

Table 4-4: Wilcoxon rank sum test of each feature in all experiments with 20-second length of pre-shock. The corresponding feature set boxplots can be found in Appendix B, figure B-13, B-14, B-15, and B-16 respectively.

Feature	Wilcoxon Rank Sum Test	
	WT	STFT-1
FM	2.11E-08	1.82E-08
FP	4.57E-08	7.73E-08
STD	0.5973	0.801
SK	0.105	0.108
KT	0.2279	0.4522
FT	1.72E-10	1.76E-10

Table 4-5: Wilcoxon rank sum test of each feature in all experiments with pre-shock locating at section A (0-10 second before countershock). The corresponding feature set boxplots can be found in Appendix B, figure B-17 and B-18 respectively.

Feature	Wilcoxon Rank Sum Test	
	WT	STFT-1
FM	6.16E-09	1.82E-08
FP	1.24E-08	1.40e-08
STD	0.7493	0.3198
SK	0.0668	0.042
KT	0.1397	0.1875
FT	1.11E-10	1.00e-13

Table 4-6: Wilcoxon rank sum test of each feature in all experiments with pre-shock locating at section B (5-15 second before countershock). The corresponding feature set boxplots can be found in Appendix B, figure B-19 and B-20 respectively.

Feature	Wilcoxon Rank Sum Test	
	WT	STFT-1
FM	7.40E-12	1.92e-12
FP	3.80E-07	1.13e-009
STD	0.6103	0.8943
SK	6.33E-05	3.08e-05
KT	1.06E-04	1.26e-04
FT	8.09E-06	4.76e-09

Table 4-7: Wilcoxon rank sum test of each feature in all experiments with pre-shock locating at section C (10-20 second before countershock). The corresponding feature set boxplots can be found in Appendix B, figure B-21 and B-22 respectively.

Feature	Wilcoxon Ranksum Test			
	WT	STFT-1	STFT-2	STFT-3
BI	2.74E-07	1.45E-07	2.63E-07	1.09E-06
R	7.95E-09	9.14E-08	7.61E-08	5.37E-08
SH	0.2425	0.8928	0.4657	0.4546

Table 4-8: Wilcoxon rank sum test of extra feature in all experiments with 5-second length of pre-shock. The corresponding feature set boxplots can be found in Appendix B, figure B-23, B-24, B-25, and B-26 respectively.

Feature	Wilcoxon Ranksum Test			
	WT	STFT-1	STFT-2	STFT-3
BI	1.72E-08	7.18E-09	8.35E-09	1.16E-08
R	2.70E-10	3.86E-09	5.28E-09	4.28E-09
SH	0.1951	0.7752	0.6651	0.6366

Table 4-9: Wilcoxon rank sum test of extra features in all experiments with 10-second length of pre-shock. The corresponding feature set boxplots can be found in Appendix B, figure B-27, B-28, B-29, and B-30 respectively.

Feature	Wilcoxon Ranksum Test			
	WT	STFT-1	STFT-2	STFT-3
BI	1.42E-08	2.84E-09	2.10E-09	1.80E-09
R	1.53E-10	1.46E-09	3.69E-09	4.76E-09
SH	0.1191	0.4686	0.9515	0.894

Table 4-10: Wilcoxon rank sum test of extra features in all experiments with 15-second length of pre-shock. The corresponding feature set boxplots can be found in Appendix B, figure B-31, B-32, B-33, and B-34 respectively.

Feature	Wilcoxon Ranksum Test			
	WT	STFT-1	STFT-2	STFT-3
BI	1.38E-09	1.88E-10	1.86E-10	1.36E-10
R	8.98E-12	2.97E-11	1.67E-10	3.01E-10
SH	0.0026	0.0151	0.1129	0.1578

Table 4-11: Wilcoxon rank sum test of extra features in all experiments with 20-second length of pre-shock. The corresponding feature set boxplots can be found in Appendix B, figure B-35, B-36, B-37, and B-38 respectively.

Feature	Wilcoxon Ranksum Test	
	WT	STFT-3
BI	1.72E-08	1.16E-08
R	2.70E-10	4.28E-09
SH	0.1951	0.6366

Table 4-12: Wilcoxon rank sum test of extra features in all experiments with pre-shock locating at section A (0-10 second before countershock). The corresponding feature set boxplots can be found in Appendix B, figure B-39 and B-40 respectively.

Feature	Wilcoxon Ranksum Test	
	WT	STFT-3
BI	2.08E-12	4.24E-12
R	1.51E-13	2.69E-12
SH	0.0057	0.5624

Table 4-13: Wilcoxon rank sum test of extra features in all experiments with pre-shock locating at section B (5-15 second before countershock). The corresponding feature set boxplots can be found in Appendix B, figure B-41 and B-42 respectively.

Feature	Wilcoxon Ranksum Test	
	WT	STFT-3
BI	8.95E-11	4.37E-11
R	2.59E-13	5.22E-12
SH	6.37E-05	0.0298

Table 4-14: Wilcoxon rank sum test of extra features in all experiments with pre-shock locating at section C (10-20 second before countershock). The corresponding feature set boxplots can be found in Appendix B, figure B-43 and B-44 respectively.

Feature	Wilcoxon Ranksum Test			
	WT	STFT-1	STFT-2	STFT-3
PCA1	1.56E-01	3.21E-12	7.00E-12	9.08E-12
PCA2	3.86E-14	8.10E-03	1.84E-02	1.58E-02
PCA3	0.5946	4.02E-04	6.06E-04	4.68E-04
PCA4	9.71E-04	4.68E-05	7.58E-06	8.29E-06
PCA5	8.50E-03	2.84E-01	2.19E-01	2.85E-01
PCA6	5.21E-04	5.61E-04	3.23E-04	5.78E-04
PCA7	0.0019	8.04E-04	3.60E-03	4.60E-03
PCA8	0.8023	0.2435	0.3433	0.0157
PCA9	0.0059	9.96E-06	2.81E-06	6.53E-05

Table 4-15: Wilcoxon rank sum test of each PCA feature in all experiments with 5-second length of pre-shock. The corresponding feature set boxplots can be found in Appendix B, figure B-45, B-46, B-47, and B-48 respectively.

Feature	Wilcoxon Ranksum Test			
	WT	STFT-1	STFT-2	STFT-3
PCA1	1.95E-02	2.24E-13	5.14E-13	7.23E-13
PCA2	6.66E-14	3.60E-03	1.14E-02	1.03E-02
PCA3	4.82E-01	1.15E-05	3.77E-05	1.05E-04
PCA4	1.40E-03	9.52E-05	1.99E-05	1.58E-05
PCA5	2.29E-04	1.70E-02	7.02E-04	4.06E-04
PCA6	5.23E-01	9.80E-01	4.93E-06	5.37E-06
PCA7	2.32E-05	1.96E-05	2.20E-03	5.10E-03
PCA8	0.6878	0.1865	0.3863	0.0034
PCA9	1.70E-03	2.01E-04	4.87E-06	1.96E-04

Table 4-16: Wilcoxon rank sum test of each PCA feature in all experiments with 10-second length of pre-shock. The corresponding feature set boxplots can be found in Appendix B, figure B-49, B-50, B-51, and B-52 respectively.

Feature	Wilcoxon Ranksum Test			
	WT	STFT-1	STFT-2	STFT-3
PCA1	3.10E-03	3.09E-14	1.40E-13	2.22E-13
PCA2	6.39E-05	6.29E-04	8.09E-04	6.55E-04
PCA3	1.86E-10	5.63E-04	2.92E-01	5.73E-01
PCA4	8.20E-05	2.14E-07	9.36E-09	1.18E-08
PCA5	4.40E-04	8.35E-04	1.20E-03	3.14E-04
PCA6	8.98E-02	7.01E-01	8.50E-03	2.71E-06
PCA7	2.03E-05	4.36E-07	2.55E-05	1.30E-03
PCA8	0.6422	0.0972	0.2629	5.96E-04
PCA9	1.39E-04	1.44E-04	3.14E-04	6.40E-03

Table 4-17: Wilcoxon rank sum test of each PCA feature in all experiments with 15-second length of pre-shock. The corresponding feature set boxplots can be found in Appendix B, figure B-53, B-54, B-55, and B-56 respectively.

Feature	Wilcoxon Ranksum Test			
	WT	STFT-1	STFT-2	STFT-3
PCA1	1.72E-05	5.40E-09	1.55E-08	2.16E-08
PCA2	9.25E-02	1.34E-06	4.32E-07	2.57E-07
PCA3	2.08E-06	3.79E-02	8.36E-01	7.03E-01
PCA4	3.15E-05	1.23E-06	1.48E-08	8.25E-09
PCA5	6.80E-04	1.07E-02	3.80E-03	3.00E-03
PCA6	9.25E-01	2.51E-02	1.61E-04	5.96E-06
PCA7	2.54E-06	1.85E-06	2.50E-04	4.34E-02
PCA8	2.88E-01	4.41E-02	4.83E-01	4.22E-01
PCA9	3.00E-02	5.60E-03	3.20E-03	1.20E-03

Table 4-18: Wilcoxon rank sum test of each PCA feature in all experiments with 20-second length of pre-shock. The corresponding feature set boxplots can be found in Appendix B, figure B-57, B-58, B-59, and B-60 respectively.

Feature	Wilcoxon Ranksum Test	
	WT	STFT-2
PCA1	1.95E-02	5.14E-13
PCA2	6.66E-14	1.14E-02
PCA3	4.82E-01	3.77E-05
PCA4	1.40E-03	1.99E-05
PCA5	2.29E-04	7.02E-04
PCA6	5.23E-01	4.93E-06
PCA7	2.32E-05	2.20E-03
PCA8	0.6878	0.3863
PCA9	1.70E-03	4.87E-06

Table 4-19: Wilcoxon rank sum test of each PCA feature in all experiments with pre-shock locating at section A (0-10 second before countershock). The corresponding feature set boxplots can be found in Appendix B, figure B-61, and B-62 respectively.

Feature	Wilcoxon Ranksum Test	
	WT	STFT-2
PCA1	0.0256	0.0198
PCA2	2.7262e-006	0.0015
PCA3	0.3542	0.0053
PCA4	3.3715e-009	0.7276
PCA5	1.0546e-004	3.4566e-009
PCA6	0.0359	8.8252e-005
PCA7	2.3030e-006	0.0029
PCA8	0.6468	0.0742
PCA9	2.2356e-004	4.1962e-005

Table 4-20: Wilcoxon rank sum test of each PCA feature in all experiments with pre-shock locating at section B (5-15 second before countershock). The corresponding feature set boxplots can be found in Appendix B, figure B-63, and B-64 respectively.

Feature	Wilcoxon Ranksum Test	
	WT	STFT-2
PCA1	2.2274e-004	2.7392e-005
PCA2	3.8820e-006	0.3449
PCA3	0.5804	0.1088
PCA4	8.0531e-006	1.5931e-008
PCA5	2.2224e-004	1.8308e-005
PCA6	5.5690e-006	1.4911e-004
PCA7	1.7212e-007	7.9883e-006
PCA8	0.0245	0.7629
PCA9	0.0182	0.0028

Table 4-21: Wilcoxon rank sum test of each PCA feature in all experiments with pre-shock locating at section C (10-20 second before countershock). The corresponding feature set boxplots can be found in Appendix B, figure B-65, and B-66 respectively.

Method	5 second pre-shock ECG		
	Original features	Normalised Features	PCA features
WT	47±1%	41±2%	48±2%
STFT1	46±3%	43±2%	49±3%
STFT2	45±4%	49±4%	39±0
STFT3	37±4%	49±3%	47±3%

(a)

Method	10 second pre-shock ECG		
	Original features	Normalised Features	PCA features
WT	58±2%	55±2%	43±2%
STFT1	57±2%	58±4%	42±6%
STFT2	52±3%	58±4%	44±8%
STFT3	53±3%	59±3%	42±6%

(b)

Method	15 second pre-shock ECG		
	Original features	Normalised Features	PCA features
WT	48±0%	50±4%	44±1%
STFT1	38±7%	53±2%	53±6%
STFT2	42±3%	51±3%	56±3%
STFT3	48±1%	51±3%	52±1%

(c)

Method	20 second pre-shock ECG		
	Original features	Normalised Features	PCA features
WT	42±9%	54±3%	43±7%
STFT1	40±9%	51±2%	44±2%
STFT2	38±15%	49±7%	39±3%
STFT3	46±9%	47±0%	46±2%

(d)

Table 4-22: The overall test specificities based on the test sensitivity over 90%: (a) 5-second of pre-shock ECG, (b) 10-second of pre-shock ECG, (c) 15-second of pre-shock ECG, (d) 20-second of pre-shock ECG

CHAPTER 5

THE SUPPLEMENT STUDIES OF THE WAVELET ANALYSIS IN THE SHOCK OUTCOME PREDICTION

CHAPTER 5
THE SUPPLEMENT STUDIES OF THE WAVELET ANALYSIS IN THE SHOCK OUTCOME PREDICTION

5.1 Introduction

This chapter describes preliminary work to further develop wavelet transform-based power spectral analysis of the surface ECG during cardiac arrest. Two studies were carried out. The first study, described in section 5.2, investigated the behaviour of the probability of successful defibrillation (PROSC) variable over time. The second study, described in section 5.3, investigated the effect of a change in the central frequency of the wavelet on the prediction of shock outcome. The chapter concludes with a summary in section 5.4.

5.2 The probability of successful defibrillation (PROSC) in VF patients

5.2.1 Introduction

The previous chapter described results from experiments which examined the prediction of shock outcome using the pre-shock trace immediately before the time of shock. It was found by the author that the combination of the FM and FT parameters gave the best performance. In 2001 our collaborating research group in Norway

proposed a method for devising a single Fourier-based variable for monitoring CPR efficiency (Eftestol et al, 2001). The probability of successful defibrillation (PROSC) was introduced as a parameter to discriminate between ROSC and NOROSC outcomes. The PROSC function was proposed as a measure of the prediction of shock outcome to display on a monitor during CPR.

Following this work of the Norwegian group, the objective of this study was to investigate the utility of the method for expressing multivariate information in a single variable using the wavelet method.

5.2.2 Methodology

An overview of the methodology is illustrated in figure 5-1. It was found from the study of the optimal length of pre-shock signal described in the previous chapter, that an analysis of 10 seconds pre-shock gave the best performance for prediction. Hence, a sliding 10-second window was employed to analyse the VF signal beginning at 20 seconds before countershock. Two characteristic features, FM and FT, were extracted from each window using wavelet power spectral analysis. The PROSC was determined from the PROSC database using the values of FM and FT. The position of the window was then shifted along the ECG signal in steps of 1 second until the end of the 20 second trace segment corresponding to the temporal location of the shock.

The database of PROSC was computed from the 821-trace ECG data set of VF immediately prior to countershock. Two characteristic features, FM and FT, were extracted from the 10 second pre-shock signal using the power spectrum-based WT method. The technique of feature preparation discussed in section 3.4.1 was employed to normalise the characterising features within the range from zero to one. The 2D PDFs of the ROSC and NOROSC database were estimated using the multidimensional histogram and Gaussian kernel smoothing techniques as detailed in section 3.5.1. The estimated *a posteriori* probability was defined as PROSC in the study. The estimated *a posteriori* probability is determined from the estimate probability distribution function PDFs as defined in the following equation:

$$PROSC(v) = \frac{p(v / \omega_{ROSC})}{p(v / \omega_{ROSC}) + p(v / \omega_{NOROSC})} \quad (5\text{-}1)$$

where $p(v/\omega_{ROSC})$ and $p(v/\omega_{NOROSC})$ are the estimate PDFs with feature vector v of the ROSC and NOROSC groups respectively. The feature vector v contains FM and FT obtained from wavelet power spectrum analysis. The 2D PDF of each class was determined using multidimensional histograms and Gaussian smoothing as described in chapter 3. The PROSC distribution of the ECG data set is shown in figure 5-2. This surface represents the probability of the successful shock in feature space.

5.2.3 Results

This section demonstrates the use of PROSC in monitoring the probability of successful shock outcome. The author investigated all 13 patient trace sets whose last shock gave a ROSC outcome for the patient. Three examples of the patient traces investigated by the author are used to illustrate the method. Each example shows the behaviour of multiple pre-shock traces from a single patient.

Figure 5-3 shows the pre-shock ECG traces of a patient who was administered with 10 countershocks. Each trace represents 20 seconds of VF signal prior to countershock with the exception of the fifth trace which exhibits ventricular tachycardia (VT). The outcomes from each shock are given in table 5-1. Pre-shock ECG numbers 1 to 9 gave a NOROSC shock outcome whereas ROSC was achieved after shock number 10. The PROSCs corresponding to each ECG trace is shown in figure 5-4. In this example, it can be clearly seen that the PROSC of the final trace segment which is associated with a ROSC outcome has a significantly higher value than the other traces for the whole of the 10 second duration of the analysis.

Figure 5-5 contains another example of the ECG traces from a single patient. This patient was administered with 6 countershocks. Each trace represents 20 seconds of VF signal prior to countershock. The shock outcome corresponding to each shock is shown in table 5-2. The pre-shock signal numbers 1 and 2 were associated with NOROSC outcomes whereas ROSC in shocks 3, 4, 5, and 6. Figure 5-6 shows the

PROSC acquired from each trace. It can be clearly seen that the PROSC curves computed from the trace segment associated with ROSC outcomes (shock 3, 4, 5, and 6) are significantly higher than the other traces associated with NOROSC outcomes (shock 1 and 2). Although this clear separation between the ROSC and NOROSC curves exists, it is interesting to note that refibrillation occurred after shocks 3,4, and 5.

Figure 5-7 contains a third example of the ECG traces from a single patient. This patient was administered with 5 countershocks. Each trace represents 20 seconds of VF signal prior to countershock. The shock outcome corresponding to each shock is shown in table 5-3. The pre-shock signal numbers 1, 2 and 3 were associated with NOROSC outcomes whereas shocks 4 and 5 were associated with a ROSC outcome. Figure 5-8 shows the PROSC acquired from each trace. Unlike the two previous examples, the PROSC curve for the last trace associated with the ROSC outcome was lower than the other traces associated with NOROSC outcomes (shock 1, 2, and 3). This experiment shows that for some cases PROSC is unreliable for accurately determining the probability of shock success.

5.2.4 Summary

PROSC was employed as a parameter to indicate the probability of the defibrillation success. Example traces from three selected patients were used to demonstrate the use of PROSC in the monitoring of probability of successful shock. From the first two examples, the pre-shock signals corresponding to successful shocks gave the higher PROSC than the pre-shock signal corresponding to unsuccessful shock. However it was noticed that in the second example, refibrillation still occurred after three successful shocks although they exhibited high PROSC values. The third example illustrated a case where PROSC did not perform well as the indicator of the probability of shock outcome. In the third example, the PROSC of the traces associated with NOROSC were higher than the PROSC of the trace associated with the final ROSC outcome.

The three examples provided above are typical of the problems encountered during the analysis of a range of patients undertaken by the author. Hence it was concluded

quite early on in the study that PROSC is not a useful parameter with which to indicate the probability of the defibrillation success, since for many cases, PROSC proved unreliable for accurately determining the probability of shock success.

5.3 The effect of a change in the central frequency of the wavelet

5.3.1 Introduction

In the numerical experiments undertaken in the main work described in chapter 4, the standard Morlet function was used as the mother wavelet function in the analysis of shock outcome prediction. The central frequency of the Morlet function used in these experiments was 5.33 rad/s (a standard value often used in the literature). Addison et al (2002) found that the use of low-oscillation complex wavelets improved the detection of localised signal features within non-destructive testing signals that were associated with reflection components. They further speculated that low oscillation wavelets could be useful for a variety of other data analysis tasks, in particular fluid turbulence signals and ECG signals. The temporal isolation of signal features is improved for the analysis using low-oscillation complex wavelets. Following this work, this section reports on a study of the effect of the central frequency of the wavelet on shock outcome prediction. The complete form of the Morlet function was used in the investigation.

5.3.2 Methodology

The Morlet wavelet can be expressed as equation 2-26 in chapter 2. This is the full expression of the Morlet wavelet. However, the correction term can be ignored if the value of $f_0 >> 0$ in which case the Morlet wavelet can be expressed as equation 2-27. The central frequency f_o can be written in term of angular frequency ω_o as follows:

$$\omega_o = 2\pi f_o \tag{5-2}$$

where the unit of ω_o is rad/s. Hence, the complete Morlet wavelet function can be expressed as:

$$\psi(t) = \pi^{-1/4}\left(e^{i\omega_0 t} - e^{-(\omega_0)^2/2}\right) e^{-t^2/2} \tag{5-3}$$

and the standard Morlet wavelet as

$$\psi(t) = \pi^{-1/4} e^{i\omega_o t} e^{-t^2/2} \tag{5-4}$$

Plots of the complete Morlet function with central frequencies set to 1, 2, 5, and 8 rad/s are shown in figures 5-9(a), (b), (c), and (d) respectively. From the plots it can be seen that Morlet functions with high central frequency are more oscillatory than those with low central frequency.

The Fourier transform of the complete Morlet wavelet is

$$\Psi(\omega) = \sqrt{2}\sqrt[4]{\pi} e^{\frac{-(\omega^2+\omega_o^2)}{2}}\left(e^{\omega\omega_o} - 1\right) \tag{5-5}$$

and the energy spectrum is

$$|\Psi(\omega)|^2 = 2\sqrt{\pi} e^{-\left(\omega^2+\omega_o^2\right)}\left(e^{\omega\omega_o} - 1\right)^2 \tag{5-6}$$

Figures 5-10 and 5-11 compare the standard Morlet wavelet and the complete Morlet wavelet and their associated spectra. Figure 5-10(a) and 5-10(b) illustrates the real and imaginary parts of the standard wavelet for ω_o = 1 and 2 rad/s respectively. Both real and imaginary parts of the wavelet are confined by the Gaussian envelope. Figure 5-10(c) shows the Fourier transform of the standard Morlet wavelet for ω_o = 1 and 2 rad/s. The standard Morlet wavelet for ω_o = 1 rad/s obviously does not satisfy the admissibility condition in equation 2-7 since the DC component (i.e. the zero frequency component) of the wavelet is not equal to zero. Hence the standard Morlet wavelet cannot be used in practice with very low central frequencies. However, the

complete Morlet wavelet does satisfy the admissibility condition and can be used. Figures 5-11(a) and 5-11(b) show the real and imaginary parts of the complete Morlet for ω_o = 1 and 2 rad/s respectively. Notice that in both figures, the real parts are not confined by the Gaussian envelope because of the correction term. However, the correction term allows the complete Morlet to satisfy the admissibility condition as shown in figure 5-11(c) where there is no zero frequency component corresponding to each wavelet.

Figure 5-12(b) shows the change in shape of the wavelet spectral density graph associated with varying central frequency obtained from the 1 Hz sinusoidal test signal shown in figure 5-12(a). The wavelet power spectral densities of this test signal were computed using the Morlet-based CWT with central frequencies set to 1, 2, 3, 4, 5, 6, 7, 8, and 9 rad/s. It can be seen in figure 5-12(b) that narrower spectra are obtained for higher central frequencies. This is to be expected as the more oscillatory wavelets provide higher spectral resolution (and correspondingly lower temporal resolution). Wavelets with very low central frequencies produced broader spectra and, more importantly, their frequency localisation becomes quite inaccurate (See for example the spectrum plot associated with 1 rad/s central frequency). This inaccurate frequency localisation occures at low values of ω_0 because of the correction term of the complete Morlet.

The following example shows how the correction term causes the frequency localisation error. Figure 5-13 illustrates the correlation between a 1 Hz sinusoid and the real part of scaling Morlet wavelet at time b (peak of sinusoidal). The complete Morlet wavelet at arbitrary scale a at location b is defined as:

$$\psi_{a,b}(t) = \frac{\pi^{-1/4}}{\sqrt{a}}\left(e^{i\omega_0\left(\frac{t-b}{a}\right)} - e^{-(\omega_0)^2/2}\right)e^{-\left(\frac{t-b}{a}\right)^2/2} \qquad (5\text{-}7)$$

The central frequency (ω_o) of the mother wavelet employed in the examples was set to 1 rad/s. The scale a is related to the central frequency as shown in equation 5-8.

$$a = \frac{\omega_o}{\omega} \tag{5-8}$$

Figures 5-13(a) and 5-13(b) present the correlation using the scaling wavelet employing the standard Morlet and complete Morlet respectively. The scale a was initially set equal to 0.16 corresponding to a frequency of 1 Hz. In figure 5-13(a), the scaled standard Morlet wavelet is in phase with the waveform giving a maximum positive correlation. On the other hand, for the complete Morlet (as shown in figure 5-13(b)) negative components of the transform are produced in the range t_1 and t_2 since the correction term has effect on the real part of the complete Morlet associated with low central frequencies. However, for the complete Morlet with scale a equal to 0.27 (corresponding to 0.6 Hz) shown in figure 5-13(c), the integral of the product of the waveform with the wavelet produces a maximum positive value (i.e. maximum correlation). In these examples we can see that the use of the complete Morlet for very low ω_0 produces erroneous frequency localisation in the wavelet transform.

5.3.3 Results

From the analysis of shock outcome prediction using the WT-based technique, described in sections 4.2.1 and 4.3.1 of chapter 4, it was found that a 10 second length of ECG signal immediately prior to the shock achieved the best performance when employing the combined FM-FT feature. It was therefore decided to employ this window length and feature combination in the study of the effect of central frequency on the analysis. In addition, the complete form of the Morlet function was applied in the study for extracting the characteristic features. The central frequencies used in the experiments were 1, 2, 3, 4, 5, 6, 7, 8, 9, and 10 rad/s. The original features values were normalised in the unit interval as described in chapter 3, section 3.4.1. The bin sizes were adjusted according to setting the number of bins equal to 50, 75, 100, 125, 150, 175, and 200 bins to cover the unit interval. The Gaussian kernel smoothing histograms were set to 0.1, 0.2, 0.3, 0.4, 0.5, 0.6, 0.7, 0.8, and 0.9 units in width. A sensitivity of ROSC of 95% outcome was set as the criterion for the training classifier. The cost functions found for each case was then used to test the remaining data. For cases where this criterion was not achieved (i.e. a test sensitivity under 90%), the experiment which gave the highest sensitivity was chosen as the highest performance

of the classifier. The cross validation technique was employed to arrange the training and test sets. Two cross validations were used in this study. That is the ROSC and NOROSC data was partitioned equally into a training group and a test group. The performances of classifier are presented as the mean of the cross-validated sensitivities and specificities.

Figure 5-14 presents a summary of the best classifier performance for all central frequencies investigated. The best performance achieved 57±0% specificity obtained at 90±4% sensitivity for a central frequency of 2 rad/s. In addition, it can be noticed that the classifications associated with ω_o of 3 rad/s or less gave relatively small errors in specificity. Overall the study shows that the change of central frequency has, within errors, no effect on the shock outcome prediction. (Note that similar results were also found by the author using both single features FM and FT).

5.3.4 Summary

This analysis studied the effect of a change of wavelet central frequency on the prediction of shock outcome. The complete Morlet wavelet with varying central frequencies was used to extract the characteristic features. This work revealed that a change in wavelet central frequency has no discernable effect on the results obtained from the classifier.

5.4 Chapter summary

This chapter described two additional studies concerning the use of wavelet analysis of the VF waveform for shock outcome prediction. The first study developed a method for devising a variable for monitoring CPR efficiency. This PROSC parameter was employed to indicate the probability of the defibrillation success. For some cases, the pre-shock signals corresponding to successful shocks produced a higher PROSC value than the pre-shock signal corresponding to unsuccessful shocks. In conclusion, it appears that the PROSC parameter is an unreliable indicator of the probability of defibrillation success. The second study considered the effect of

wavelet central frequency on the shock outcome prediction using the wavelet analysis of the VF waveform. The complete form of the Morlet wavelet was used as the wavelet function in this study. No marked change in performance was found by varying the central frequency. Hence, the results indicate that central frequency is not a key parameter in the performance of the shock outcome prediction classifier.

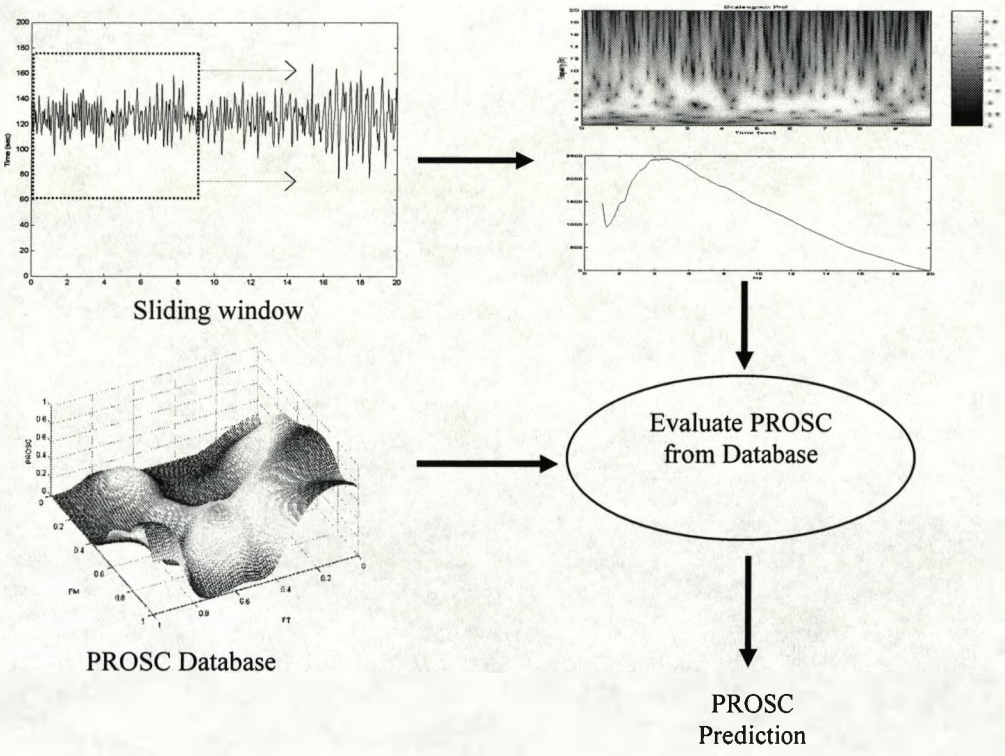

Figure 5-1: Schematical diagram of PROSC analysis

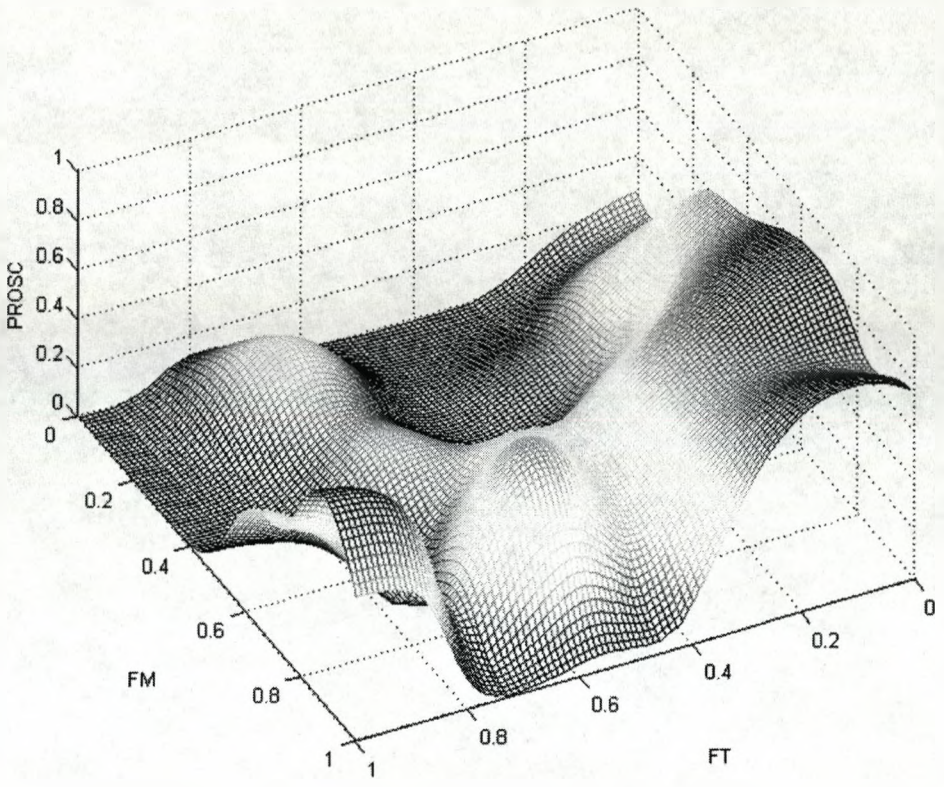

Figure 5-2: The database of PROSC

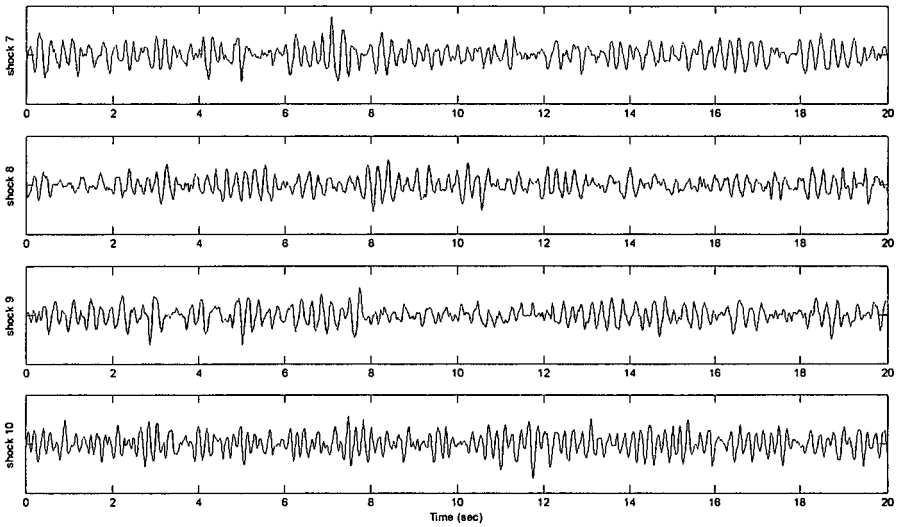

Figure 5-3: ECG traces of the first example patient

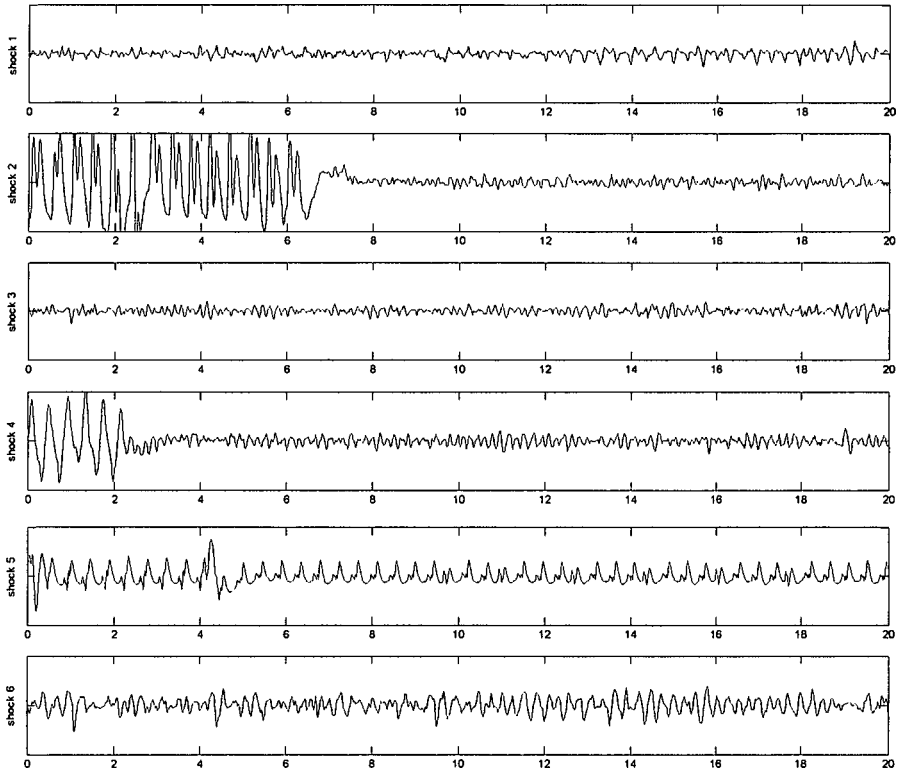
shock 1
shock 2
shock 3
shock 4
shock 5
shock 6
0
2
4
6
8
10
12
14
16
18
20

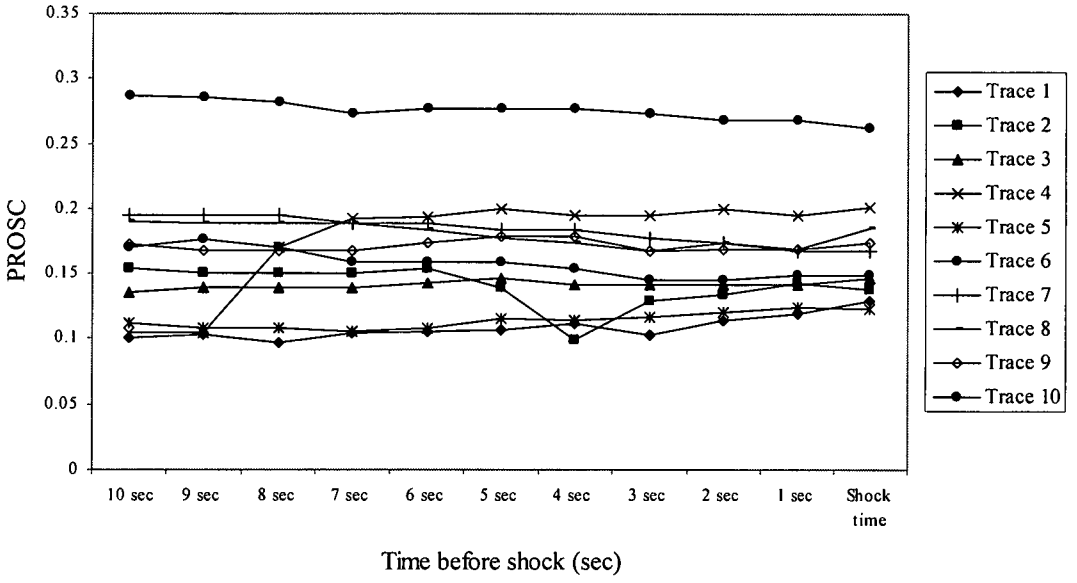

Figure 5-4: PROSC for each trace from the first example patient

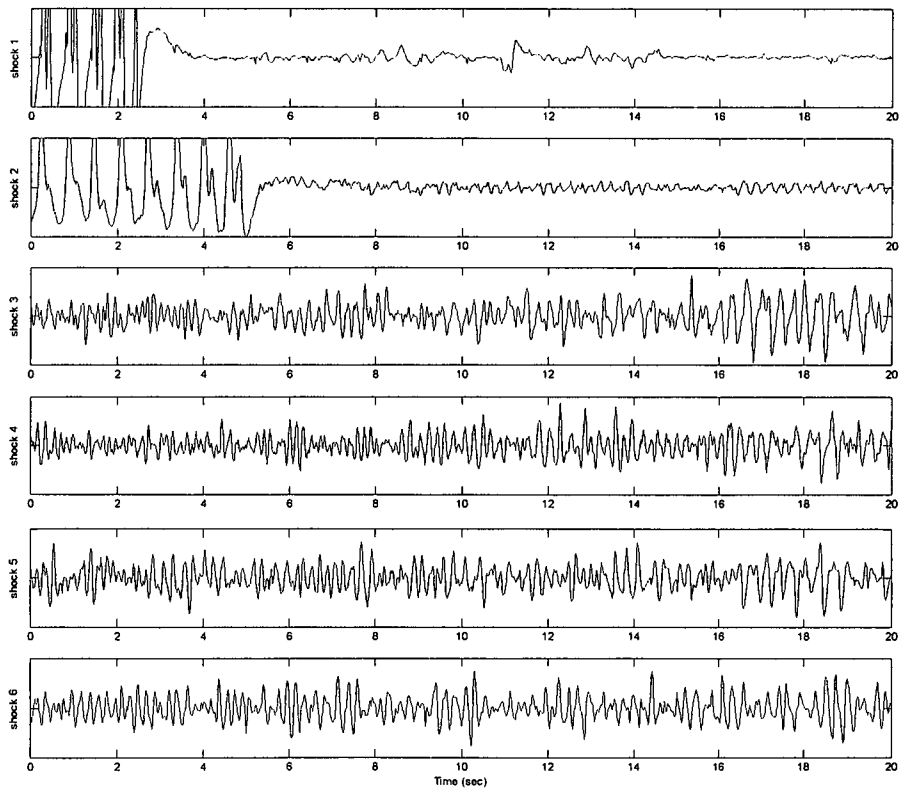

Figure 5-5: ECG traces of the second example patient

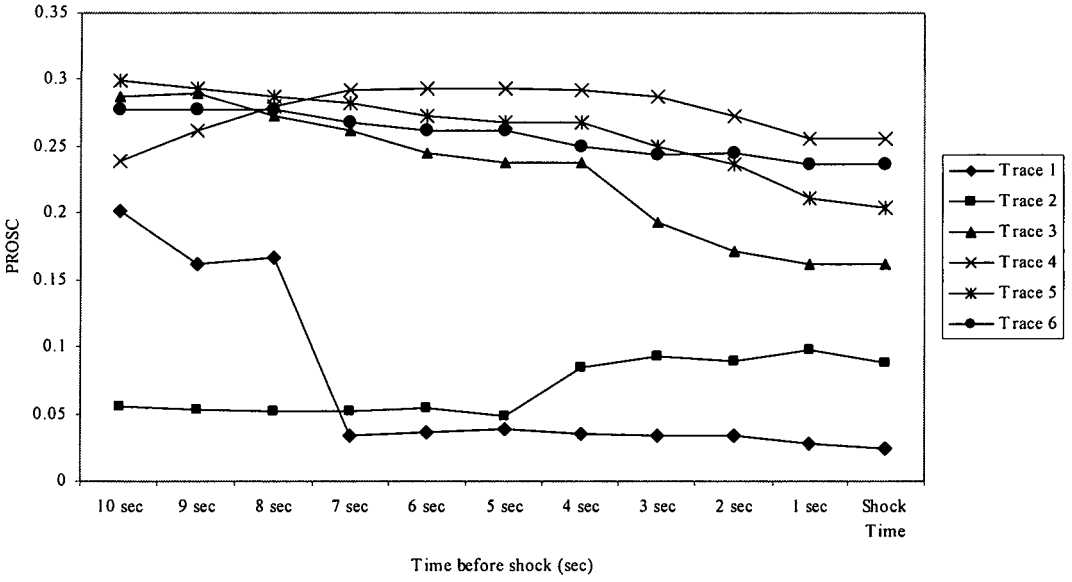

Figure 5-6: PROSC for each trace from the second example patient

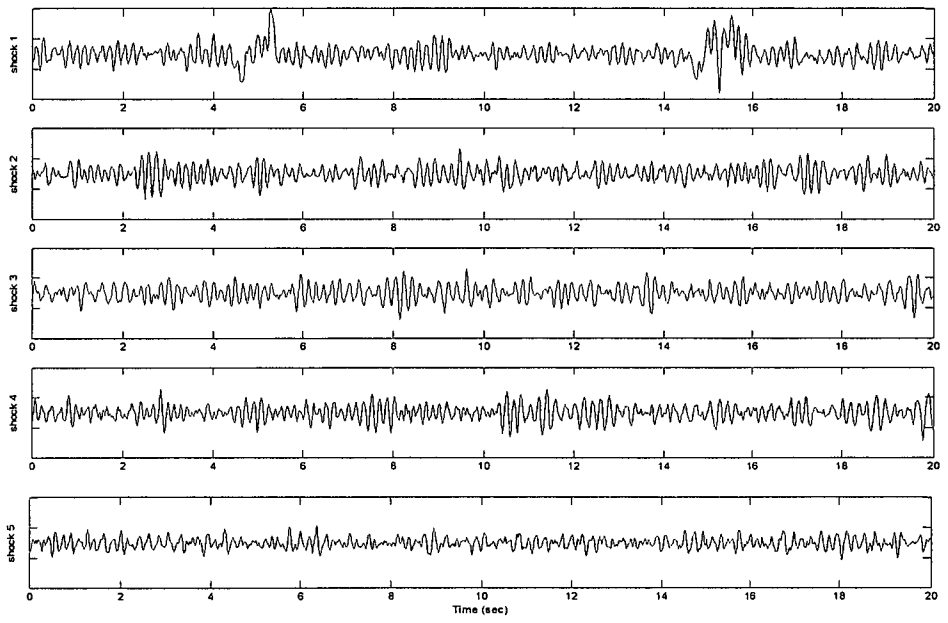

Figure 5-7: ECG traces of the third example patient

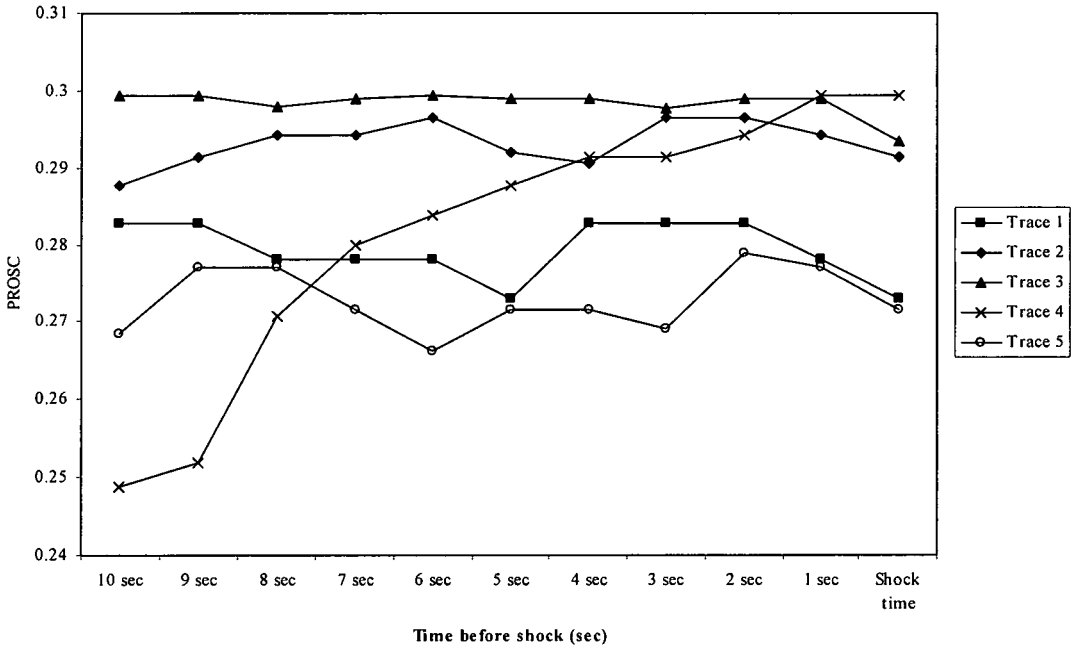

Figure 5-8: PROSC for each trace from the third example patient

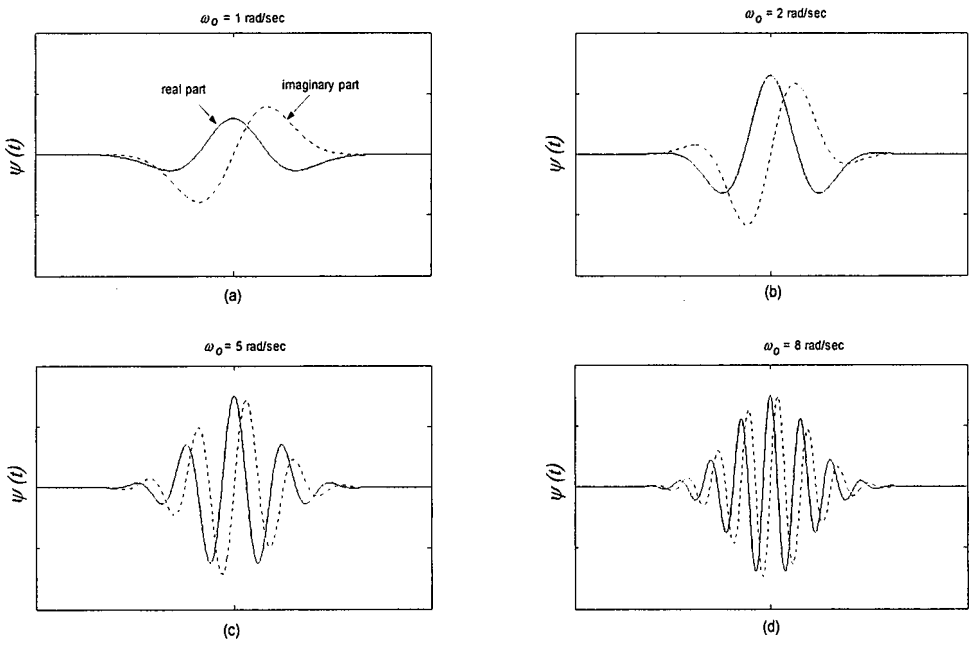

Figure 5-9: The Complete Morlet function with varying central frequencies: (a) $\omega_o = 1$ rad/s; (b) $\omega_o = 2$ rad/s; (c) $\omega_o = 5$ rad/s; (d) $\omega_o = 8$ rad/s

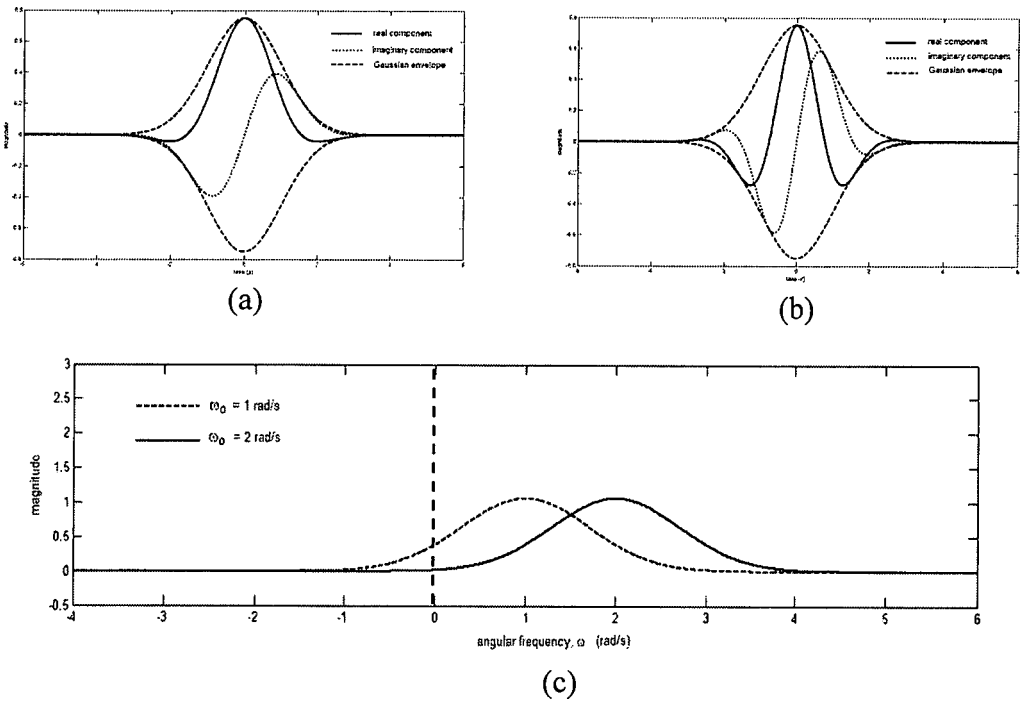

Figure 5-10: The Standard Morlet wavelet at (a) $\omega_o = 1$, (b) $\omega_o = 2$, (c) The Fourier transform $\omega_o = 1$ and 2

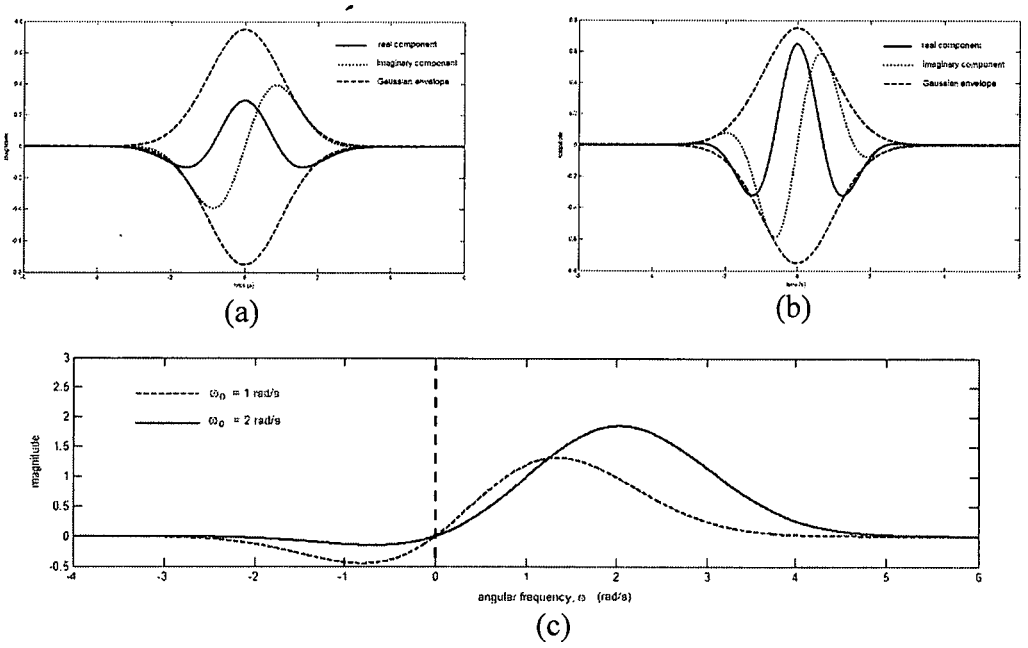

Figure 5-11: The complete Morlet wavelet at (a) $\omega_o = 1$, (b) $\omega_o = 2$, (c) The Fourier transform $\omega_o = 1$ and 2

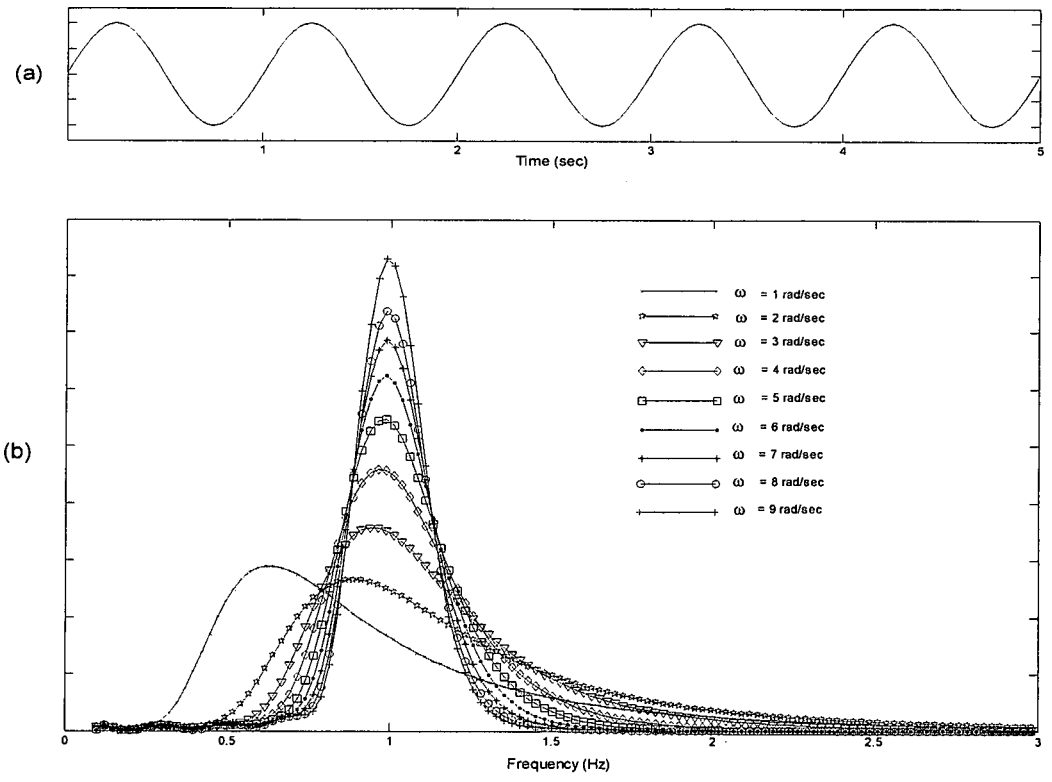

Figure 5-12: The wavelet power spectral of the example signal

Studied signal; (b) Wavelet power spectra with varying central frequency

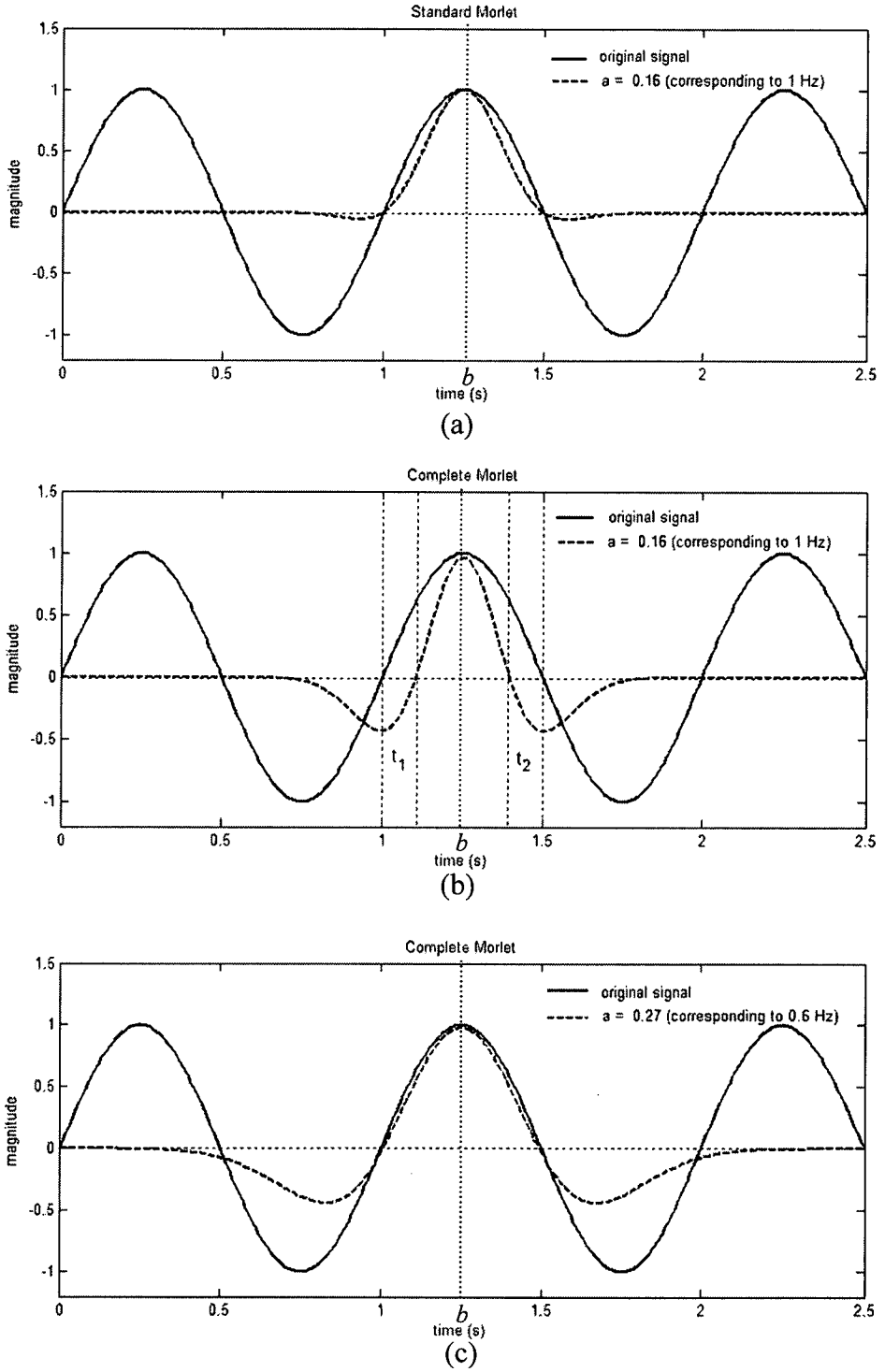

Figure 5-13: A wavelet interrogating a sinusoidal waveform

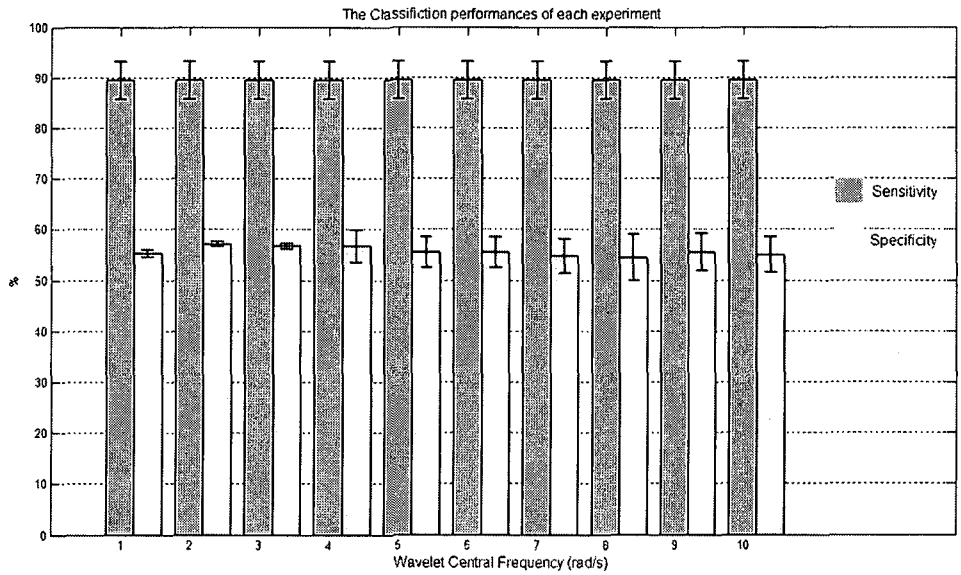

Figure 5-14: The best performances of the classifier for each ω_o

Shock Number	Pre-Shock	Shock Outcome
1	VF	Asystole
2	VF	Asystole
3	VF	Asystole
4	VF	EMD
5	VT	VF non-resest
6	VF	VF non-resest
7	VF	VF non-resest
8	VF	VF non-resest
9	VF	EMD
10	VF	ROSC

Table 5-1: The shock outcome of each shock in the first example

Shock Number	Pre-Shock	Shock Outcome
1	VF	Asystole
2	VF	EMD
3	VF	ROSC
4	VF	ROSC
5	VF	ROSC
6	VF	ROSC

Table 5-2: The shock outcome of each shock in the second example

Shock Number	Pre-Shock	Shock Outcome
1	VF	VF non-reset
2	VF	VF non-reset
3	VF	VF non-reset
4	VF	ROSC
5	VF	ROSC

Table 5-3: The shock outcome of each shock in the third example

CHAPTER 6

CONCLUSIONS, DISCUSSION, AND RECOMMENDATIONS

CHAPTER 6
CONCLUSIONS, DISCUSSION, AND RECOMMENDATIONS

6.1 Introduction

The aim of this research was to improve shock outcome prediction from the VF signal through the use of wavelet transform (WT) and short time Fourier transform (STFT) based time-frequency analysis methods. This fits with current work by other groups in this area investigating alternative techniques (e.g. Eftestol et al, 2000; Strohmenger et al, 2001; and Calloway et al, 2001) all of whom have the global aim of improving the resuscitation technique for VF patients. A time-frequency-based methodology was developed by the author to provide an enhanced method of prediction of defibrillation shock outcome. This final chapter summarises the results of the study as follows: section 6.2 contains an overview of the main results; a brief discussion on a new resuscitation protocol is given in section 6.3; finally, recommendations for future work are provided in the last section of the chapter: section 6.4.

6.2 Overview of the results

The data set used in this study contained 821 ECG traces of VF immediately prior to countershock obtained from 156 patients with out-of hospital cardiac arrest of cardiac etiology. The shock outcomes were categorised as either ROSC or NOROSC which included EMD, asystole, and VF. Characteristic features correlating with shock outcome were extracted from the CWT and STFT spectra computed from the VF signals before countershock.

A Bayes classifier was developed in this work for classifying between ROSC and NORSC outcomes. The *a posteriori* probability was determined from the probability distribution functions (PDFs) estimated using multidimensional histogram and Gaussian kernel smoothing techniques. In the system validation carried out by the author, both 1D and 2D classifiers in general performed well with synthetic test data sets. It was shown that, although achieving good training performances (as one would expect), the use of a large number of bins and narrow Gaussian widths for the PDF estimation technique produced poor test performances. Cross validation was employed to improve the confidence of results. After a series parametric studies involving a variety of candidate cross validation numbers it was found that two cross validations was the best choice for the main work involving the Oslo data set.

A comprehensive series of parametric tests were then conducted to determine the optimal configuration of the technique. This was carried out for PDF estimation generated using a range of bin sizes and Gaussian kernel widths. The training sensitivity was set to 95%. The best performance was determined from the classifier which achieved the highest specificity at a test sensitivity criterion (within 5% of training sensitivity). A brief overview of the results of this analysis is presented as follows:

6.2.1 Shock outcome prediction employing power spectral analysis based on WT and STFT

6.2.1.1 Results

This section summarises the results of the parametric study of shock outcome prediction carried out by the author utilising both the WT and the STFT. Three different feature formats were used in the study. These were the original feature sets, normalised feature sets, and PCA-based feature sets. Each of these was tested for shock outcome performance based on pre-shock window length (immediately prior to countershock, summarised in table 4.22) and the temporal location of the analysis segment prior to the shock.

- **Shock outcome prediction using the original feature sets**

The first sets of results were obtained from the original characterising features where the minimum and maximum values of the features were confined to a range between zero and twenty. For these experiments, a 10 second period of pre-shock signal was found to be the optimal length of trace to use for the shock outcome prediction using the WT and the STFT. The highest performance achieved was 58±2% specificity at 90±4% sensitivity and was obtained from the WT. However, within errors, the analysis using the STFT1 also produced results similar results achieving 57±2% specificity at 90±4% sensitivity. In addition the results obtained using STFT2 and STFT3 achieved around 5% less specificity for the same level of sensitivity.

- **Shock outcome prediction using the normalised feature sets**

The features used in this second series of classification studies were normalised from the original features. The normalisation technique is detailed in chapter 3. For these experiments, a 10 second of pre-shock signal was found to be the optimal length for the shock outcome prediction using both the WT and the STFT. The highest performance was obtained using the STFT3 method which achieved 59±3% specificity at 90±4% sensitivity. In several experiments, it was found that the use of the normalised feature sets improved the performances of classifiers which employ the STFT features (in particular those classifiers associated with the FT feature). The normalisation technique solves the problem of the localised feature distribution found in the original sets. However, within errors, the performances were not significantly different from the results using the original feature sets in the WT analysis.

- **Shock outcome prediction using the PCA feature sets**

The features used here were derived from the PCA analysis. Nine 1D-PCA features were investigated and the four features giving the highest performances were combined together to provide a number of 2D feature sets. The analysis using the STFT (2 second window) gave the highest performance for these experiments, achieving 56±3% specificity at 92±4% sensitivity. Overall the classifier using the PCA feature sets was found to improve the analysis of the STFT with a 15 second

length of pre-shock. In contrast, the use of PCA feature sets in the analysis of 5, 10, and 20 second pre-shock length produced worse performances when compared to the analysis employing the original and normalised feature formats.

- **The position dependence of time-frequency analysis**

An investigation was also carried out into the relationship between the performance of shock outcome prediction and the temporal distance of the analysis window from the shock event. The results showed that the predictive information contained in the ECG is in general independent of the temporal distance to the shock event for both the WT and STFT-based method. This is contrary to initially reported findings (Addison et al, 2002) which suggested that such a correlation did exist.

6.2.1.2 Discussion of results

For the past two decades, several studies have attempted to improve the resuscitation protocol for VF patients. The prediction of defibrillation outcome has been analysed in both animal models (Brown et al, 1989 and 1991; Noc et al, 1999; Patwardhan et al, 1999; Amann et al, 2001 and 2002; Hamprecht et al, 2001; Marn-Pernat et al, 2001) and human models (Weaver et al, 1985; Monsieurs et al, 1998; Eftestol et al, 2000; Calloway et al, 2001; Strohmenger et al, 2001; Podbregar et al, 2003; Watson et al, 2004). It is believed that studies involving human datasets are essential for the development of a resuscitation protocol (Watson et al, 2005).

Calloway et al (2001) examined the prediction of defibrillation success using a scaling exponent. Their work used ECG waveform recordings from automated external defibrillators obtained for 75 VF adult patients collected using a Medtronic Lifepack 300. The study showed that lower values of the scaling component correlated with increased probability of successful defibrillation (including EMD). However, only the first shock (before other advanced life support) was investigated in their study. The author believes that the subsequent shocks may have provided extra useful information for their analysis. Figure 6-1 compares the ROC using time-frequency based-methods to a reference data ROC curve published by Calloway et al (2001). Considering performances at sensitivities in the range 90-92%, the best

results found by the author and presented in this thesis achieved specificities of 58%, 59%, and 56% obtained from the use of the original feature sets, normalised feature sets, and PCA feature sets respectively. The Calloway ROC curve, however, shows that their system achieves only 39% specificity at the same level of sensitivity. The Calloway ROC curve was obtained using a different data set collected on different defibrillator machines. A standard data set is necessary for rigorous comparative studies between these two (and other) techniques.

Strohmenger et al (2001) investigated shock outcome prediction during human VF episodes using amplitude variables based on the same Oslo data set used in this thesis. The best result achieved by this group using the amplitude variable was 67% specificity at 73% sensitivity obtained for a 3000 ms length of pre-shock signal. This performance was obtained from the data ROC curve at a pre-selected threshold. No reason was given for their choice of threshold. This can be compared to the wavelet based-study of this thesis where the system ROC curve based on the original FM-FT feature (figure 4-31) which shows that 74±4% specificity can be achieved at 73±6% sensitivity. It should also be noted that data cross validation was not applied in Strohmenger's study; hence there is an inherent lack of confidence in their results. Furthermore, the quoted sensitivity of 73% used by Strohmenger is too small for use in practice since a high sensitivity is necessarily required for system implementation. (It is believed that a 90 to 95% sensitivity will be required for use in practice.) Strohmenger et al (2001) also reported that prediction using a dominant frequency marker achieved 42% specificity at 92% sensitivity using their method. The author's classifier achieved 56±3% specificity at 92±4% sensitivity using a PCA feature set for the STFT2 method. It is clearly seen that the analysis of time-frequency-based methods achieves better performance when compared to Strohmenger's results.

In another study, our collaborating research group in Norway (Eftestol et al 2000) employed a standard Fourier frequency-domain method (i.e. not a time-frequency method, e.g. STFT or WT) for shock outcome prediction. Again, this study was based on the same data in this thesis. The best performance of the classifier corresponded to a combination of PCA based spectral features, achieving 42±1% specificity at 92±1% sensitivity. As described in the previous section the author achieved 56±3% specificity at 92±4% sensitivity using a PCA feature set for the STFT2 method. It is

clearly seen that the performance of shock outcome prediction corresponding to the time-frequency-based method gave significantly better performance than the results associated with FFT analysis. In addition, Eftestol et al (2000) found that the use of PCA features improved the performances of prediction using their Fourier analysis-based method. However no consistent improvement was found by the author using PCA features in the present study associated with either the WT or STFT analysis.

Overall it can be concluded that the time-frequency power spectrum methods developed by the author produced consistently superior results to other currently available methods. Further, within errors, no real difference could be found between the WT and STFT-based methods investigated by the author or between the original, normalised and PCA features. This suggests that the key factor for the superior results is the time-frequency decomposition itself.

There are however some limitations in the author's study which must be stated here. An insufficient number of ROSC data (9.26% of whole data set) limits the use of a high cross validation number. The small number of ROSC data causes a large variance in test sensitivity and specificity in the classifier when high cross validation numbers are employed as described in section 3.8, chapter 3. Multidimensional analysis is limited because of a sparse number of ROSC data. For example, in a three dimensional classification if each dimension is divided into 100 bins, a 1,000,000 bin 3D ROSC PDF must be described by just 87 points. In addition, but of secondary concern, the speed of computation drops markedly as the dimensionality of the analysis increases.

6.2.2 The probability of successful defibrillation (PROSC)

6.2.2.1 Results

This study aimed to develop a 'real time' variable for monitoring CPR efficiency. PROSC was employed as a parameter to indicate the possibility of the defibrillation success. PROSC was defined as the *a posterior* probability function associated with two characteristic features: FM and FT. Several cases which gave a ROSC outcome in the last shocks for the patient were investigated in this study. From the results it

became clear that a high value of PROSC does not necessarily correlate with a high probability of shock success. In many cases a high PROSC variable was associated with a NOROSC outcome and vice versa. In addition, refibrillation often occurred after the successful shocks associated with high values of PROSC. It was therefore concluded that PROSC is not a reliable parameter with which to indicate the probability of the defibrillation success.

6.2.2.2 Discussion of results

Our collaborating research group in Norway (Eftestol et al 2001) investigated the PROSC variable derived from frequency spectrum features. In their study, they stated that the PROSC 'may be useful' as guidance during CPR to optimise shock timing in the VF resuscitation. However, only two patient trace examples were presented in their paper. As stated in the previous section, the author found that PROSC is not a reliable parameter with which to indicate the probability of successful defibrillation.

6.2.3 The effect of a change in wavelet central frequency on shock outcome prediction

6.2.3.1 Results

The effect of a change in wavelet central frequency on the prediction of defibrillation outcome was investigated. The complete form of the Morlet function was used as the mother wavelet function in this analysis. The central frequency range considered in the study was between 1 and 10 rad/s. The best performance achieved was 57±0% specificity obtained at 90±4% sensitivity for a central frequency of 2 rad/s. However, the results obtained from other central frequencies varied only slightly from this optimal performance (i.e. within errors).

6.2.3.2 Discussion of results

Addison et al (2002) found that the use of low-oscillation complex wavelets improved the detection of localised signal features within non-destructive testing signals that were associated with reflection components. The use of low wavelet

central frequency is relatively new, and although Addison et al (2002) suggested its use for the analysis of the ECG, the author believes that the work presented in this thesis represents the first attempt to do so. However, as shown by the results of the analysis, a change in wavelet central frequency has no significant effect on the shock outcome prediction. Therefore, it was concluded that wavelet central frequency is not a key parameter to be considered for the optimisation of the shock outcome prediction technique.

6.3 The development of a new resuscitation protocol

The European Resuscitation Council (ERC) issued the guidelines for Advanced Life Support (ALS) in 2000 (Latorre et al, 2001). The ALS algorithm contained in these guidelines for the management of cardiac arrest in adults is shown in the diagram of figure 6-2. Cardiac arrest rhythms can be categorised into two groups:

- Ventricular Fibrillation / Pulseless Ventricular Tachycardia (VF/VT)
- Asystole and Electromechanical Dissociation(EMD)

The heart rhythms associated with VF/VT requires an immediate defibrillation attempt after basic life support (BLS). Within the protocol, up to three sequential shocks, if required, are given initially with energies of 200 J, 200 J, 360 J. A few seconds after delivery of the final shock in the sequence, one minute of cardiopulmonary resuscitation (CPR) is administered. For non-VF/VT rhythms (i.e. asystole and EMD), 3 minutes of CPR is performed, if the patient is in cardiac arrest. (Note that 1 minute of CPR is performed for a non-VF/VT rhythm if it occurs after defibrillation.)

According to the ERC guidelines, the heart rhythms associated with VF/VT requires an immediately defibrillation attempt after BLS (Latorre et al, 2001). However, Xie et al (1997) reported that an unsuccessful defibrillation causes tissue damage during the shock period. A rhythm qualification stage could be added to the original protocol as shown in figure 6-3. This stage will classify VF signal as shockable or nonshockable signal. The shockable VF will be treated with immediate defibrillation whereas the

nonshockable VF will follow a course of CPR prior to defibrillation. Several studies have indicated that pre-shock CPR can have a positive influence on the success of defibrillation (Strohmenger et al, 2001; Cobb et al, 1999; Berg et al, 2002; and Achleitner et al, 2001). Based on the best results achieved in the work of the author (59±3% specificity at 90±4% sensitivity), 59% of the unsuccessful shocks (439 of 745) would be candidates for an alternative approach: either CPR or the administration of a drug to enhance the myocardium prior to shock. Thus for the Oslo dataset used by the author, pre-shock analysis of the characteristics of the patient traces would have led to 439 out of 745 shocks not being administered immediately.

6.4 Recommendations for future work

This final section provides brief suggestions for future work with stemming from this project. These are as follows:

6.4.1 Temporal characteristic study

In the research reported in this thesis, the spectral characteristics of time-frequency transforms for shock outcome prediction were investigated through a series of wide ranging parametric studies based on the power spectra derived from both the WT and STFT. The temporal characteristics of the time-frequency analysis were not considered. However, in recent work, our group have investigated the performance of temporal wavelet-based features on shock outcome prediction (Watson et al, 2004). This allows the advantageous time-frequency localisation of the WT (over the STFT) to be fully realised. The work showed an improvement in prediction using a novel wavelet entropy measure to quantify the pertinent temporal characteristics. The author suggests that this is a promising area of investigation for future work.

6.4.2 The use of alternative classifiers

In the work reported here, Bayes classification was employed for the prediction of the defibrillation outcome. Future work could compare the results presented here with those derived using alternative classifiers. Guterman et al (1996), for example,

reported that a neural network was more useful than a Bayes classifier in a system which they developed for diagnosis of multiple sclerosis from evoked potential (EEG) signals. It would be interesting to see if the combination of the time-frequency method and other classifiers (e.g. Neural Network (NN) and linear discriminant analysis (LDA)) could improve the performance of VF shock outcome prediction.

6.4.3 Further development of PROSC

It was found by the author that PROSC is not a reliable measure for the probability of successful defibrillation. In this study, PROSC was determined from the estimated *a posteriori* probability which was derived from the estimation PDFs. To improve the results, PROSC could be derived from other estimate techniques, for example, a radial basis network (RBN). In the RBN technique, *a posteriori* probability is estimated from a number of Gaussian functions. The learning weight and width of each Gaussian function is dependent on the location and density of data around the centre of each Gaussian function. The author believes that the use of multi-scaled Gaussian functions may be useful for the further development of the PROSC variable.

6.4.4 Optimal shock timing analysis

In the past few years, some research groups have considered the effect of shock timing on defibrillation success. *Carlisle et al* (1988) found that there was no significant difference in threshold-delivered energy or threshold-delivered current between shocks synchronised to the peaks of VF, shocks synchronised to the troughs of VF, and unsynchronised shocks. *Hsia et al* (1992, 1996) have studied the effect of peak time of Absolute VF Voltage (AVFV) on the shock outcome. However, *Patwardhan et al* (1998) found that comparison of envelope voltage between successful and unsuccessful outcome was not significant. *Shu et al* (1997, 1998) found that the probability of successful shock during up-slope amplitude is better than the shock during down-slope amplitude. *Li et al* (1994) examined the effect of shock timing within the QRS complex on defibrillation of ventricular tachycardia. In future work time-frequency methods should be investigated to determine their ability to identify optimal shock timing during the defibrillation process.

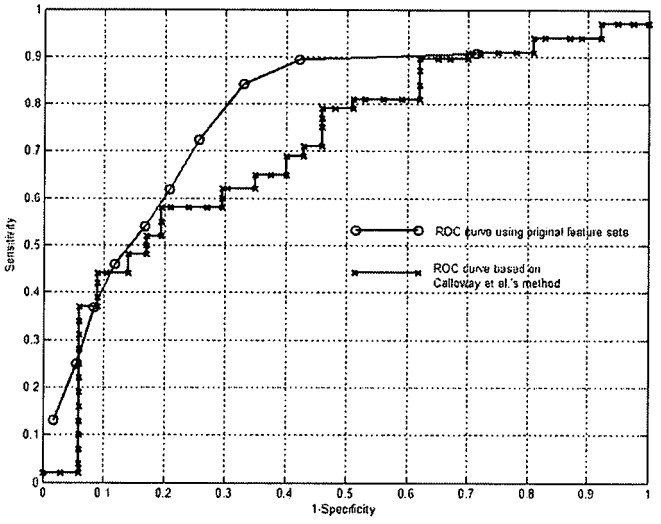

(a) original feature sets

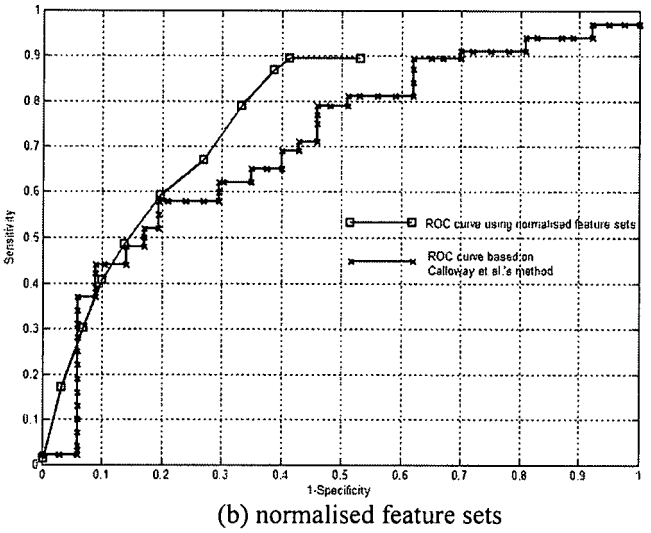

(b) normalised feature sets

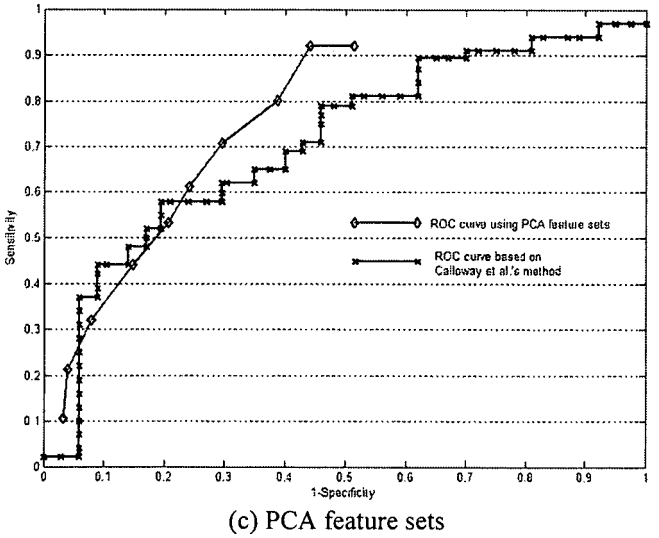

(c) PCA feature sets

Figure 6-1: ROC curves plotted against those of Calloway et al (2001)

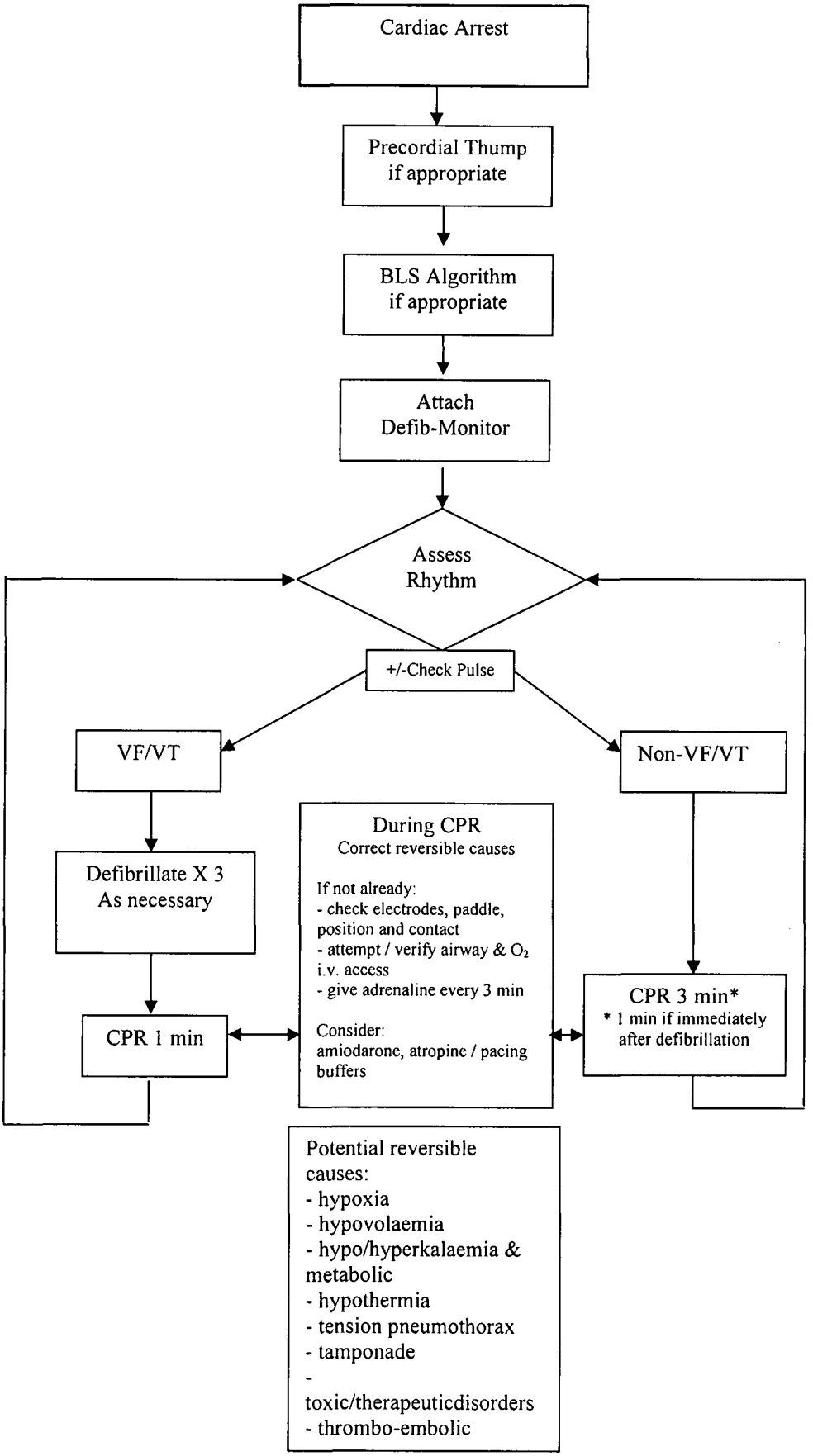

Figure 6-2: The ALS algorithm for the management of cardiac arrest in adults

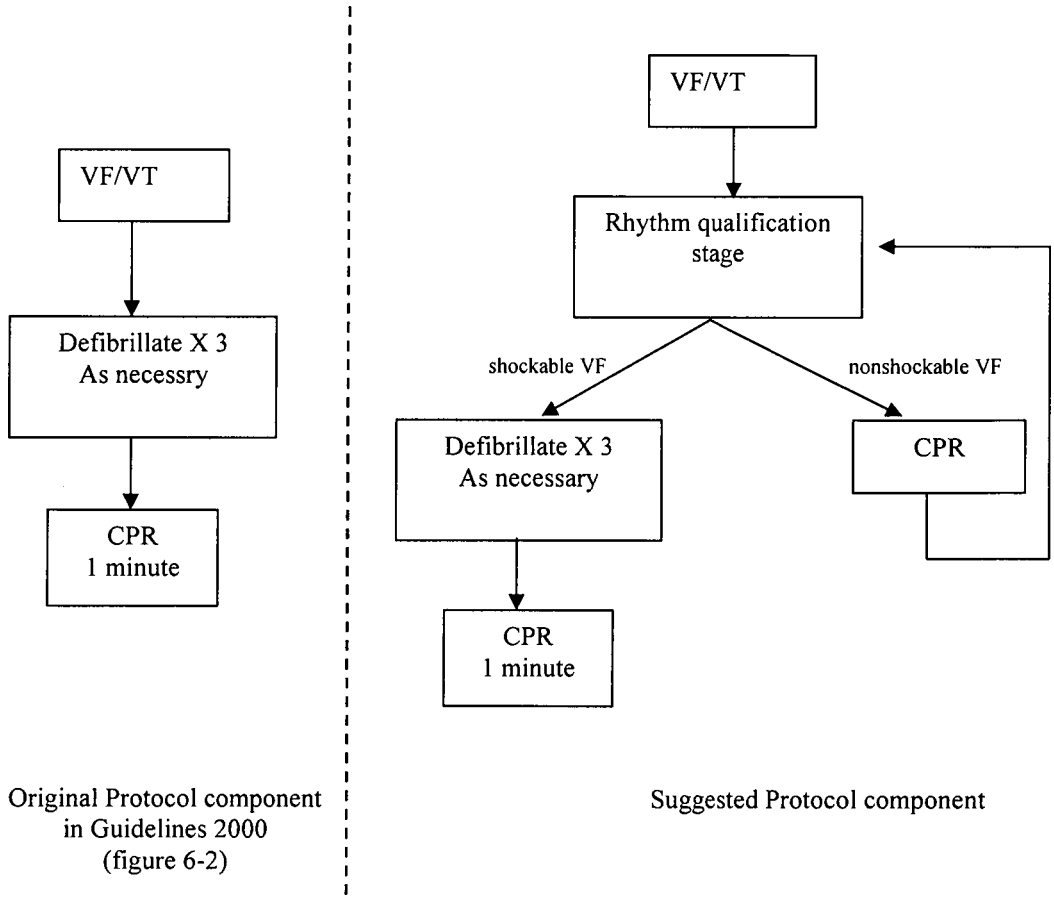

Figure 6-3: Suggested amendment to the ALS algorithm

APPENDICES

APPENDIX A

PROGRAM SOURCE CODE

Program: wt_extract.m

Extracting characteristic features using wavelet transform

```
Cg=1.20;                                % %% admissibility constant
bpass=pi*sqrt(2/log(2));
b=linspace(0,dt*(length(dat)-1),length(dat));
fmin=1;    fmax=20;
ff = linspace(fmax,fmin,200);           %%frequency range
cfreq = 5.3364                          %% wavelet central frequency rad/sec
a = (cfreq/2/pi)./ff;                   %% scaling matrix
z=jcwt(dat,a,dt,wavelet);               %% CWT transform
zall=z;                                 %%keep all transform for energy calc
z=z(:,1:end);
E=(2*pi).*(abs(z).^2)./(Cg*bpass);      %%change to energy with respect to frequency
PE = sum(E')                            %% calculate power spectrum

%%%%%%%% Feature Extraction %%%%%%%
num = sum(log(PE));den = sum(PE);
newflat = num/den;                      %% Flatness

m = meanf(PE,a);                        %% Mean frequency

index = localmax(PE);
[ma,aa] = max(PE(index));
mf = a(index(aa));
if isempty(mf);   mf = 20   ;end
if mf == 1;
  index(aa) = [];
  [ma,aa] = max(PE(index));
        mf = a(index(aa));
  if isempty(aa)
        mf = 1;
  end
end                                     %% Peak Frequency

 v = 0;
for i =1 :length(a)
        v = v + ((a(i)-mf)^2*PE(i));    %%Variance
end
s = skew(PE,a);                         %% skewness
k = kurt(PE,a);                         %% kurtosis

lowband = sum(PE(179:195)); highband = sum(PE(147:163));
r = lowband/highband;                   %% Energy ratio

area = 0;
for i = 1:200
  area = area+PE(i);
  bi = a(i);
  if area > 0.5
          break;
  end
end                                     %% Bisector frequency

PE = PE./sum(PE) ;                      %% Normalised power spectrum

shan = PE.*log(PE);                     %% Shanon entropy

para = [m mf v s k newflat,r,bi,shan,flat]';
```

Program: stft_extract.m

Extracting characteristic features using STFT

```
t =(T:T:length(x)*T);
%%%%%%%% Generate Gaussian Window Function) %%%%%%%%%%%
sigma = 33;
width = 6*sigma + 1;
central = (width + 1) /2;
for t = 1 : width
        h(t) = exp((-0.5/sigma^2)*(t-central)^2)/(sigma*(2*pi)^0.5);
 end
%%%%%%%%%%%%%%%%%%%%%%%%%%%%%%%%%%%%%%%%%%%
x = x-mean(x);

dat1=x;
sxx=length(x);
dat(1:central-1)=zeros(central-1,1);
dat(central:central+sxx-1)=dat1;
dat(central+sxx:2*(central-1)+sxx)=zeros(central-1,1);% zero padding on either side

x = dat;

index = 0;
for i = central-central+1 : 5 :length(x)-width+1
  index = index+1;
  p = x(i:width-1+i);
  for j = 1 : length(p)
        m(j) = p(j)*h(j);
  end
  m = m - mean(m);
  temp = fft(m,1024);
  temp = temp.*conj(temp)/1024;
  ft = temp(1:513)';
  y(:,index) = ft;
end
E = y;                          %% STFT
f = (0:512)/1024/T;
b = (1:r)*T*5;
a = f(1:200);
[row,col] = size(y);
for i = 1 : 200
  sm = 0;
  for j = 1 : col
        sm = sm + E(i,j);
  end
  PE(i) = sm;                   %% STFT power spectrum
end
%%% Feature extraction%%%%
num = sum(log(PE));den = sum(PE);
newflat = num/den;              %% Flatness
m = meanf(PE,a);                %% FM
index = localmax(PE);
[ma,aa] = max(PE(index));
mf = a(index(aa)); %%% FP
if isempty(mf)
  mf = 20
end
if mf == 1
  index(aa) = [];
  [ma,aa] = max(PE(index));
```

```
        mf = a(index(aa));                      %% Peak frequency

end

v = 0;
for i =1 :length(a)
        v = v + ((a(i)-mf)^2*PE(i));            %%Variance
end
s = skew(PE,a);                                 %% Skewness
k = kurt(PE,a);                                 %% Kurtosis

lowband = sum(PE(16:32));
highband = sum(PE(47:63));
r = lowband/highband;                           %% Ratio

area = 0;
for i = 1:200
  area = area+PE(i);
  bi = a(i);                                    %% bisector frequency
  if area > 0.5
        break;
  end
end
shan = 0;
for i = 1:200
        shan = shan + (PE(i)*log(PE(i)));       %% Shannon Entropy
end

para = [m mf v s k newflat,r,bi,shan,flat]';
```

Program: newsmoothex.m

1D PDF Estimation of feature x with k bins and w of Gaussian width

```
top = 2;                                        %% maximum
delta = top/k;                                  %% resulotion
gap = top/200;
num = 200;
y = zeros(1,k);

for j = 1:length(x)
   n = round(x(j)/delta);
  if n > k; n = k;   end
  if  n < 1; n = 1;  end
  y(n) = y(n)+1;
end

%%%%%%Generate Histogram %%%%%%%%%%
ex = zeros(1,num);
for i = 1 :k
  mid = (i*delta) - (delta/2);
  tt = round(mid/gap);
  ex(tt) = y(i);
end
b = (1:200)*gap;
%%%%%%% Generate Gaussian window%%%%%%%%%%%%%%%%%%

width = round(w/gap);
sigma = (width-1)/6;
central = round((width+1)/2);
for t = 1 : width
          h(t) = exp((-0.5/sigma^2)*(t-central)^2)/(sigma*sqrt(2*pi));

end
temp(1:1000) = 0;

xx = length(h);

%%%%% Smooth Histogram with Gaussian window %%%%%
for i = 1 : num
  guas = ex(i).*h;
  temp(i:i+xx-1) = temp(i:i+xx-1)+guas;
end

pdf = temp(central:central+num-1);
pdf = pdf/sum(pdf);
```

Program: newsmooth2ex.m

2D PDF Estimation of feature x_1 and x_2 with k bins and w of Gaussian width

```
top = 2; delta = top/k;
num = 200; gap = top/num;
y = zeros(k,k);

%%%%% Generate Histogram %%%%%%%%%%%%%%%
for j = 1:length(x1);
  fm = round(x1(j)/delta);
  fp = round(x2(j)/delta);
  if fm > k;  fm = k;  end
  if fm < 1; fm = 1;  end
  if fp > k;  fp = k;  end
  if fp < 1;  fp = 1;  end
  y(fm,fp) = y(fm,fp)+1;
end
ex = zeros(num,num);
for i = 1 :k
  midfm = (i*delta) - (delta/2);
  ttfm = round(midfm/gap);
  for j = 1 :k
        midfp = (j*delta) - (delta/2);
        ttfp = round(midfp/gap);
        ex(ttfm,ttfp) = y(i,j);
  end
end
 [rr,qq] = find(ex>0);

%%%%%%% Generate bivariate Gaussian function %%%%%%%%%%

width = round(w/gap);
sigma = (width-1)/6;
central = round((width+1)/2);
p=0;
for i = 1 : width
for j = 1 : width
  temp1 = ((i-central)/sigma)^2;
  temp2 = 2*p*((i-central)/sigma)*((j-central)/sigma);
  temp3 = ((j-central)/sigma)^2;
  temp = -1/(2*(1-p^2))*(temp1 - temp2 + temp3);
  t(i,j) = (1/sqrt(2*pi*sigma*sigma*(1-p^2)))*exp(temp);
end
end
temp(1:1000,1:1000) = 0;
[xx,yy] = size(t);le = length(rr);

%%%% Smooth histogram %%%%%%%%%%%
for i = 1: le
   guas = ex(rr(i),qq(i)).*t;
  temp(rr(i):rr(i)+xx-1,qq(i):qq(i)+yy-1) = temp(rr(i):rr(i)+xx-1,qq(i):qq(i)+yy-1)+guas(:,:);
end
pdf = temp(central:central+num-1,central:central+num-1);
pdf = pdf/sum(sum(pdf));
```

Program: classify1d_2.m

1D Bayes classifier with N cross validations

```
 bins = [50, 75, 100, 125, 150,175,200]; %%% Bin Numbers
 width = 0.1:0.1:1; %%% Gaussian width
lbins = length(bins);
lwidth = length(width);

%%%%%% Train and test each all experiments%%%%%%
for i = 1 : lbins
  bins(i)
  for j = 1 : lwidth
    bin = bins(i);
    wid = width(j);
    [trainrosc,trainnorosc,testrosc,testnorosc,pdfrosc,pdfnorosc,prosc,pnorosc] =
dataprepare(p1,p2,p3,p4,p5,N,bin,wid);
    beta = 1; alpha = 0.5; gam = 0.9; senstrain = 0; its = 0;
    sens_target = 0.95; dis = abs(senstrain-sens_target);
    %%%%% train sensitivity to 95%
     while dis > 0.03 & its <1500
     cost = [gam gam; 0 beta; 1 0];

     for in = 1 : N
      [sn(in) sp(in)] = perform(trainrosc{in},trainnorosc{in},prosc{in},pnorosc{in},cost);
     end

     senstrain = mean(sn);
     dis = abs(senstrain-sens_target);
     its = its+1 ;
     beta = beta + (alpha*(senstrain-0.95));
    end
  %%%%%%%%%%%%%%%% Test with beta%%%%%%%%%%%%%%%%
   for in = 1 : N
      [sn(in) sp(in)] = perform(testrosc{in},testnorosc{in},prosc{in},pnorosc{in},cost);
   end
    sens(i,j) = mean(sn) %%% avarage test sensitivity
    stdsens(i,j) = std(sn);
    spec(i,j) = mean(sp) %%% avarage specificity
    stdspec(i,j) = std(sp);
    beta(i,j) = beta; %%%% cost value
  end
end

%%%%%%%%%%%%%%%%%%%%%%
function [trainrosc,trainnorosc,testrosc,testnorosc,pdfrosc,pdfnorosc,prosc,pnorosc] =
dataprepare(p1,p2,p3,p4,p5,N,bin,wid)

rosc = p1;  norosc = [p2;p3;p4;p5];
PROSC = length(rosc)/(length(rosc)+length(norosc));
PNOROSC = length(norosc)/(length(rosc)+length(norosc));

for in = 1 : N

if in ~= N

    temp = rosc;
    testrosc{in} = rosc(len1*(in-1)+1:len1*in,:);
    temp(len1*(in-1)+1:len1*in,:)=[];
    trainrosc{in}= temp;
```

```
    temp = norosc;
    testnorosc{in} = norosc(len2*(in-1)+1:len2*in,:);
    temp(len2*(in-1)+1:len2*in,:)=[];
    trainnorosc{in}= temp;
else
    temp = rosc;
    testrosc{in} = rosc(len1*(in-1)+1:end,:);
    temp(len1*(in-1)+1:end,:)=[];
    trainrosc{in}= temp;

    temp = norosc;
    testnorosc{in} = norosc(len2*(in-1)+1:end,:);
    temp(len2*(in-1)+1:end,:)=[];
    trainnorosc{in}= temp;
end

pdfrosc{in} = newsmoothex(trainrosc{in}(:,1),bin,wid); %%%% estimate pdf of rosc set
pdfnorosc{in} = newsmoothex(trainnorosc{in}(:,1),bin,wid); %%%% estimate pdf of norosc set

%%%%%%%%%% find posterior probability from Bayes function%%%%%%
[row,col] = size(pdfrosc{in});
      for i = 1 :row
                              for j = 1 :col
                             mm = (PROSC)*pdfrosc{in}(i,j);
          kk = (PNOROSC)*pdfnorosc{in}(i,j);
          dd = (PROSC)*pdfrosc{in}(i,j) + (PNOROSC)*pdfnorosc{in}(i,j);
          if dd == 0
            prosc{in}(i,j) = 0;
            pnorosc{in}(i,j) = 1;
          else
                    prosc{in}(i,j) = mm/dd;
           pnorosc{in}(i,j) = kk/dd;
          end
                end
      end
end

%%%%%%%%%%%%%%%%%%%%%%%%%%%%%%%%%%%%%%%%%%%%%%%%%%%%%%%%

function [sens,spec] = perform(trainrosc,trainnorosc,prosc,pnorosc,cost)

sens = 0;
spec = 0;
   fm = round(trainrosc(:,1).*100);
     ss = find(fm<1);
   fm(ss) = 1;
   ss = find(fm>100);
   fm(ss) = 100;

   for i = 1 :length(fm)
    P = [prosc(fm(i)) ; pnorosc(fm(i))];
    R = cost*P;
     [nn mm] = min(R);
     switch mm
     case 2
       sens = sens+1;
     end

  end
sens = sens/length(trainrosc);
```

```
    fm = round(trainnorosc(:,1).*100);
    ss = find(fm<1);
    fm(ss) = 1;
    ss = find(fm>100);
    fm(ss) = 100;

    for i = 1 :length(fm)
     %P = [prosc(fm(i),fp(i)) ; pnorosc(fm(i),fp(i))];
     P = [prosc(fm(i)) ; pnorosc(fm(i))];
     R = cost*P;
     [nn mm] = min(R);

     switch mm
     case 3
       spec = spec+1;
     end
          end
spec = spec/length(trainnorosc);

%%%%%%%%%%%%%%%%%%%%%%%%%%%%%%%%%%%%%%%%%%%%%%%%%%%%%%%%%%%%%%%%%%%%%%%%%%%%%%%
```

Program: classify2d_2.m

2D Bayes classifier with N cross validations

```
bins = [50, 75, 100, 125, 150,175,200]; %%% Bin Numbers
 width = 0.1:0.1:1; %%% Gaussian width

lbins = length(bins); lwidth = length(width);

for i = 1 : lbins
  bins(i)
  for j = 1 : lwidth
    bin = bins(i);
    wid = width(j);
    [trainrosc,trainnorosc,testrosc,testnorosc,pdfrosc,pdfnorosc,prosc,pnorosc] =
dataprepare(p1,p2,p3,p4,p5,N,bin,wid);
    beta = 1; alpha = 0.8; gam = 0.9; senstrain = 0; its = 0;
     sens_target = 0.95; dis = abs(senstrain-sens_target);

     %%% train system%%%%%%%%%%%%
     while dis > 0.03 & its <1500
    cost = [gam gam; 0 beta; 1 0];
     for in = 1 : N
      [sn(in) sp(in)] = perform(trainrosc{in},trainnorosc{in},prosc{in},pnorosc{in},cost);
     end
      senstrain = mean(sn);
      dis = abs(senstrain-sens_target);
     its = its+1 ;
     beta = beta + (alpha*(senstrain-0.95));
    end
   %%%%%%%%%%%%%% Test system%%%%%%%%%%%%%%
   for in = 1 : N
      [sn(in) sp(in)] = perform(testrosc{in},testnorosc{in},prosc{in},pnorosc{in},cost);
    end
   senstrain
    sens(i,j) = mean(sn)
    stdsens(i,j) = std(sn);
    spec(i,j) = mean(sp)
    stdspec(i,j) = std(sp);
    beta(i,j) = beta;
  end
end

%%%%%%%%%%%%%%%%%%%%%%%%%%%%%%%%%%%%%%%%%%%%%%%%%%%%%%%%%%%%%%%%%%%%%%%%%%%%%%%%
%%%%%%%%%%%%%%%%%%%%%%%%%%%%%%%%%%%%%%%%%%%%%%%%%%%%%%%%%%%%%%%%%%%%%%%%%%%%%%%%
function [trainrosc,trainnorosc,testrosc,testnorosc,pdfrosc,pdfnorosc,prosc,pnorosc] =
dataprepare(p1,p2,p3,p4,p5,N,bin,wid)


rosc = p1;
norosc = [p2;p3;p4;p5];
PROSC = length(rosc)/(length(rosc)+length(norosc));
PNOROSC = length(norosc)/(length(rosc)+length(norosc));

if in ~= N

    temp = rosc;
    testrosc{in} = rosc(len1*(in-1)+1:len1*in,:);
    temp(len1*(in-1)+1:len1*in,:)=[];
    trainrosc{in}= temp;
```

```
    temp = norosc;
    testnorosc{in} = norosc(len2*(in-1)+1:len2*in,:);
    temp(len2*(in-1)+1:len2*in,:)=[];
    trainnorosc{in}= temp;
else
    temp = rosc;
    testrosc{in} = rosc(len1*(in-1)+1:end,:);
    temp(len1*(in-1)+1:end,:)=[];
    trainrosc{in}= temp;

    temp = norosc;
    testnorosc{in} = norosc(len2*(in-1)+1:end,:);
    temp(len2*(in-1)+1:end,:)=[];
    trainnorosc{in}= temp;
end


pdfrosc{in} = newsmooth2ex(trainrosc{in}(:,1),trainrosc{in}(:,2),bin,wid);%%%% estimate pdf of
rosc set
pdfnorosc{in} = newsmooth2ex(trainnorosc{in}(:,1),trainnorosc{in}(:,2),bin,wid);%%%% estimate
pdf of norosc set

 %%%%%%%%%% find posterior probability from Bayes function%%%%%%
[row,col] = size(pdfrosc{in});
      for i = 1 :row
                              for j = 1 :col
                             mm = (PROSC)*pdfrosc{in}(i,j);
          kk = (PNOROSC)*pdfnorosc{in}(i,j);
          dd = (PROSC)*pdfrosc{in}(i,j) + (PNOROSC)*pdfnorosc{in}(i,j);
          if dd == 0
            prosc{in}(i,j) = 0;
            pnorosc{in}(i,j) = 1;
          else
                   prosc{in}(i,j) = mm/dd;
           pnorosc{in}(i,j) = kk/dd;
          end
                end
      end
end

%%%%%%%%%%%%%%%%%%%%%%%%%%%%%%%%%%%%%%%%%%%%%%%%%%%%%%%%%%%%%%%%%%%%%%%%%%%%%%%


function [sens,spec] = perform(trainrosc,trainnorosc,prosc,pnorosc,cost)

sens = 0;
spec = 0;
   fm = round(trainrosc(:,1).*100);
   fp = round(trainrosc(:,2).*100);
   ss = find(fm<1); fm(ss) = 1;
   ss = find(fm>100);fm(ss) = 100;

    ss = find(fp<1); fp(ss) = 1;
   ss = find(fp>100);fp(ss) = 100;

          for i = 1 :length(fm)
    P = [prosc(fm(i),fp(i)) ; pnorosc(fm(i),fp(i))];
    R = cost*P;
    [nn mm] = min(R);
    switch mm
    case 2
      sens = sens+1;
```

```
    end

  end
sens = sens/length(trainrosc);
%%%%%%%%%%%%%%%%%%%%%%%%%%%%%%%%%%%%%%%%%%%%%%%%

   fm = round(trainnorosc(:,1).*100);
   fp = round(trainnorosc(:,2).*100);

   ss = find(fm<1); fm(ss) = 1;
   ss = find(fm>100);fm(ss) = 100;

    ss = find(fp<1); fp(ss) = 1;
   ss = find(fp>100);fp(ss) = 100;

          for i = 1 :length(fm)
    P = [prosc(fm(i),fp(i)) ; pnorosc(fm(i),fp(i))];
    R = cost*P;
    [nn mm] = min(R);

    switch mm
    case 3
      spec = spec+1;
    end
          end
spec = spec/length(trainnorosc);

%%%%%%%%%%%%%%%%%%%%%%%%%%%%%%%%%%%%%%%%%%%%%%%%
```

APPENDIX B

Boxplots of characteristic feature sets

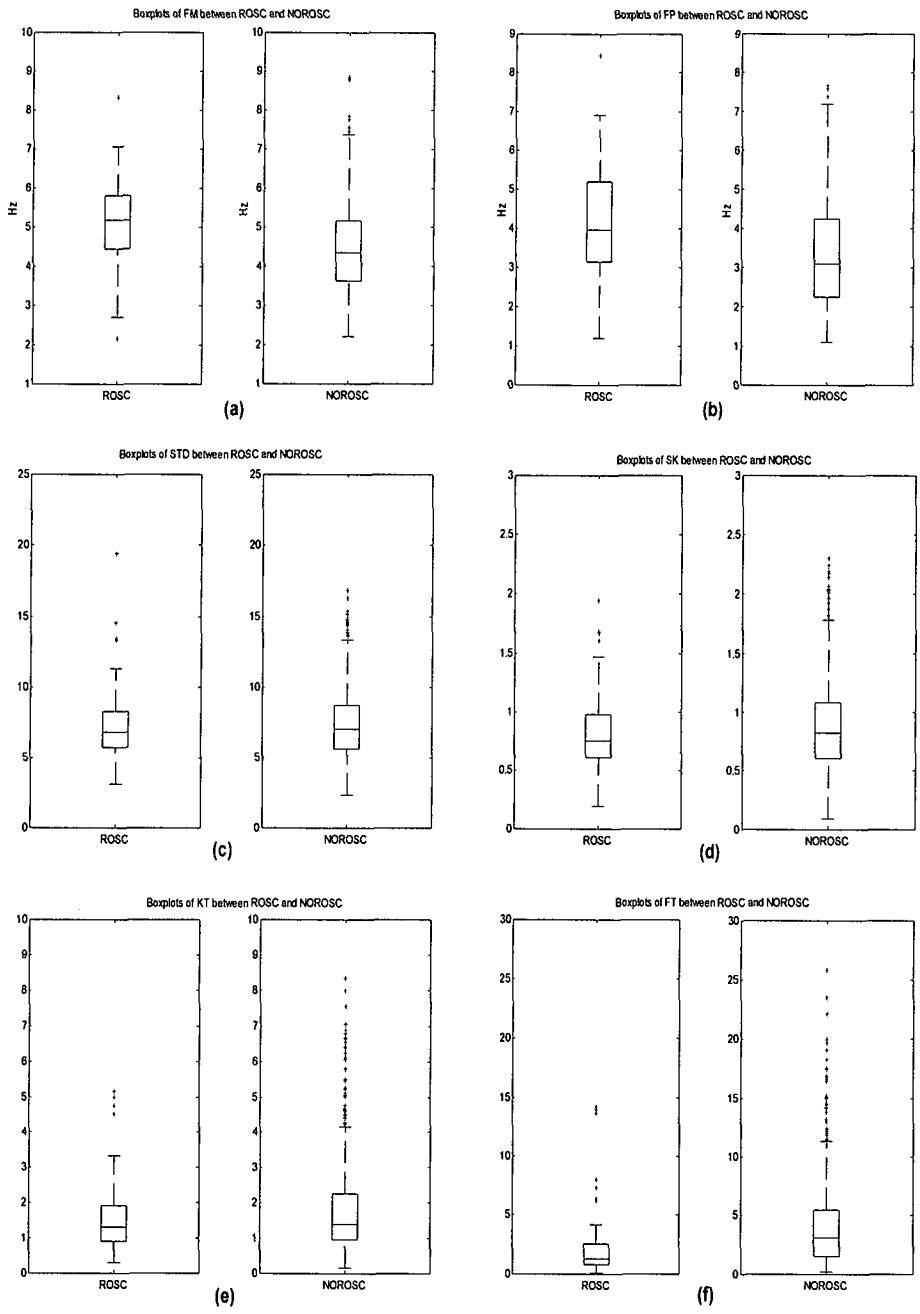

Figure B-1: Feature boxplots for the ROSC and NOROSC cases obtained from the WT-based method with 5 second length of pre-shock ECG: (a) FM feature boxplots, (b) FP feature boxplots, (c) STD feature boxplots, (d) SK feature boxplots, (e) KT feature boxplots, and (f) FT feature boxplots

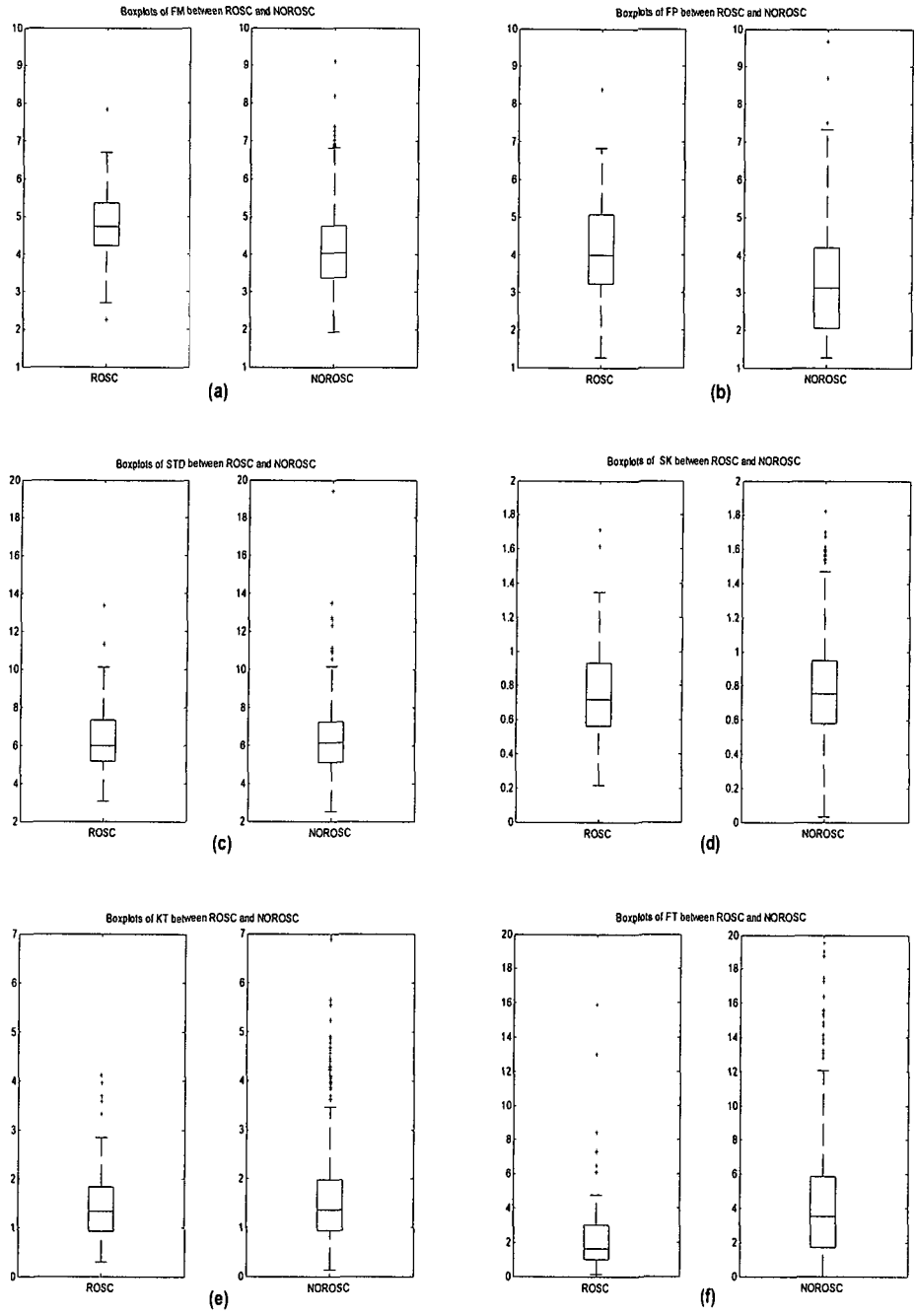

Figure B-2: Feature boxplots for the ROSC and NOROSC cases obtained from the STFT1-based method with 5 second length of pre-shock ECG: (a) FM feature boxplots, (b) FP feature boxplots, (c) STD feature boxplots, (d) SK feature boxplots, (e) KT feature boxplots, and (f) FT feature boxplots

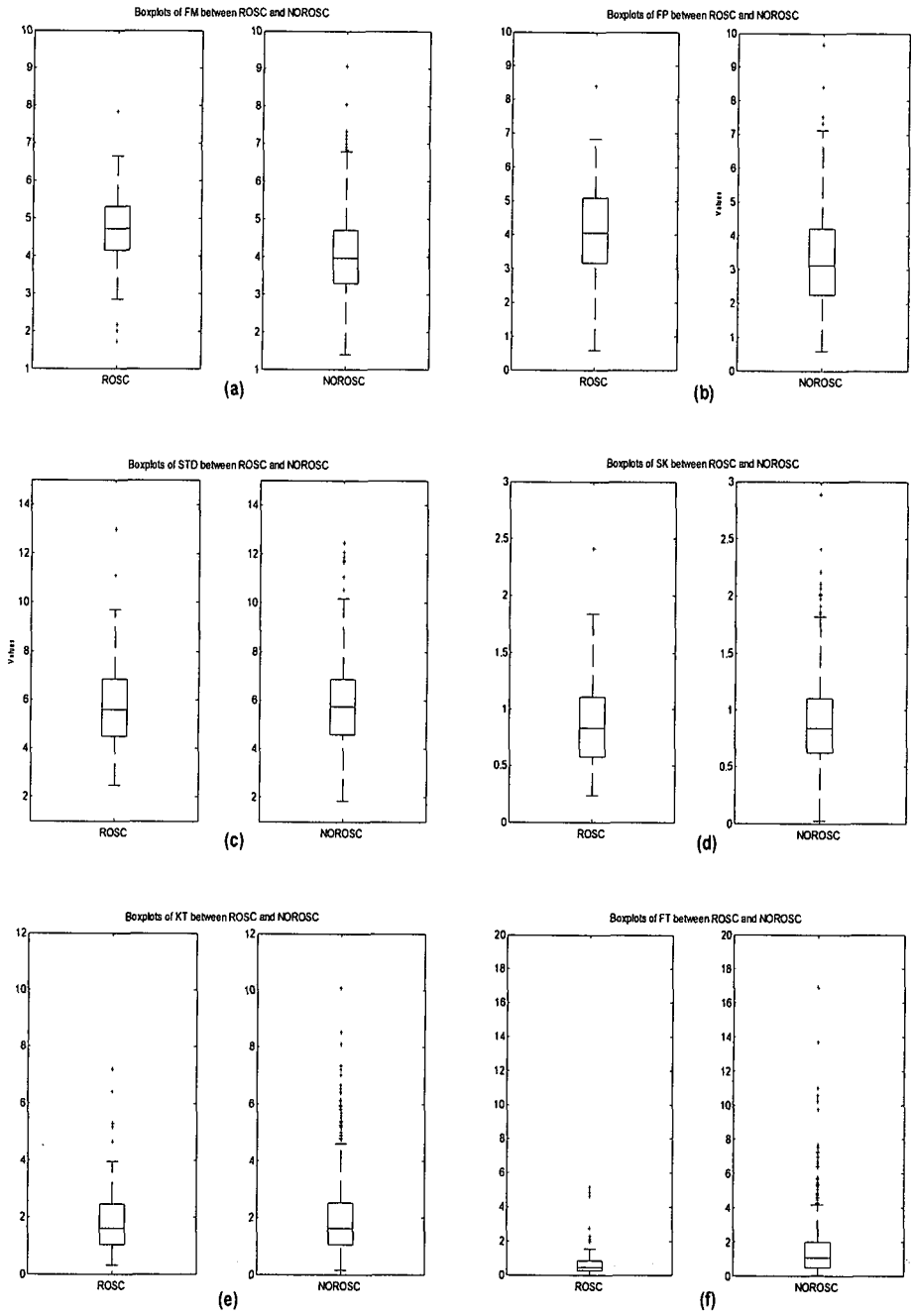

Figure B-3: Feature boxplots for the ROSC and NOROSC cases obtained from the STFT2-based method with 5 second length of pre-shock ECG: (a) FM feature boxplots, (b) FP feature boxplots, (c) STD feature boxplots, (d) SK feature boxplots, (e) KT feature boxplots, and (f) FT feature boxplots

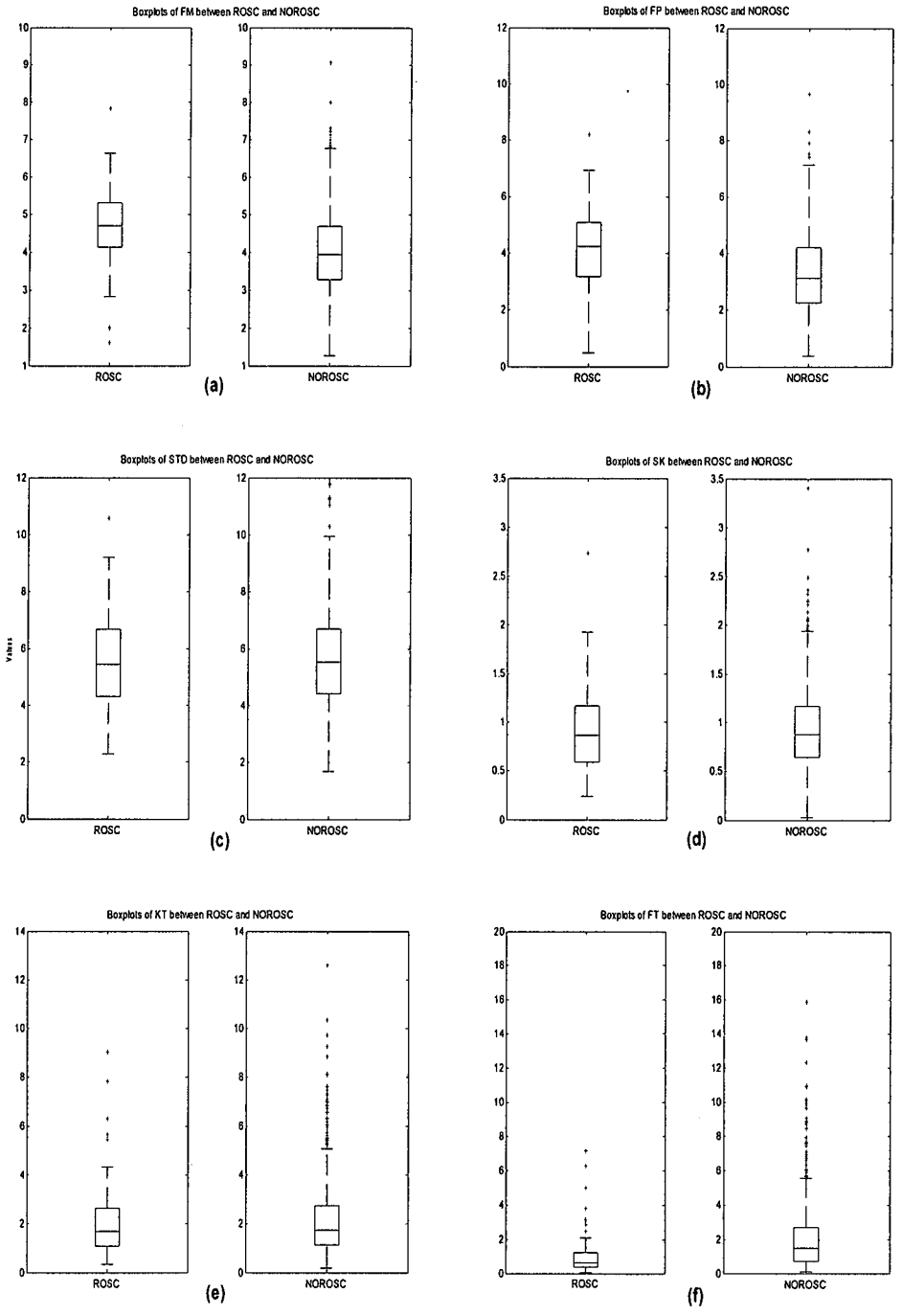

Figure B-4: Feature boxplots for the ROSC and NOROSC cases obtained from the STFT3-based method with 5 second length of pre-shock ECG: (a) FM feature boxplots, (b) FP feature boxplots, (c) STD feature boxplots, (d) SK feature boxplots, (e) KT feature boxplots, and (f) FT feature boxplots

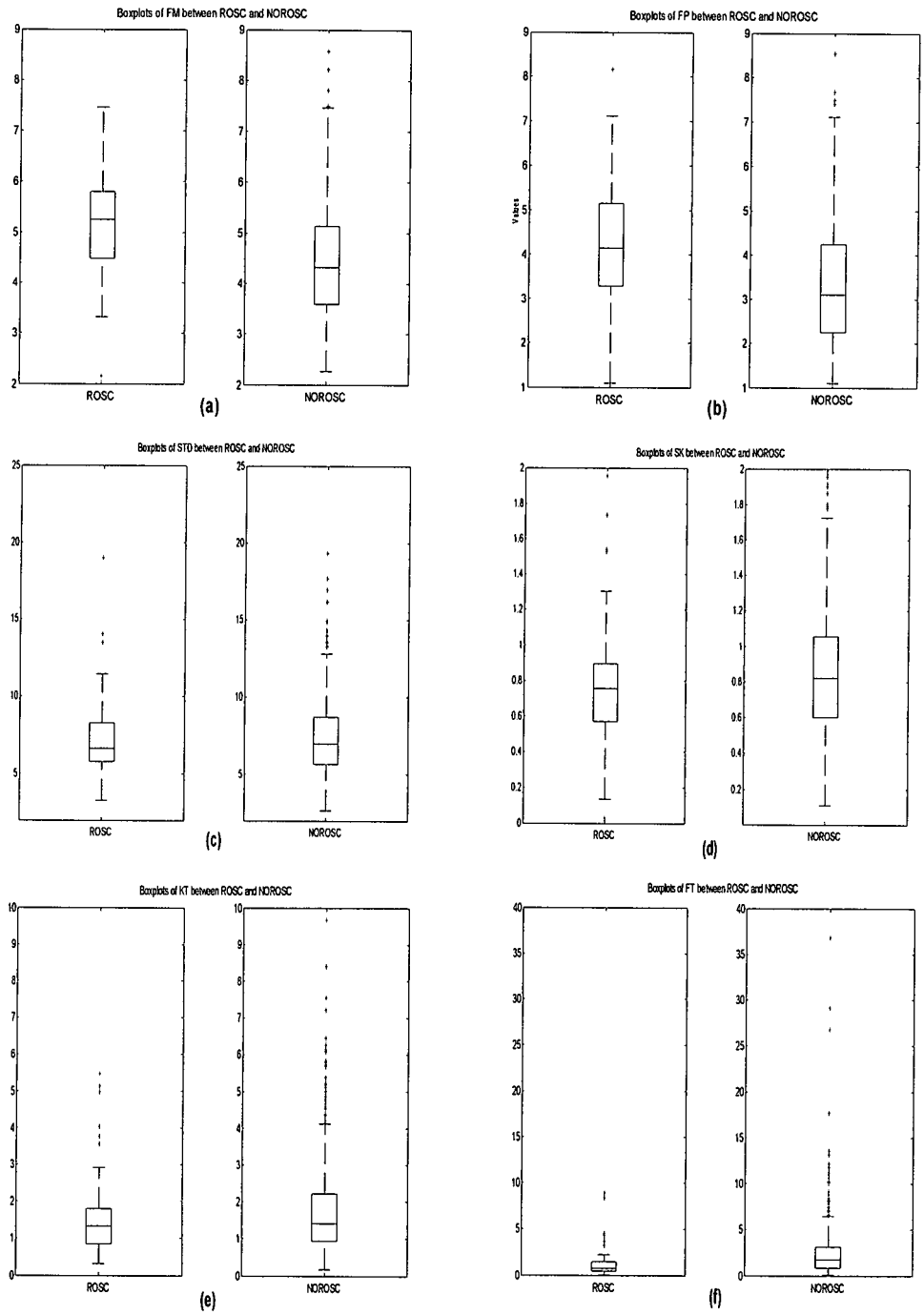

Figure B-5: Feature boxplots for the ROSC and NOROSC cases obtained from the WT-based method with 10 second length of pre-shock ECG: (a) FM feature boxplots, (b) FP feature boxplots, (c) STD feature boxplots, (d) SK feature boxplots, (e) KT feature boxplots, and (f) FT feature boxplots

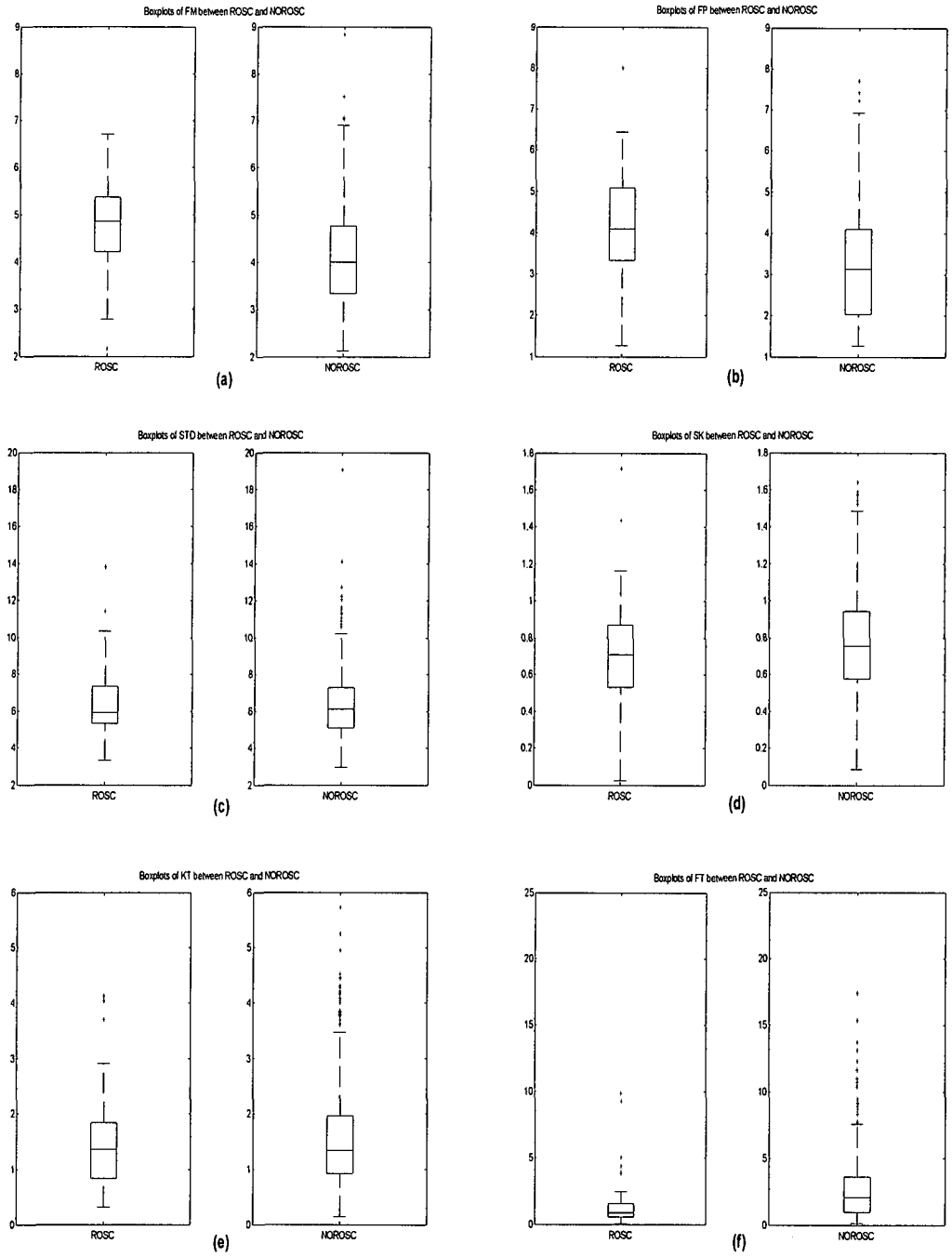

Figure B-6: Feature boxplots for the ROSC and NOROSC cases obtained from the STFT1-based method with 10 second length of pre-shock ECG: (a) FM feature boxplots, (b) FP feature boxplots, (c) STD feature boxplots, (d) SK feature boxplots, (e) KT feature boxplots, and (f) FT feature boxplots

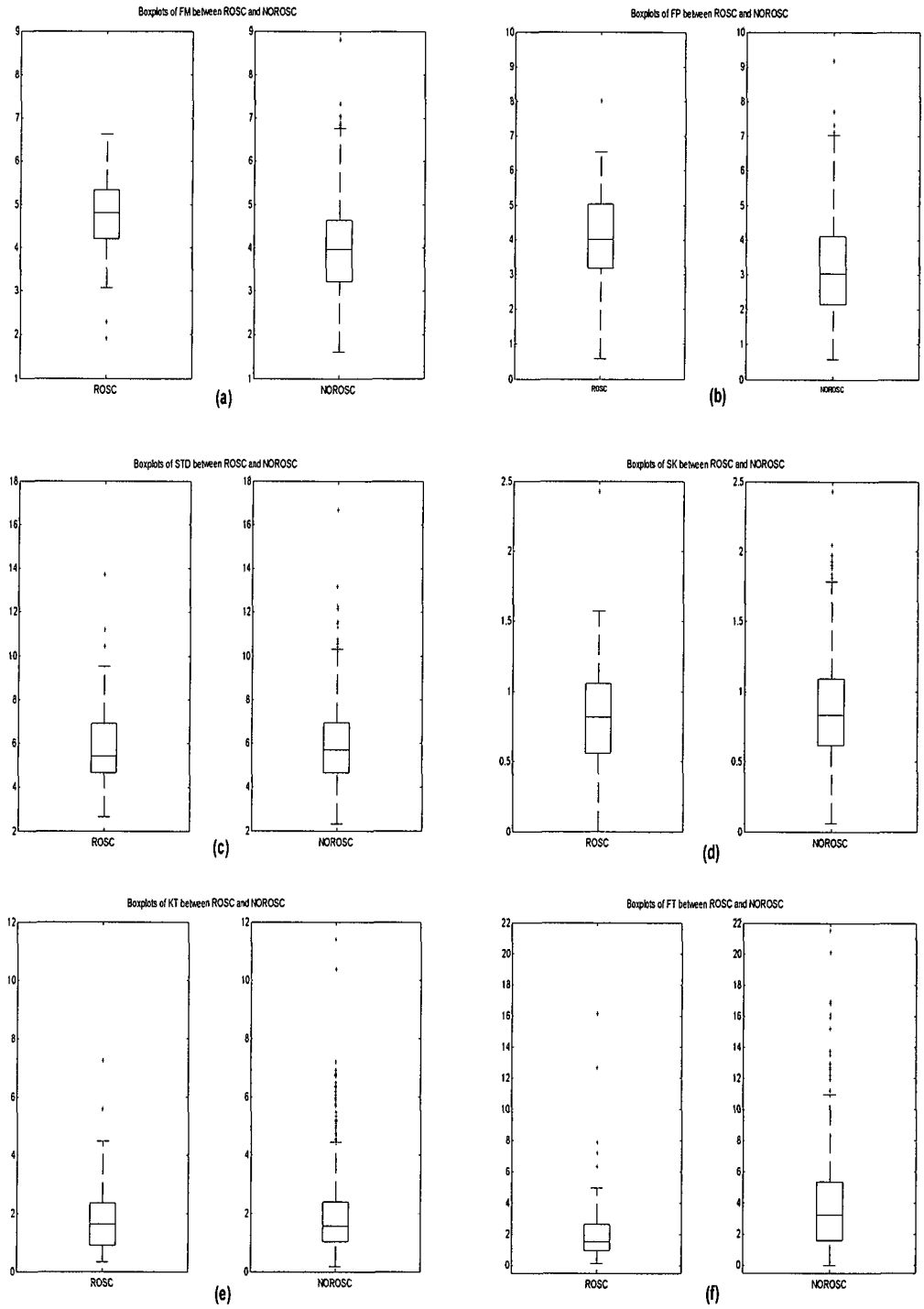

Figure B-7: Feature boxplots for the ROSC and NOROSC cases obtained from the STFT2-based method with 10 second length of pre-shock ECG: (a) FM feature boxplots, (b) FP feature boxplots, (c) STD feature boxplots, (d) SK feature boxplots, (e) KT feature boxplots, and (f) FT feature boxplots

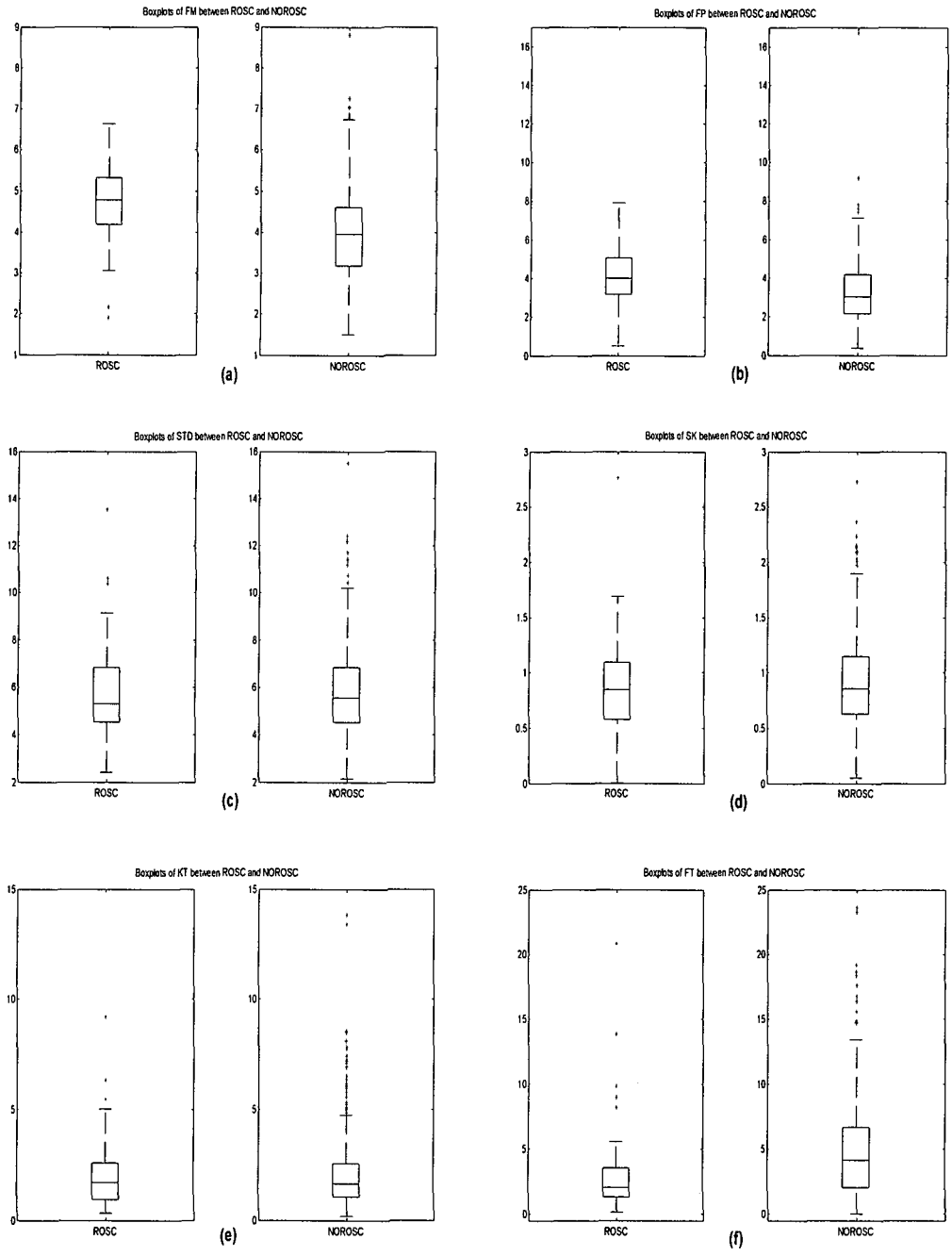

Figure B-8: Feature boxplots for the ROSC and NOROSC cases obtained from the STFT3-based method with 10 second length of pre-shock ECG: (a) FM feature boxplots, (b) FP feature boxplots, (c) STD feature boxplots, (d) SK feature boxplots, (e) KT feature boxplots, and (f) FT feature boxplots

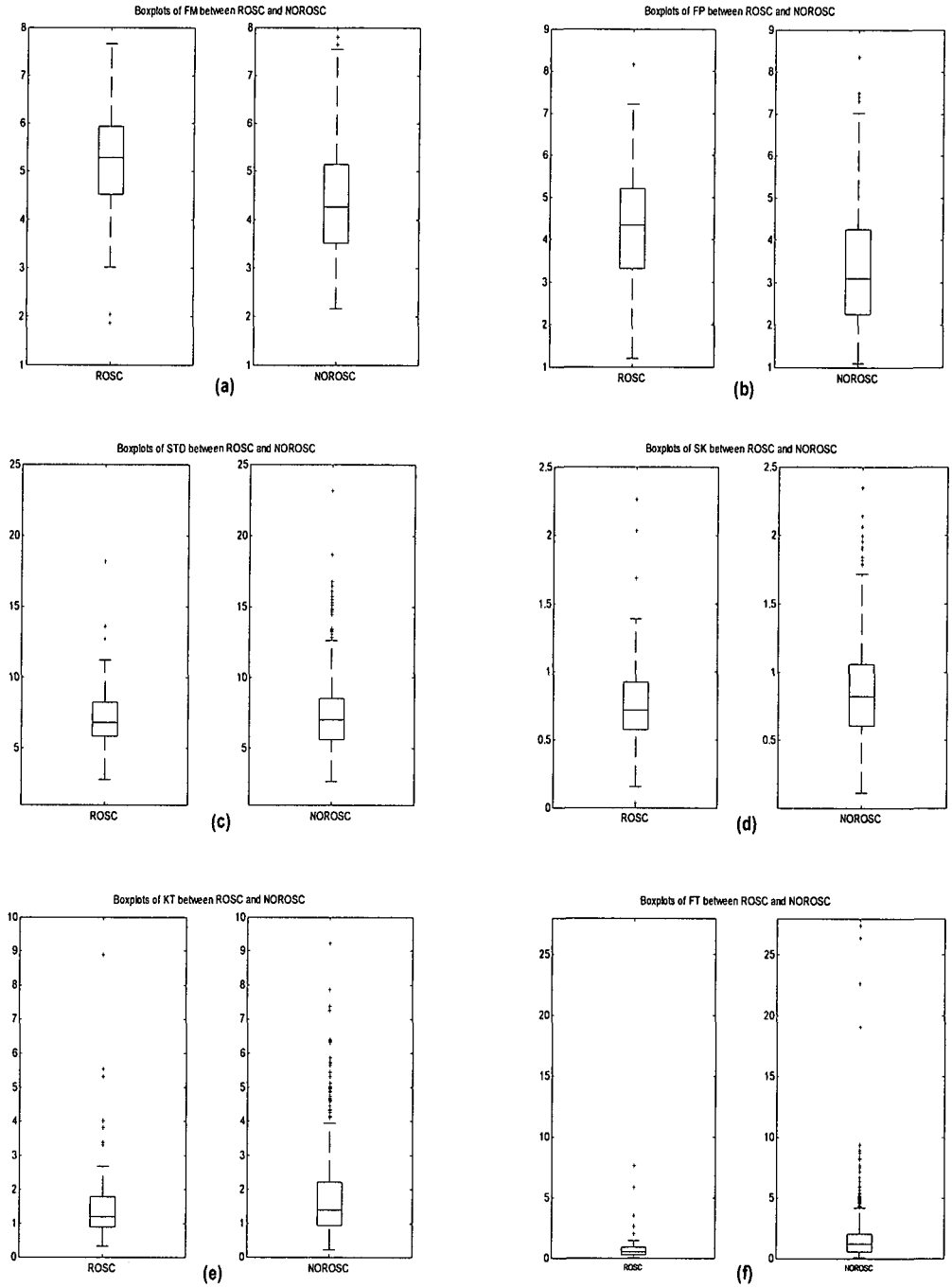

Figure B-9: Feature boxplots for the ROSC and NOROSC cases obtained from the WT-based method with 15 second length of pre-shock ECG: (a) FM feature boxplots, (b) FP feature boxplots, (c) STD feature boxplots, (d) SK feature boxplots, (e) KT feature boxplots, and (f) FT feature boxplots

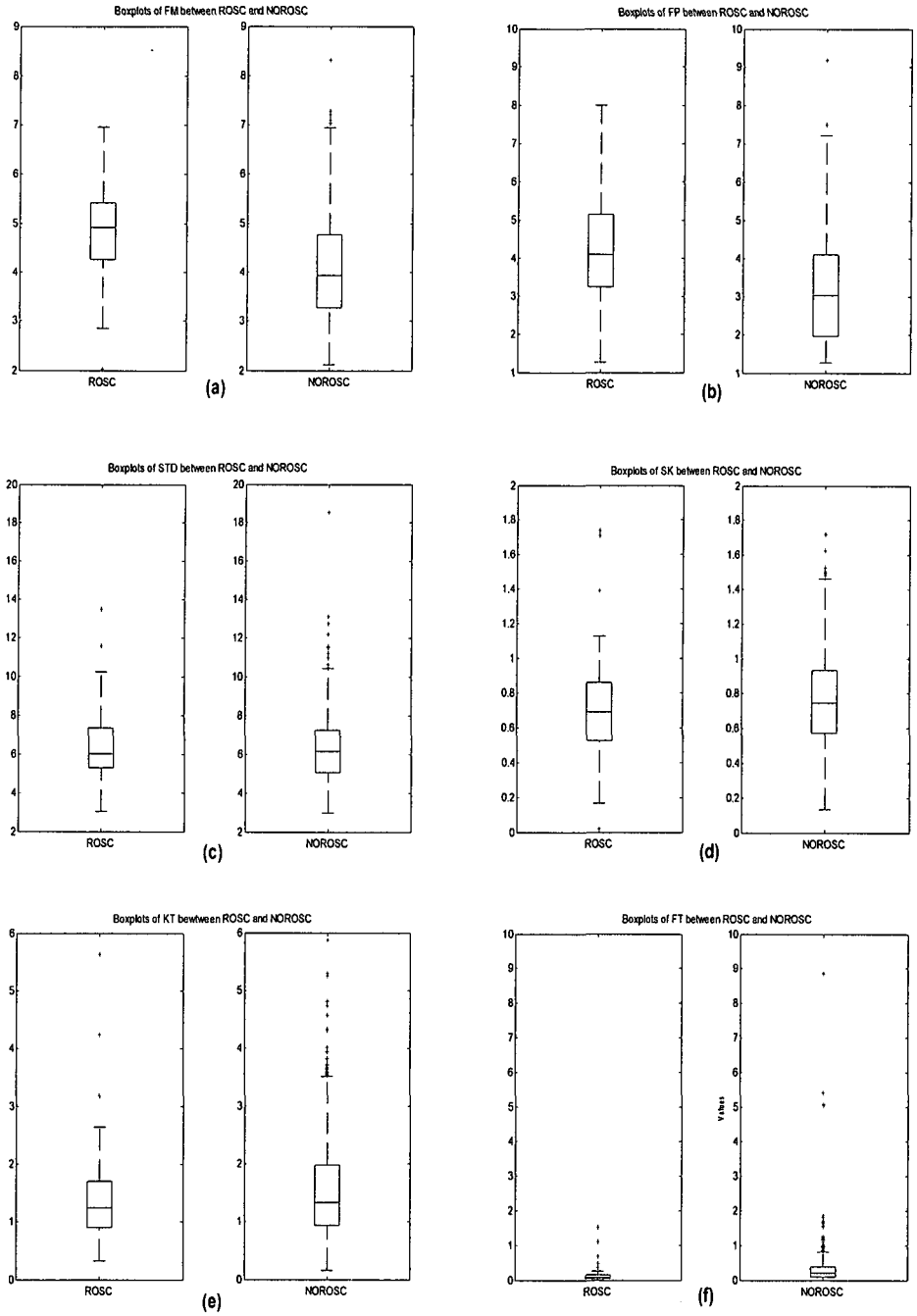

Figure B-10: Feature boxplots for the ROSC and NOROSC cases obtained from the STFT1-based method with 15 second length of pre-shock ECG: (a) FM feature boxplots, (b) FP feature boxplots, (c) STD feature boxplots, (d) SK feature boxplots, (e) KT feature boxplots, and (f) FT feature boxplots

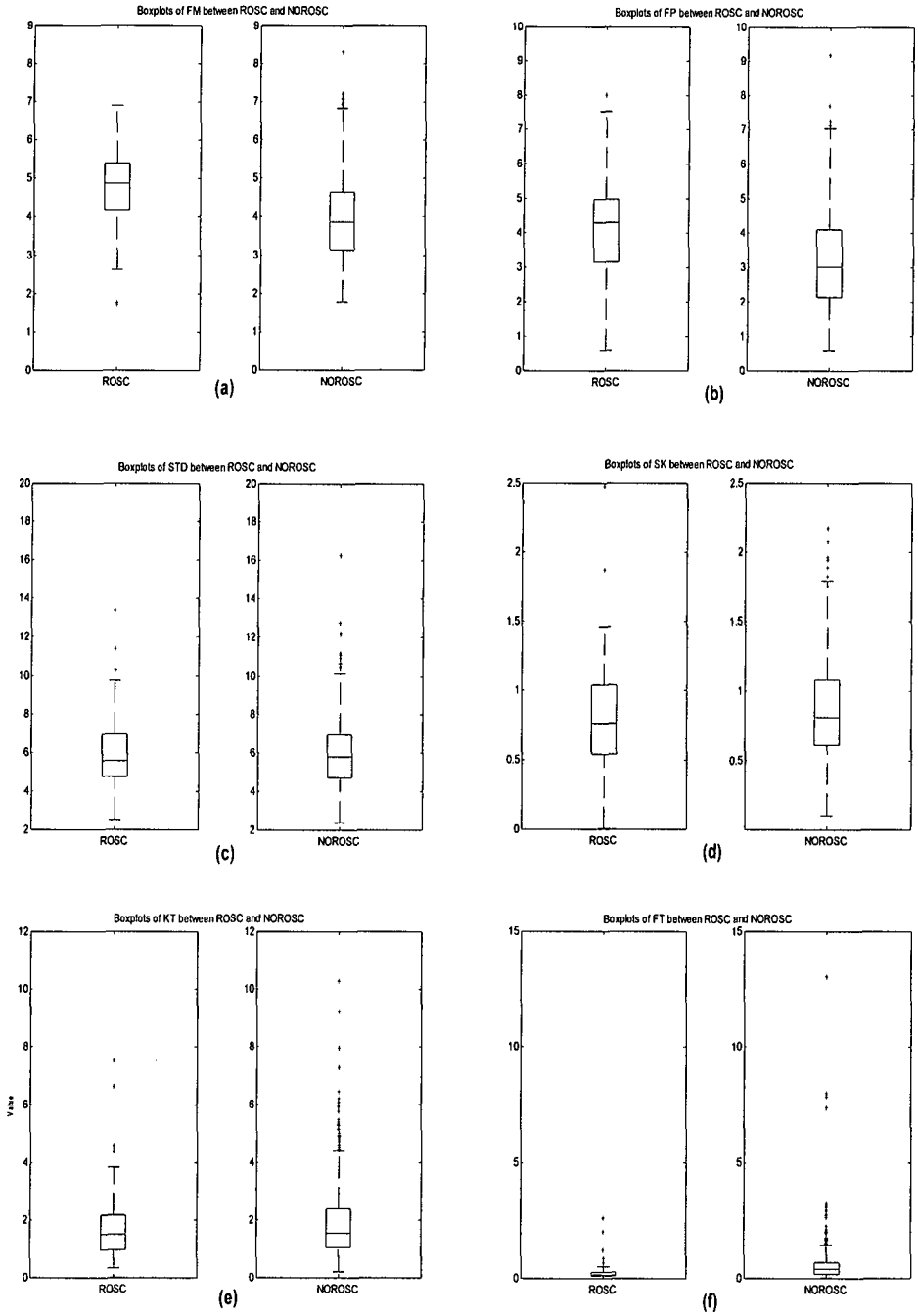

Figure B-11: Feature boxplots for the ROSC and NOROSC cases obtained from the STFT2-based method with 15 second length of pre-shock ECG: (a) FM feature boxplots, (b) FP feature boxplots, (c) STD feature boxplots, (d) SK feature boxplots, (e) KT feature boxplots, and (f) FT feature boxplots

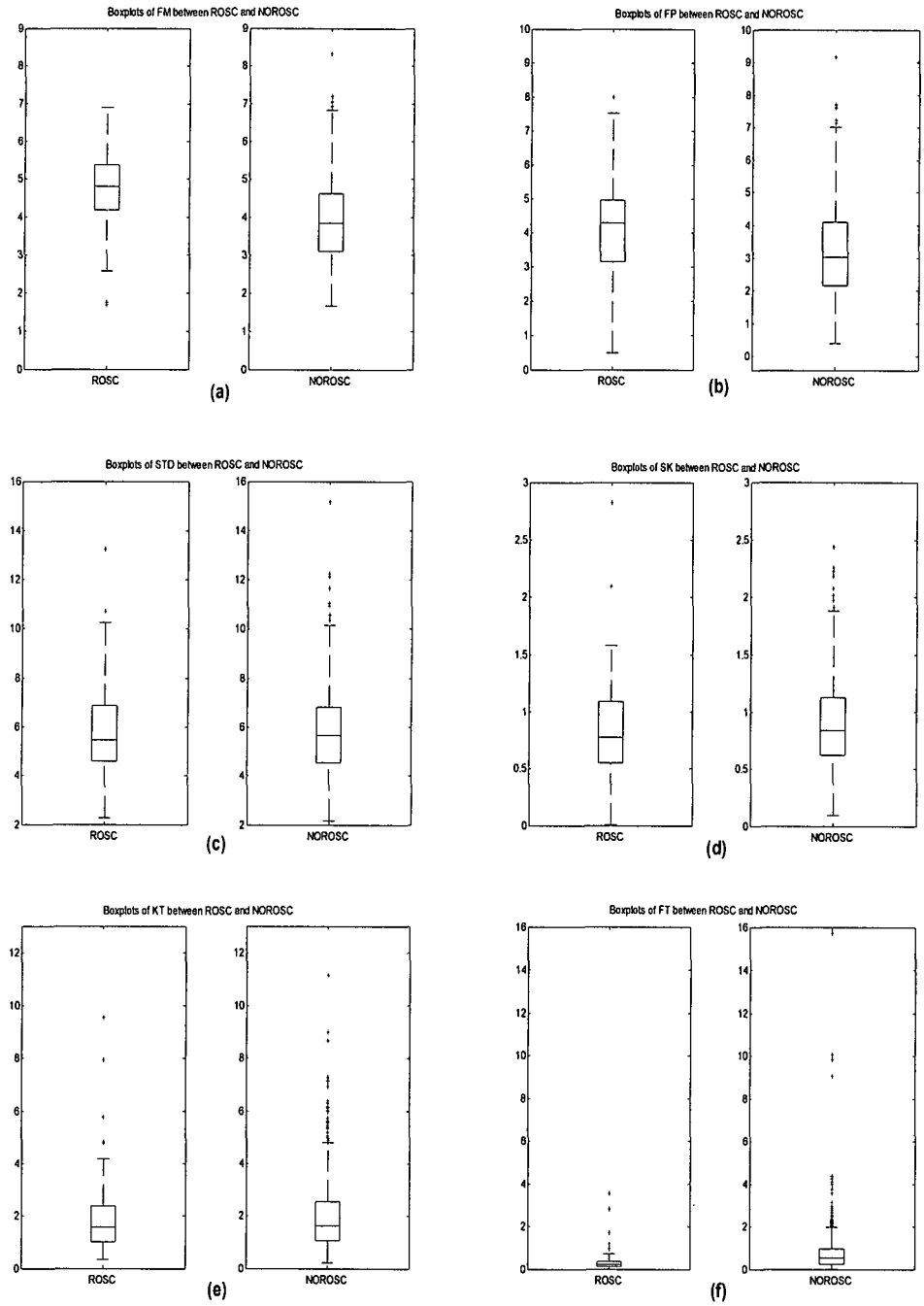

Figure B-12: Feature boxplots for the ROSC and NOROSC cases obtained from the STFT3-based method with 15 second length of pre-shock ECG: (a) FM feature boxplots, (b) FP feature boxplots, (c) STD feature boxplots, (d) SK feature boxplots, (e) KT feature boxplots, and (f) FT feature boxplots

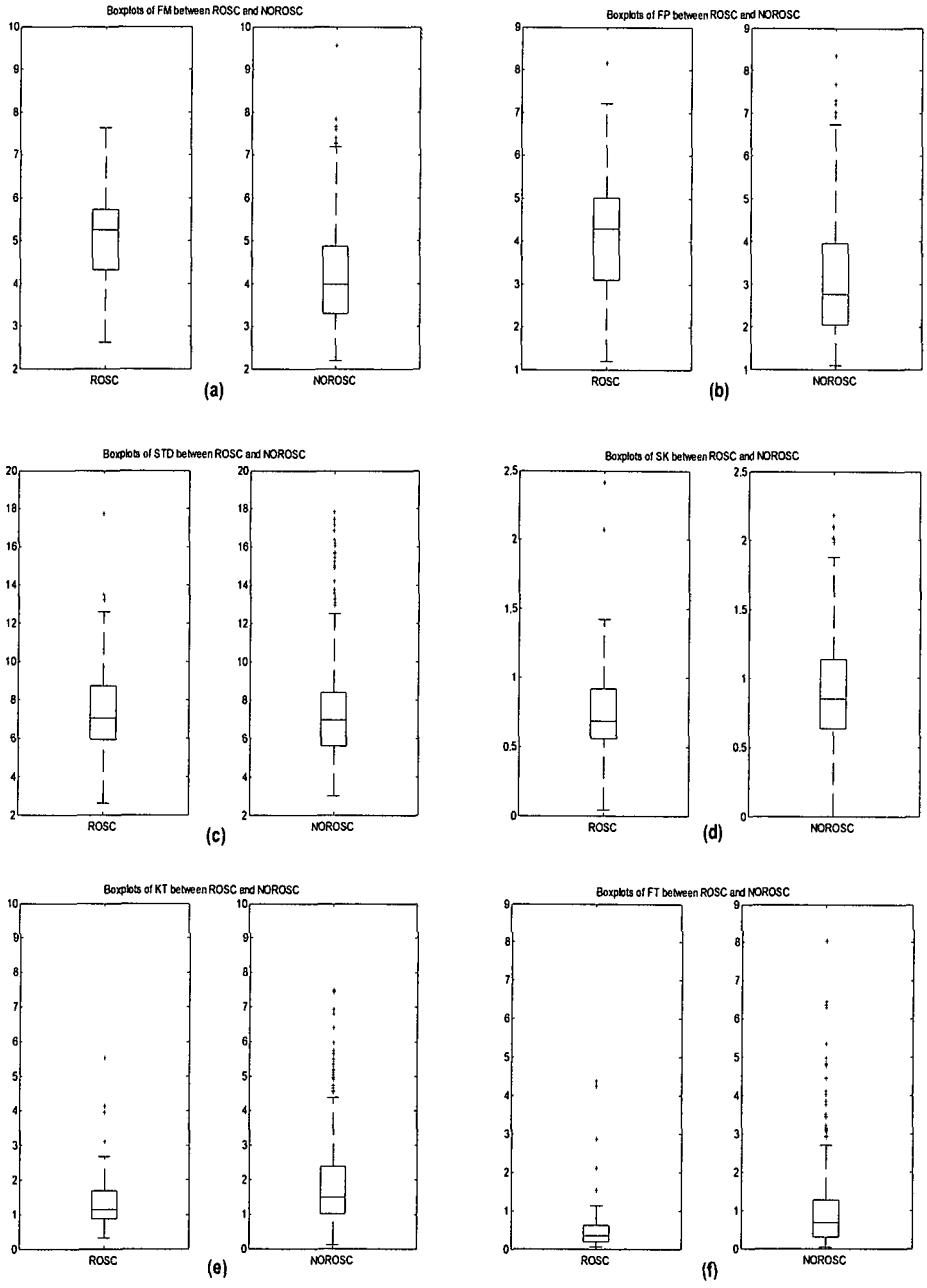

Figure B-13: Feature boxplots for the ROSC and NOROSC cases obtained from the WT-based method with 20 second length of pre-shock ECG: (a) FM feature boxplots, (b) FP feature boxplots, (c) STD feature boxplots, (d) SK feature boxplots, (e) KT feature boxplots, and (f) FT feature boxplots

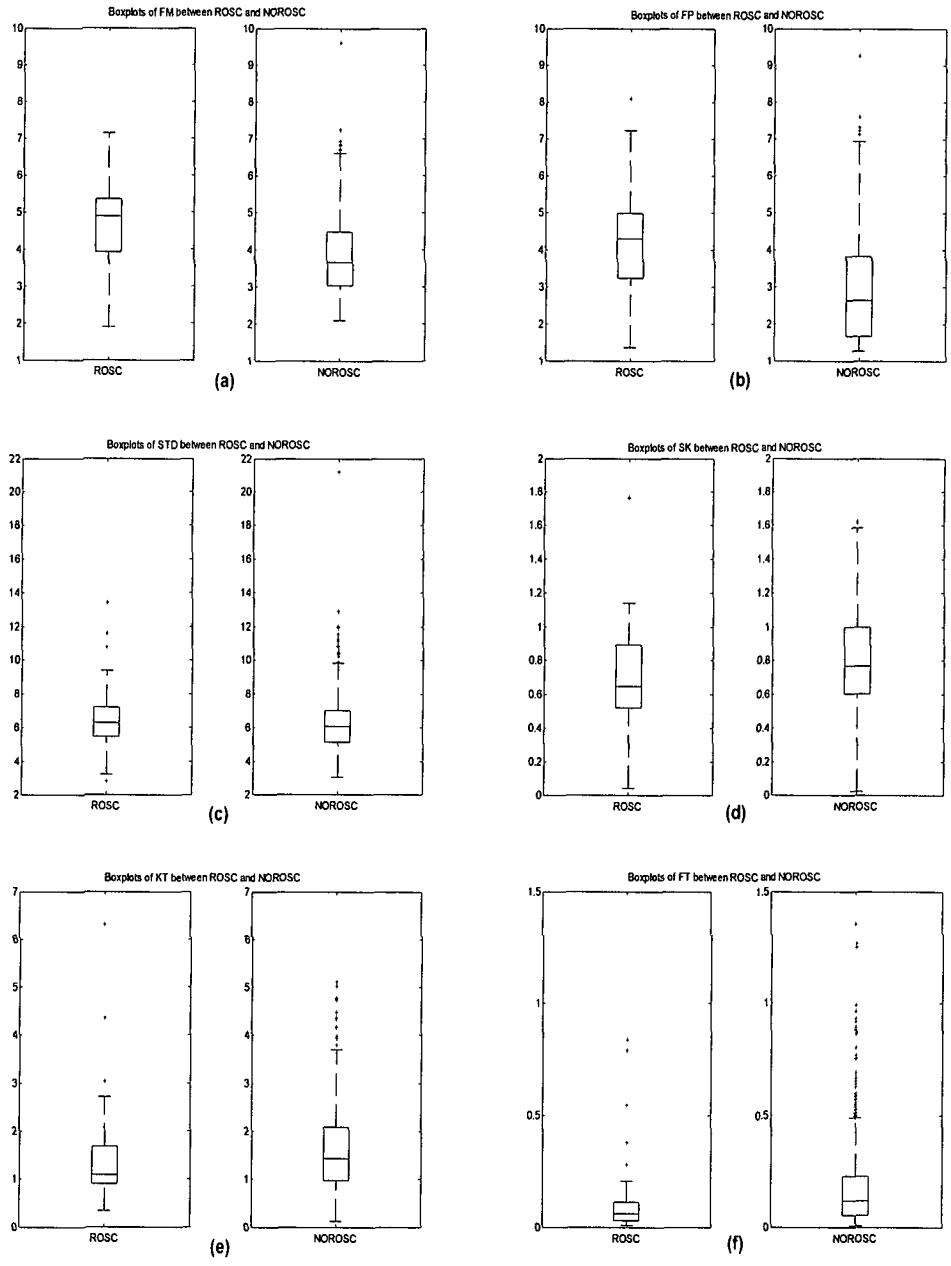

Figure B-14: Feature boxplots for the ROSC and NOROSC cases obtained from the STFT1-based method with 20 second length of pre-shock ECG: (a) FM feature boxplots, (b) FP feature boxplots, (c) STD feature boxplots, (d) SK feature boxplots, (e) KT feature boxplots, and (f) FT feature boxplots

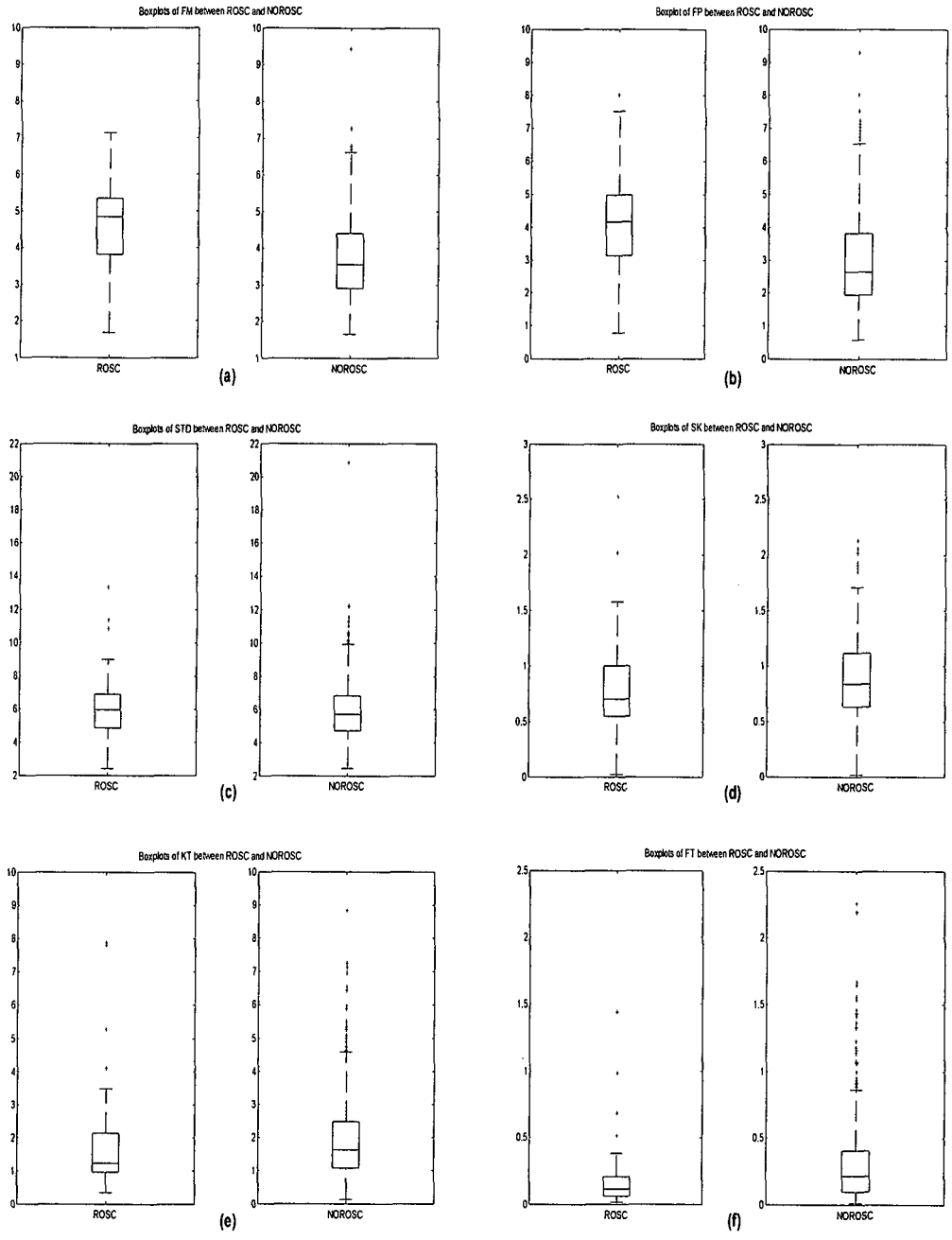

Figure B-15: Feature boxplots for the ROSC and NOROSC cases obtained from the STFT2-based method with 20 second length of pre-shock ECG: (a) FM feature boxplots, (b) FP feature boxplots, (c) STD feature boxplots, (d) SK feature boxplots, (e) KT feature boxplots, and (f) FT feature boxplots

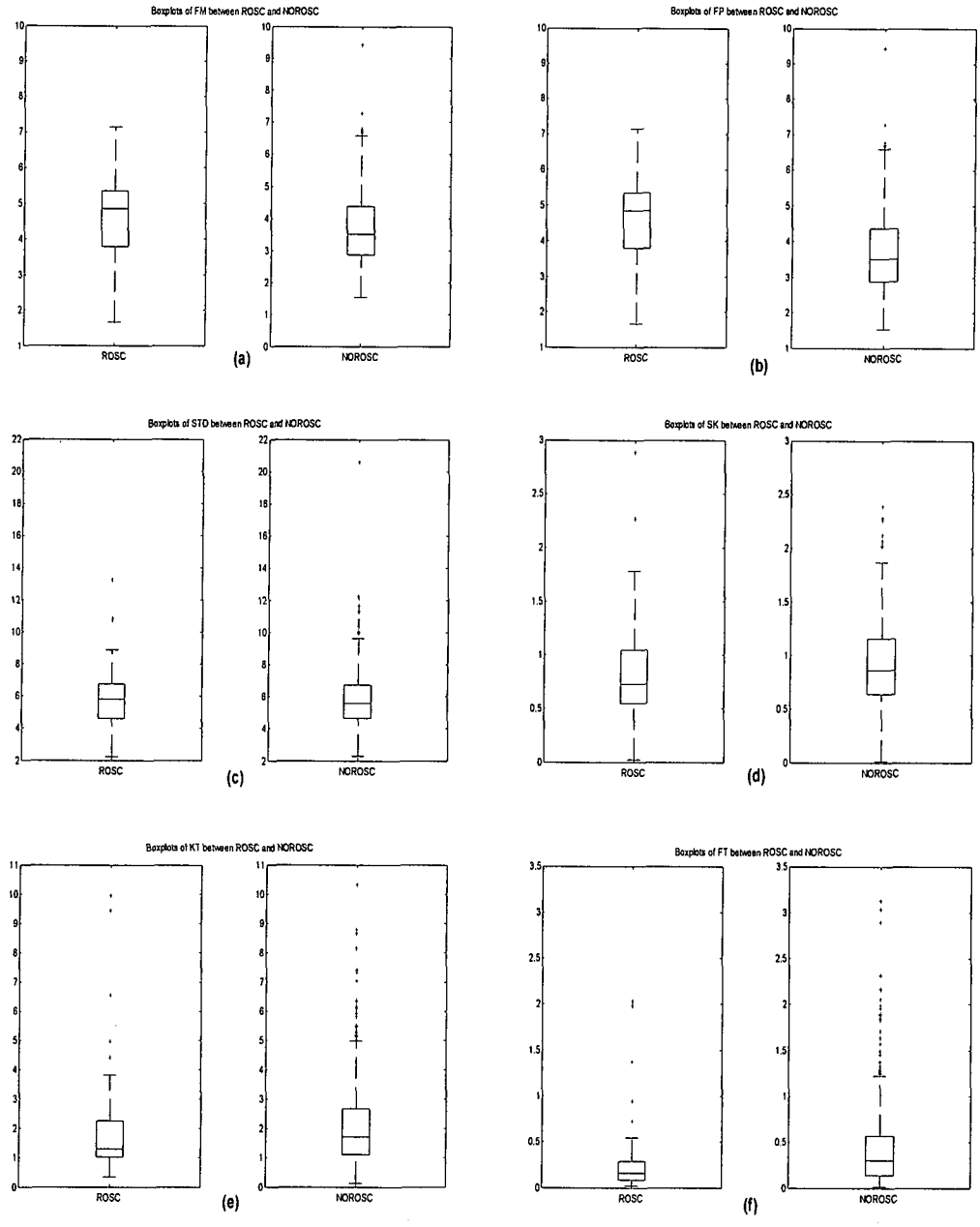

Figure B-16: Feature boxplots for the ROSC and NOROSC cases obtained from the STFT3-based method with 20 second length of pre-shock ECG: (a) FM feature boxplots, (b) FP feature boxplots, (c) STD feature boxplots, (d) SK feature boxplots, (e) KT feature boxplots, and (f) FT feature boxplots

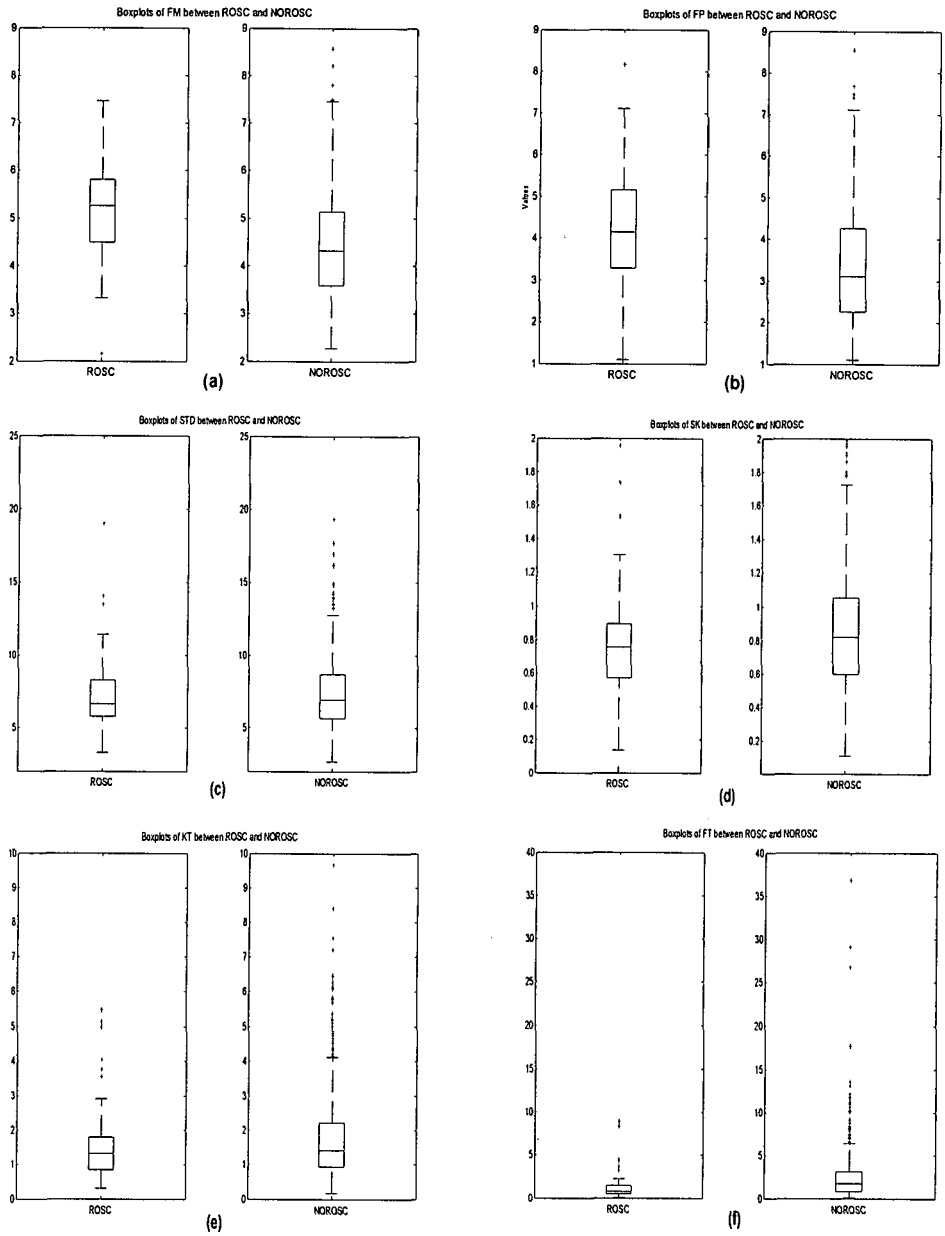

Figure B-17: Feature boxplots for the ROSC and NOROSC cases obtained from the WT-based method at location A in figure 4-22: (a) FM feature boxplots, (b) FP feature boxplots, (c) STD feature boxplots, (d) SK feature boxplots, (e) KT feature boxplots, and (f) FT feature boxplots

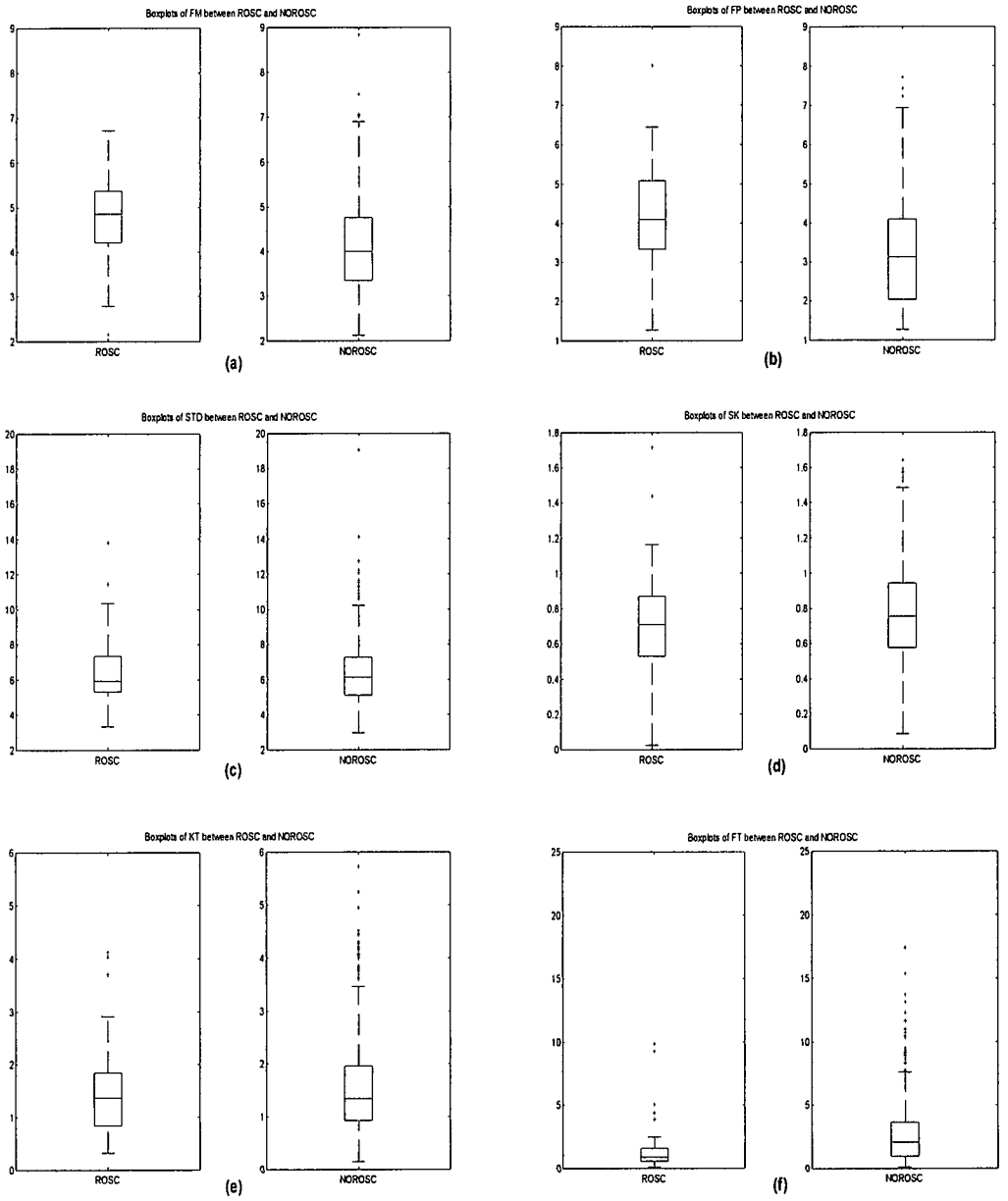

Figure B-18: Feature boxplots for the ROSC and NOROSC cases obtained from the STFT1-based method at location A in figure 4-22: (a) FM feature boxplots, (b) FP feature boxplots, (c) STD feature boxplots, (d) SK feature boxplots, (e) KT feature boxplots, and (f) FT feature boxplots

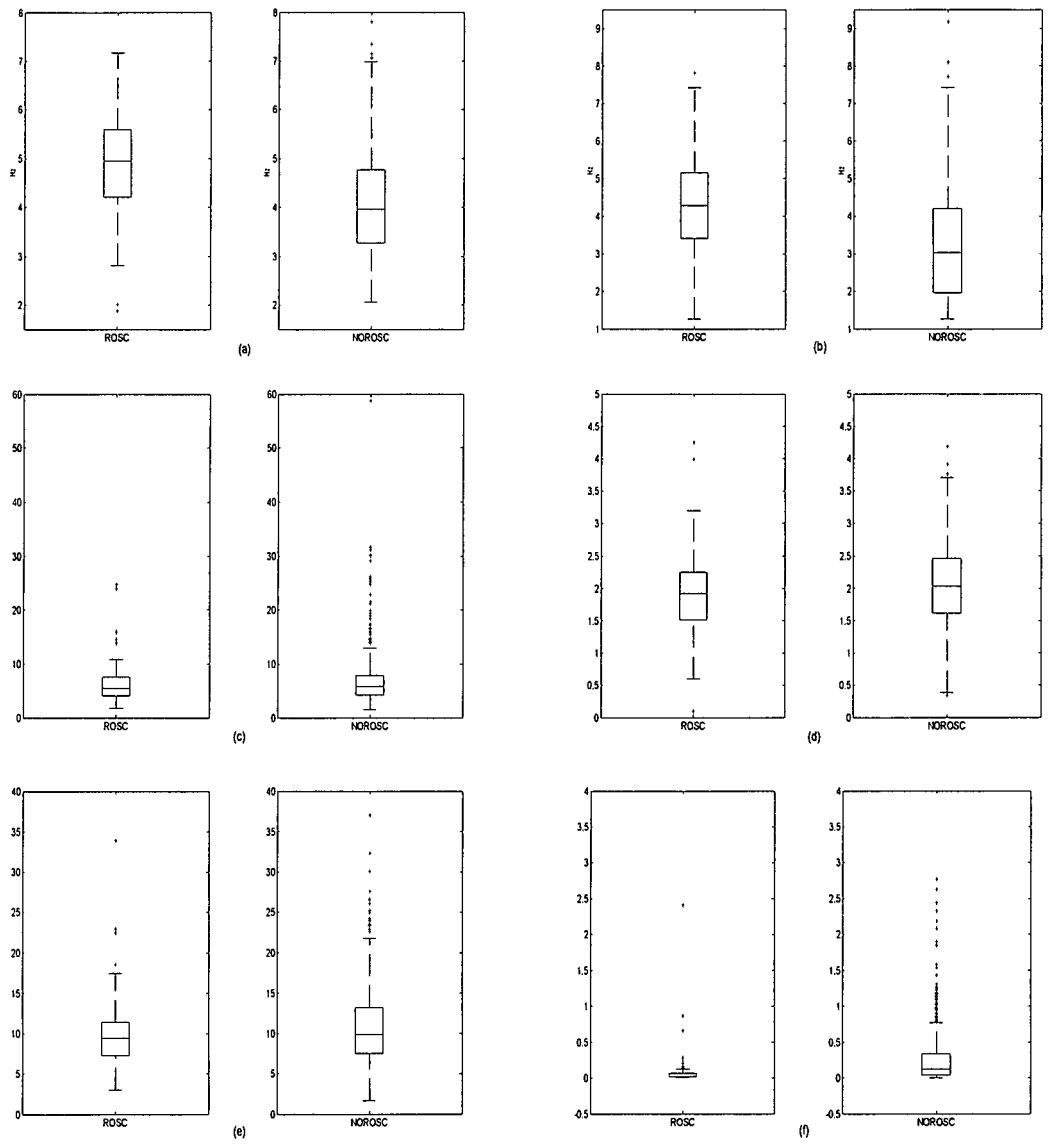

Figure B-19: Feature boxplots for the ROSC and NOROSC cases obtained from the WT-based method at location B in figure 4-22: (a) FM feature boxplots, (b) FP feature boxplots, (c) STD feature boxplots, (d) SK feature boxplots, (e) KT feature boxplots, and (f) FT feature boxplots

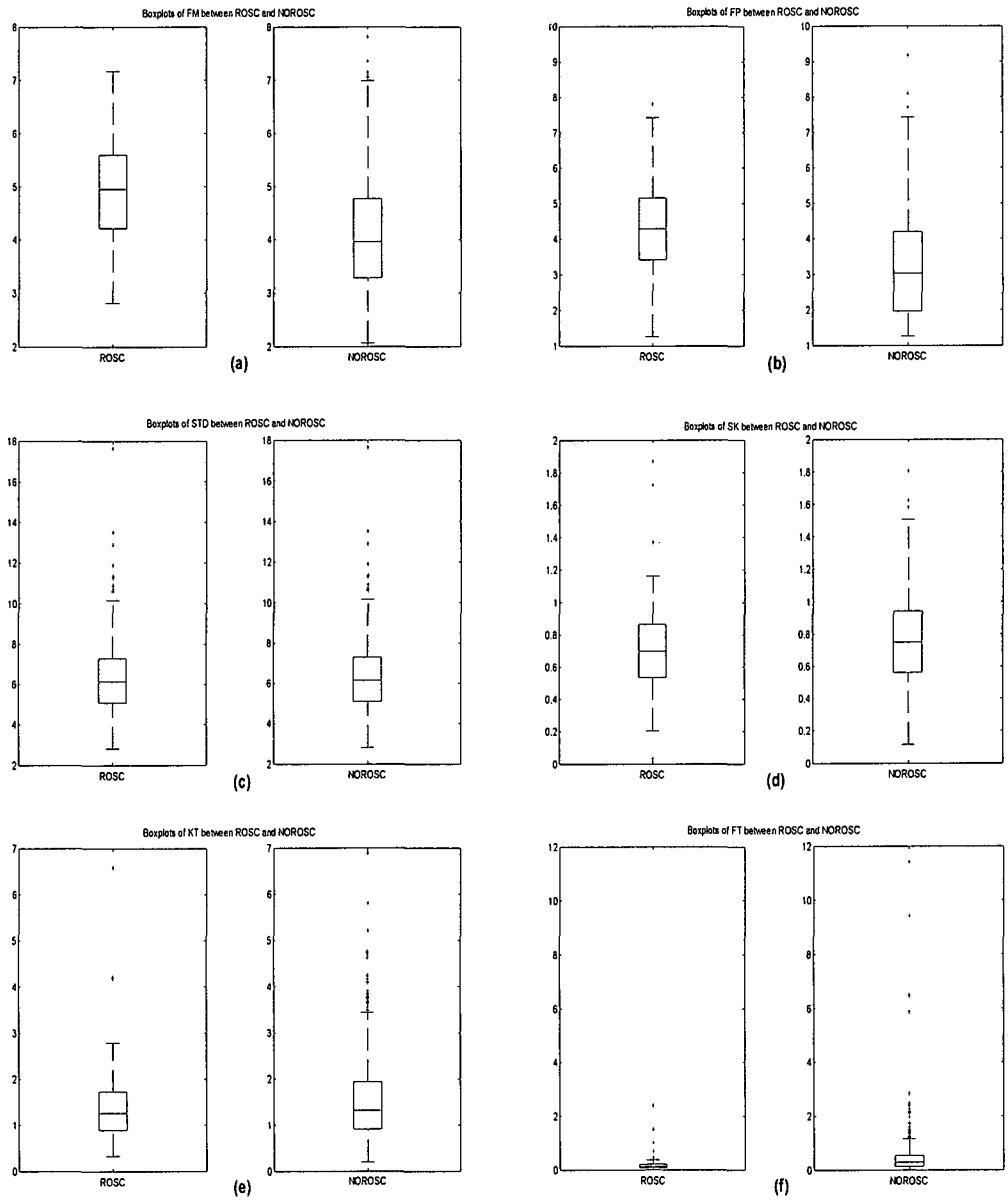

Figure B-20: Feature boxplots for the ROSC and NOROSC cases obtained from the STFT1-based method at location B in figure 4-22: (a) FM feature boxplots, (b) FP feature boxplots, (c) STD feature boxplots, (d) SK feature boxplots, (e) KT feature boxplots, and (f) FT feature boxplots

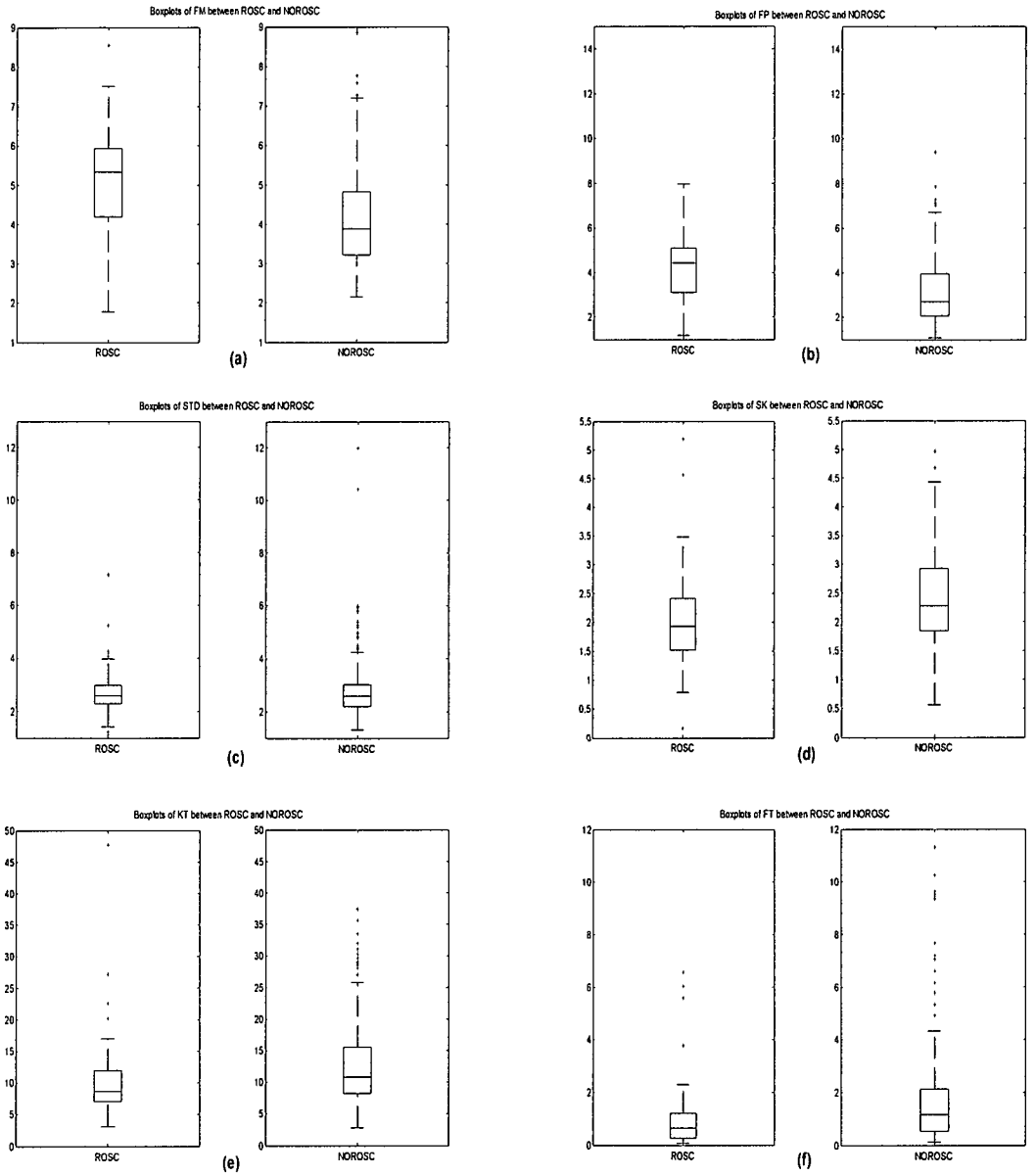

Figure B-21: Feature boxplots for the ROSC and NOROSC cases obtained from the WT-based method at location C in figure 4-22: (a) FM feature boxplots, (b) FP feature boxplots, (c) STD feature boxplots, (d) SK feature boxplots, (e) KT feature boxplots, and (f) FT feature boxplots

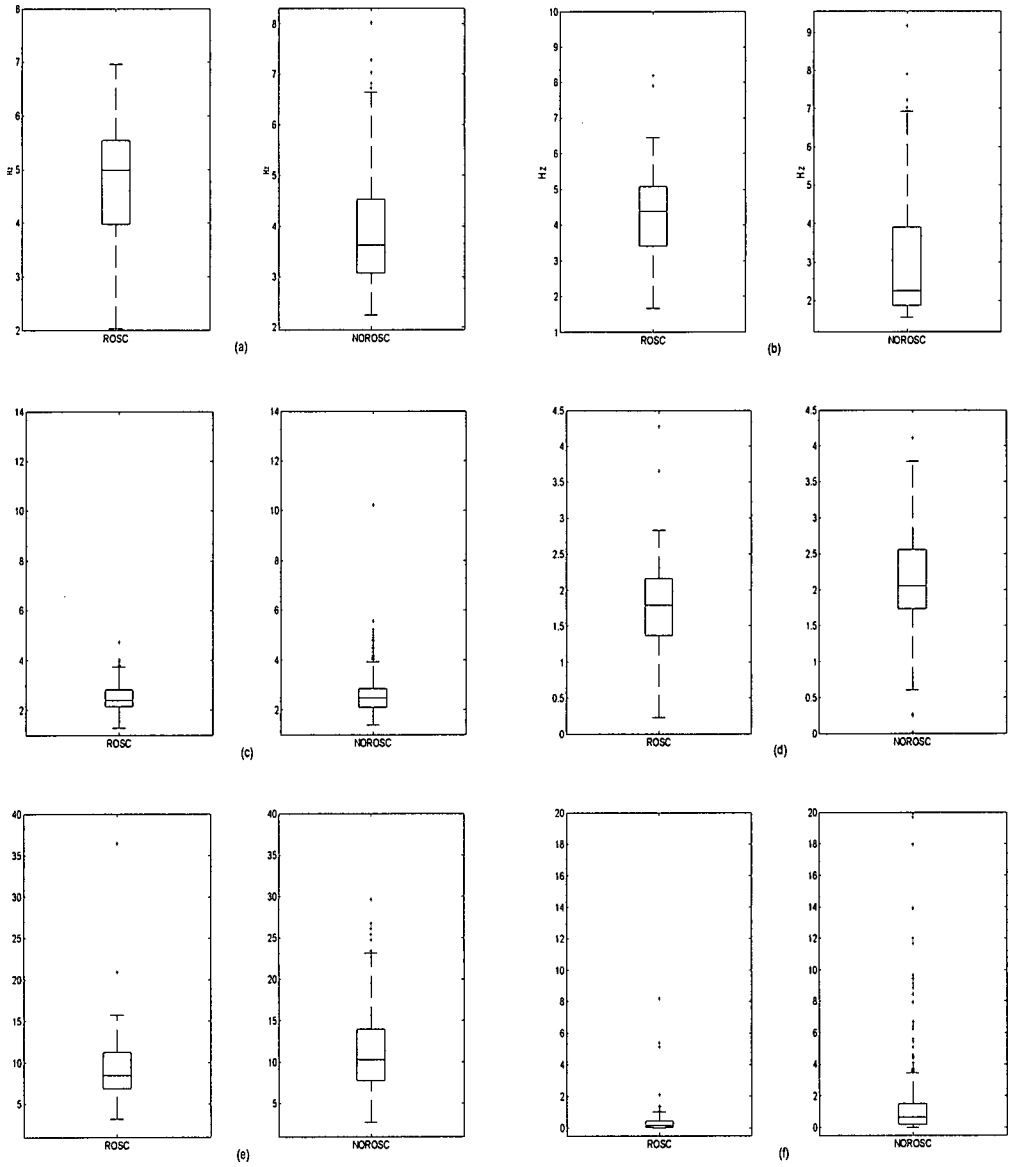

Figure B-22: Feature boxplots for the ROSC and NOROSC cases obtained from the STFT1-based method at location C in figure 4-22: (a) FM feature boxplots, (b) FP feature boxplots, (c) STD feature boxplots, (d) SK feature boxplots, (e) KT feature boxplots, and (f) FT feature boxplots

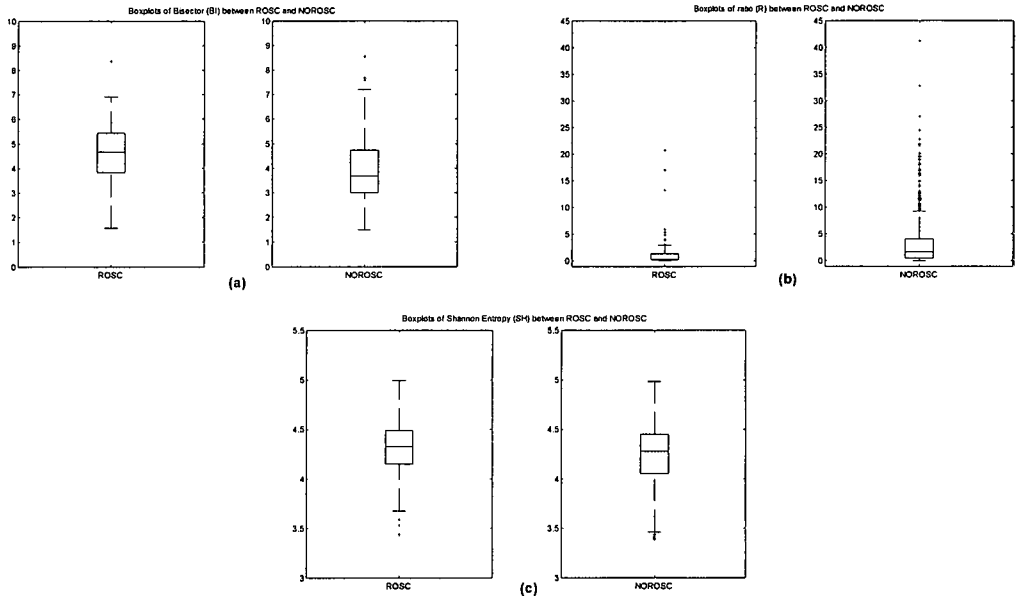

Figure B-23: Extra feature boxplots for the ROSC and NOROSC cases obtained from the WT-based method with 5 second length of pre-shock ECG: (a) BI feature boxplots, (b) R feature boxplots, and (c) SH feature boxplots

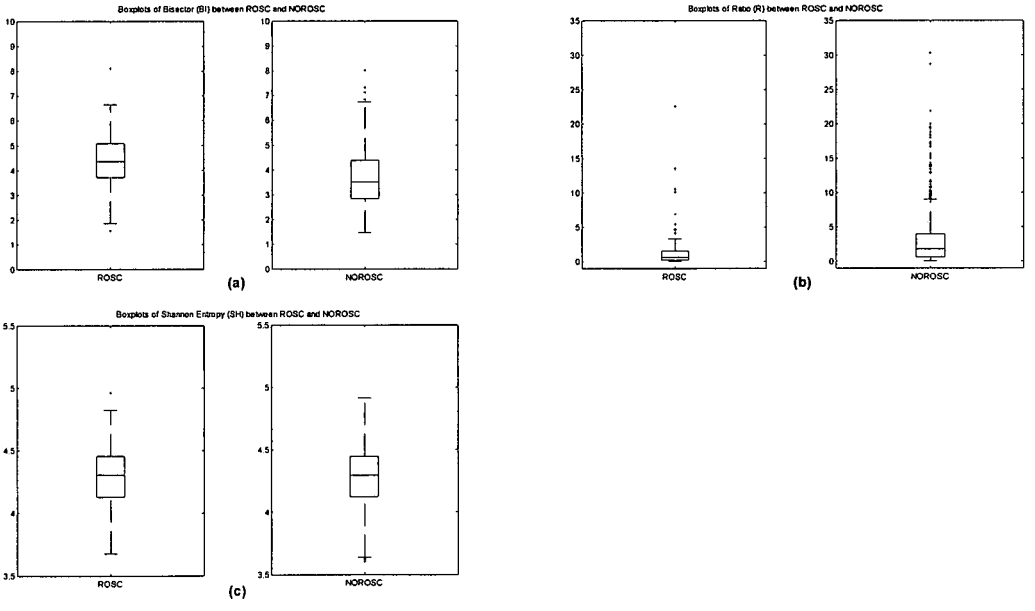

Figure B-24: Extra feature boxplots for the ROSC and NOROSC cases obtained from the STFT1-based method with 5 second length of pre-shock ECG: (a) BI feature boxplots, (b) R feature boxplots, and (c) SH feature boxplots

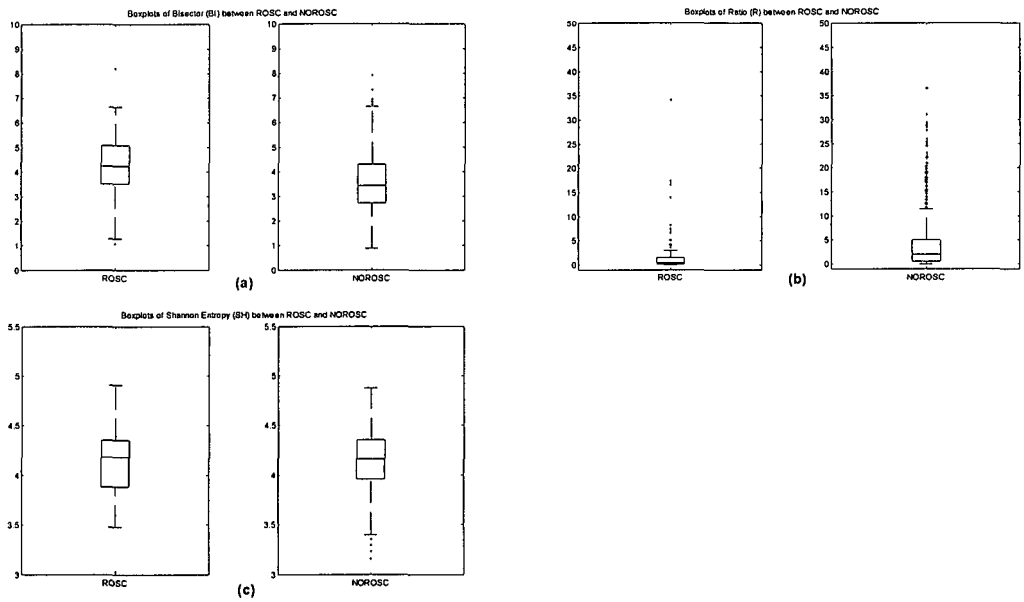

Figure B-25: Extra feature boxplots for the ROSC and NOROSC cases obtained from the STFT2-based method with 5 second length of pre-shock ECG: (a) BI feature boxplots, (b) R feature boxplots, and (c) SH feature boxplots

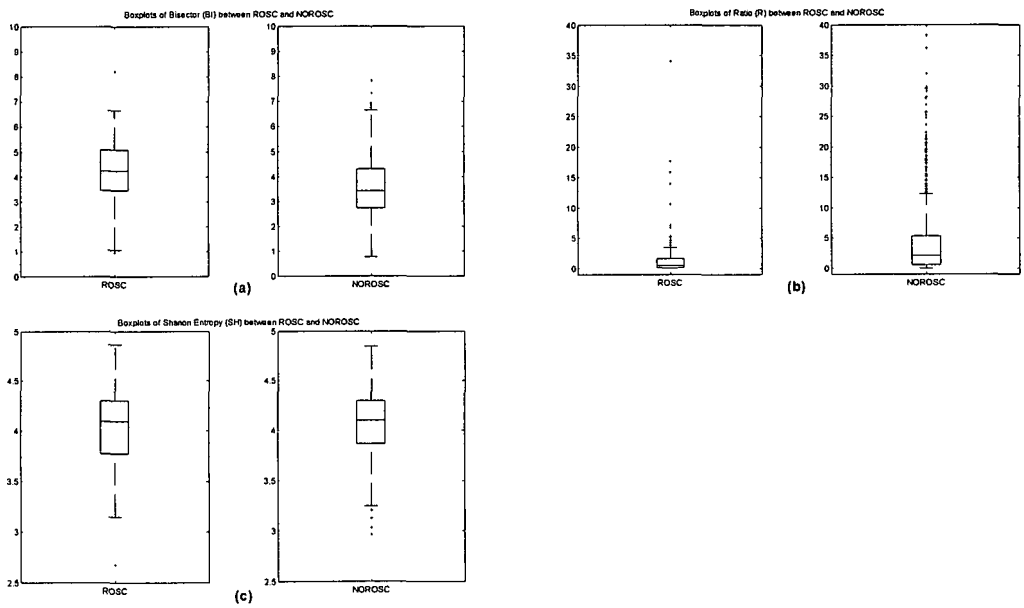

Figure B-26: Extra feature boxplots for the ROSC and NOROSC cases obtained from the STFT3-based method with 5 second length of pre-shock ECG: (a) BI feature boxplots, (b) R feature boxplots, and (c) SH feature boxplots

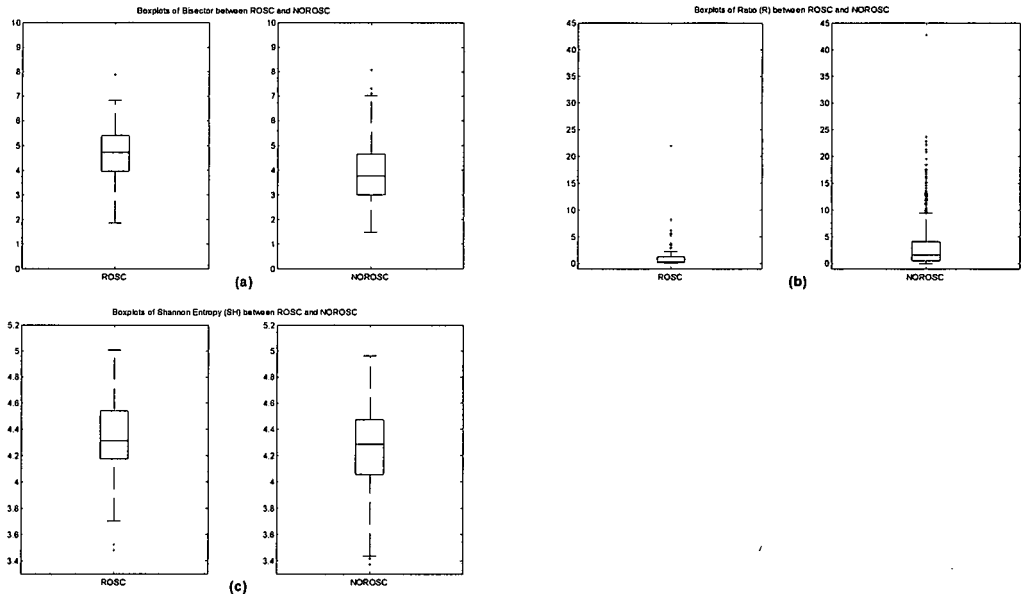

Figure B-27: Extra feature boxplots for the ROSC and NOROSC cases obtained from the WT-based method with 10 second length of pre-shock ECG: (a) BI feature boxplots, (b) R feature boxplots, and (c) SH feature boxplots

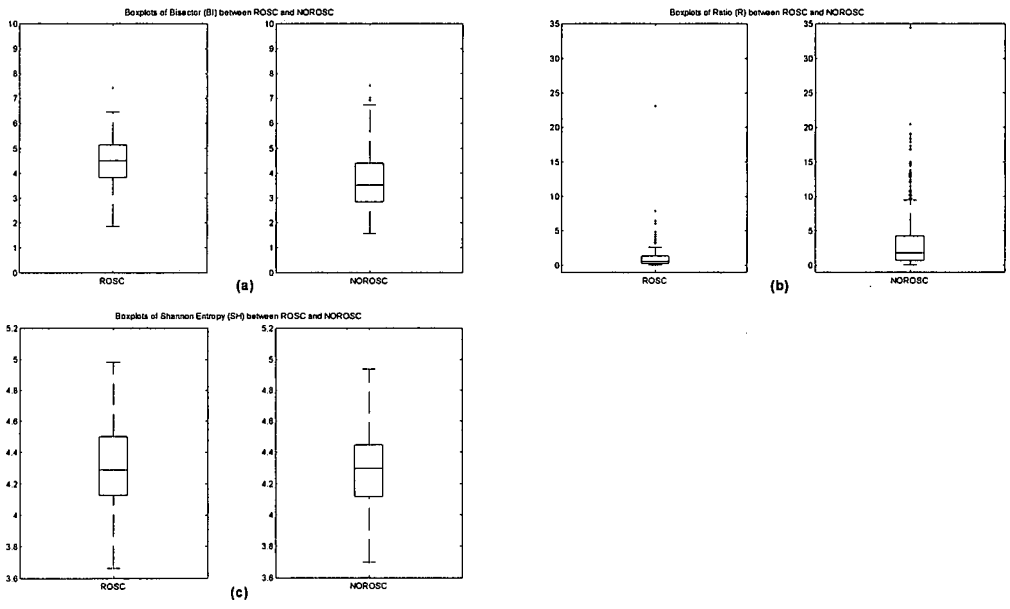

Figure B-28: Extra feature boxplots for the ROSC and NOROSC cases obtained from the STFT1-based method with 10 second length of pre-shock ECG: (a) BI feature boxplots, (b) R feature boxplots, and (c) SH feature boxplots

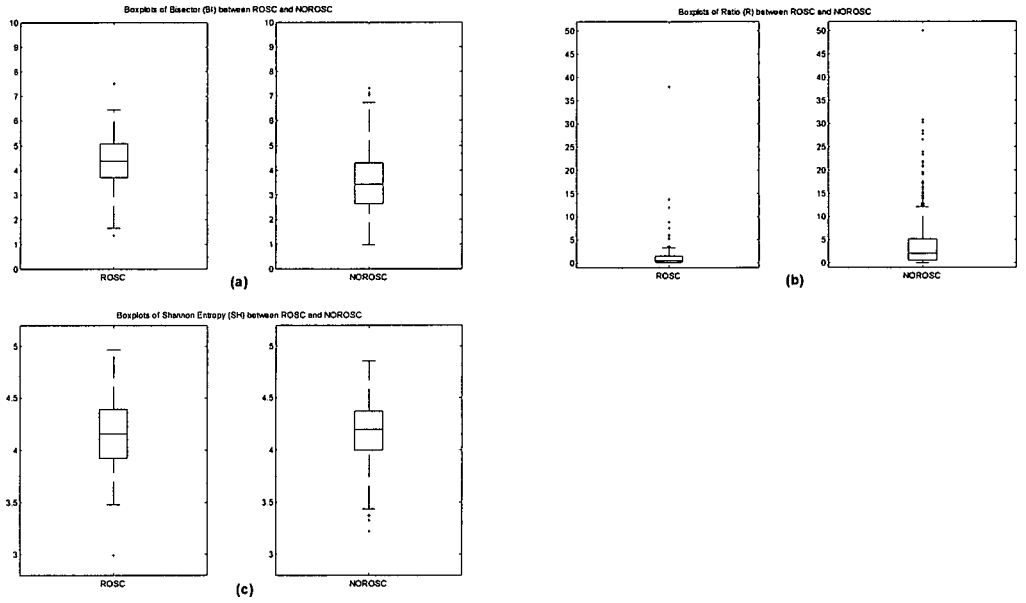

Figure B-29: Extra feature boxplots for the ROSC and NOROSC cases obtained from the STFT2-based method with 10 second length of pre-shock ECG: (a) BI feature boxplots, (b) R feature boxplots, and (c) SH feature boxplots

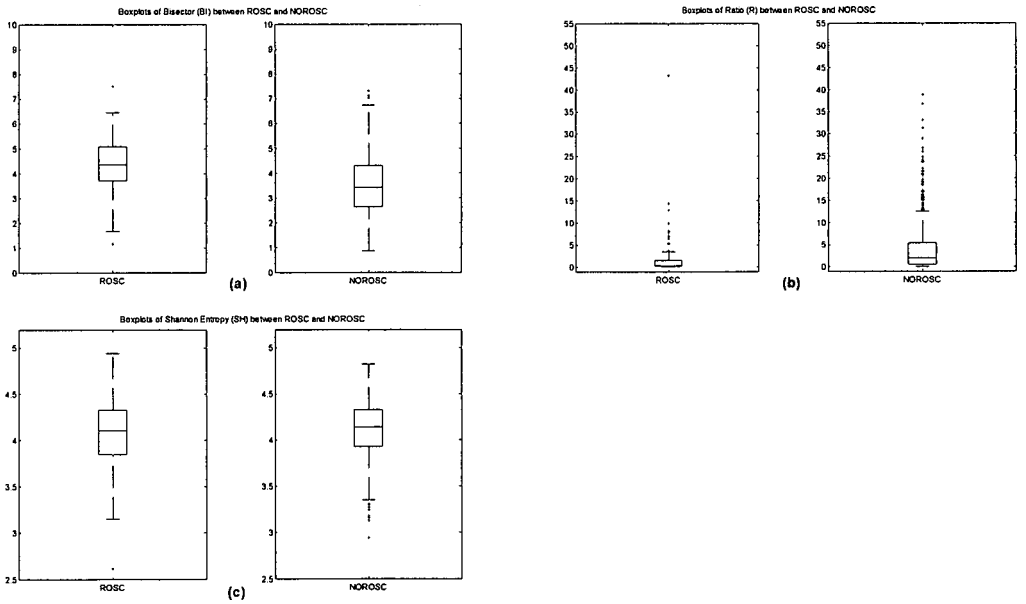

Figure B-30: Extra feature boxplots for the ROSC and NOROSC cases obtained from the STFT3-based method with 10 second length of pre-shock ECG: (a) BI feature boxplots, (b) R feature boxplots, and (c) SH feature boxplots

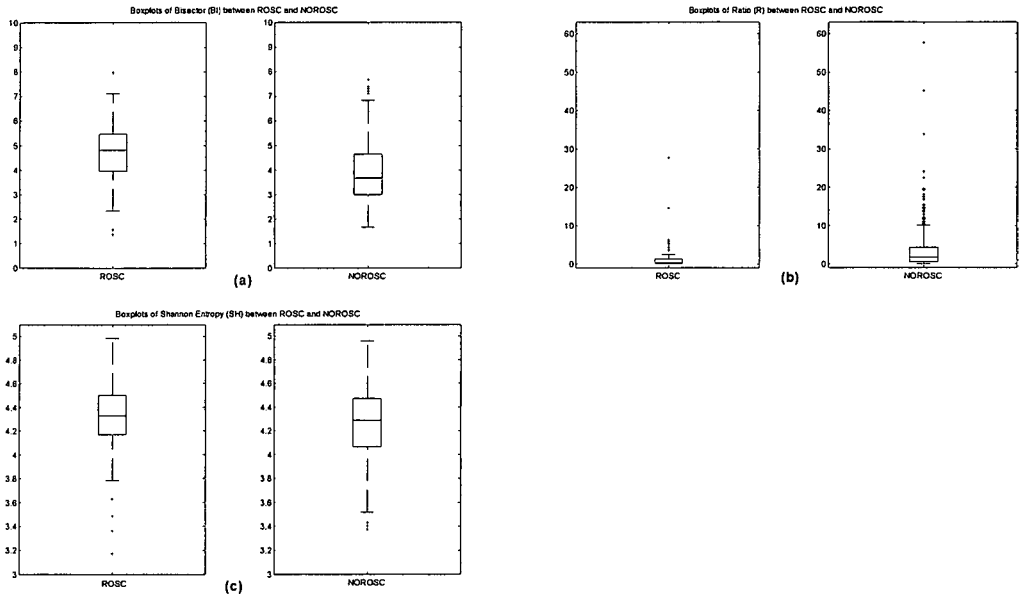

Figure B-31: Extra feature boxplots for the ROSC and NOROSC cases obtained from the WT-based method with 15 second length of pre-shock ECG: (a) BI feature boxplots, (b) R feature boxplots, and (c) SH feature boxplots

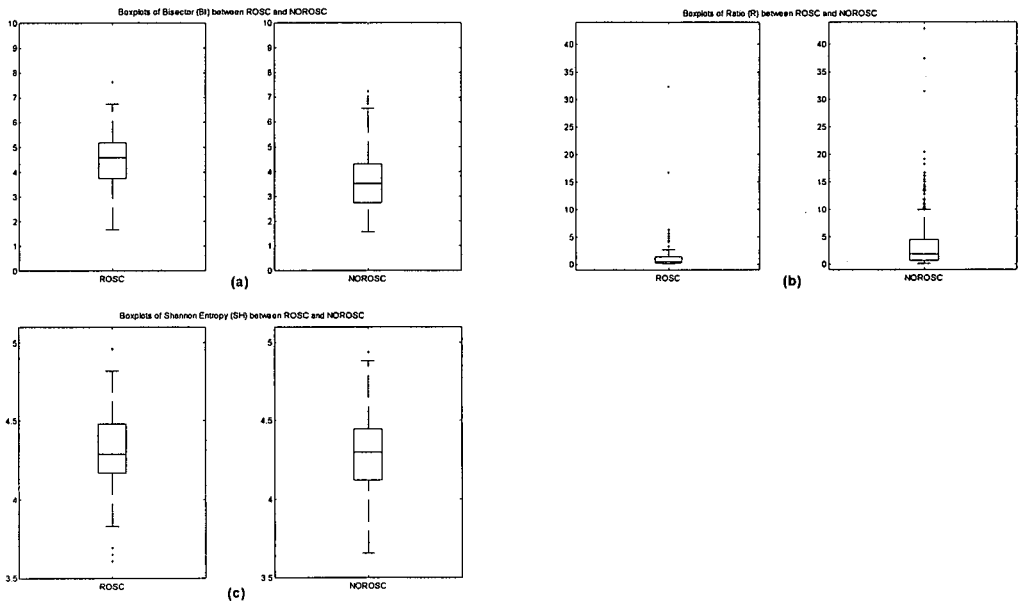

Figure B-32: Extra feature boxplots for the ROSC and NOROSC cases obtained from the STFT1-based method with 15 second length of pre-shock ECG: (a) BI feature boxplots, (b) R feature boxplots, and (c) SH feature boxplots

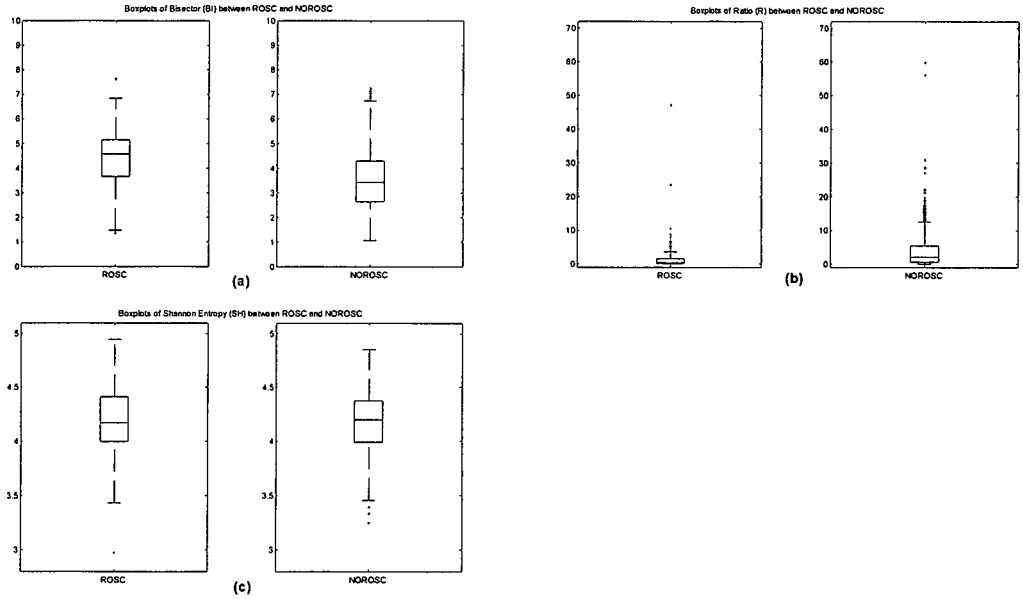

Figure B-33: Extra feature boxplots for the ROSC and NOROSC cases obtained from the STFT2-based method with 15 second length of pre-shock ECG: (a) BI feature boxplots, (b) R feature boxplots, and (c) SH feature boxplots

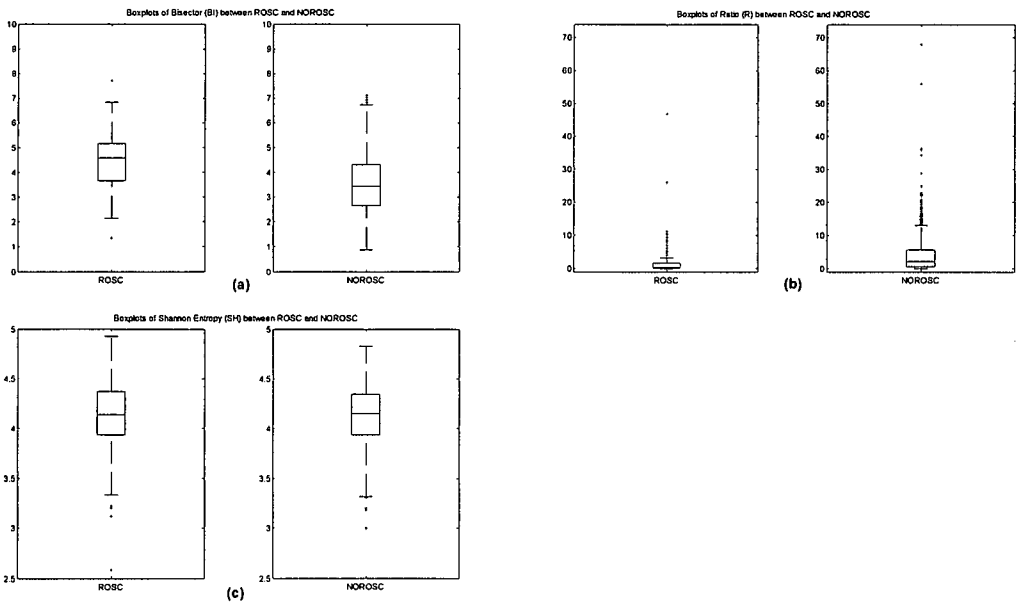

Figure B-34: Extra feature boxplots for the ROSC and NOROSC cases obtained from the STFT3-based method with 15 second length of pre-shock ECG: (a) BI feature boxplots, (b) R feature boxplots, and (c) SH feature boxplots

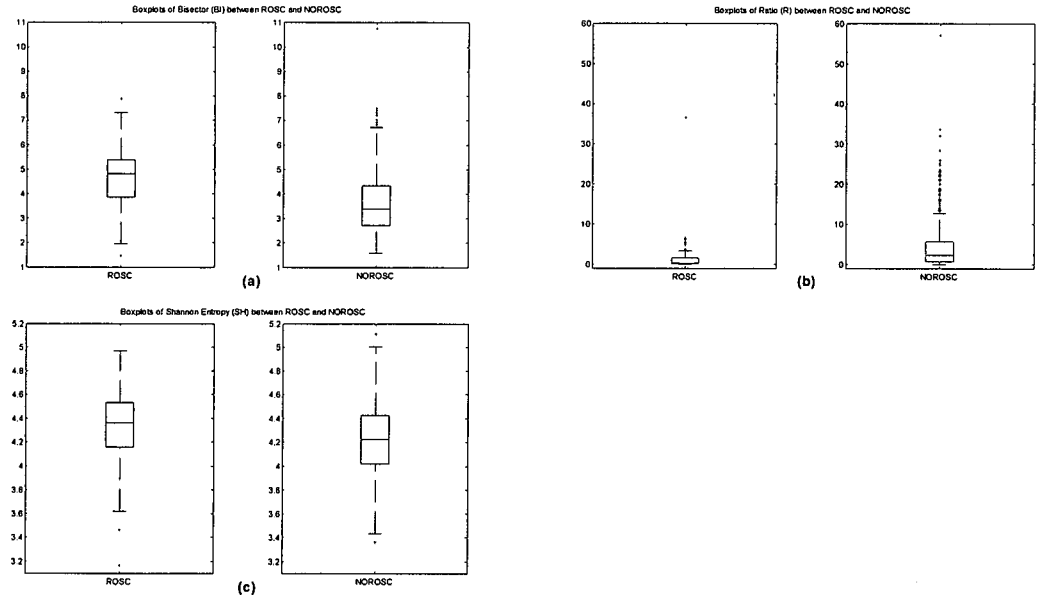

Figure B-35: Extra feature boxplots for the ROSC and NOROSC cases obtained from the WT-based method with 20 second length of pre-shock ECG: (a) BI feature boxplots, (b) R feature boxplots, and (c) SH feature boxplots

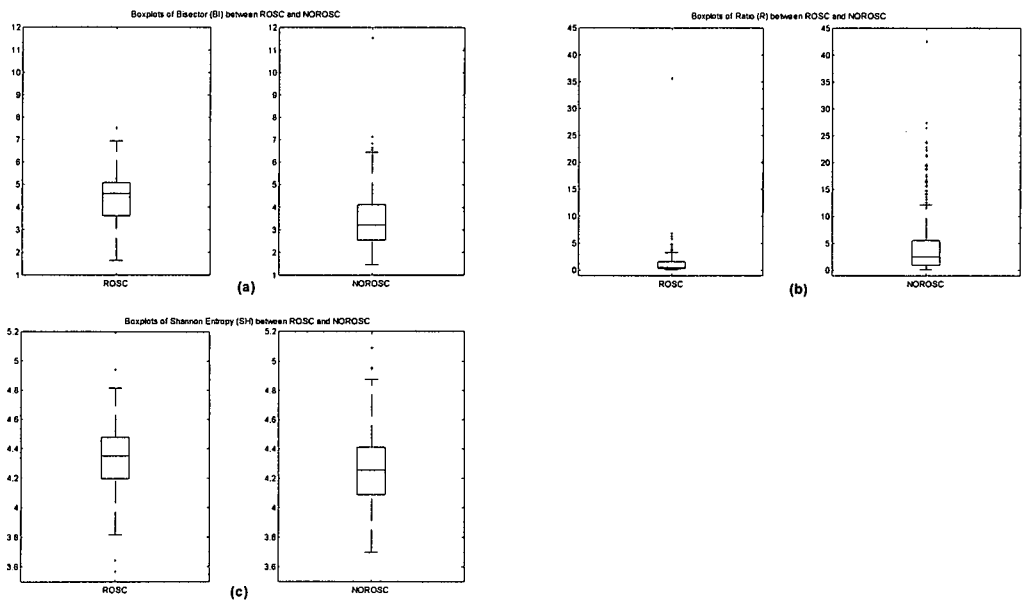

Figure B-36: Extra feature boxplots for the ROSC and NOROSC cases obtained from the STFT1-based method with 20 second length of pre-shock ECG: (a) BI feature boxplots, (b) R feature boxplots, and (c) SH feature boxplots

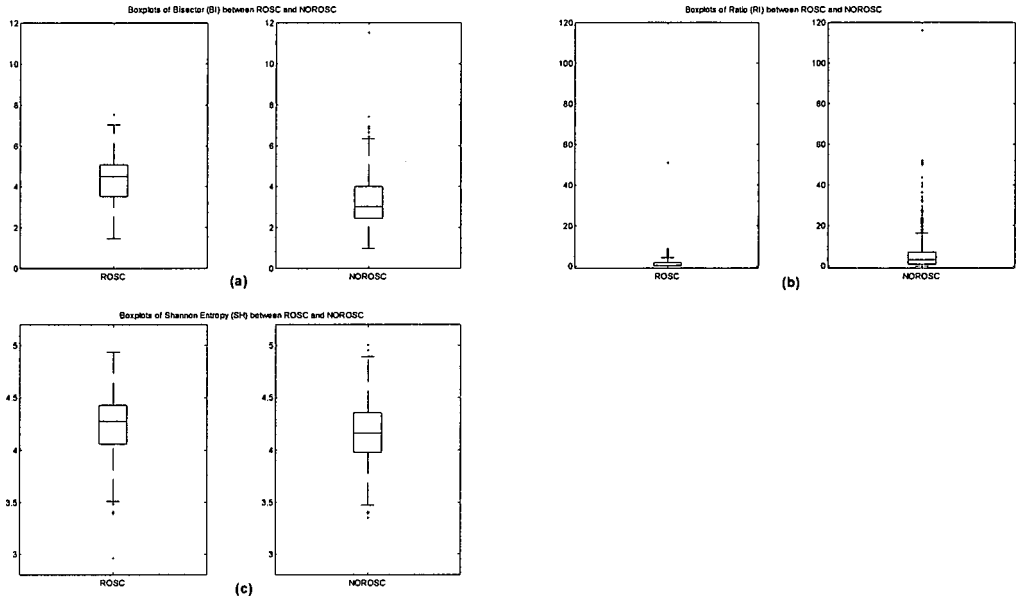

Figure B-37: Extra feature boxplots for the ROSC and NOROSC cases obtained from the STFT2-based method with 20 second length of pre-shock ECG: (a) BI feature boxplots, (b) R feature boxplots, and (c) SH feature boxplots

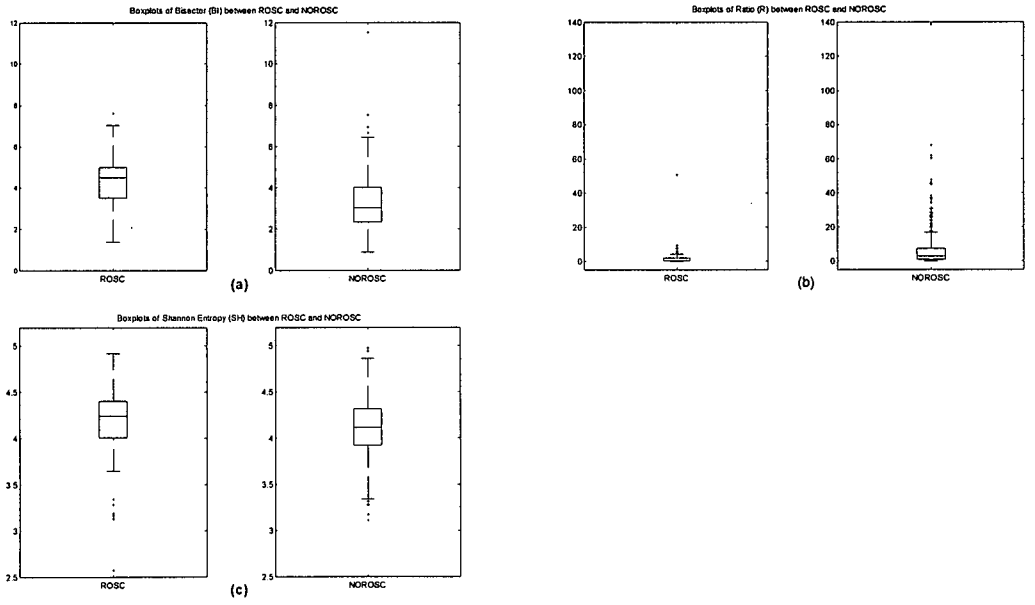

Figure B-38: Extra feature boxplots for the ROSC and NOROSC cases obtained from the STFT3-based method with 20 second length of pre-shock ECG: (a) BI feature boxplots, (b) R feature boxplots, and (c) SH feature boxplots

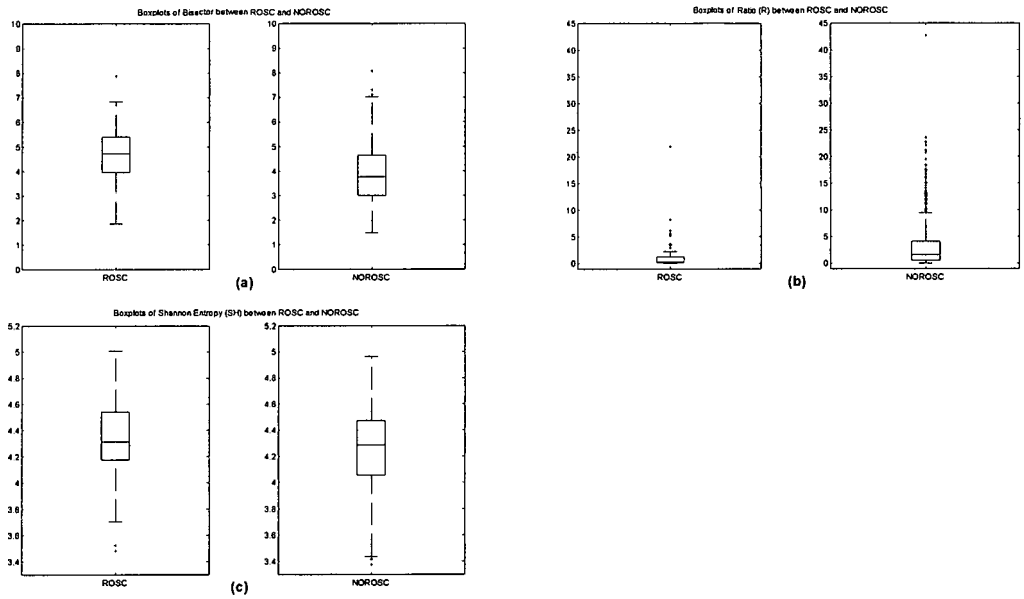

Figure B-39: Extra feature boxplots for the ROSC and NOROSC cases obtained from the WT-based method with at location A: (a) BI feature boxplots, (b) R feature boxplots, and (c) SH feature boxplots

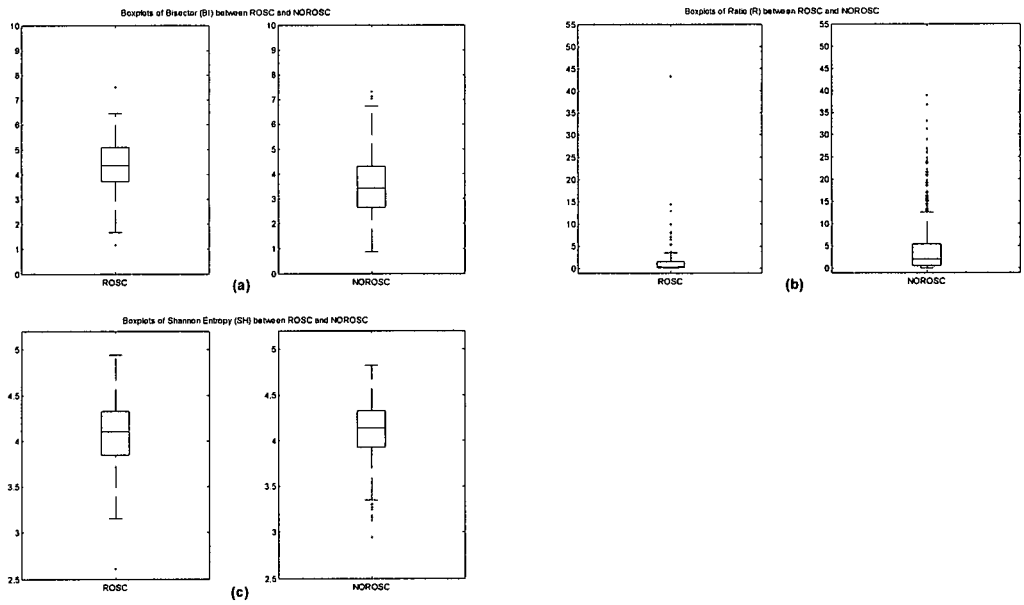

Figure B-40: Extra feature boxplots for the ROSC and NOROSC cases obtained from the STFT3-based method with at location A: (a) BI feature boxplots, (b) R feature boxplots, and (c) SH feature boxplots

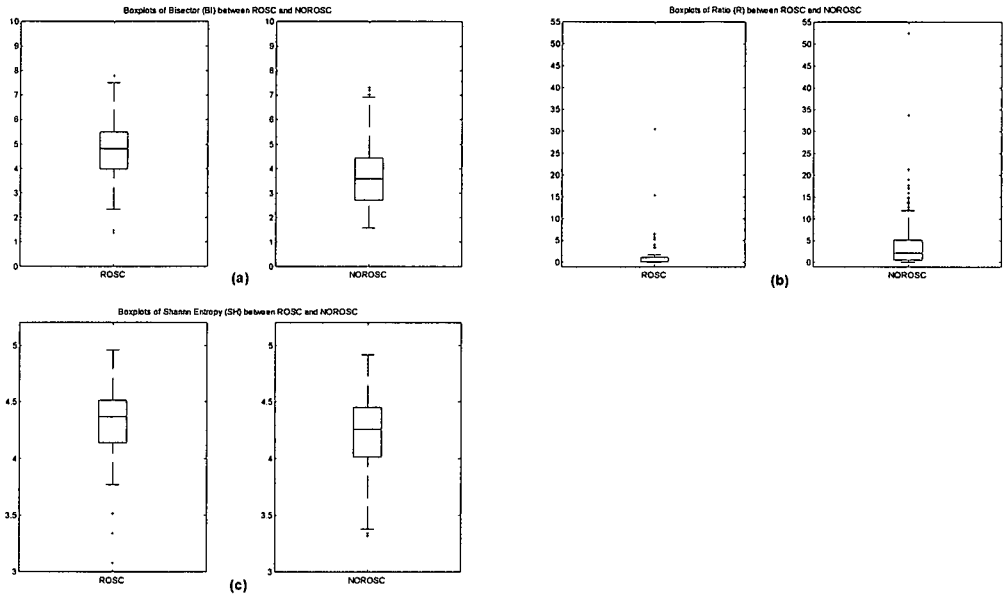

Figure B-41: Extra feature boxplots for the ROSC and NOROSC cases obtained from the WT-based method with at location B: (a) BI feature boxplots, (b) R feature boxplots, and (c) SH feature boxplots

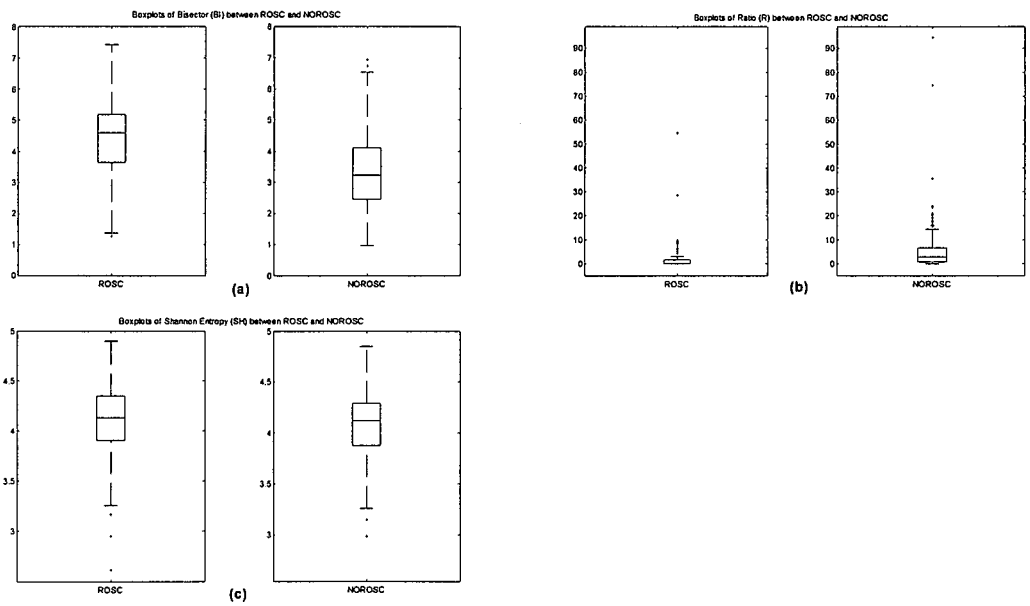

Figure B-42: Extra feature boxplots for the ROSC and NOROSC cases obtained from the STFT3-based method with at location B: (a) BI feature boxplots, (b) R feature boxplots, and (c) SH feature boxplots

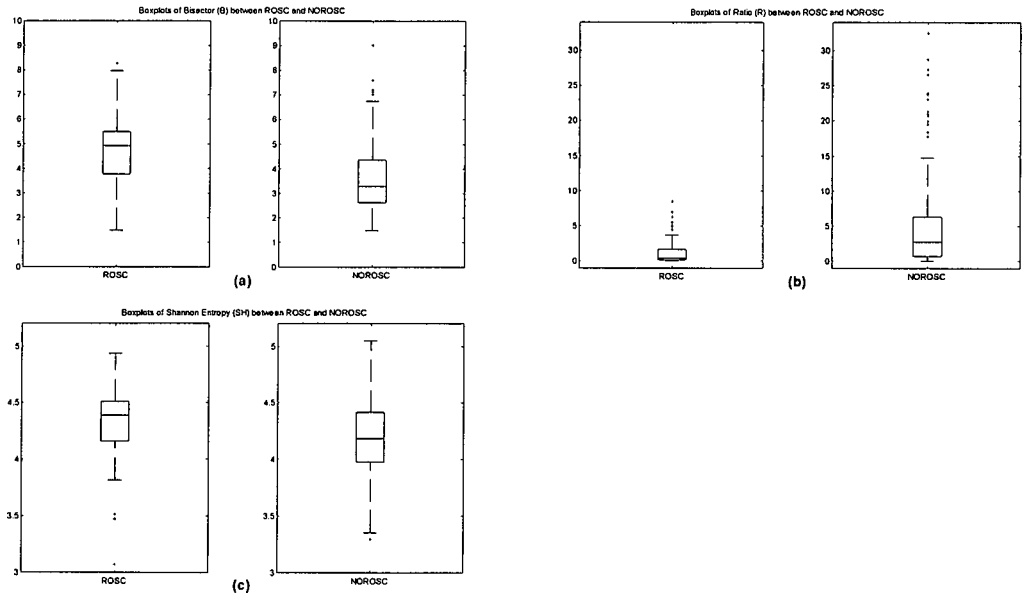

Figure B-43: Extra feature boxplots for the ROSC and NOROSC cases obtained from the WT-based method with at location C: (a) BI feature boxplots, (b) R feature boxplots, and (c) SH feature boxplots

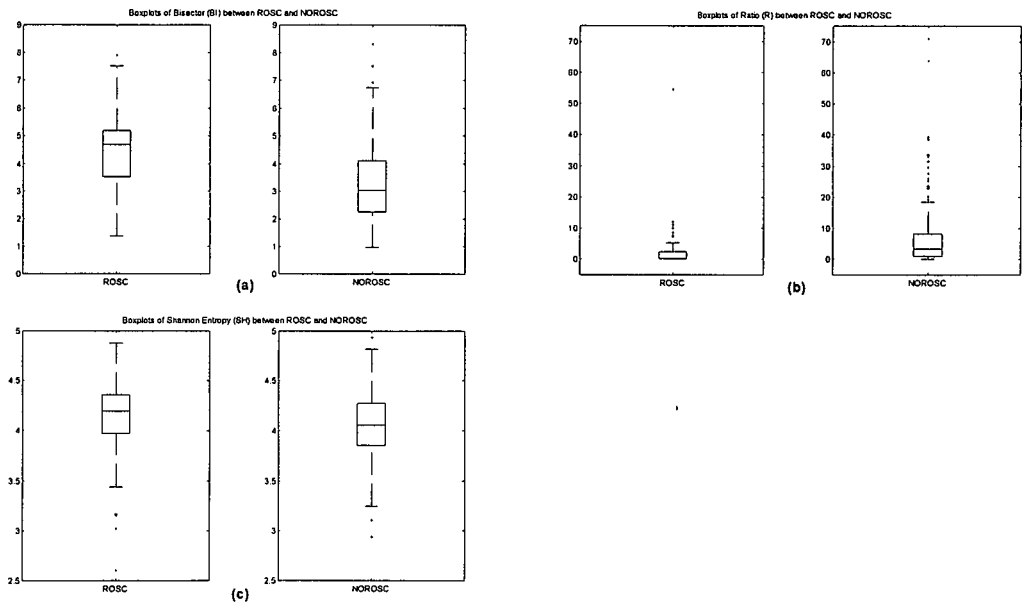

Figure B-44: Extra feature boxplots for the ROSC and NOROSC cases obtained from the STFT3-based method with at location C: (a) BI feature boxplots, (b) R feature boxplots, and (c) SH feature boxplots

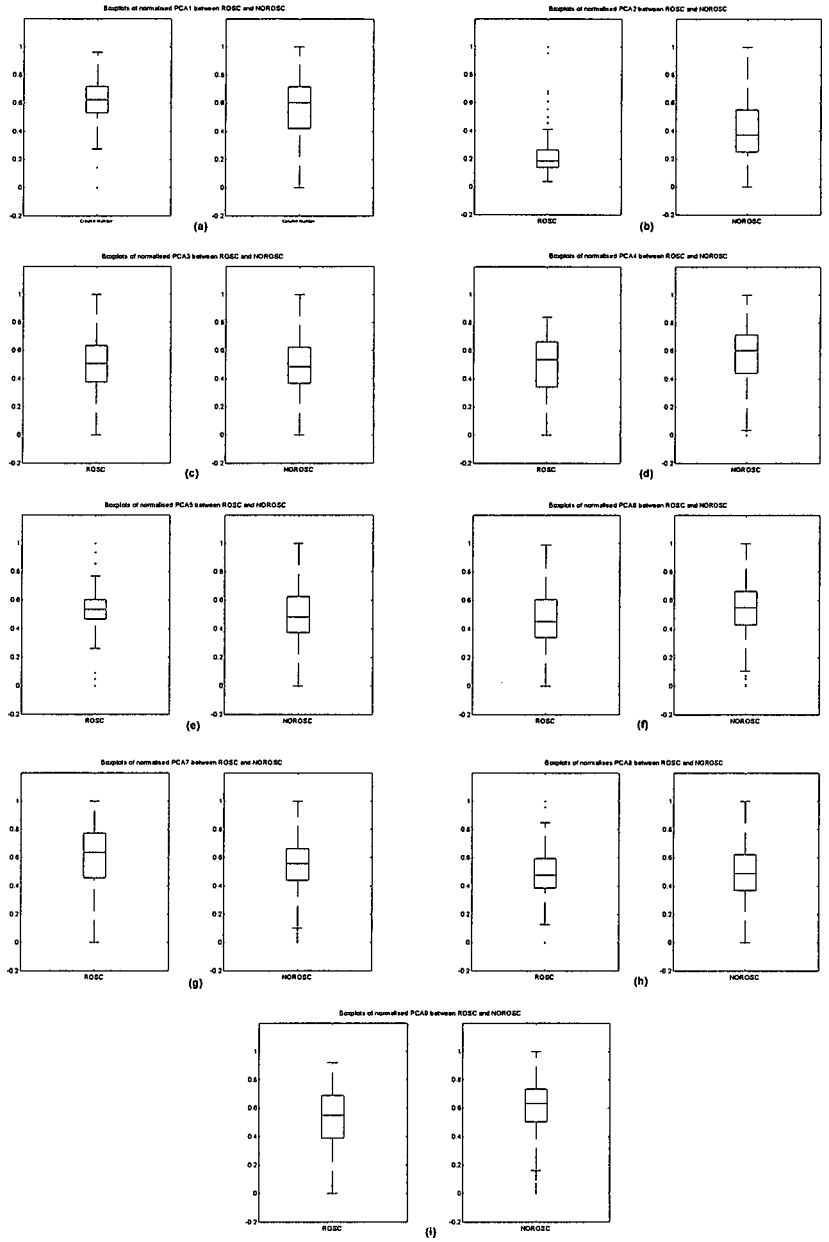

Figure B-45: PCA feature boxplots for the ROSC and NOROSC cases obtained from the WT-based method with 5 second length of pre-shock: (a) PCA1 feature boxplots, (b) PCA2 feature boxplots, (c) PCA3 feature boxplots, (d) PCA4 feature boxplots, (e) PCA5 feature boxplots, (f) PCA6 feature boxplots, (g) PCA7 feature boxplots, (h) PCA8 feature boxplots, and (i) PCA9 feature boxplots

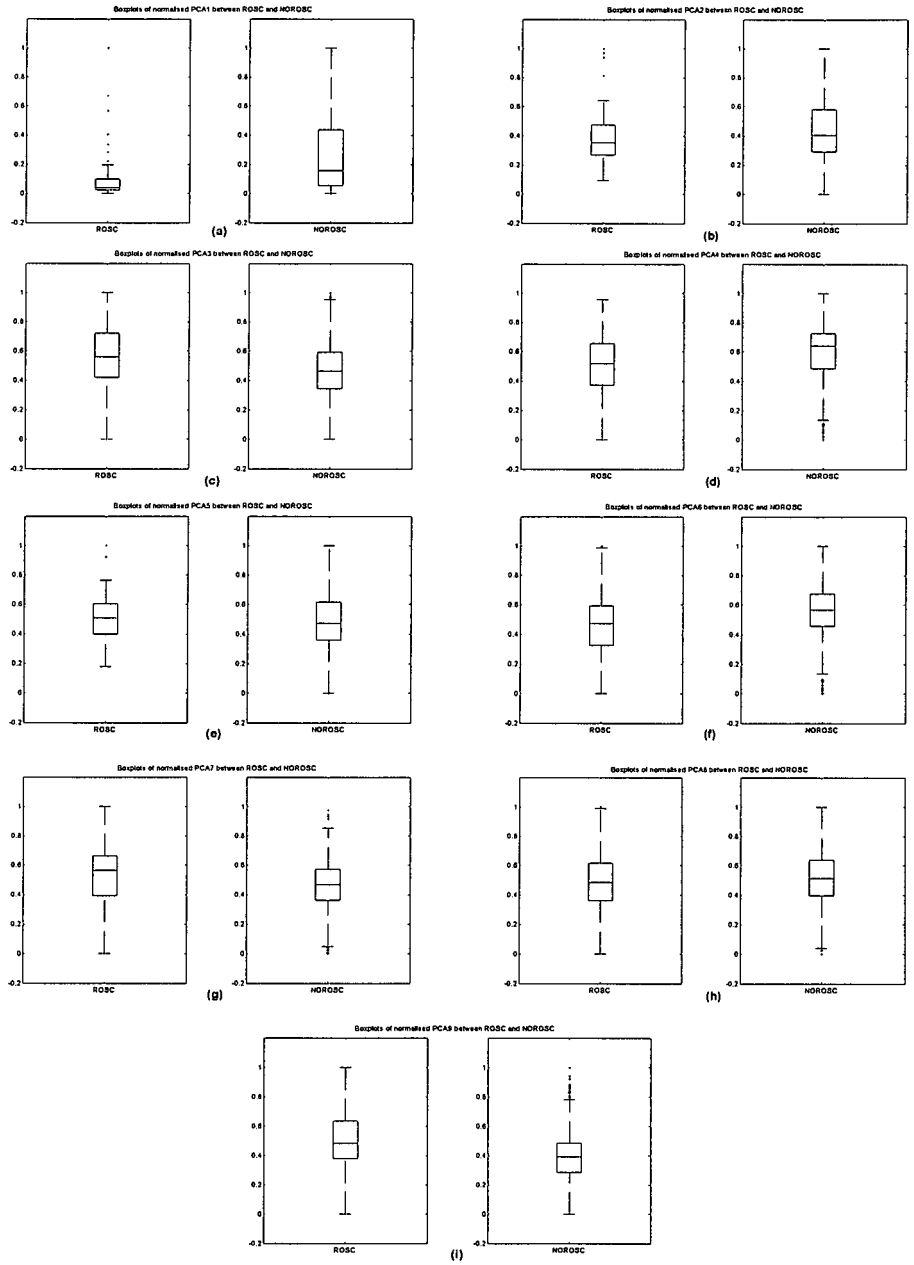

Figure B-46: PCA feature boxplots for the ROSC and NOROSC cases obtained from the STFT1-based method with 5 second length of pre-shock: (a) PCA1 feature boxplots, (b) PCA2 feature boxplots, (c) PCA3 feature boxplots, (d) PCA4 feature boxplots, (e) PCA5 feature boxplots, (f) PCA6 feature boxplots, (g) PCA7 feature boxplots, (h) PCA8 feature boxplots, and (i) PCA9 feature boxplots

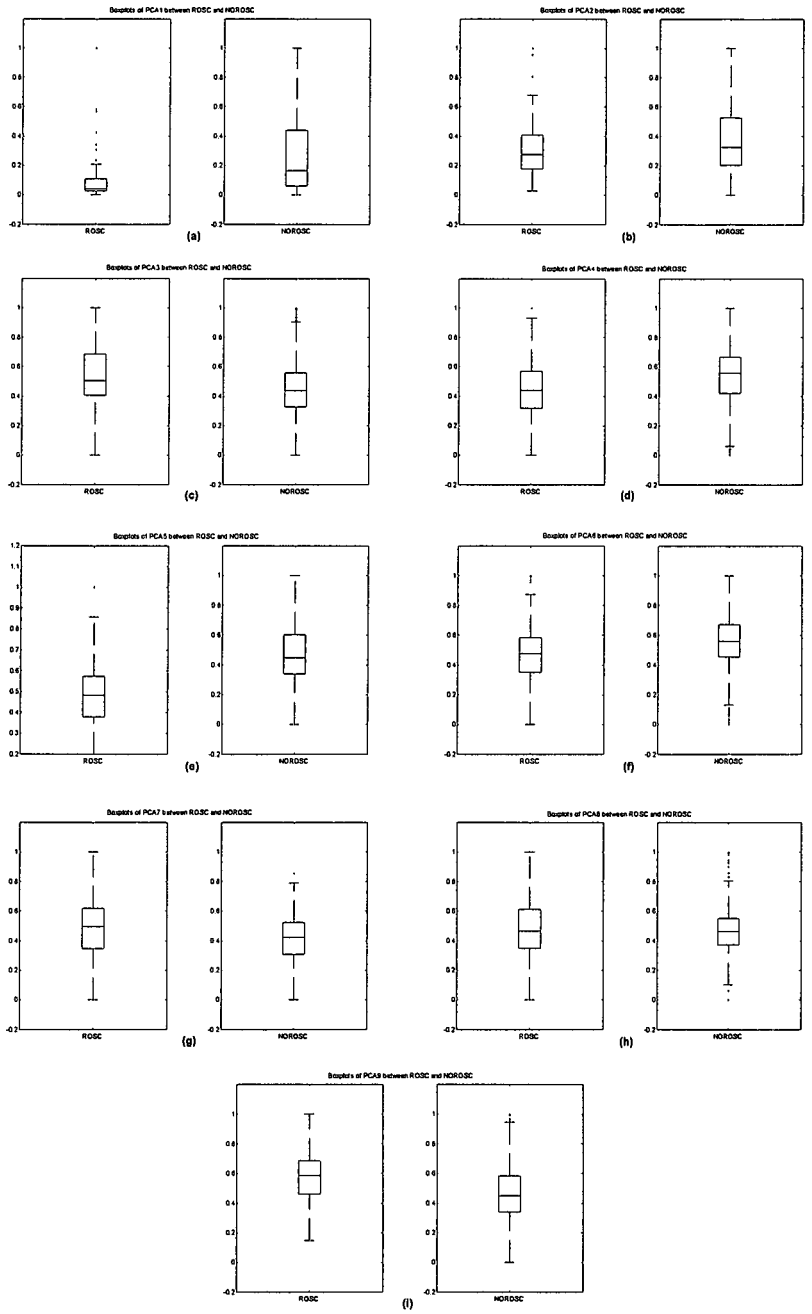

Figure B-47: PCA feature boxplots for the ROSC and NOROSC cases obtained from the STFT2-based method with 5 second length of pre-shock: (a) PCA1 feature boxplots, (b) PCA2 feature boxplots, (c) PCA3 feature boxplots, (d) PCA4 feature boxplots, (e) PCA5 feature boxplots, (f) PCA6 feature boxplots, (g) PCA7 feature boxplots, (h) PCA8 feature boxplots, and (i) PCA9 feature boxplots

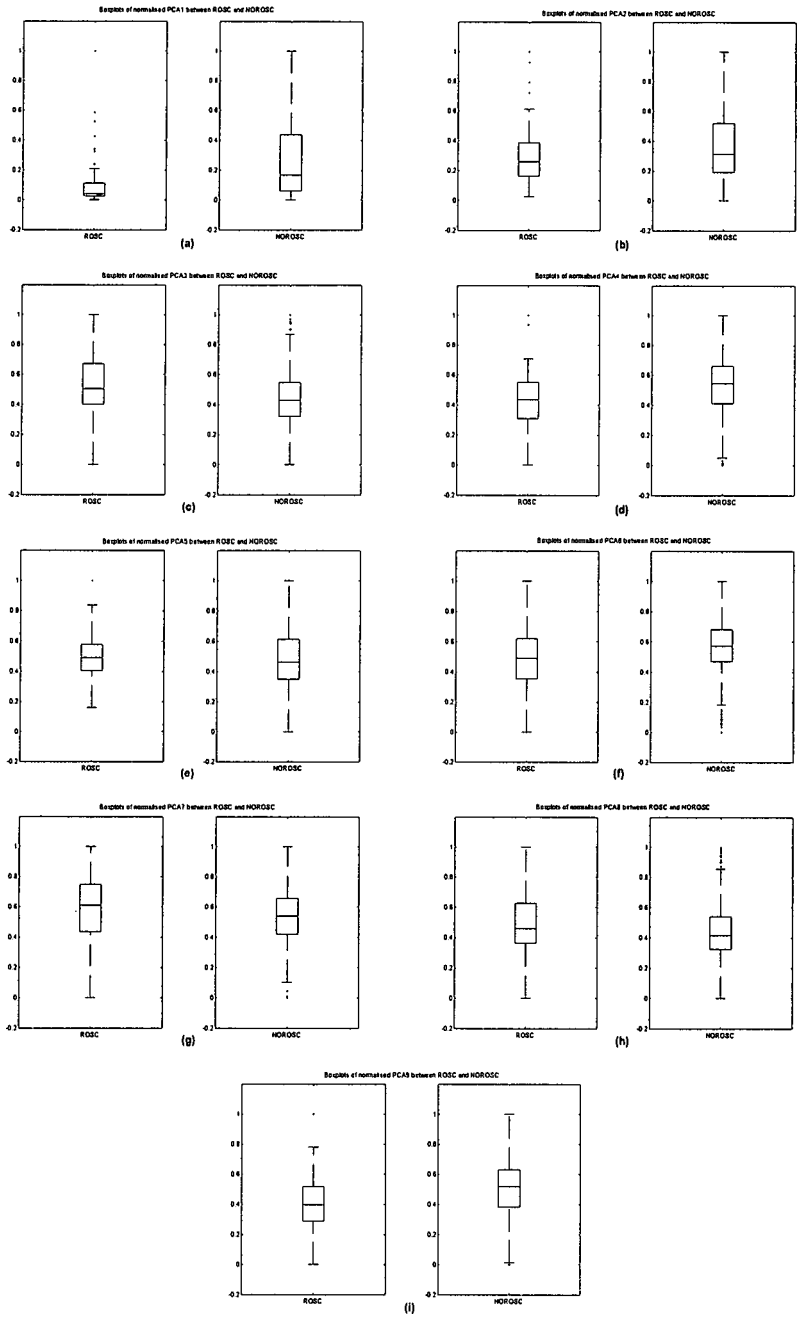

Figure B-48: PCA feature boxplots for the ROSC and NOROSC cases obtained from the STFT3-based method with 5 second length of pre-shock: (a) PCA1 feature boxplots, (b) PCA2 feature boxplots, (c) PCA3 feature boxplots, (d) PCA4 feature boxplots, (e) PCA5 feature boxplots, (f) PCA6 feature boxplots, (g) PCA7 feature boxplots, (h) PCA8 feature boxplots, and (i) PCA9 feature boxplots

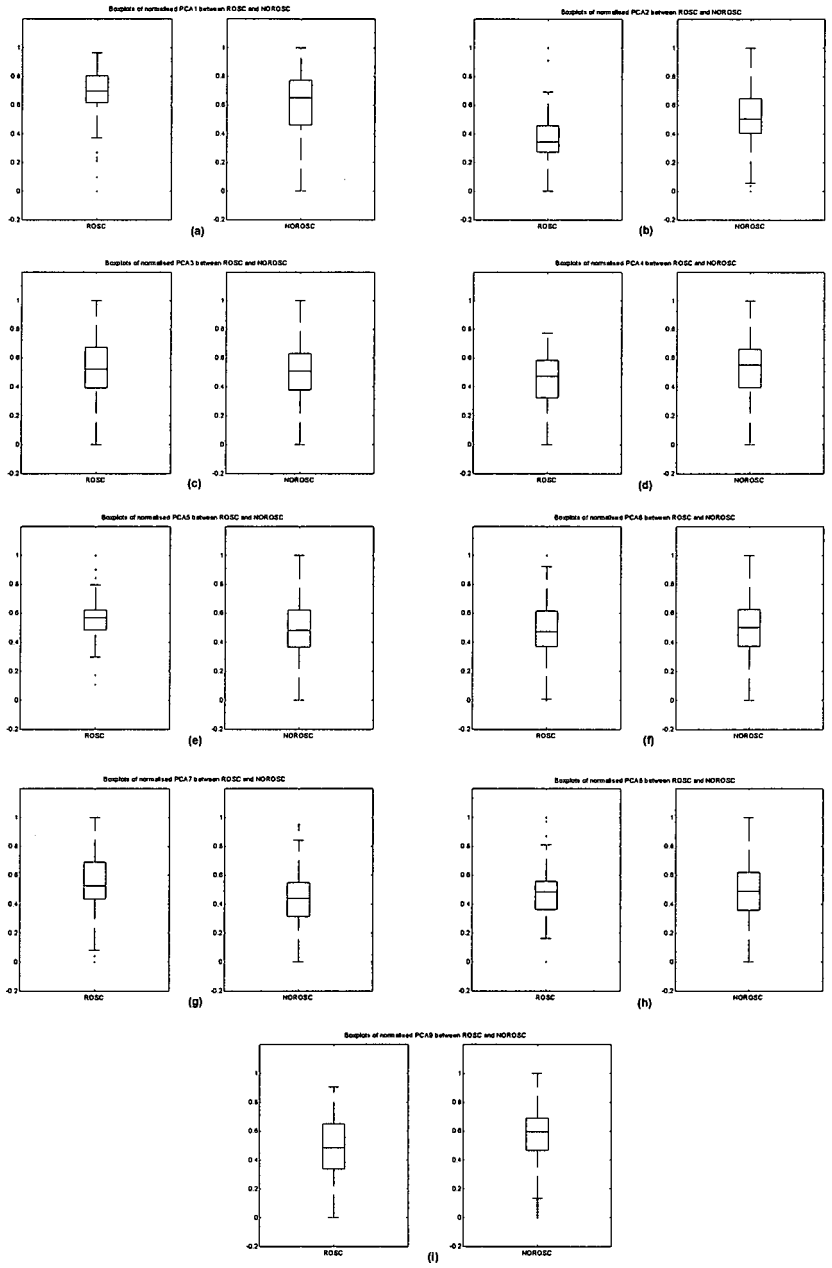

Figure B-49: PCA feature boxplots for the ROSC and NOROSC cases obtained from the WT-based method with 10 second length of pre-shock: (a) PCA1 feature boxplots, (b) PCA2 feature boxplots, (c) PCA3 feature boxplots, (d) PCA4 feature boxplots, (e) PCA5 feature boxplots, (f) PCA6 feature boxplots, (g) PCA7 feature boxplots, (h) PCA8 feature boxplots, and (i) PCA9 feature boxplots

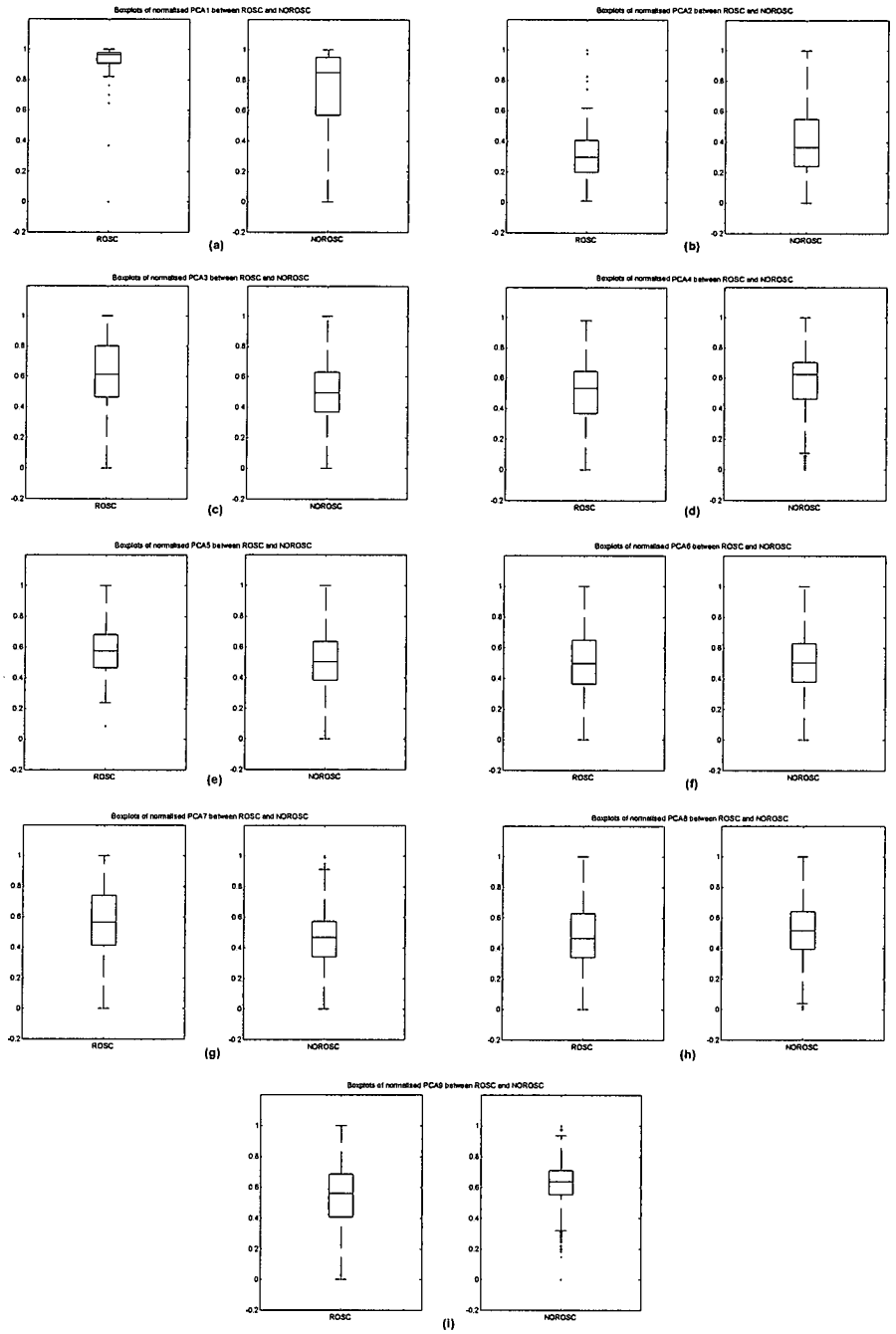

Figure B-50: PCA feature boxplots for the ROSC and NOROSC cases obtained from the STFT1-based method with 10 second length of pre-shock: (a) PCA1 feature boxplots, (b) PCA2 feature boxplots, (c) PCA3 feature boxplots, (d) PCA4 feature boxplots, (e) PCA5 feature boxplots, (f) PCA6 feature boxplots, (g) PCA7 feature boxplots, (h) PCA8 feature boxplots, and (i) PCA9 feature boxplots

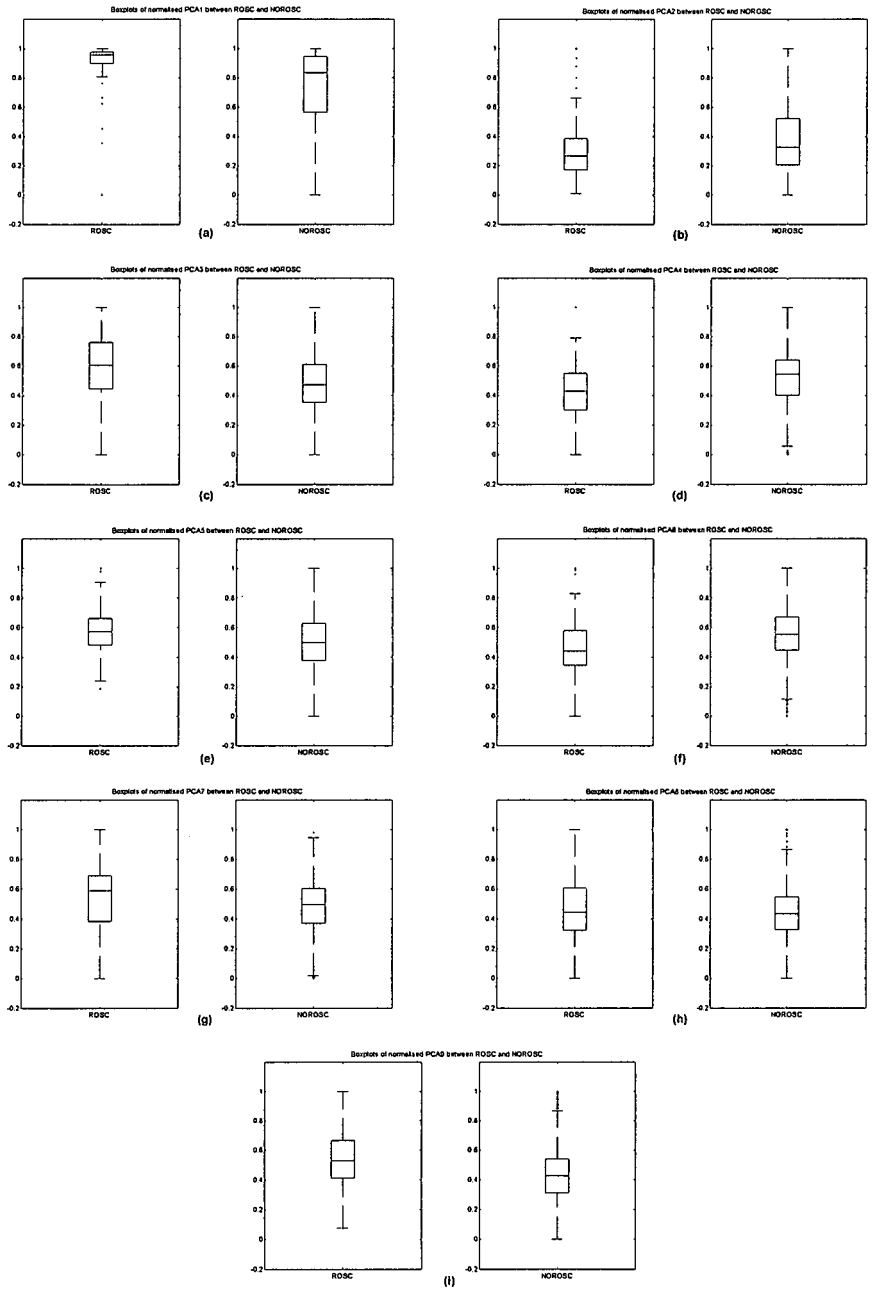

Figure B-51: PCA feature boxplots for the ROSC and NOROSC cases obtained from the STFT2-based method with 10 second length of pre-shock: (a) PCA1 feature boxplots, (b) PCA2 feature boxplots, (c) PCA3 feature boxplots, (d) PCA4 feature boxplots, (e) PCA5 feature boxplots, (f) PCA6 feature boxplots, (g) PCA7 feature boxplots, (h) PCA8 feature boxplots, and (i) PCA9 feature boxplots

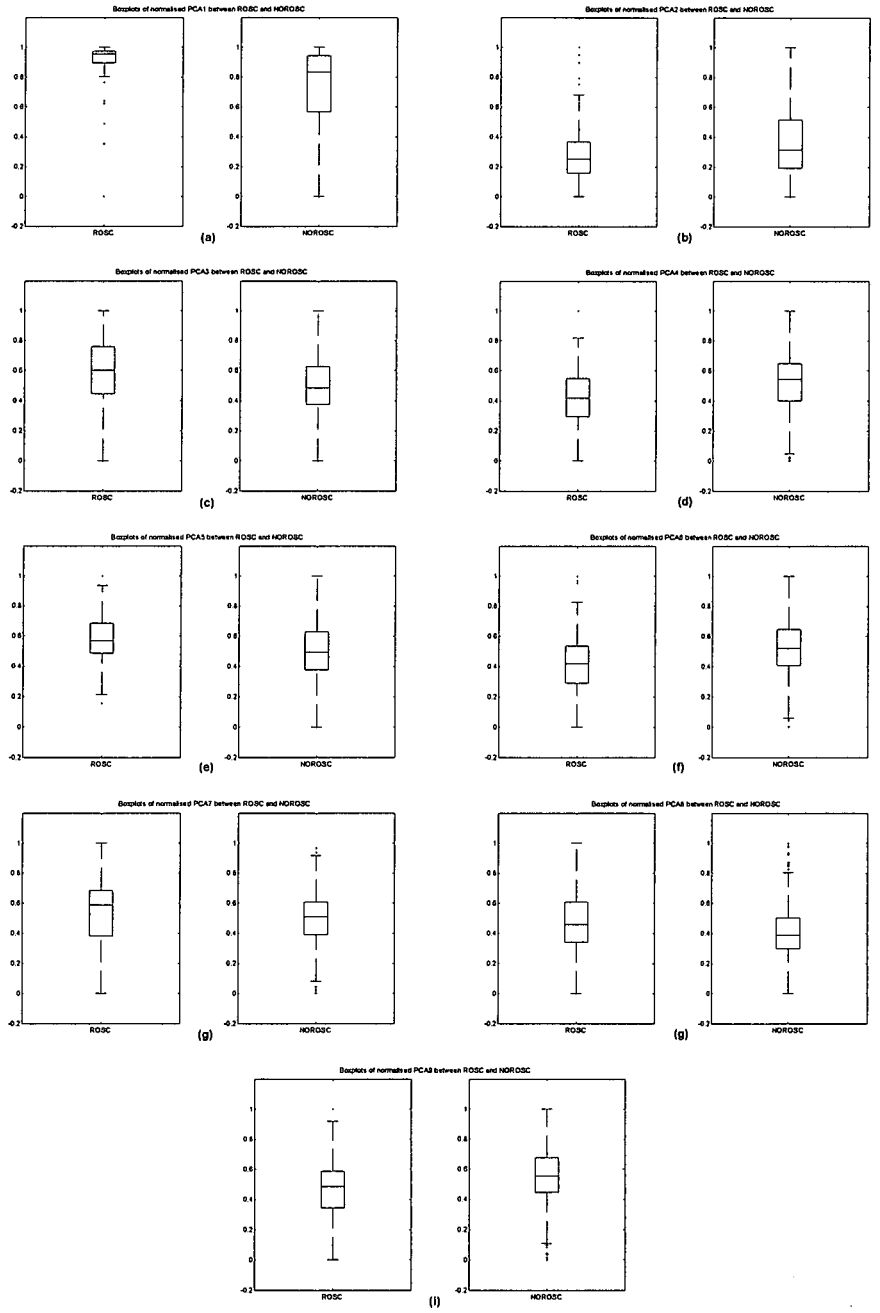

Figure B-52: PCA feature boxplots for the ROSC and NOROSC cases obtained from the STFT3-based method with 10 second length of pre-shock: (a) PCA1 feature boxplots, (b) PCA2 feature boxplots, (c) PCA3 feature boxplots, (d) PCA4 feature boxplots, (e) PCA5 feature boxplots, (f) PCA6 feature boxplots, (g) PCA7 feature boxplots, (h) PCA8 feature boxplots, and (i) PCA9 feature boxplots

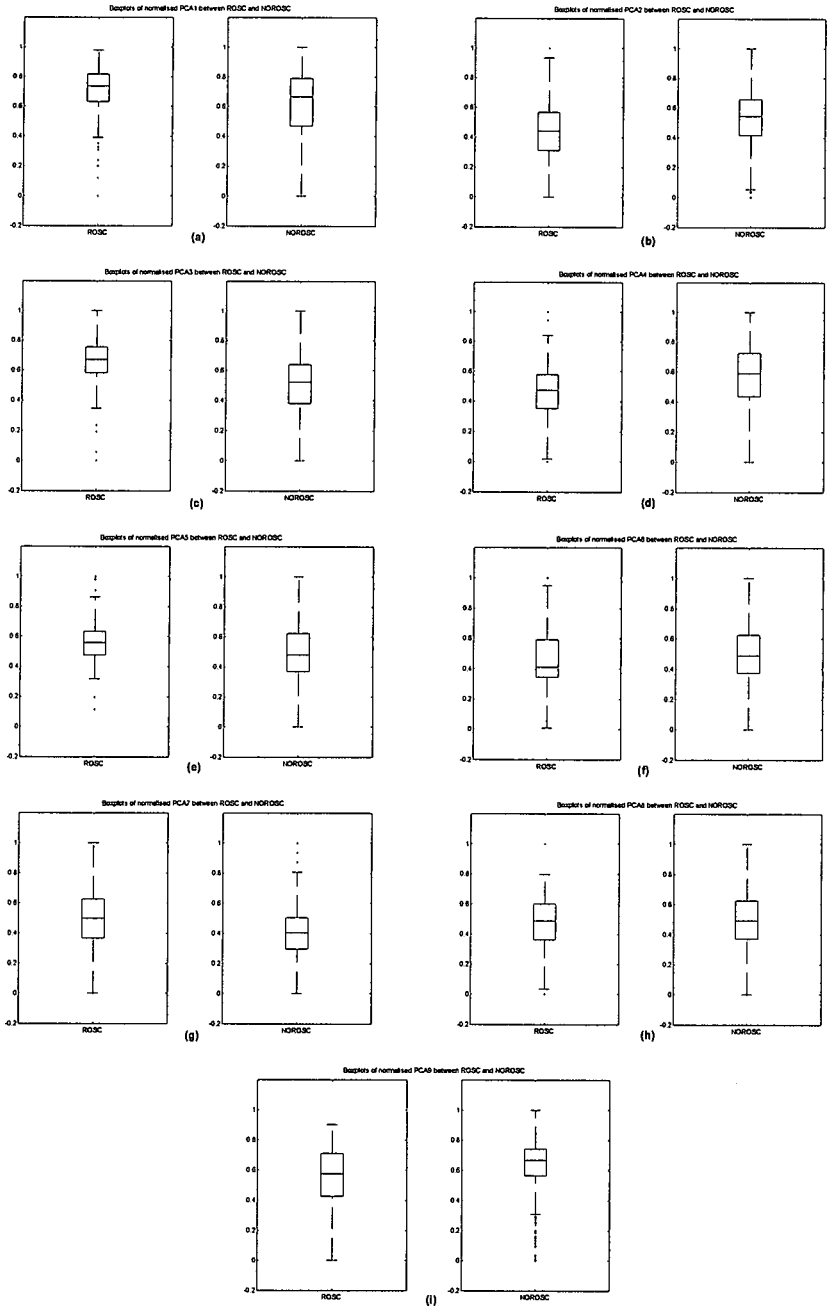

Figure B-53: PCA feature boxplots for the ROSC and NOROSC cases obtained from the WT-based method with 15 second length of pre-shock: (a) PCA1 feature boxplots, (b) PCA2 feature boxplots, (c) PCA3 feature boxplots, (d) PCA4 feature boxplots, (e) PCA5 feature boxplots, (f) PCA6 feature boxplots, (g) PCA7 feature boxplots, (h) PCA8 feature boxplots, and (i) PCA9 feature boxplots

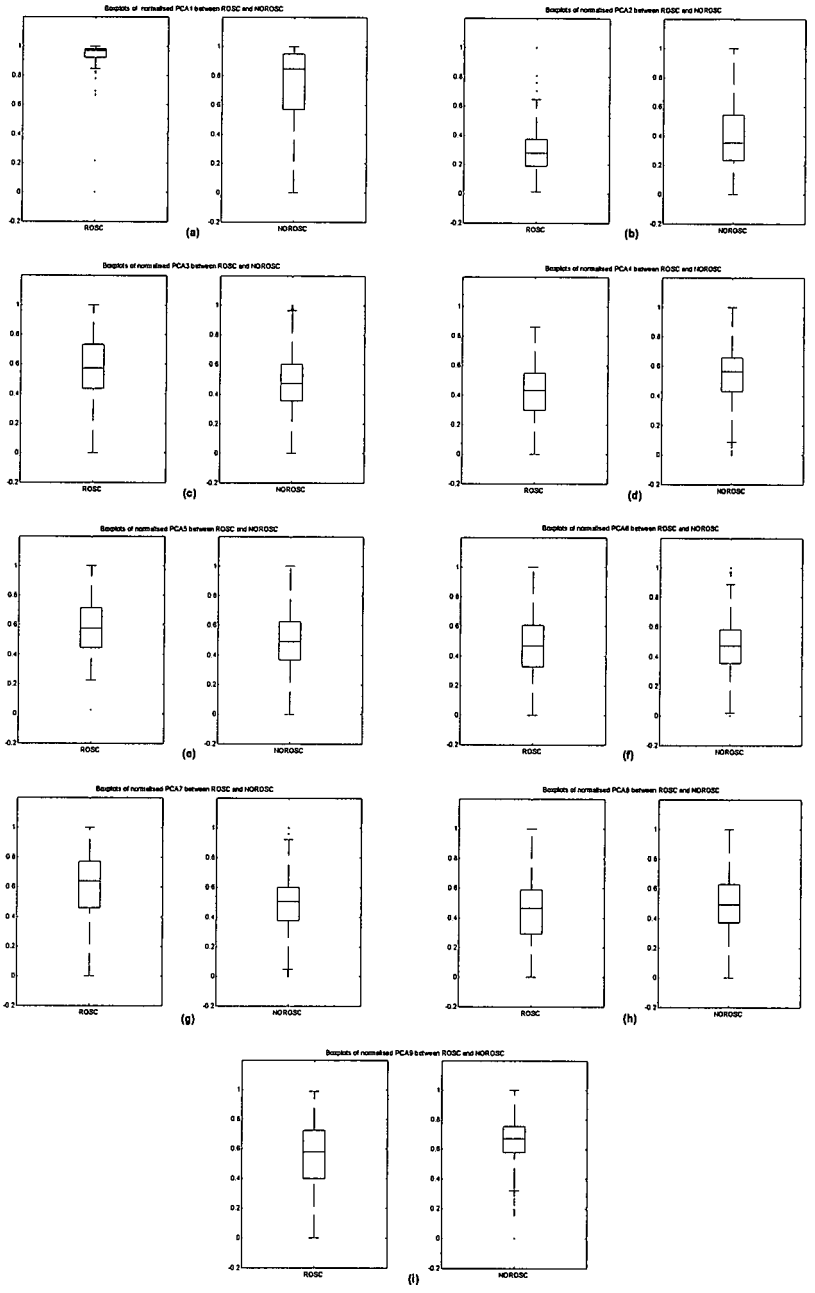

Figure B-54: PCA feature boxplots for the ROSC and NOROSC cases obtained from the STFT1-based method with 15 second length of pre-shock: (a) PCA1 feature boxplots, (b) PCA2 feature boxplots, (c) PCA3 feature boxplots, (d) PCA4 feature boxplots, (e) PCA5 feature boxplots, (f) PCA6 feature boxplots, (g) PCA7 feature boxplots, (h) PCA8 feature boxplots, and (i) PCA9 feature boxplots

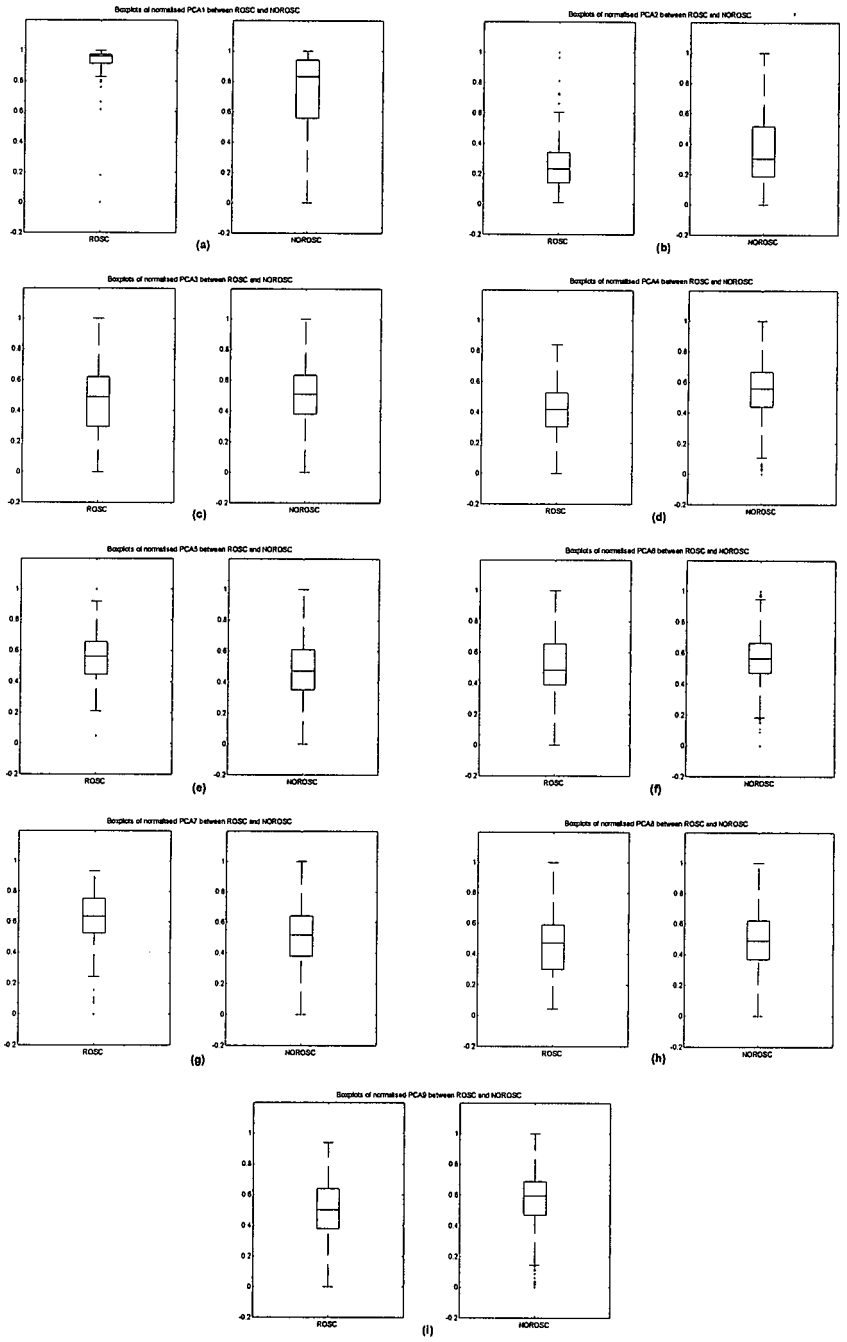

Figure B-55: PCA feature boxplots for the ROSC and NOROSC cases obtained from the STFT2-based method with 15 second length of pre-shock: (a) PCA1 feature boxplots, (b) PCA2 feature boxplots, (c) PCA3 feature boxplots, (d) PCA4 feature boxplots, (e) PCA5 feature boxplots, (f) PCA6 feature boxplots, (g) PCA7 feature boxplots, (h) PCA8 feature boxplots, and (i) PCA9 feature boxplots

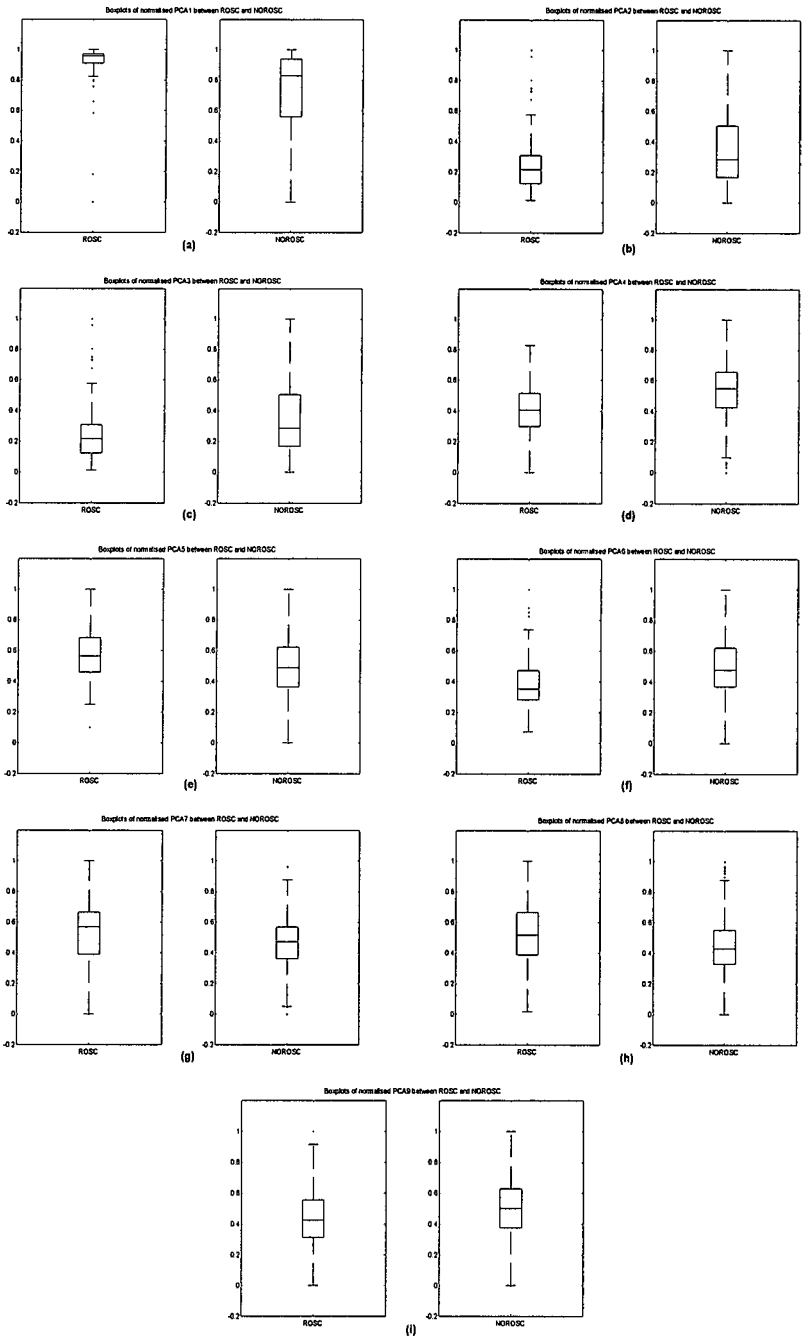

Figure B-56: PCA feature boxplots for the ROSC and NOROSC cases obtained from the STFT3-based method with 15 second length of pre-shock: (a) PCA1 feature boxplots, (b) PCA2 feature boxplots, (c) PCA3 feature boxplots, (d) PCA4 feature boxplots, (e) PCA5 feature boxplots, (f) PCA6 feature boxplots, (g) PCA7 feature boxplots, (h) PCA8 feature boxplots, and (i) PCA9 feature boxplots

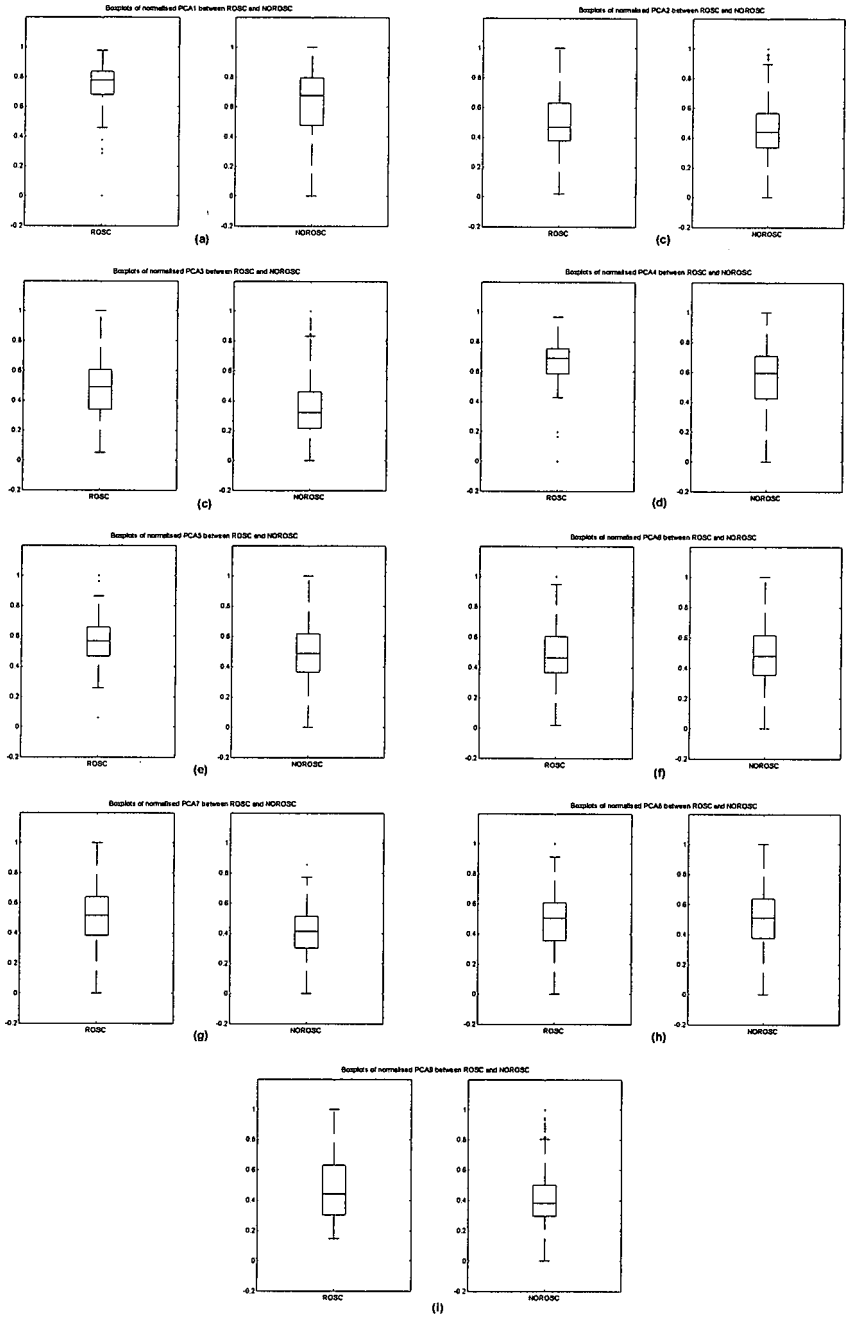

Figure B-57: PCA feature boxplots for the ROSC and NOROSC cases obtained from the WT-based method with 20 second length of pre-shock: (a) PCA1 feature boxplots, (b) PCA2 feature boxplots, (c) PCA3 feature boxplots, (d) PCA4 feature boxplots, (e) PCA5 feature boxplots, (f) PCA6 feature boxplots, (g) PCA7 feature boxplots, (h) PCA8 feature boxplots, and (i) PCA9 feature boxplots

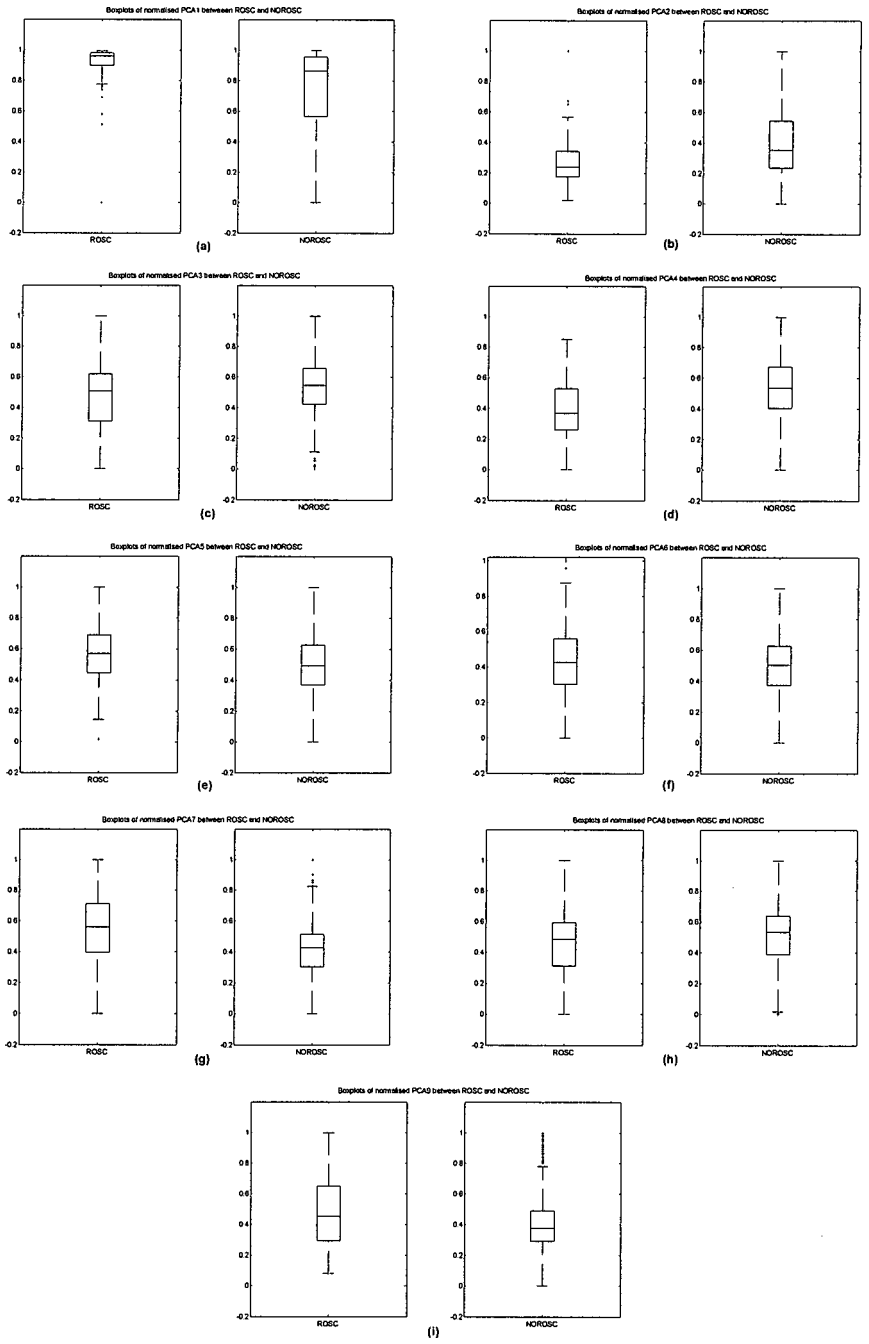

Figure B-58: PCA feature boxplots for the ROSC and NOROSC cases obtained from the STFT1-based method with 20 second length of pre-shock: (a) PCA1 feature boxplots, (b) PCA2 feature boxplots, (c) PCA3 feature boxplots, (d) PCA4 feature boxplots, (e) PCA5 feature boxplots, (f) PCA6 feature boxplots, (g) PCA7 feature boxplots, (h) PCA8 feature boxplots, and (i) PCA9 feature boxplots

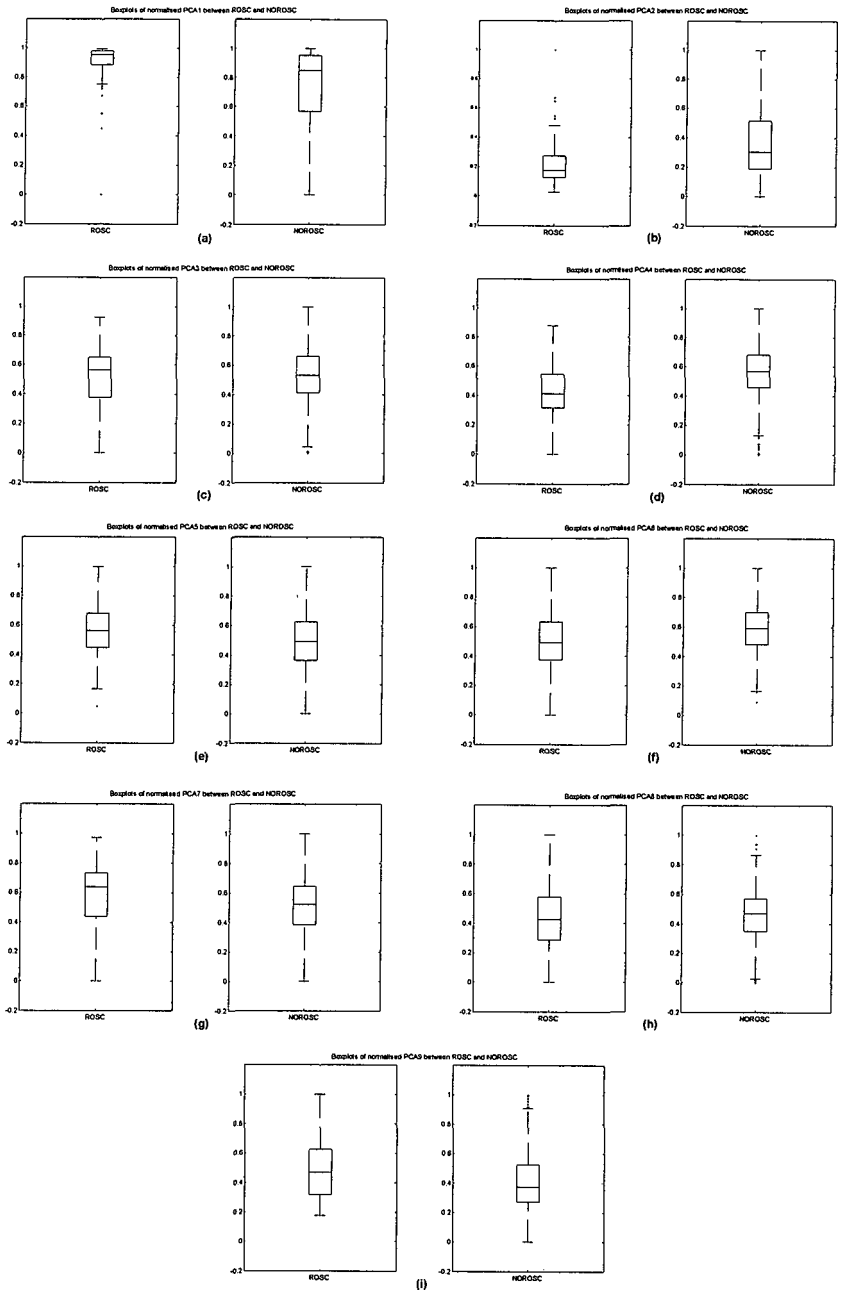

Figure B-59: PCA feature boxplots for the ROSC and NOROSC cases obtained from the STFT2-based method with 20 second length of pre-shock: (a) PCA1 feature boxplots, (b) PCA2 feature boxplots, (c) PCA3 feature boxplots, (d) PCA4 feature boxplots, (e) PCA5 feature boxplots, (f) PCA6 feature boxplots, (g) PCA7 feature boxplots, (h) PCA8 feature boxplots, and (i) PCA9 feature boxplots

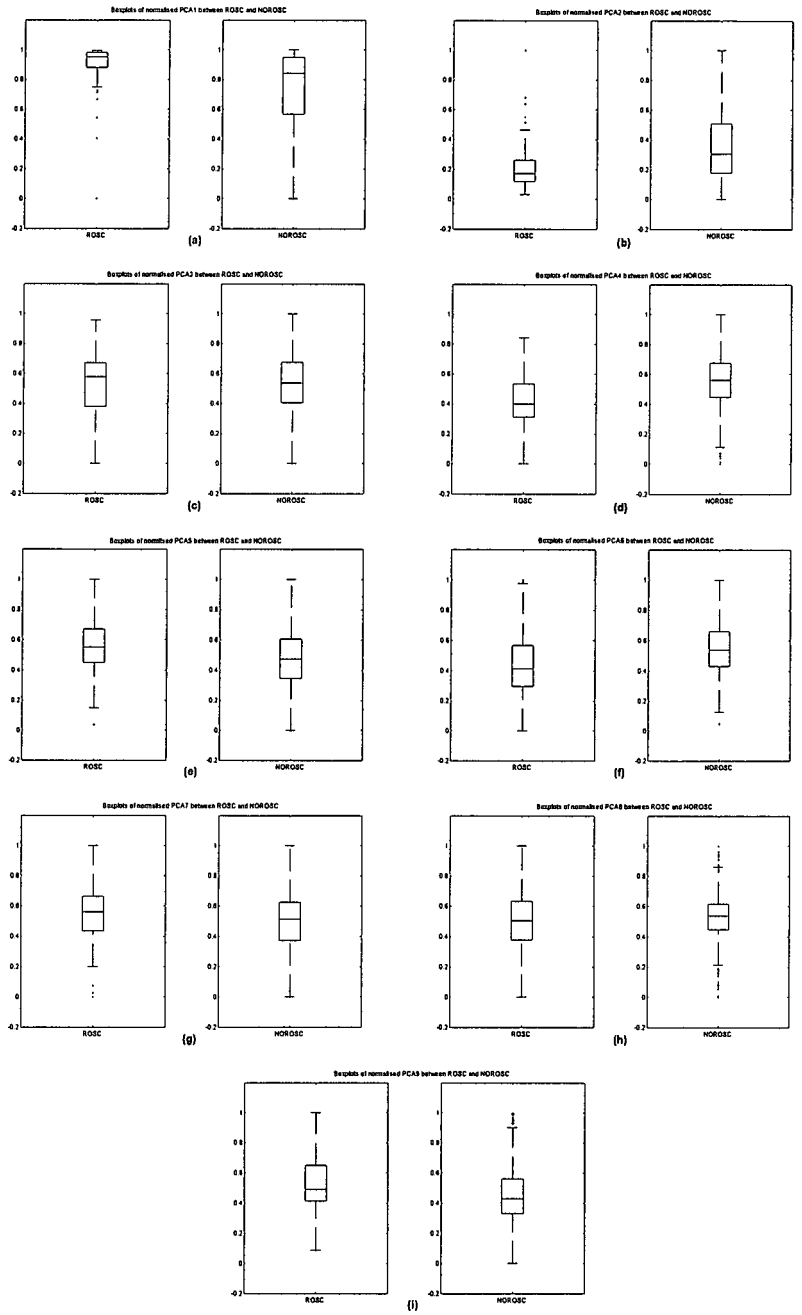

Figure B-60: PCA feature boxplots for the ROSC and NOROSC cases obtained from the STFT3-based method with 20 second length of pre-shock: (a) PCA1 feature boxplots, (b) PCA2 feature boxplots, (c) PCA3 feature boxplots, (d) PCA4 feature boxplots, (e) PCA5 feature boxplots, (f) PCA6 feature boxplots, (g) PCA7 feature boxplots, (h) PCA8 feature boxplots, and (i) PCA9 feature boxplots

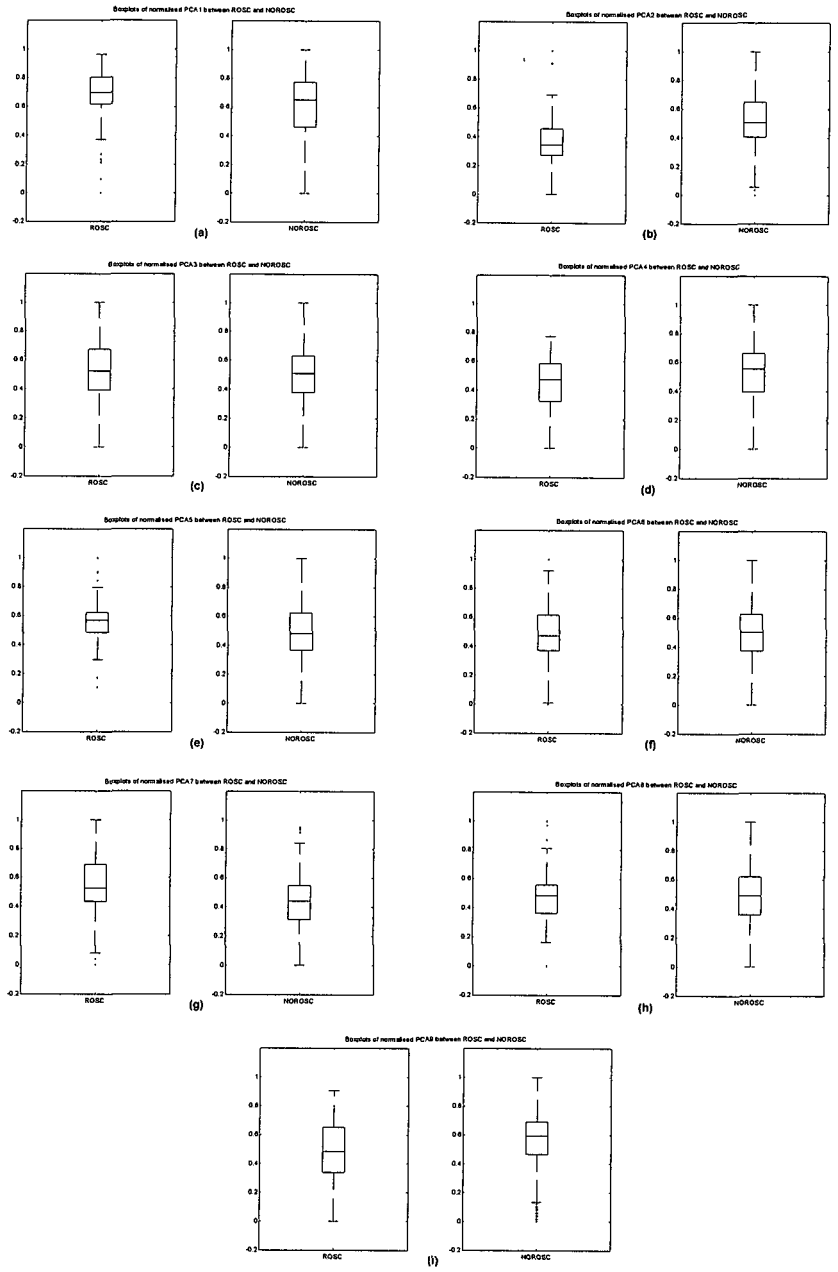

Figure B-61: PCA feature boxplots for the ROSC and NOROSC cases obtained from the WT-based method at location A: (a) PCA1 feature boxplots, (b) PCA2 feature boxplots, (c) PCA3 feature boxplots, (d) PCA4 feature boxplots, (e) PCA5 feature boxplots, (f) PCA6 feature boxplots, (g) PCA7 feature boxplots, (h) PCA8 feature boxplots, and (i) PCA9 feature boxplots

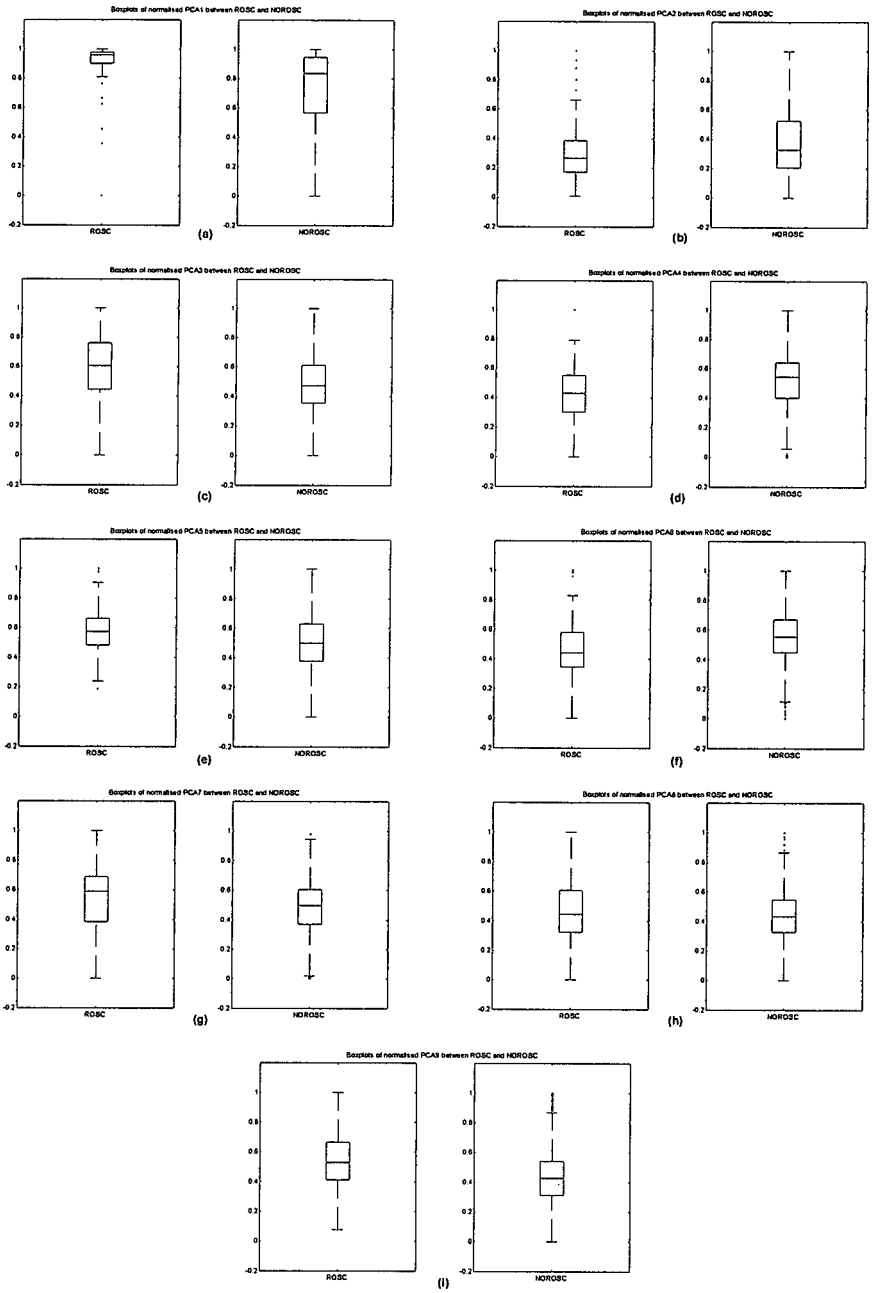

Figure B-62 PCA feature boxplots for the ROSC and NOROSC cases obtained from the STFT2-based method at location A: (a) PCA1 feature boxplots, (b) PCA2 feature boxplots, (c) PCA3 feature boxplots, (d) PCA4 feature boxplots, (e) PCA5 feature boxplots, (f) PCA6 feature boxplots, (g) PCA7 feature boxplots, (h) PCA8 feature boxplots, and (i) PCA9 feature boxplots

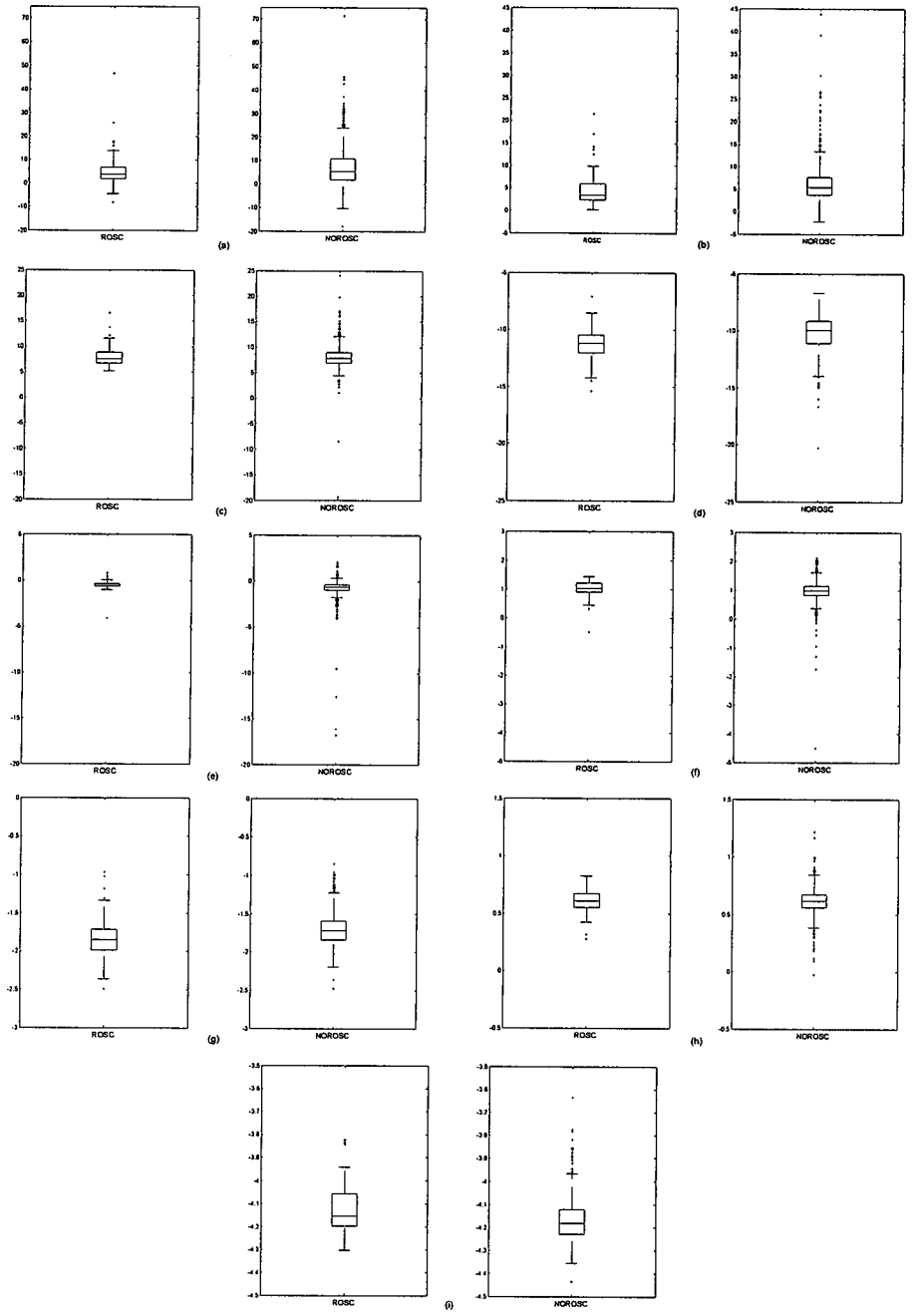

Figure B-63: PCA feature boxplots for the ROSC and NOROSC cases obtained from the WT-based method at location B: (a) PCA1 feature boxplots, (b) PCA2 feature boxplots, (c) PCA3 feature boxplots, (d) PCA4 feature boxplots, (e) PCA5 feature boxplots, (f) PCA6 feature boxplots, (g) PCA7 feature boxplots, (h) PCA8 feature boxplots, and (i) PCA9 feature boxplots

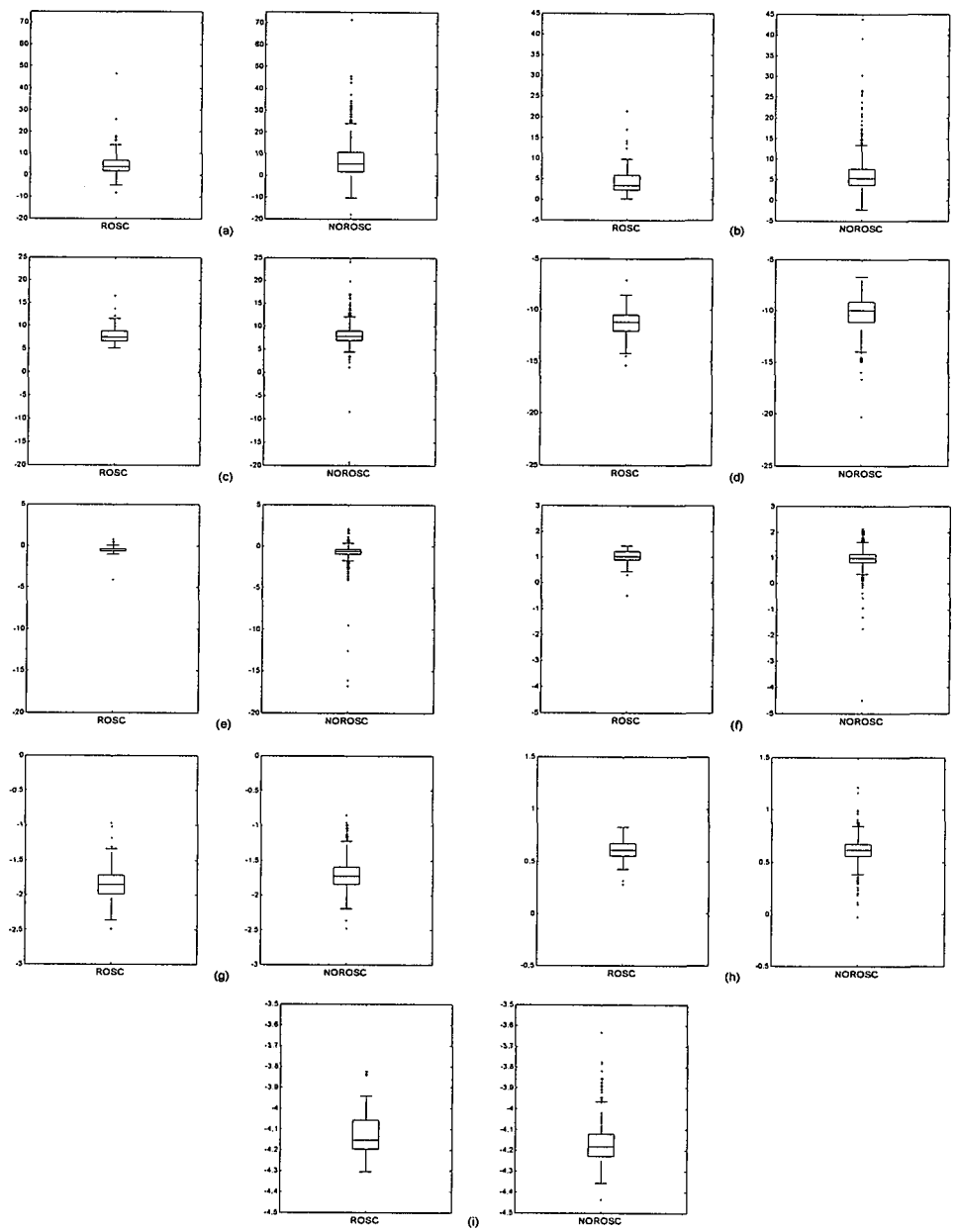

Figure B-64: PCA feature boxplots for the ROSC and NOROSC cases obtained from the STFT2-based method at location B: (a) PCA1 feature boxplots, (b) PCA2 feature boxplots, (c) PCA3 feature boxplots, (d) PCA4 feature boxplots, (e) PCA5 feature boxplots, (f) PCA6 feature boxplots, (g) PCA7 feature boxplots, (h) PCA8 feature boxplots, and (i) PCA9 feature boxplots

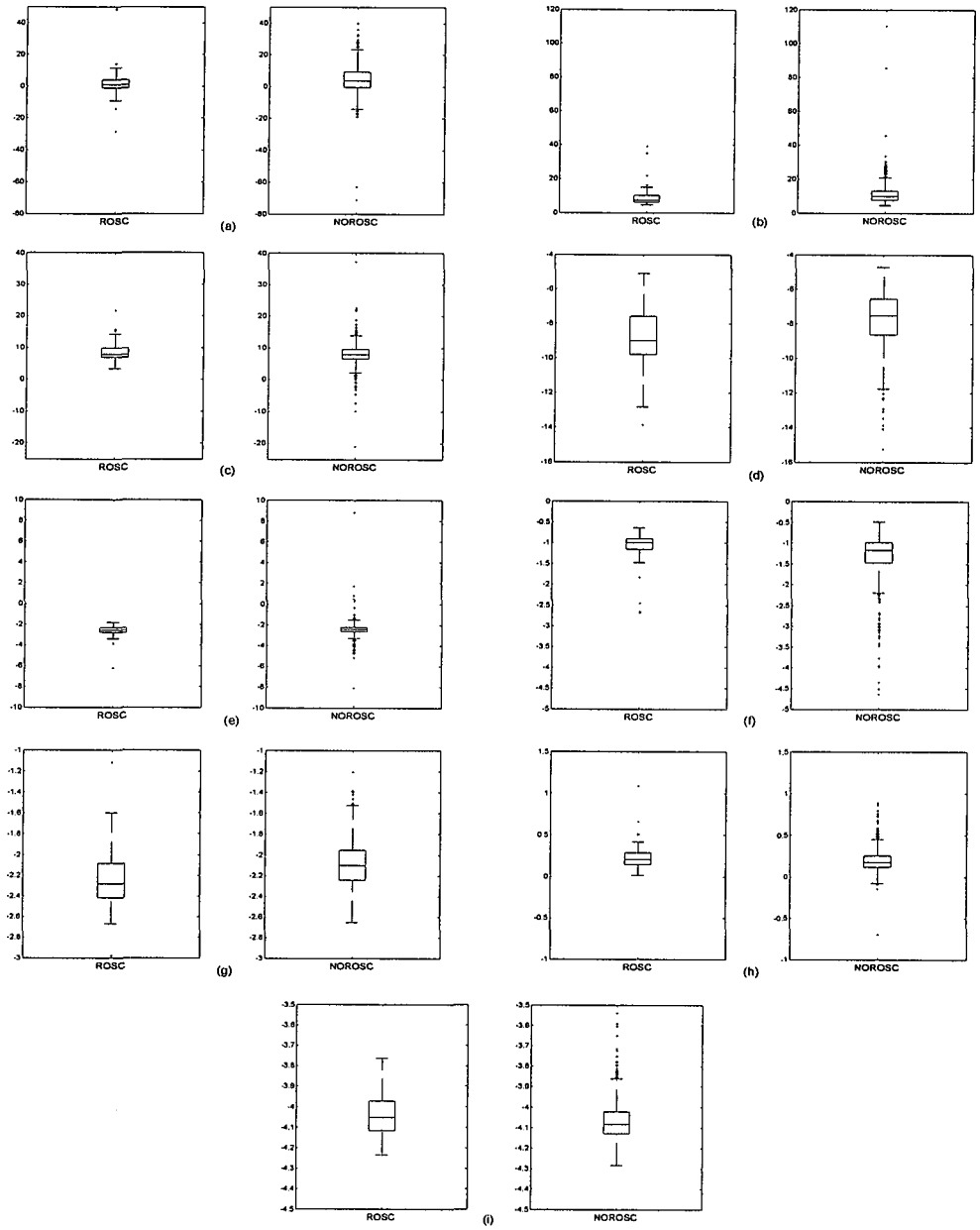

Figure B-65: PCA feature boxplots for the ROSC and NOROSC cases obtained from the WT-based method at location C: (a) PCA1 feature boxplots, (b) PCA2 feature boxplots, (c) PCA3 feature boxplots, (d) PCA4 feature boxplots, (e) PCA5 feature boxplots, (f) PCA6 feature boxplots, (g) PCA7 feature boxplots, (h) PCA8 feature boxplots, and (i) PCA9 feature boxplots

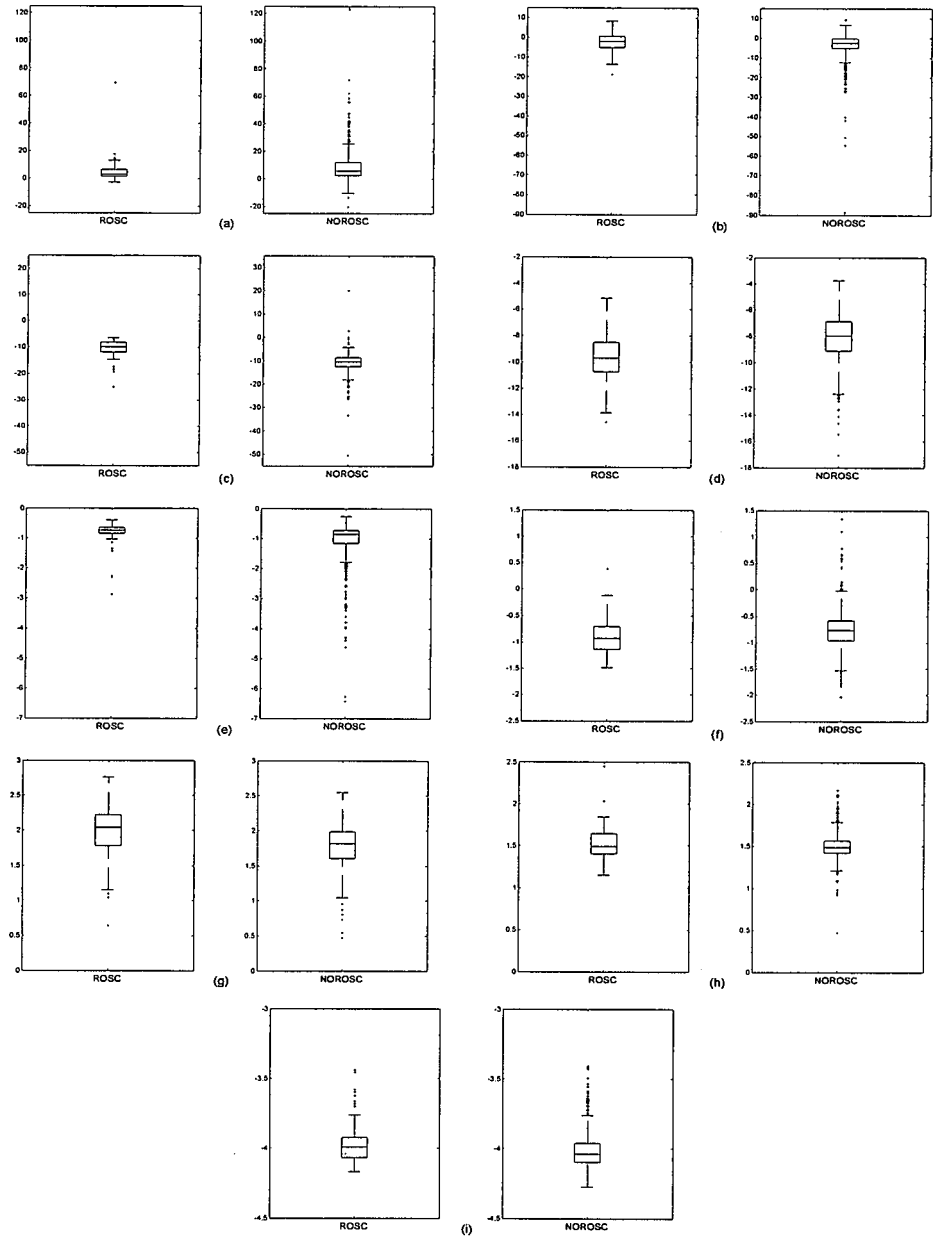

Figure B-66: PCA feature boxplots for the ROSC and NOROSC cases obtained from the STFT2-based method at location C: (a) PCA1 feature boxplots, (b) PCA2 feature boxplots, (c) PCA3 feature boxplots, (d) PCA4 feature boxplots, (e) PCA5 feature boxplots, (f) PCA6 feature boxplots, (g) PCA7 feature boxplots, (h) PCA8 feature boxplots, and (i) PCA9 feature boxplots

REFERENCES

Achleitner U., Wenzel V., Strohmenger H.U., Lindner K.H., Baubin M.A., Krismer A.C., Mayr V.D., Amann A., "The beneficial effect of basic life support on ventricular fibrillation mean frequency and coronary perfusion pressure", *Resuscitation*, Vol. 51(2), pp. 151-158, 2001

Addison P.S., "Wavelet analysis of the breakdown of a pulsed vortex flow", *Proc. I Mech E, Part C: J. Mech. Eng. Sci.,* vol.213, pp.217-229, 1999

Addison P.S., *The illustrated wavelet transform handbook: Introductory theory and applications in science, engineering, medicine and finance*, Bristol and Philadelphia, Institute of Physics Publishing, 2002

Addison P.S., Murray K.B., and Watson J.N., "Wavelet transform analysis of open channel wake flows," *ASCE Journal of Engineering Mechanics*, vol.127, pp.58-70, 2001

Addison P.S., Sibbald A., and Watson J., "Wavelet analysis: a mathematical microscope with civil engineering applications", *Insight*, Vol. 39, No. 7, pp.493-497, 1997

Addison P.S., Watson J.N., Clegg G.R., Holzer M., Sterz F. and Robertson C.E., "Evaluating arrhythmias in ECG signals using wavelet transforms", *IEEE Engineering in Medicine and Biology Magazine*, Vol. 19(5), pp. 104-109, 2000

Addison P.S., Watson J.N., Clegg G.R., Holzer M., Sterz F., and Robertson C.E., "A novel wavelet based analysis reveals hidden structure in ventricular fibrillation," *IEEE Engineering in Medicine and Biology*, vol.19(4), pp.383-392, 2000

Addison P.S., Watson J.N., Clegg G.R., Holzer M., Sterz F., and Robertson C.E., "Continuous wavelet transforms reveal rich structure in ventricular fibrillation," *Technology and Health Care*, vol.9 (1,2), pp.42-44, 2001

Addison P.S., Watson J.N., and Feng T., "Low-oscillation complex wavelets", *Journal of Sound and Vibration*, Vol. 254(4), pp. 733-762, 2002

Addison P.S., Uchaipichat N., Watson J.N., Clegg G.R., Robertson C.E., Steen P.A., and Eftestol T., "Wavelet power spectrum-based prediction of successful defibrillation from ventricular fibrillation", *Proceeding of the 23rd Annual International conference of the IEEE Engineering in Medicine and Biology Society in Istanbul, Turkey*, October 2001.

Addison P.S., Uchaipichat N., Watson J.N., Clegg G.R., Robertson C.E., Steen P.A., and Eftestol T., "Positional dependence of time-frequency information in the ECG used for the prediction of defibrillation success", *Proceeding of 2nd European Medical & Biological Engineering Conference in Vienna*, 2002

Ahmeda S.M., Al-Shrouf A., and Abo-zahhad M., "ECG data compression using optimal non-orthogonal wavelet transform", *Med Eng Phys*, Vol. 22(1), pp. 39-46, 2000

Ahmeda S.M. and Abo-Zahhad M, "A new hybrid algorithm for ECG signal compression bease on the wavelet transformation of the linearly predicted error", *Medical Engineering & Physics*, Vol. 23, pp. 117-126, 2001

Al-Fahoum A.S. and Howitt I., "Combined wavelet transformation and radial basis neural networks for classifying life-threatening cardiac arrhythmias", *Medical & Biological Engineering & Computing*, Vol. 37, pp.566-573, 1999

Amann A., Achleitner U., Antretter H., Bonatti J.O., Krismer A.C., Lindner K.H., Rieder J., Wenzel V., Voelkel W.G., and Strohmenger H.U., "Analysis ventricular fibrillation ECG-signals and predicting defibrillation success during cardiopulmonary resuscitation employing N(α)-histograms", *Resuscitation*, Vol. 50, pp.77-85, 2001

Amann A., Mayr G., and Strohmenger H.U., "N(α)-histogram analysis of the ventricular fibrillation ECG-signal as predictor of countershock success", *Chaos, Solitons and Fractals*", Vol. 11, pp.1205-1212, 2000

Amann A., Rheinberger K., Achleitner U., Krismer A.C., Lingnau W., Linder K.H., and Wenzel V., "The prediction of defibrillation outcome using a new combination of mean frequency and amplitude in porcine models of cardiac arrest", *Anesthesia & Analgesia*, Vol. 95(3), pp. 716-722, 2002

Bahoura M., Hassani M., and Hubin M., "DSP implemention of wavelet transform for real time ECG wave forms detection and heart rate analysis", *Computer Methods and Programs in Biomedicine*, Vol. 52, pp.35-44, 1997

Berg R.A., Hilwig R.W., Kern K.B., and Ewy G.A., "Precountershock cardiopulmonary resuscitation improves ventricular fibrillation median frequency and myocardial readiness for successful defibrillation from prolonged ventricular fibrillation: a randomized, controlled swine study", *Annal of Emergency Medicine*, Vol. 40(6), pp. 571-574, 2002

Brown C.G. and Dzwonczyk R., "Signal analysis of the human electrocardiogram during ventricular fibrillation: frequency and amplitude parameters as predictors of successful countershock", *Annal of Emergency Medicine*, vol.27 (2), pp. 184-188, 1995

Brown C.G., Dzwonczyk R., Werman H.A., and Hamlin R.L., "Estimating the during of ventricular fibrillation", *Annals of Emergency Medicine*, vol.18 (11), pp.1181-1185, 1989

Brown C.G., Griffith R.F., Ligten P.V., Hoekstra J., Nejman G., Mitchell L., and Dzwonczyk R., "Median frequency – a new parameter for predicting defibrillation success rate", *Annals of Emergency Medicine*, vol.20 (7), pp.787-789, 1991

Brush J.E., Brand D.A., Acampora D., Chalmers B., and Wackers F.J., "Use of the initial electrocardiogram to predict in-hospital complications of acute myocardial infarction," *New Engl. J Med.* vol.312, pp.1137-41, 1985

Burman P., "A comparative study of ordinary cross-validation, *v*-fold cross validation and the repeated learning-testing methods", *Biometrika*, Vol. 76, Iss. 3, pp. 503-514, 1989

Callaway C.W., Sherman L.D., Mosesso V.N., Dietrich T.J., Holt E., and Clarkson M.C., "Scaling exponent predicts defibrillation success for out-of-hospital ventricular fibrillation cardiac arrest", *Circulation*, Vol. 103(12), pp.1656-1661, 2001

Carlisle E.J.F., Allen J.D., Bailey A., Kernohan W.G., Anderson J., and Adgey A.A.J., "Fourier analysis of ventricular fibrillation and synchronization of DC countershocks in defibrillation", *Journal of Electrocardiology*, Vol. 21, No.4, pp. 337-343, 1988

Chatfield C. and Collins A.J, *Introduction to Multivariate Analysis*, London: Chapman and Hall, 1980

Chen J., Itoh S., and Hashimoto T., "ECG data compression by using wavelet transform", *IEICE Transactions on Information and Systems* , Vol. E76-D, No. 12, pp. 1454-1461, 1993

Clayton R.H. and Murray A., "Estimation of the ECG signal spectrum during ventricular fibrillation using the fast Fourier transform and maximum entropy methods", *Computers in Cardiology, IEEE Computer Society Press.,* pp. 867-870, 1993

Clayton R.H., Murray A., and Campbell R.W.F., "Frequency analysis of ventricular fibrillation in three surface ECG leads", *Computers in Cardiology,* IEEE Computer Society Press., pp. 155-158, 1992

Clayton R.H., Murray A., and Campbel R.W.F., "Frequency analysis of ventricular fibrillation", *IEE Colloquium 1995/043: Signal processing in cardiography*, IEE, London ; 3/1-3/4, 1995

Cobb L.A., Fahrenbruch C.E., Walsh T.R., Copass M.K., Olsufka M., Breskin M., and Hallstrom A.P., "Influence of cardiopulmonary resuscitation prior to defibrillation in patients with out-of-hospital ventricular fibrillation", *JAMA*, Vol. 281(13), pp. 1182-1188, 1999

Crowe J.A., Gibson N.M., Woolfson M.S., and Somekh M.G., "Wavelet transform as a potential tool for ECG analysis and compression", *Journal of Biomedical Engineering*, Vol. 14, pp.268-272, May 1992

Eftestol T., Sunde K., Aase S.O., Husoy J.H., and Steen P.A., "Predicting outcome of defibrillation by spectral characterization and nonparametric classification of ventricular fibrillation in patients with out-of-hospital cardiac arrest", *Circulation*, vol. 102, pp. 1523-1529, 2000

Eftestol T., Sunde K., Aase S.O., Husoy J.H., and Steen P.A., "Probability of successful defibrillation as a monitor during CPR in out-of-hospital cardiac arrested patients", *Resuscitation*, vol.48, pp. 245-254, 2001

Gade S. and Gram-Hansen K. "The analysis of nonstationary signals", *Sound and Vibration*, 30th Anniversary Issue, Vol. 31(2), pp.40-46, January 1997

Goldstein J., Landis R., Leighton R., Ritter G., and Vasu C.M., "Characteristics of the resuscitated out-of-hospital cardiac arrest victim with coronary disease," *Circulation* vol. 64 (5), pp. 977-986, 1981

Guterman H., Nehmadi Y., Chistyakov A., Soustiel J.F., and Feinsod M., "A comparison of neural network and Bayes recognition approaches in the evaluation of the brainstem trigeminal evoked potentials in multiple sclerosis", *International Journal Biomedical Computing*, Vol. 43 (3), pp. 203-213, 1996

Hamprecht F.A., Achleitner U., Krismer A.C., Lidner K.H., Wenzel V., Strohmenger H.U., Thiel W., Gunsteren W.F., and Amann A., "Fibrillation power, an alternative method of ECG spectral analysis for prediction of countershock success in a porcine model of ventricular fibrillation", *Resuscitation*, Vol. 50, pp.287-296, 2001

Houghton A.R. and Gray D., *Making Sense of the ECG, A hands-on guide*, ARNOLD, 1997

Hsia P.W., Frerk S., Allen C.A., Wise R.M., Cohen N.M., and Damiano R.J., "A critical period of ventricular fibrillation more susceptible to defibrillation: real-time waveform analysis using a single ECG lead", *PACE*, Vol. 19, pp. 418-430, April 1996

Hsia P.W., Kuelz K.W., Wise R.M., Mahmud R., and Damiano R.J., "Ventricular fibrillation voltage and patch-to-patch impedance predict successful defibrillation during fixed energy DC shocks", *Computers in Cardiology 1992, IEEE Proceedings*, pp. 383-386, 1992

Hsu W., Lin Y, Heil J.E., Jones J., and Lang D.J., "Effect of shock timing on defibrillation success", *PACE*, Vol. 20, pp. 153-157, January 1997

Hsu W., Lin Y., Lang D.J., and Jones J.L., "Improved internal defibrillation success with shocks timed to the morphology electrogram", *Circulation*, Vol. 98, pp.808-812, 1998

Ivanov P.C., Rosenblum M.G., Peng C.K., Meitus J., Havlin S., Stanley H.E., and Goldberger A.L., "Scaling behaviour of heartbeat intervals obtained by wavelet-based time-series analysis," *Nature*, vol. 383, pp. 323-327, 1996

Jacobs I.G. and Oxer H.F., "A review of prehospital defibrillation by ambulance officers in Perth, Western Australia," *Med J Aust*; vol. 153, pp. 662-664, 1990

Johnson R.A. and Wichern D.W., *Applied Multivariate Statistical Analysis*, Fourth Edition, Prentice Hall, Upper Saddle River, New Jersey, 1998

Khadra L., Al-Fahoum A.S., and Al-Nashash H., "Detection of life-threatening cardiac arrhythmias using the wavelet transformation", *Medical & Biological Engineering & Computing*, Vol. 35, pp. 626-632, 1997

Khadra L., Dickhaus H., and Lipp A., "Representations of ECG – late potentials in the time-frequency plane", *Journal of Medical Engineering & Technology*, Vol. 17, November 6, pp. 228-231, 1993

Khadra L., Matalgah M., El-Asir B., and Mawagdeh S., "The wavelet transform and its applications to phonocardiogram signal analysis", *Medical Informatics*, Vol. 16, No. 3, pp. 271-277, 1991

Latorre F.D., Nolan J, Robertson C., Chamberlain D., and BaskettP., "European resuscitation council guidelines 2000 for adults advanced life support: a statement from the advanced life support working group and approved by the executive committee of the European resuscitation council", *Resuscitation*, Vol. 48, pp. 211-221, 2001

Lemire D., Pharand C., Rajaonah J.C., Dube B., and LeBlance A.R., "Wavelet time entropy, T wave morphology and myocardial ischemia", *IEEE Transactions on Biomedical Engineering*, Vol. 47, No. 7, pp. 967-970, 2000

Li C., Zheng C., and Tai C., " Detection of ECG characteristic points using wavelet transforms," *IEEE Trans Biomedical Engineering,* vol. 42, pp.21-28, 1995

Li H.G., Yee R., Mehra R., DeGroot P., Klein G.J., Zardini M., Thakur R.K., and Morillo C.A., "Effect of shock timing on efficacy and safety of internal cardioversion

for ventricular tachycardia", *Journal of the American College of Cardiology*, Vol. 24, No. 3, pp. 703-708, 1994

Link A., Endt P., Oeff M., and Trahms L., "Variability of the QRS signal in high-resolution electrocardiograms and magnetocardiograms", *IEEE Transactions on Biomedical Engineering*, Vol. 48, No. 2, pp. 133-142, 2001

Lu Z., Kim D.Y., and Pearlman W.A., "Wavelet compression of ECG signals by the set partitioning in hierarchical trees algorithm", *IEEE Transactions on Biomedical Engineering*, Vol. 47, No. 7, pp. 849-855, 2000

Mallat S., *A wavelet tour of signal processing*, San Diego, Academic Press, 1998

Marn-Pernat A., Weil M.H., Tang W., Pernat A., and Bisera J., "Optimizing timing of ventricular fibrillation", *Critical Care Medicine*, Vol. 29, No.12, pp. 2360-2365, 2001

Martin D.R., Brown C.G., and Dzwonczyk R., "Frequency analysis of the human and swine electrocardiogram during ventricular fibrillation", *Resuscitation*, Vol. 22, pp.85-91, 1991

Masson C. and Rieu R., "Time-frequency analysis of the noise produced by the closing of artificial heart valves: an in vitro study", *Medical Engineering & Physis*, Vol. 20, pp. 418-431, 1998

Mojsilovic A., Popovic M.V., Neskovic A.N., and Popvic A.D., "Wavelet image extesion for analysis and classification of infarcted myocardial tissue", *IEEE Transactions on Biomedical Engineering*, Vol. 44, No. 9, pp. 856-865, 1997

Monsieurs K.G., Cauwer H.D., Wuyts F.L., and Bossaert L.L., "A rule for early outcome classification of out-of-hospital cardiac arrest patients presenting with ventricular fibrillation", *Resuscitation*, Vol. 36, pp.37-44, 1998

Noc M., Weil M.H., Tang W., Sun S., Pernat A., and Bisera J., "Electrocardiographic prediction of the success of cardiac resuscitation", *Critical Care Medicine*, Vol. 27 (4), pp.708-714, 1999

Obaidat M.S., "Phonocardiogram signal analysis: techniques and performance comparison", *Journal of Medical Engineering & Technology*, Vol. 17, No. 6, pp.221-227, 1993

Park K.L., Lee K.J., and Yoon H.R., "Application of a wavelet adaptive filter to minimise distortion of the ST-segment", *Medical & Biological Engineering & Computing*, Vol. 36, pp. 581-586, 1998

Patwardhan A., Moghe S., Wang K., Cruise H., and Leonelli F., "Relation between ventricular fibrillation voltage and probability of defibrillation shocks", *Journal of Electrocardiology*, Vol. 31, No. 4, pp.317-325, 1998

Patwardhan A., Wang KE., Morghe S., and Leonelli F., "Bispectral with energies within electrocardiograms during ventricular fibrillation are correlated with shock outcome", *Annals of Biomedical Engineering*, vol. 27, pp. 171-179, 1999

Podbregar M., Kovacic M., Podbregar-Mars A., and Brezocnik M., "Predicting defibrillation success by 'genetic' programming in patients with out-of-hospital cardiac arrest", *Resuscitation*, Vol. 57, pp. 153-159, 2003

Povoas H.P., Weil M.H., Tang W., Bisera J. Klouche K., and Barbatsis A., "Predicting the success of defibrillation by electrocardiographic analysis", *Resuscitation*, Vol. 53, pp. 77-82, 2002

Rakotomamonjy A., Migeon B., and Marche P., "Automated neural network dectection of wavelet preprocessed electrocardiogram late potentials", *Medical & Biological Engineering & Computing*, Vol. 36, pp.346-350, 1998

Richard A. and Dean W., *Applied Multivariate Statistical Analysis*, Fourth Edition, Prentice Hall 1998

Rioul O and Vetterli M., *Wavelets and Signal Processing*, *IEEE SP Magazine*, pp. 14-38, October 1991

Rude R.R., Poole W.K., Muller J.E., Turi Z., Rutherford J., Parker C., Roberts R., Raabe D.S., Gold H.K., and Stone P.H., Willerson J.T., Braunwald E., "Electrocardiographic and clinical criteria for recognition of acute myocardial infarction based on analysis of 3,697 patients," *Am J Cardiol,* vol. 52: pp. 936-942, 1983

Sahambi J.S., Tandon S.N., and Bhatt R.K.P., "Quantitative analysis of errors due to power-line interference and based-line drift in detection of onsets and offsets in ECG using wavelets", *Medical & Biological Engineering & Computing*, pp. 747-751, November 1997

Sahambi J.S., Tandon S.N., Bhatt R.K.P., "Using wavelet transforms for ECG characterisation," *IEEE Engineering in Medicine and Technology,* vol. 16(1), pp. 77-83, Jan./Feb 1997

Sahambi J.S., Tandon S.N., Bhatt R.K.P., "Wavelet based ST-segment analysis", *Medical & Biological Engineering & Computing*, pp. 568-572, September 1998

Singer I. And Lang D., "Defibrillation threshold: clinical utility and therapeutic implications", *PACE*, Vol.15, pp. 932-949, 1992

Stefanovska A., Bracic M., and Kvernmo H.D., "Wavelet analysis of oscillations in the peripheral blood circulation measured by laser doppler technique", *IEEE Transactions on Biomedical Engineering*, Vol. 46, No. 10, pp. 1230-1239, 1999

Stewart A.J., Allen J.D., and Adgey A.A.J., "Frequency analysis of ventricular fibrillation and resuscitation success", *Quarterly Journal of Medicine*, New Series 85, No. 306, pp.761-769, 1992

Strohmenger H.U., Eftestol T, Sunde K., Wenzel V., Mair M., Ulmer H., Lindner K.H., and Steen P.A., "The predictive value of ventricular fibrillation electrocardiogram signal frequency and amplitude variables in patients with out-of-hospital cardiac arrest", *Anesthesia & Analgesia*, Vol. 93(6), pp.1428-1433, 2001

Strohmenger H.U., Linder K.H., and Brown C.G., "Analysis of the ventricular fibrillation ECG signal amplitude and frequency parameters as predictors of countershock success in humans", *Chest*, Vol. 111, pp.584-589, 1997

Strohmenger H.U., Linder K.H., Lurie K.G., Welz A., and Georgieff M., "Frequency of ventricular fibrillation as a predictor of defibrillation success during cardiac surgery", *Anesthesia & Analgesia*, Vol. 79, pp.434-438, 1994

Strohmenger H.U., Lindner K.H., Keller A. Lindner I.M., and Pfenninger E.G., "Spectral analysis of ventricular fibrillation and closed cardiopulmonary resuscitaiton", *Resuscitaiton*, Vol. 33, pp.155-161, 1996

Strohmenger H.U., Lindner K.H., Prengel A.W., Pfenninger E.G. Bothner U., and Lurie K.G., "Effect of Epinephrine and Vasopressin on median fibrillation frequency and defibrillation success in a porcine model of cardiopulmonary resuscitation", *Resuscitation*, Vol. 31, pp. 65-73, 1996

Thakor N.V., Sun Y.C., Rix H. and Caminal P., "Multiwave: a wavelet-based ECG data compression algorithm", *IEICE Transactions on Information and Systems*, Vol. E76-D, No.12, pp. 1462-1469, 1993

Thurner S., Feurstein M.C., and Teich M.C., "Multiresolution wavelet analysis of heartbeat intervals discriminates healthy patients from those with cardiac pathology," *Physical Review Letters,* vol. 80, pp. 1544-1547, 1998

Uchaipichat N., Addison P.S, Clegg G.R., Robertson C.E., Steen P.A., Eftestol T., and Watson J.N., "Wavelet transform-based methods to assess pre-shock probability of successful defibrillation in patients with ventricular fibrillation", *Proceeding of 2nd IEEE EMBS UK&RoI Postgraduate Conference on Biomedical Engineering & Medical Physics, Birmingham, UK (2003)*

Uchaipichat N., Addison P.S., Watson J.N., Clegg G.R., Robertson C.E., Steen P.A., and Eftestol T., "Wavelet power spectrum analysis of cardiac arrhythmias: ventricular fibrillation", *Proceeding of the 24th Electrical Engineering Conference Thailand*, 2001

Uchaipichat N., Watson J.N., Addison P.S., Clegg G.R., Robertson C.E., Steen P.A., and Eftestol T., "Optimal pre-shock signal length for time-frequency classification used in the prediction of successful defibrillation", *Proceeding of International Congress on Biological and Medical Engineering in Singapore*, 2002

Vetterli M. and Kovacevic J., *Waveletes and subband coding*, Englewoods Cliffs, New Jersy, Prentice Hall, 1995

Watson J.N., Addison P.S., Clegg G.R., Holzer M., Sterz F., and Robertson C.E., "Evaluation of arrhythmic ECG signals using a novel wavelet transform method," *Resuscitation*, vol.43, no.2, pp. 121-127, 2000

Watson J.N., Addison, P.S., Clegg G.R., Steen P.A., and Robertson C.E., "Practical issues in the evaluation of methods for the prediction of shock outcome success in out-of-hospital cardiac arrest patients", *Resuscitation,* 2005, (In Press)

Watson J.N., Addison P.S., and Sibbald A., "The de-noising of sonic echo test data through wavelet transform reconstruction," *Journal of Shock and Vibration*, vol. 6, pp. 267-272, 1999

Watson J.N., Uchaipichat N., Addison P.S., Clegg G.R., Robertson C.E., Eftestol T., and Steen P.A., "Improved prediction of defibrillation success for out-of-hospital VF cardiac arrest using wavelet transform methods", *Resuscitation*, Vol. 63, pp. 269-275, 2004

Weaver W.D., Cobb L.A., Dennis, D. Ray R., Hallstrom A.P., and Copass M.K., "Amplitude of ventricular fibrillation waveform and outcome after cardiac arrest", *Annal of Internal Medicine*, vol.102, pp.53-55, 1985

White R.D., and Russell J.K., "Refibrillation, resuscitation and survival in out-of-hospital sudden cardiac arrest victims treated with biphasic automated external defibrillators", *Resuscitation*, Vol. 55, pp.17-23, 2002

Wiklund U., Akay M., and Niklasson U., "Short-term analysis of heart-rate variability by adapted wavelet transforms," *IEEE Engineering in Medicine and Biology* vol. 16(5), pp. 113-118, Sept/Oct 1997

Xie J., Weil M.H., Sun S., Tang W., Sato Y., Jin X., and Bisera J. "High-energy defibrillation increases the severity of postresuscitation myocardial dysfunction", *Circulation*, vol.96, pp.683-688, 1997